Development of Supported 1D Nanomaterials by Vacuum and Plasma Technologies: From Sensors to Nanogenerators

Alejandro Nicolás Filippin Emilio
Instituto de Ciencias de Materiales de Sevilla (US-CSIC)
Universidad de Sevilla
Ph.D. thesis

Fabrication of 1D nanostructures by vacuum and plasma processes: From sensors to nanogenerators

Alejandro Nicolás Filippin Emilio

Supervised by:

Dr. Ana Isabel Borrás Martos
Tenured scientist of CSIC
Instituto de Ciencia de Materiales de Sevilla
(CSIC-Universidad de Sevilla)

Dr. Ángel Barranco Quero
Tenured scientist of CSIC
Instituto de Ciencia de Materiales de Sevilla
(CSIC-Universidad de Sevilla)

Dr. Juan Ramón Sánchez Valencia
Postdoctoral fellow
Instituto de Ciencia de Materiales de Sevilla
(CSIC-Universidad de Sevilla)

Tutor:
Prof. Alfonso Caballero Martínez
Full Professor
Departamento de Química Inorgánica
(Universidad de Sevilla)

A la memoria de mis abuelos y tíos

1. Introduction

…"What could we do with layered structures with just the right layers? What would the properties of materials be if we could really arrange the atoms the way we want them? They would be very interesting to investigate theoretically. I can't see exactly what would happen, but I can hardly doubt that when we have some control of the arrangement of things on a small scale we will get an enormously greater range of possible properties that substances can have, and of different things that we can do."…

This is a transcription of a fragment of the famous talk given by Richard P. Feynman to the American Physical Society in Pasadena on December 1959. It is notorious how these words, more than 50 years later, are more present than ever before.

The main motivation behind nanotechnology is not to decrease drastically the amount of material/s required for a given application, which is indeed desired in a world of limited resources and can be effectively addressed by nanotechnology, but to exploit novel and enhanced materials properties as a consequence of the extreme size reduction of matter. By lowering down dimensions to the nanoscale, not only the specific surface area increases significantly but also the electronic properties may change considerably (owing for example to quantum size effects, strong contribution of surface reconstruction or surface curvature can be obtained). These effects might also contribute to drastically improve the reaction/interaction between a device and the surrounding media, thereby making the system more effective [Diebold U., Surf. Sci. Rep. 2003][Eustis S., Chem. Soc. Rev. 2006], or even opening entirely novel reaction pathways.

Naturally, the technology involved in the fabrication of these nanostructures has its limitations. It is still difficult to scale up these processes and vacuum technology continues to be expensive (in comparison to solution-processed methods). Nevertheless, the constant miniaturization of technology, the necessity of more environmentally friendly production methods, the search for high quality high-tech devices, etc. have triggered the development and expansion of these fabrication processes. Furthermore, the vacuum technology related to them has been evolving steadily and it is maturing reasonably fast, which in turn will bring costs down and stimulate its use.

1.1. Classification and fabrication of nanomaterials

Nanomaterials is the term given to a wide range of systems whose size is above molecular dimensions and with at least one of their dimensions below 100 nm. Nanomaterials may be classified in several ways according to their applications and

philosophy adopted. For instance, they can be classified by their dimensionality (Siegel), type of nanomaterial (carbon based, metal based, dendrimers, and composites), crystalline form and chemical composition (Gleiter), etc. [Gleiter H., Acta mater. 2000][Siegel R. W., Springer 1994][Ngô C. & van der Voorde M., Atlantis Press 2014].

According to their dimensionality, nanomaterials can be classified into:

- 0D: All dimensions of the nanostructure are below 100 nm. e.g. nanoparticles or clusters.
- 1D: One dimension above 100 nm. e.g. Nanowires, nanobelts, nanorods, nanotubes, etc.
- 2D: Two dimensions above 100 nm. eg. nanocoatigns, grids, thin films of molecular monolayers, etc.
- 3D: All three dimensions escape from the nanoscale, but the material is formed by lower-dimensionality nanomaterials. e.g. polycristals, powders, frameworks, colloids, networks, nanoboxes, etc.

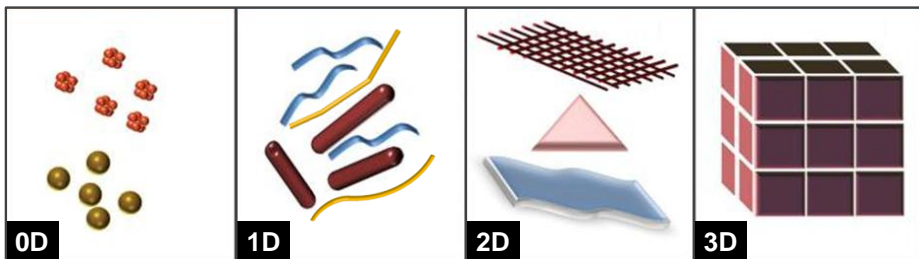Fig. 1 illustrates the four cases.

Figure 1. Different types of nanomaterials: 0D, 1D, 2D and 3D. Modified from [Sajanlal P. R., Nano Rev. 2011].

More complex or hierarchical nanostructures require a slightly more sophisticated classification which takes into account the dimensionality of the final nanostructure and that of the elementary units or building blocks. A relatively simple and straightforward classification nomenclature that encompass several combinations of nanostructures was introduced by Pokropivny V. V. and is known as kDlmn classification, shown and self-explained in Fig. 2 (here it has been limited to 0D and 1D nanostructures).

Figure 2. kDlmn dimensionality classification of nanostructures (truncated up to 1D) [Pokropivny V. V., Mater. Sci. Eng. C 2007].

Due to the fact that this thesis is focused on 1D nanostructures, only the classification involved with this dimensionality will be commented.

Different types of 1D nanostructures are presented in Fig. 3. According to the kDlmn classification, nanowires, nanobelts, nanorods and nanotubes are just 1D materials. Hierarchical nanostructures such as nanotrees, axial and radial junctions (core@shell) are all designated as 1D11, whereas 1D materials decorated with nanoparticles are regarded as 1D10. Naturally, these systems are being considered as isolated ones for the sake of simplicity, but for example, a highly interconnected array of nanotrees falls into the category of 3D11 nanomaterials.
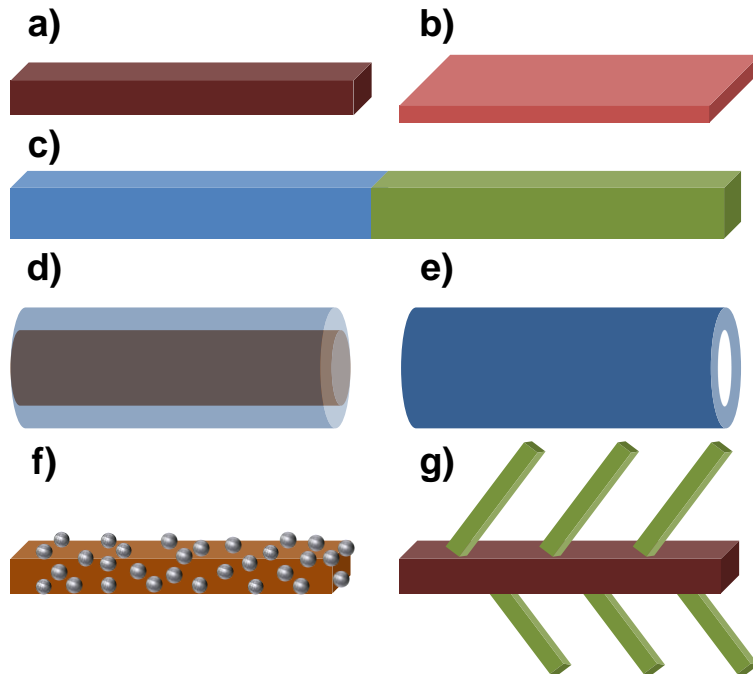
Figure 3. Some examples of 1D nanostructures. a) square nanowire, b) nanobelt, c) axial junction, d) radial junction (core@shell), e) nanotube, f) nanowire decorated with nanoparticles, and g) branched nanowire (nanotree).

There are two well-established general approaches for the fabrication of nano-objects, the top-down and bottom-up procedures (Fig. 4). Independently of the method chosen, it should be taken into consideration the manufacturing costs, yields, environmental impact, etc. which will ultimately decide the viability of the material.

- ❖ Top-down approach: consists in the "erosion" of macroscopic materials by implementing subsequently finer tools to create nanometer-size structures. Examples include lithographic techniques, micromachining, laser ablation, etching, grinding, etc.
- ❖ Bottom-up approach: atomic and molecular units are assembled to form molecular structures ranging from atomic dimensions to nano-sized structures and above. Examples span from physical methods such as evaporation techniques, sputtering, spray pyrolysis, inert gas phase condensation technique, etc. to chemical methods such as electrochemical deposition, hydrothermal and solvothermal techniques, chemical vapor deposition, sol-gel, etc. [Ngô C. & van der Voorde M., Atlantis Press 2014][Tiwari J. N., Prog. Mater. Sci. 2012].
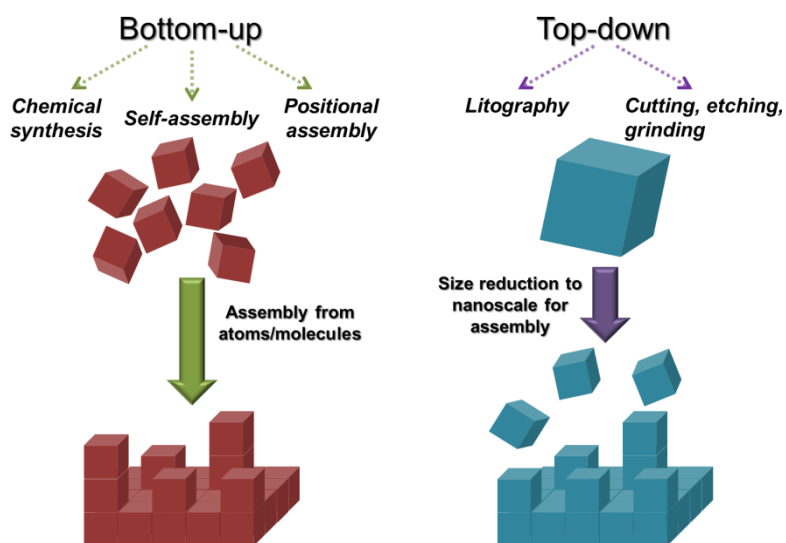
Figure 4. Illustration of the top-down and bottom-up processes.

1.1.1. Description of 1D Core@Shell nanostructures

Among the different nanostructures already mentioned, 1D core@shell materials have been of central interest for this thesis. These materials have been extensively studied an applied in a diversity of fields, including water splitting [Hernández S., ACS Appl Mater Interfaces 2014], catalysis [Wei H., Nano-Micro Lett. 2011][Hasan M., J. Electrochem. Soc. 2012], supercapacitors [Singh A. K., J. Mater. Chem. A 2013], solar cells [Adachi M. M., Sci. Rep. 2013][Tamang A., Opt. Express 2014], electronics [Dong Y., Nano Lett. 2008], etc.

The combination of Organic nanowires (ONWs) produced by Physical vapor deposition (PVD) and metal oxides fabricated by Plasma enhanced chemical vapor deposition (PECVD) to produce 1D core@shell nanostructures originates an enormous field of exciting possibilities and new challenges, with promising potential in the fields of wettability, solar cells, waveguides, sensors, etc. [Macías M., Adv. Funct. Mater. 2013]. The fabrication and characterization of these nanostructures began in the Ph.D. thesis of Dr. Manuel Macías Montero, but here the complexity (e.g. number and nature of the shells) and applicability of these systems has been augmented. Furthermore, the relatively unexplored fabrication of 1D organic core@shell has been studied and significantly developed during this work.

The extremely high aspect ratio of these nanostructures confers them unique properties and advantages (compared to thin films), just to mention but a few:

- Remarkably high surface area: it can be controlled by adjusting the density of NWs, their length, width, the possibility of adding branches to the main NW and thus generating branched/hyperbranched nanostructures (nanotrees), the microstructure determining the porosity/roughness of the inorganic shell, etc.
- Multilayer 1D nanostructures: Several shells of different metals/metal oxides/organic compounds may be produced one over the other (Mamushka structure) in order to attain the desired properties for the application in question. In addition, shells of mixtures may be produced as well.
  Metal oxide shells can be fabricated by PECVD as already mentioned, or by plasma oxidation of a shell formed by metalorganic molecules such as porphyrins or phthalocyanines, whereas metallic shells can be formed by a reductive plasma of these compounds or an oxidative plasma of those containing precious metals in their structure.
- Highly interconnected networks of NWs are easily attainable (nanotrees), which can increase even further the surface area of the final core@shell array [Borras A., Adv. Mater. 2009].
- The use of organic molecules for the cores allows for the production of these nanostructures to be compatible with sensible substrates and flexible ones, which cannot stand temperatures much beyond 100 ºC under vacuum. Moreover, a wide range of substrates may be employed due to large diversity of porphyrins and phthalocyanines, i.e., it is often possible to find a suitable molecule to grow ONWs in a particular substrate, after which a shell may be formed [Macías M., Adv. Funct. Mater. 2013].
- Less requirement of raw materials when compared to thin films.
- Whole 1D devices can be readily fabricated using a combination of PVD, PECVD, plasma post-treatment, etc.

In Fig. 5 some ONW@ZnO can be appreciated. Fig. 5b demonstrates the compatibility of the various techniques for the fabrication of hybrid nanostructures.
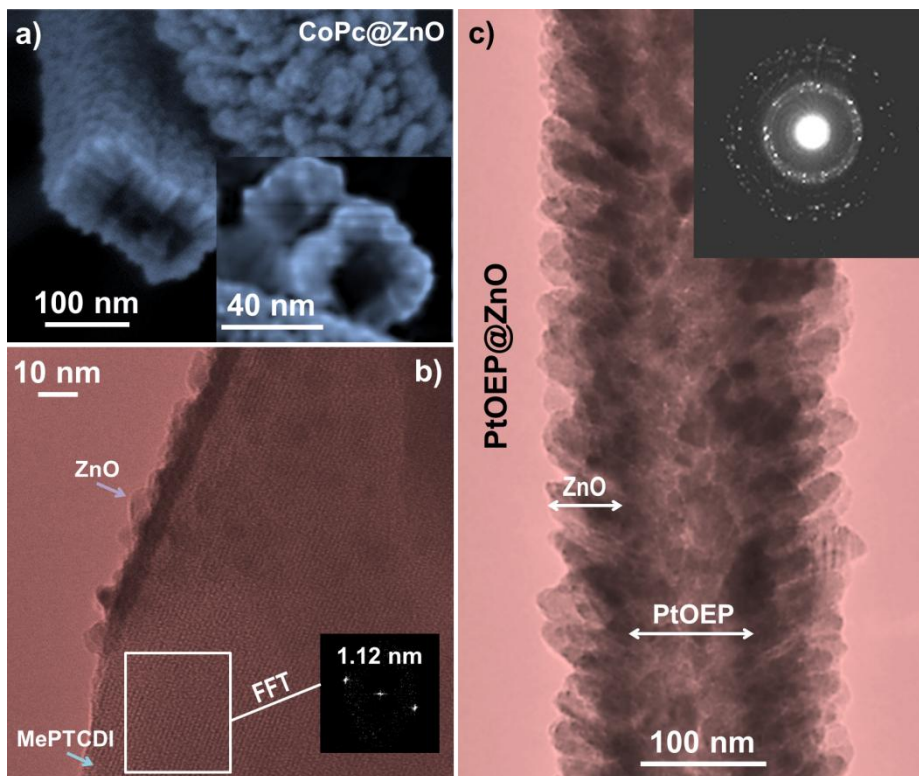
Figure 5. a) Cross-section view of broken hybrid NWs. b-c) TEM images and selected area diffraction (SAED) (inset) of two distinct hybrid NWs by bright field mode. In (c) the molecular planes of MePTCDI are clearly visible [Macías-Montero M., Adv. Funct. Mater. 2013].

1.2. Device Fabrication and concept of One-reactor

1.2.1. *ONE-REACTOR*. In chemistry, there is an upward trend in coupling several steps of a multi-step chemical reaction into just one reactor. This strategy is generally known as *One-pot synthesis* and it is of much interest for chemists and the chemical industry due to economic and environmental advantages [Zhao W., Curr. Org. Synth 2012]. The *One-pot synthesis* may be extrapolated as well to a vacuum reactor where numerous deposition techniques and sample treatment processes are demanded. A chamber capable of performing all required fabrication operations without the necessity of transferring the samples to other equipments can be regarded as a *One-reactor*. This concept present several potential advantages in comparison with usual reactors limited to only one operation:

- ➤ Faster fabrication process. Every cycle of pumping and breaking the vacuum it is considerable time-consuming. By reducing the number of these cycles to a minimum, production time drops significantly.
- ➤ Lower manufacturing costs. An increase in sample/device output due to a fabrication time reduction obviously brings costs down. Furthermore, by adapting a chamber to work as a One-reactor, the number of equipments and power consumption are drastically decreased, making the whole process cheaper and more environmentally friendly.
- ➤ Less reproducibility issues and higher yields. Avoiding exposure of fresh samples to air in-between preparation stages (samples transfer), contamination problems and undesired reactions are diminished.

The One-reactor approach could make the fabrication of highly integrated and complex devices more feasible. It could be applied to the production of a fully operational Lab-on-chip, implementing different types of nanostructures to enhance the functionality of the device and reduce its size and cost as far as possible. A concept of a "nanostructured" Lab-on-chip is shown in Fig. 6, briefly describing all its individual components. The possibility of creating novel 1D nanostructures and applying them to real devices, such as in the Lab-on-chip, has been one of the main motivations behind this work.
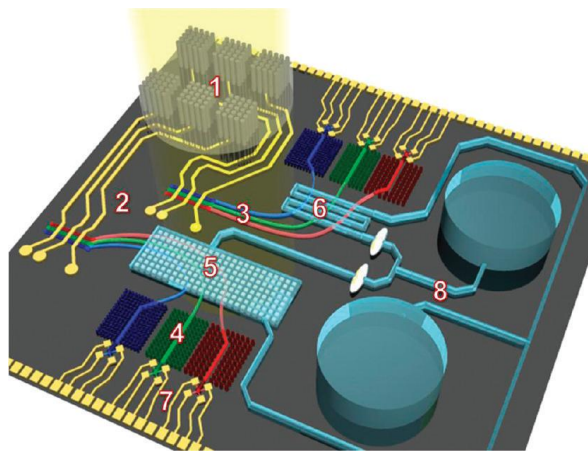
Figure 6. "Nanostructured" Lab-on-chip scheme. Some possible components would be: solar cells as on-chip power supplies (1), laser diodes/LEDs as light sources (2), nanoribbons (3) and 2D photonic bandgap (PBG) nanowire arrays (4) as filters and waveguides to select and route input and output signals; (6) sample analysis chambers, such as silver nanocube arrays for SERS (5) or nanoribbon/sample

intersection for absorption analysis; nanowire based photodectectors (7) and a microfluidic system for liquid sample transport (8) [Yang P., Nano Lett. 2010].   .

Some advanced 1D nanostructured devices that could also be fabricated by means of a One-reactor include:

Piezoelectric nanogenerators. Even though the progress made in microelectronics and nanotechnology has helped to greatly cut down the power consumption of electronic and electromechanical devices, they still require a small amount of energy to fulfill their function. This energy can be effectively provided by a piezoelectric generator integrated in the same chip, exploiting the movement of animals, humans, plants (due to wind), blood, muscles, organs, wind, water currents, sound, etc. and thus creating self-powered devices [Wang Z. L. Adv. Func. Mater. 2008][Yang R., Nano Lett. 2009][Wang Z. L., Sci. Am. 2008]. The photograph in Fig. 7 is an example of a piezoelectric attached to a living heart which could provide energy to a peacemaker and avoid surgeries for battery replacement.
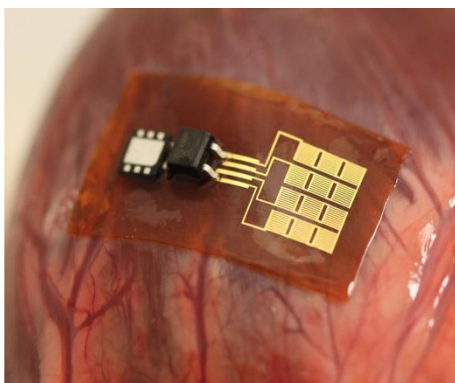
Figure 7. Flexible piezoelectric device installed on a living animal heart [Dagdeviren C, PNAS 2014].

Excitonic solar cells. Modern solar cells may be split into two categories: conventional solar cells, such as the well-established silicon p-n junctions, and excitonic solar cells (XSCs). Dye sensitized solar cells (DSSCs) and the majority of organic solar cells belong to the second class. The main difference between both types of cells lies in the electron-hole pair generation mechanism. In XSCs, carriers are photogenerated and simultaneously separated across a heterointerface, while in conventional solar cells carriers emerge throughout the bulk of the semiconductor and are separated lately at their arrival to the junction. XSCs present an alternative to conventional cells despite they cannot compete in terms of efficiency, but they do have

the potential to become cheaper and more environmentally friendly. Moreover, they can be made flexible, a characteristic that facilitates their implementation in portable electronic devices and wearables. Furthermore, DSSCs may exhibit a rich and eye-catching gamut of colors while still being semi-transparent, which is attractive in buildings (Fig. 8) [Gregg B. A., J. Phys. Chem. B 2003][Mehmood U., Adv. Mater. Sci. Eng. 2014].

The work carried out here has been focused on "classical" DSSCs, but could be extended to organic cells or solid state DSSCs.
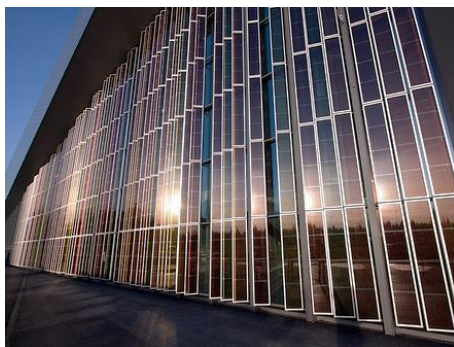
Figure 8. DSSCs installed at the Swiss Tech convention center.

Nanosensors. Optical and conductometric sensors are greatly demanded in areas such as chemical analysis, health care and environment control. The current challenge consists in the development of nanoscale sensors compatible within photonic and optoelectronic devices with a higher selectivity and sensibility and, as far as possible, multisensing performance. Organic and metalorganic nanowires, nanotrees and both organic and hybrid core@shells nanostructures are expected to increase the sensing sensitivity by virtue of their higher surface when compared to their 2-D counterparts (thin films). A nanoengineered sensor which acts as an electronic nose for the detection of toxins in the food supply chain is presented in Fig. 9.
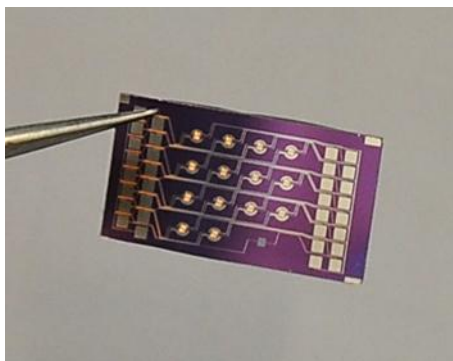
Figure 9. Nanosensor array for the detection of harmful airbone substances [http://ucrtoday.ucr.edu/15913].

1.3. Methodology

Vacuum Deposition

Vacuum deposition is the name given to a family of techniques used to deposit layers of material atom-by-atom or molecule-by-molecule on a solid surface. Material from a thermal vaporization source reaches the substrate with little or no collision with gas molecules in the space between the source and substrate. The trajectory of the vaporized material is "line of sight." The vacuum environment also provides the ability to reduce gaseous contamination in the deposition system to a low level. Typically, vacuum deposition takes place in the gas pressure range of 10^{-1} mTorr to 10^{-9} mTorr, depending on the level of gaseous contamination that can be tolerated in the deposition system and the process requirements. Vacuum deposition is generally used to form optical interference coatings, mirror coatings, decorative coatings, permeation barrier films on flexible packaging materials, electrically conducting films, wear resistant coatings, and corrosion protective coatings [Mattox D., Elsevier 2010]. These are all examples of compact layers, but the technique can be equally employed to create porous films [Parra-Barranco J., ACS Appl. Mater. Interfaces 2015][Vick D., J. Mater. Res. 2002][Gil-Rostra J., Sol. Energy Mater. Sol. Cells. 2014][Sánchez-Valencia J. R., Adv. Mater. 2011][González-García L., J. Mater. Chem. 2010].

If the vapor source is a solid or a liquid, the process is designated as Physical Vapor Deposition (PVD), whereas in Chemical Vapor deposition (CVD) the source material is a reagent which undergoes chemical reactions during the deposition. Before describing each technique, a brief description of plasmas will me made due to their relevance in many vacuum deposition processes.

Introduction to plasmas

Plasmas make up more than 99% of visible matter in the universe. They consist of positive ions, electrons or negative ions, and neutral particles. Plasma is regarded as the fourth state of matter. When a solid (the first state of matter) is heated, the particles in it get sufficient energy to loosen their structure and thus melt to form a liquid (the second state of matter). After obtaining sufficient energy, the particles in a liquid escape from it and vaporize to gas (the third state of matter). Subsequently, when a significant amount of energy is applied to the gas through mechanisms such as an electric discharge, the electrons that escape from atoms or molecules not only allow ions to move more freely but also produce more electrons and ions via collisions after accelerating rapidly in an electric field. Eventually, the higher number of electrons and ions change the electrical property of the gas, which thus becomes ionized gas or plasma.

Plasmas can be classified into three categories according to their thermal equilibrium:

- ❖ Thermal Equilibrium Plasma: The electron temperature (T_e), ion temperature (T_i), and neutral temperature (T_n) are identical in thermal equilibrium plasma. Examples include the natural fusion reactor (Sun), a magnetic field (of tokamak design), or inertial (laser) confinement of a plasma.
- ❖ Nonthermal Equilibrium Plasma: the electron temperature (T_e) is considerably higher than in ions (T_i) and neutrals (T_n), that is, $T_e \gg T_i, T_n$. Nonthermal equilibrium plasmas are generated by corona discharge, glow discharge, arc discharge, capacitively coupled discharge, inductively coupled discharge, wave heated plasma, and so on. Applications of nonthermal plasma have expanded to cover a large number of fields including environmental engineering, aeronautics and aerospace engineering, biomedicine, textile technology, and analytical chemistry.
- ❖ Local Thermal Equilibrium Plasma: the electron, positive ion, and neutral temperatures are in the same range. The ion temperature of local thermal equilibrium plasma is 3,000–10,000 K (0.4–1 eV), which is much higher than that of nonthermal plasma, but its electron temperature is much lower (0.4–1 eV compared with 2–10 eV of nonthermal plasma). Local thermal equilibrium plasma can be generated by DC and RF arcs, or by an inductively coupled torch. They are used for plasma spraying (coating) and thermal plasma chemical and physical vapor deposition [Chu P. K., CRC Press 2014].

In this work only nonthermal equilibrium plasmas were involved.

1.3.1. Physical Vapor Deposition

Physical vapor deposition (PVD) processes are atomistic deposition processes in which material is vaporized from a solid or liquid source in the form of atoms or molecules, transported in the form of a vapor through a vacuum or low pressure gaseous environment to the substrate where it condenses. Typically, PVD processes are used to deposit films with thicknesses in the range of a few nanometers to thousands of nanometers of elements and alloys as well as compounds using reactive deposition processes; however they can also be used to form multilayer coatings, graded composition deposits, very thick deposits and freestanding structures [Holleck H., Surf. Coat. Technol. 1995]. The PVD process can be modified or adapted to cover substrates of an incredible range of sizes and geometries like silicon wafers, cutting tools, watchbands, windows, etc. (Fig. 10) [Knotek O., Surf. Coat. Technol. 1993][faltaría agregar otra referencia] Moreover, the deposition on flexible substrates has successfully been addressed as well (Fig. 13) [Silva N. L., J. Mater. Sci.: Mater. Electron.][Han T., Nat. Photonics 2012][Wang Z. B., Nat. Photonics 2011].

The main categories of PVD processing are vacuum evaporation, sputter deposition, arc vapor deposition, and ion plating. Here the focus will be put on the first two techniques used to fabricate organic, inorganic and hybrid materials.

Figure 10. Objects which require one or more PVD processes for their production: A drill covered with TiCN (left) and a 65" UHD OLED TV (right).

In this thesis up to 3 distinct PVD techniques were employed for the fabrication of organic and inorganic thin films and 1D nanostructures: *Glancing Angle Deposition (GLAD), DC and magnetron sputtering and Organic Physical Vapor Deposition (OPVD).*

a) Glancing Angle deposition (GLAD)

By employing the technique known as Glancing Angle Deposition (GLAD) it is possible to fabricate nanometric columnar films with controlled shape and porosity. The technique consists in the evaporation of a given material, which arrives at the substrate surface with a high zenith angle with respect to surface normal (Fig. 11). As a result, self-aligned tilted nanocolumnar structures can be produced due to shadowing effects during the film growth. There are several parameters controlling the morphology of the columns, from which it is worth mentioning the evaporation angle and rate [Hawkeye M. M., John Wiley & Sons 2014].
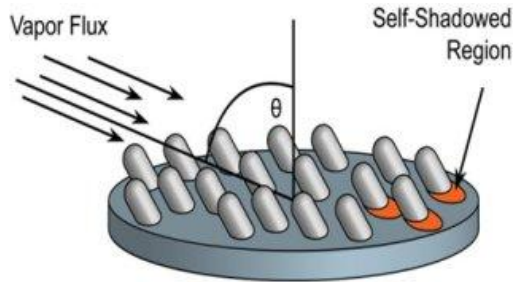
Figure 11. Illustration of the growth mechanism in GLAD [Schubert F. M., Appl. Phys. Lett. 2007].

b) DC and magnetron sputtering

The DC sputtering system is composed of a pair of electrodes, a cathode and an anode. The top plasma-facing surface of the cathode, known as the target, is covered with the material to be deposited on the substrates, which placed on the anode. When the sputtering chamber is kept in argon gas at around 0.1 torr and several kilovolts of dc voltage are applied between the electrodes, the glow discharge is initiated. The Ar ions* in the glow discharge are accelerated at the cathode fall and sputter the target; these sputtered particles collide with gas molecules and eventually diffuse to the substrate resulting in the deposition of thin film on the substrates. The process can be observed in Fig. 12 where the cathode is a Ag wire.

Figure 12. DC sputtering of Ag at the Nanotechnology on Surfaces group, ICMS.

* Other gases may be used besides Ar.

DC sputtering allows higher deposition rates than electron or ion beam processes. A limitation is that the ion flux cannot be controlled independently of the ion energy. Even higher deposition rates may be achieved with magnetron sputtering configuration, where electrons are magnetically confined close to the target, increasing the ionization of the gas and thus the sputtering rate. Furthermore, in the last case there are virtually no restrictions in the target nature, whereas in DC configuration the target should be conductive [Wasa K., William Andrew Inc. 2004][Harry J. E., Wiley-VCH 2010].

c) Organic Physical Vapor Deposition (OPVD)

Going organic. While it is true that organic semiconductors still cannot rival their inorganic counterparts in terms of performance, the gap is getting narrower and organics will certainly become superior in a wide range of applications, an irrefutable proof of which are living organisms. Of course, nature has had much more time to develop and refine its designs, but organic research and technology has advanced at a tremendous speed. To a great extent, this research effort has been triggered by the possibility of creating low-cost, light-weight and flexible electronics such as OLEDs, memory devices based on molecular spintronics, sensors, wearables, solar cells, field effect-transistors and integrated circuits, flexible and transparent electrodes, etc. [Feature, Nat. nanotechnol. 2013][Smits E. C.P., Nat. Lett. 2008][Xia Y., Adv. Mater. 2012].

The progress made in the field of organic semiconductors has already been materialized in many functional prototypes and cutting-edge technologies: microchips, OLEDs for stunning displays and lighting, organic photovoltaics, non-volatile memory, medical sensors, etc. [Myny K., J. SOLID-STATE CIRCUITS 2012][Heliatek, 2013][Liu Y., Nat. Commun. 2014][Kim R. H., Nat. Commun. 2014][Lochner C. M., Nat. Commun. 2014]. Some of these devices are shown in Fig. 13.
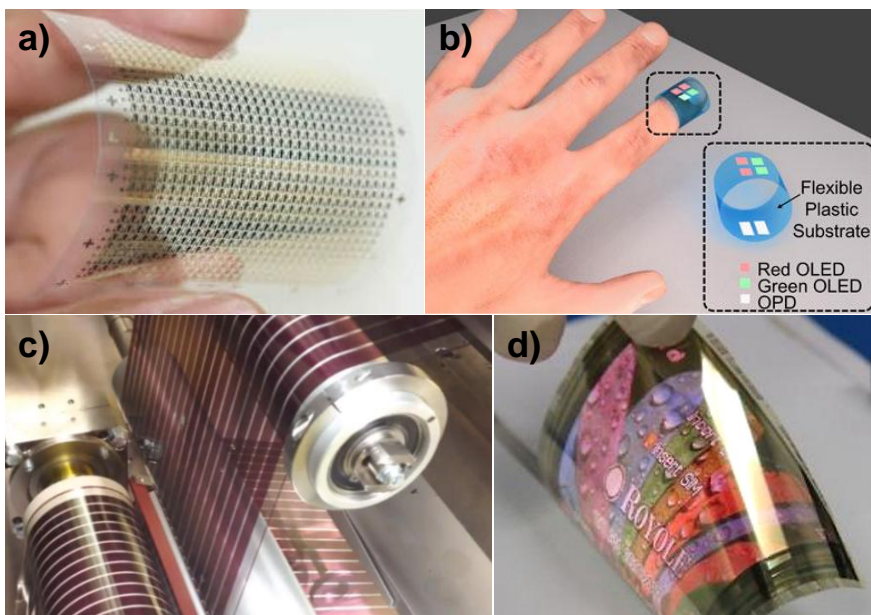
Figure 13. Examples of organic semiconductors in real devices. a) Organic nonvolatile memory [Sekitani T., Science 2009] b) All-organic pulse oximeter [Lochner C. M., Nat. Commun. 2014], c) Organic solar cell produced by [Andersen T. R., Energy Environ. Sci. 2014] and d) 0.01 mm thick full-color flexible AMOLED [Royale corporation, 2014].

OPVD relies in the evaporation of organic molecules, generally by thermal evaporation, to generate organic thin films. By a proper choice of the deposition conditions, i. e. deposition rate, substrates nature and temperature, pressure, etc., 1D organic nanostructures can be growth, such as nanowires, nanobelts, nanorods, etc. Due to their incredible high aspect ratio, intrinsic anisotropy, two-dimensional quantum confinement, electronic properties, etc. 1D semiconductor nanowires, nanorods, nanobelts and so on have attracted special attention among researchers [Zhang C., Annu. Rep. C 2013]. Owing to their relevance in this thesis, a brief description of the growth mechanism of ONWs will be given.

c1) Mechanism of formation of Organic Nanowire (ONWs)

The force for the formation of organic nanowires (ONWs) from **planar** aromatic molecules is the π-stacking, which directs the crystallization process responsible for the growth mechanism of these 1D nanostructures. A supersaturarion regime leads the crystallization process, and the extent of the former depends upon:

➢ The number of molecules arriving at the substrate per unit area and time. This is the flux of molecules and is given by the deposition rate. A very low rate will not satisfy de supersaturation condition and no crystals will develop, whereas at very high rates the quality of the crystals will diminish dramatically.

➢ The temperature of the substrate. If it is too low the molecules simply do not have enough energy to move freely on the surface of the substrate and distribute themselves at the nucleation sites, so as a result a film is formed. On the other hand, if the temperature is too high, the molecules do not stick to the substrates and no material is deposited on them. Moreover, there is a range of temperatures where the density and width of the NWs may be tuned, e.g., at a higher temperature the density and width of the NWs usually decrease.

➢ The chemical nature, roughness and morphology of the substrates. The surface free energy of the substrates depends on the former, and hence their sticking properties and optimal NW formation temperature will change, while the morphology and roughness provide the adequate and necessary nucleation sites. It is worth mentioning that if the size of the nucleation site is smaller than the average diameter of the NWs, then their formation is severely inhibited [Mbenkum Beri M., Nano Lett. 2006][Borrás A., Langmuir 2010 26(3)][Borras A., Langmuir 2010 26(8)].

All the aforementioned variables can be experimentally controlled, and the density, length and width of the NWs may be varied at will.

The formation of the NWs comprises several stages as illustrated in Fig. 14:

i. Presence of nucleation sites: defects, rough surfaces, metallic nanoparticles, etc.
ii. Arrival of the molecules to the surface of the substrate in an appropriate concentration (to satisfy the supersaturation condition) and molecular diffusion until reaching the nucleation sites.
iii. Formation of the crystal by self-assembly of the molecules.
iv. Development of the nanowire.
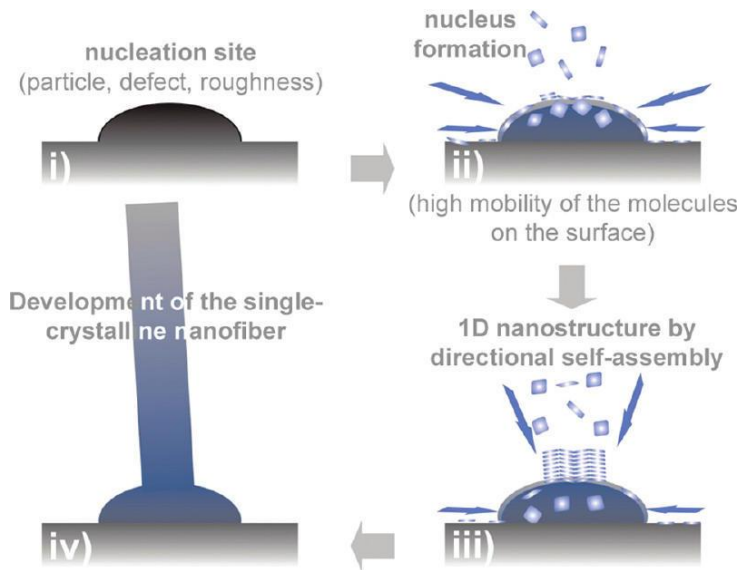
Figure 14. Stages of ONWs formation and growth [Borras A., Langmuir 26(8) 2010].

As shown in Figure 15, an ONW is actually a single-crystal 1D nanostructure. In the cropped image at the right it is even possible to visualize the molecular planes along the longest axis of the NW.
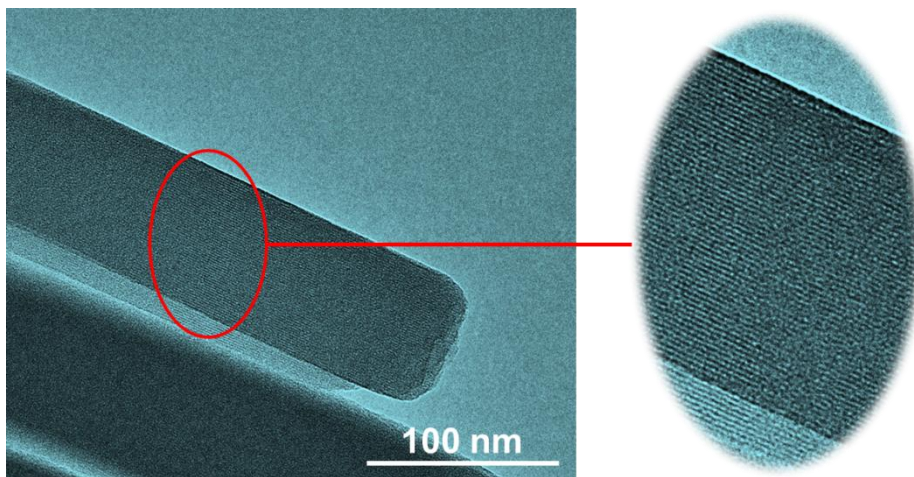

Figure 15. Bright field TEM image of iron phthalocyanine NWs and a cropped image of one section of the NWs.

c2) Remote Plasma Assisted Vacuum Deposition (RPAVD)

This method has been completely developed by the group of Nanotechnology on Surfaces and is devoted to the fabrication of composite thin films containing luminescent organic molecules. One of the aims of this work is to extend the procedure to the deposition of conformal organic shells on the ONWs and to incorporate new material precursors such as n- or p-type semiconducting molecules including (metal) phthalocyanines and (metal) porphyrins, which may be post-treated to generate metallic or oxide shells/nanowires.

In contrast to conventional plasma polymerization, the precursor molecules may suffer negligible fragmentation by the discharge due to a fine regulation of the interaction between the low/medium power microwave plasma and the precursor molecules sublimated in the afterglow region. This is achieved by the simultaneous adjustment of different deposition parameters, namely MW power, the total pressure, the sublimation rate and the geometrical arrangement used for the deposition. From previous results, the distance between the plasma and the growing film is one of the main operating parameters of RPAVD process, given that it controls the interaction between plasma discharge and precursors molecules. This distance, limiting the plasma-precursor interaction, makes the deposition process highly versatile, inasmuch as gradually regulates the film properties. By only modifying it, the method provides a wide range of films, from a highly cross-linked plasma polymer without the retention of original precursor monomers (deposition at the glow discharge), to plasma films containing a controllable amount of active dye molecules (deposition in the afterglow). By further increasing the plasma-to-substrate distance or the deposition rate, one obtains films which resemble more to those prepared by vacuum deposition (without plasma) [Aparicio F. J., J. Phys. Chem. C 2012][Aparicio F. J., J. Mater. Chem. C 2014].

In Fig. 16, the difference in morphology between a vacuum sublimated perylene thin film and its RPAVD film counterpart can be easily appreciated. RPAVD film looks much more homogeneus, continuous and without the presence of islands or aggregates.
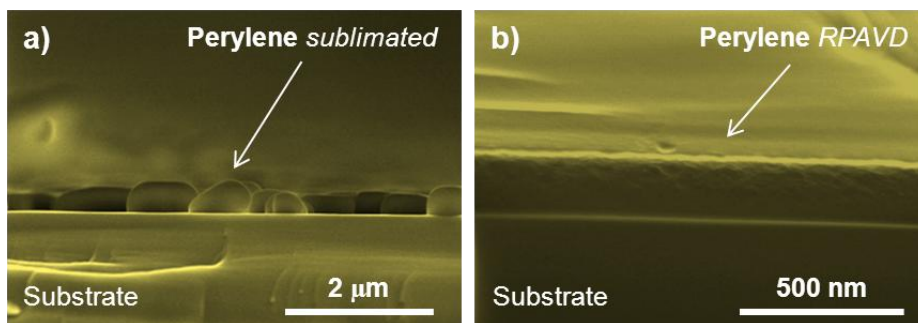
Figure 16. Microstructure of a sublimated perylene (a) and its RPAVD thin film counterpart (b) [Alcaire Martín M., Ph.D. thesis 2015].

c3) Reagents for OPVD and RPAVD

Porphyrins and Phtalocyanines

These compounds are structurally related and have been extensively studied and implemented as dyes, catalysts, semiconductors, sensors, etc. [Livshits, J. Struct. Chem. 1967][Castillero P., App. Mater. Interfaces 2010][Wang Z., Adv. Mater. 2006][Lloyd M., Mater. Today 2007]. Their versatile characteristics and properties can be largely attributed to the extensively delocalized π-system which is electronically highly sensitive and tunable. Furthermore, the nature of peripheral substituents and identity of the central metal ion have great ability to tune the electronic levels of these molecules. The nature of interaction between the metal ion and the porphyrinato or phthalocyanato moieties is such that both species mutually influence their electronic levels [Falk J. E., Elsevier 1964].

Porphyrins and phthalocyanines can be used as building blocks for the fabrication of organic nanostructures through self-assembly which is driven by supremolecular interactions, i.e., van der Waals forces, π-π interactions, metal coordination and hydrogen bonding. They possess an extensive network of delocalized electrons, the so called π-electrons, which allows this class of molecules to undergo aromatic-aromatic interactions and stack one over the other, which is known as π-stacking [Kadish, Porphyrin handbook]. The self-assembly in highly π-conjugated planar systems is mainly dominated by this π-π interactions, but it is largely affected by the type of substituents and central metal ion which can lead to different nanostructured motifs, such as tubes, rods, sheets, nanowires, etc [di Natale, Mater. Today 2010]. The formation of Nanowires is of central interest in this thesis and will be further explained.

The molecular structures of a general porphyrin and phthalocyanie are shown in Fig. 17a and 17b, whereas in figure 17c and 17d their metalloderivatives counterparts are represented. In the latter, the existence of central cations with oxidation states higher than two was taken into account by the addition of axial substituents, which originate non-planar molecules.

2,9-DIMETHYL-ANTHRA(2,1,9-DEF,6,5,10-'E'F')DIISOQUINOLINE-1,3,8,10-TETRAONE (MePTCDI)

Red DPP is a perylene derivative frequently used as a pigment in the industry, mainly the automotive industry, and this substance along with other perylenes have attracted a great deal of attention due to their optical, sensing and electronic properties.[Aparicio F.J.,J. Phys. Chem. C 2012][Karthaus O, Jap. J. App. Phys. 2008] The fused aromatic system in this molecules also gives rise to π- π interactions, which in turn opens up the possibility for the formation of several 1D nanostructures [Yan P., J. Phys. Chem. B 2005][Zang L., Acc. Chem. Res. 2008].

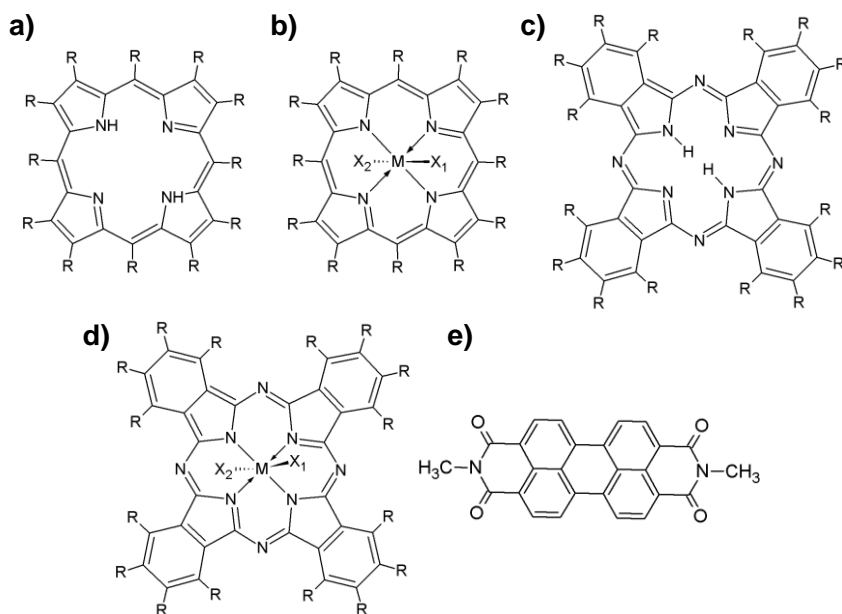Fig. 17e shows the chemical structure of MePTCDI.

Figure 17. a) Porphyrin; b) Metalloporphyrin c) Phthalocyanine; d) Metallophthalocyanine; e) MePTCDI.

1.3.2. Chemical Vapor Deposition (CVD)

Chemical vapor deposition (CVD) is the process of chemically reacting a volatile compound with gases introduced in the reactor to produce a nonvolatile solid that deposits atomistically on a suitably placed substrate.

High-temperature CVD processes for producing thin films and coatings have found increasing applications in such diverse technologies as the fabrication of solid-state electronic devices, the manufacture of ball bearings and cutting tools, and the production of rocket engine and nuclear reactor components. In particular, the need for high-quality epitaxial semiconductor films for both Si bipolar and MOS transistors, coupled with the necessity to deposit various insulating and passivating films at low temperatures, has served as a powerful impetus to spur development and implementation of CVD processing methods.

Many variants of CVD processing have been researched and developed in recent years, including low-pressure (LPCVD), plasma-enhanced (PECVD), and laser-enhanced (LECVD) chemical vapor deposition. Only a brief description of PECVD will be given here.

a) Plasma-Enhanced Chemical Vapor Deposition (PECVD)

In PECVD processing, glow discharge plasmas are sustained within chambers where simultaneous CVD reactions occur. Generally, the radio frequencies employed range from about 100 kHz to 40 MHz at gas pressures between 50 mtorr to 5 torr. Under these conditions, electron and positive-ion densities number between 10^9 and $10^{12}/cm^3$, and average electron energies range from 1 to 10 eV. This energetic discharge environment is sufficient to decompose gas molecules into a variety of component species, such as electrons, ions, atoms, and molecules in ground and excited states, free radicals, etc. The net effect of the interactions among these reactive molecular fragments is to cause chemical reactions to occur at much lower temperatures than in conventional CVD reactors without benefit of plasmas. Therefore, previously unfeasible high-temperature reactions can be made to occur on temperature-sensitive substrates.

An important advance in PECVD relies on the use of microwave radiation along with magnetic confinement, originating what is called electron cyclotron resonance (ECR) plasmas. In this operation mode, microwave energy is coupled to the natural resonant frequency of the plasma electrons in the presence of a static magnetic field (scheme shown in Fig 18). The condition for energy absorption is that the microwave frequency ω, (commonly 2.45 GHz) be equal to qB/m, where q is the elementary charge (~

1.6x10^{-19} C), m the electron mass (~ 9.1x10^{-31}kg), and *B* is the magnetic field (T). Physically, plasma electrons then undergo one circular orbit during a single period of the incident microwave.

Whereas rf plasmas contain a charge density of ~ 10^{10} cm^{-3} in a 10^{-2} to 10^{-1} torr environment, the ECR discharge is easily generated at pressures of 10^{-5} to 10^{-3} torr. Therefore, the degree of ionization is about 1000 times higher than in the rf plasma. This coupled with low-pressure operation, controllability of ion energy, low-plasma sheath potentials, high deposition rates, absence of source contamination (electrodeless system), etc., has made ECR plasmas attractive for both film deposition as well as etching processes [Ohring M., Academic Press 1992][Wilhelm R., ATBWBGP 1999].
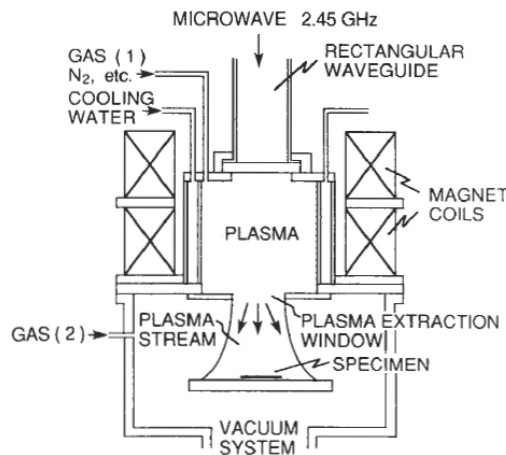
Figure 18. ECR Plasma deposition reactor [Ohring M., Academic Press 1992].

a1) Reagents for PECVD

The necessity of obtaining highly conformal metal oxides with different types of microstructure and crystallinity, and therefore with variable physical properties, while maintaining the nature of the organic template unaltered has been addressed with the technique of PECVD. The chemical structure of the reagents employed for PECVD and the experimental conditions required in each case are shown in Fig. 19 and table 1*, respectively [Barranco Á., J. Vac. Sci. Technol. A 2004][Borrás A., J. Electrochem.

Soc. 2007][Borras A., Crys. Growth. Des. 2009][Borrás A., Mic. Mes. Mat. 2012][Romero G., J. of Phy. Chem. C 2010].
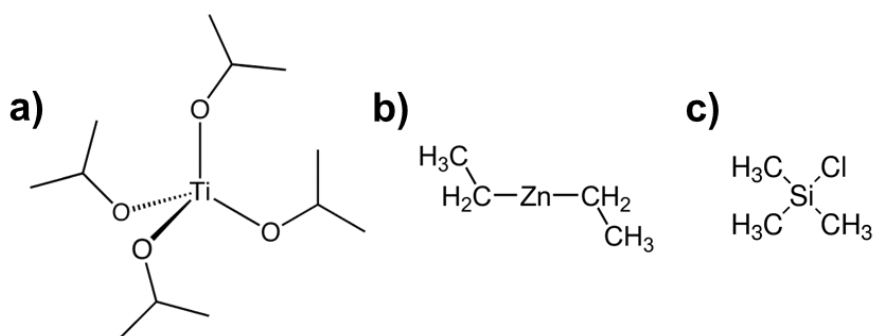
Figure 19. a) Titanium isopropoxide (TTIP), b) Diethylzinc ($ZnEt_2$), c) Chlorotrimethylsilane (TMCS).

Precursor	Microstructure	Working pressure (mbar)	Gas	Substrate Temperature (ºC)	Plasma power (W)
$ZnEt_2$	Columnar	1.5×10^{-2}	O_2	RT	400
$ZnEt_2$	Columnar	1.5×10^{-2}	O_2/H_2	170	400
TTIP	Columnar	9×10^{-3}	O_2	RT	400
TTIP	Columnar (Anatase)	9×10^{-3}	O_2	280	400
TTIP	Continuous	6×10^{-3}	O_2/Ar	RT	400
TMCS	Continuous	2×10^{-2}	O_2/Ar	RT	400

Table 1. Experimental conditions for the preparation of TiO_2, ZnO and SiO_2 by PECVD.

The corresponding microstructures obtained by PECVD may be observed in Fig. 20.
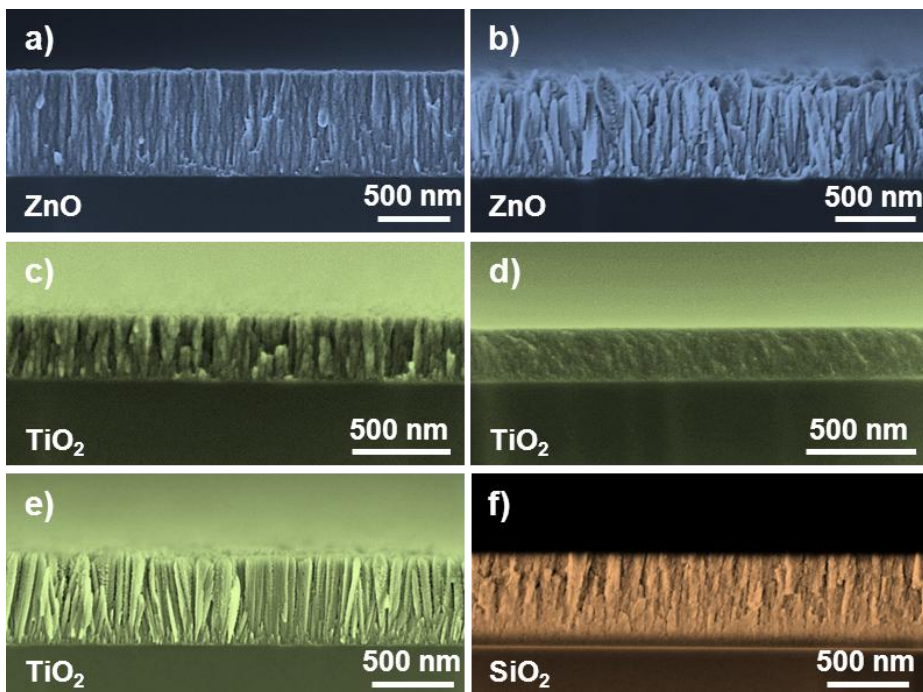
Figure 20. SEM cross section of: a) Columnar ZnO, b) Columnar ZnO (H$_2$), c) Columnar TiO$_2$ d) nano-TiO$_2$, e) Anatase, f) Microporous SiO$_2$.

1.3.3. Deposition chambers and reactors

a) Vacuum deposition system for PVD and RPAVD

The deposition chamber and the instruments associated to it are shown in Fig. 21. It consists of two OLED evaporators (up to 500 ºC) and two high temperature RADAK evaporators (up to 1350 ºC), all of which can be varied in height (i.e. distance to plasma and/or sample holder) and their respective evaporation angles adjusted at will. An automatic pressure controller valve is used to precisely regulate the pressure inside the chamber in the range of 10^{-4}-10^{-1} mbar, although the ultimate vacuum may reach 10^{-7} mbar. The pressure is monitored at all time employing a full-range pressure gauge and the flux of gases into the chamber is regulated by several mass flow controllers, one for each type of gas.

The chamber is equipped with a 2.45 GHz microwave ECR plasma source with a maximum power output of 1200 W, capable of delivering stable plasmas even at low pressures (10^{-4} mbar) or low power (<100 W), the latter being extremely useful for soft-plasma treatments.

The samples are placed in rotatable and heatable (up to 300 ºC) holder, which can be turned to face the evaporators or the plasma. If required, the holder can be placed on large screws fixed to the base of the evaporators-holder so as to vary its distance to the plasma. Moreover, the substrates and samples are normally protected with a shutter before deposition begins and once it has finalized.

The deposition rate and nominal thickness of the deposit can be followed by one or two refrigerated quartz crystal monitor (QCM) conveniently placed so as to obtain the most accurate and realistic measurements as possible.

The whole system, including the pipes for gases, is pumped by an oil rotatory pump for rough vacuum and a turbomolecular pump for attaining high vacuum.

1	LT evaporation source
2	HT evaporation source
3	Heatable and rotatable sample holder
4	QCM
5	Shutter
6	ECR microwave plasma source
7	Pressure control valve
8	Full range pressure gauge
9	Pumping system
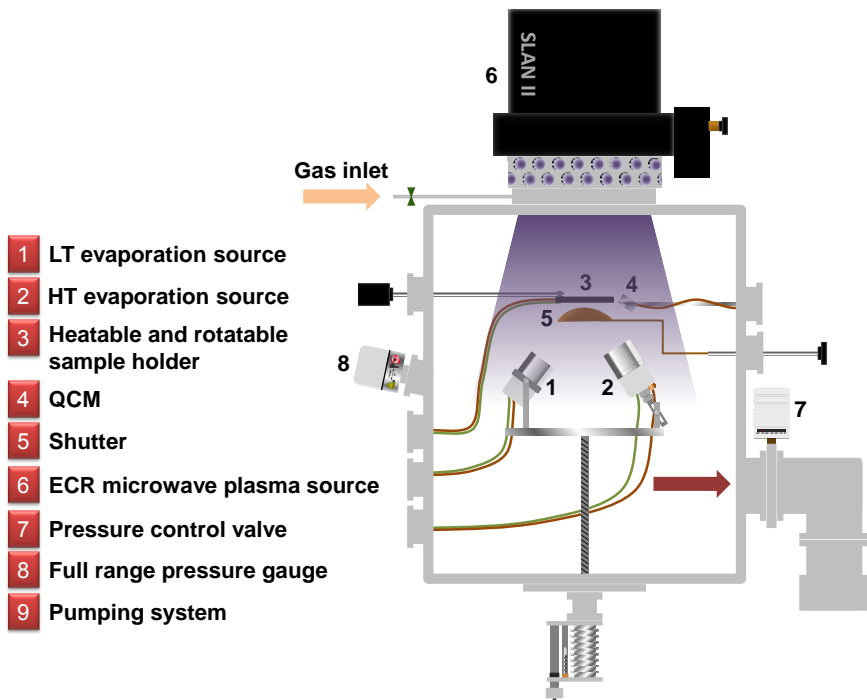
Figure 21. Scheme of the PVD and RPAVD reactor.

b) Vacuum deposition system for PECVD

This equipment is mainly used for the fabrication of metal oxides with different types of microstructure. It comprises a 2.45 GHz microwave ECR plasma source with a maximum power output of 2000 W. The plasma is feed with several gases which are

introduced into the chamber using the appropriate mass flow controller and the pressure of the system is varied employing a mechanical pressure control valve.

The precursors are finely dispersed just over the substrates by means of a housemade shower, allowing the correct distribution of the metal oxide in relatively large areas. Furthermore, the sample holder may be heated up to 450 ºC using halogen lamps, which is sometimes necessary for obtaining crystallinity and/or particular microstructures in certain materials.

A scheme of the PECVD reactor used is shown in Fig. 22.

1	Precursor source	4	Pumping system	7	Full range pressure gauge
2	Shutter	5	Pressure control valve		
3	Heatable sample holder	6	ECR microwave plasma source		
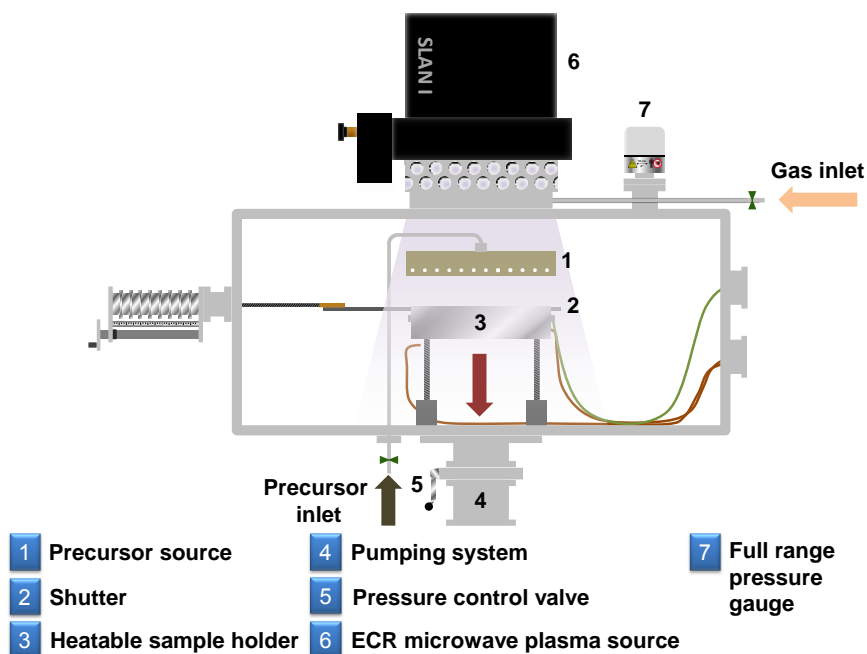
Figure 22. Scheme of the PECVD reactor.

1.4. Objectives

1) Fabrication of new 1D hybrid and heterostructured nanomaterials by combining self-assembly and plasma assisted deposition of organic molecules, plasma assisted deposition of semiconducting oxides and metal nanoparticles and soft-plasma etching for the formation of ultra-thin metal layers in a one-reactor approach. These nanostructures will comprise different combinations of organic functional small-molecules such as phthalocyanines and perylenes, semiconducting oxides (ZnO and TiO_2) and metal nanoparticles, and ultrathin metal layers (Au, Ag, Pt). A main goal to

achieve is the determination of the experimental protocol to provide a strict control on the nanostructures properties yielding high density arrays of nanostructures with a high homogeneity on processable substrates, including sensible and soft materials for defined applications.

2) Advanced characterization of hybrid materials as both individual identities and in the form of high density arrays.

3) Comprehensive understanding of the growth mechanisms. Single crystal organic nanowires (ONWs) will play a critical role as core in the organic@organic/inorganic configuration but also as precursor materials in the soft-plasma etching treatment and sacrificial template in the case of ZnO and TiO_2 and metal decorated nanotubes.

4.1) Fabrication of gases nanosensors. Prototype for optical and electrical sensing of hybrid nanostructures. Probe of concept of the light (UV and Vis) activation of electrical sensors.

4.2) Fabrication of dissolved organic molecules nanosensors. Study of the sensing capabilities by SERS of 1D TiO_2 nanostructures decorated with silver nanoparticles.

5.1) Fabrication of excitonic solar cells. Implementation of 1D hybrid nanostructures into DSSCs and study of the influence of hyperbranched nanostructures (nanotrees) and multi-shell systems on the overall performance of the cell. Development of nanometric/micrometric transparent electrodes for solar energy harvesting.

5.2) Fabrication of nanogenerators based on piezoelectric effect. Fabrication of several prototypes applicable to thin films, NWs and nanotrees.

1.5. References

Adachi M. M. et al., Core-shell silicon nanowire solar cells. Scientific Reports 3 (1546), 1-6 (2013).

Alcaire Martín M., Ph.D. thesis: Remote plasma assisted fabrication of functional organic and hybrid thin films and supported nanostructures. Universidad de Sevilla, España (2015).

Andersen T. R. et al., Scalable, ambient atmosphere roll-to-roll manufacture of encapsulated large area, flexible organic tandem solar cell modules. Energy & Environmental Science 7(9), 2925-2933 (2014).

Aparicio F. J. et al., Plasma Deposition of Perylene−Adamantane Nanocomposite Thin Films for NO$_2$ Room-Temperature Optical Sensing. Journal of Physical Chemistry C 116(15), 8731−8740 (2012).

Aparicio F. J. et al., Luminescent 3-hydroxyflavone nanocomposites with a tuneable refractive index for photonics and UV detection by plasma assisted vacuum deposition. Journal of Materials Chemistry 2(32), 6561-6573 (2014).

Barranco A. et al., Room temperature synthesis of porous SiO2 thin films by plasma enhanced chemical vapor deposition. Journal of Vacuum Science and Technology A 22(4), 1275-1284 (2004).

Borrás A. et al., Type of Plasmas and Microstructures of TiO$_2$ Thin Films Prepared by PECVD. Journal of the Electrochemical Society 154(12), 152-157 (2007).

Borrás A. et al., Porosity and microstructure of plasma deposited TiO$_2$ thin films. Microporous and Mesoporous Materials 118 (1-3), 314-324 (2009).

Borras A. et al., Connecting organic nanowires. Advanced Materials 21(47), 4816-4819 (2009).

Borras A. I. et al., Growth of Crystalline TiO$_2$ by Plasma Enhanced Chemical Vapor Deposition. Crystal Growth & Design 9(6), 2868-2876 (2009).

Borras A. et al., One-Step Dry Method for the Synthesis of Supported Single-Crystalline Organic Nanowires Formed by π-Conjugated Molecules. Langmuir 26(8), 5763–5771 (2010).

Borrás A. I. et al., Air- and Light-Stable Superhydrophobic Colored Surfaces Based on Supported Organic Nanowires. Langmuir 26(3), 1487-1492 (2010).

Borrás A. I. et al., Critical thickness and nanoporosity of TiO$_2$ optical thin films. Microporous and Mesoporous Materials 160, 1-9 (2012).

Castillero P. et al., Active and Optically Transparent Tetracationic Porphyrin/TiO$_2$ Composite Thin Films. Applied Materials and Interfaces 2(3), 712-721 (2010).

Chu Paul K., Lu XinPei, Low Temperature Plasma Technology, Methods and Applications. ISBN: 978-1-4665-0991-7. CRC Press. Boca Raton, USA (2014).

Dagdeviren C., Yang B.D., Su Y. et al., Conformal piezoelectric energy harvesting and storage from motions of the heart, lung, and diaphragm. Proceedings of the national academy of sciences 111(5), 1927–1932 (2014).

Diebold U., The Surface science of titanium dioxide. Surface Science Reports 48(5-8), 53-229 (2003).

Di Natale C. et al., Chemical sensitivity of porphyrin assemblies. Materials Today 13 (7-8), 46-52 (2010).

Dong Y. et al., Si/a-Si Core/Shell Nanowires as Nonvolatile Crossbar Switches. Nano Letters 8(2), 386-391 (2008).

Eustis S., El-Sayed M. A., Why gold nanoparticles are more precious than pretty gold: Noble metal surface plasmon resonance and its enhancement of the radiative and nonradiative properties of nanocrystals of different shapes. Chemical Society Review 35(3), 209-217 (2006).

Falk J. E., Porphyrins and Metalloporphyrins. Their General, Physical and Coordination Chemistry and Laboratory Methods.1. Elsevier Publ. Comp. DM 42. Aufl. 266 S., 21 Abb., 36 Tab. Amsterdam, The Netherlans (1964).

Gil-Rostra J. et al., Tuning the transmittance and the electrochromic behavior of $Co_xSi_yO_z$ thin films prepared by magnetron sputtering at glancing angle. Solar Energy Materials & Solar Cells 123, 130-138 (2014).

Gleiter H., NANOSTRUCTURED MATERIALS: BASIC CONCEPTS AND MICROSTRUCTURE. Acta Materialia 48(1), 1-29 (2000).

González-García L. et al., TiO_2–SiO_2 one-dimensional photonic crystals of controlled porosity by glancing angle physical vapour deposition. Journal of Materials Chemistry 20(31). 6408-6412 (2010).

Gregg B. A., Excitonic Solar Cells. Journal of Physical Chemistry B 107(20), 4688-4698 (2003).

Han T. et al., Extremely efficient flexible organic light-emitting diodes with modified graphene anode. Nature Photonics 6, 105-110 (2011).

Harry J. E., Introduction to Plasma Technology. ISBN: 978-3-527-32763-8. WILEY-VCH Verlag & Co. Weinheim, Germany (2010).

Hasan M. et al., Porous Core/Shell Ni@NiO/Pt Hybrid Nanowire Arrays as a High Efficient Electrocatalyst for Alkaline Direct Ethanol Fuel Cells. Journal of The Electrochemical Society 159(7), F203-F209 (2012).

Hawkeye M. M., Taschuk M. T., Brett M. J., Glancing Angle Deposition of Thin Films: Engineering the Nanoscale. ISBN: 9781118847565. John Wiley & Sons. West Sussex, United Kingdom (2014).

Heliatek, Heliatek consolidates its technology leadership by establishing a new world record for organic solar technology with a cell efficiency of 12%. http://www.heliatek.com/newscenter/latest_news/neuer-weltrekord-fur-organische-solarzellen-heliatek-behauptet-sich-mit-12-zelleffizienz-als-technologiefuhrer/?lang=en (2013).

Hernández S. et al., Optimization of 1D ZnO@TiO2 core-shell nanostructures for enhanced photoelectrochemical water splitting under solar light illumination. ACS Applied Materials & Interfaces 6(15), 2153-2167 (2014).

Holleck H., Schier V., Multilayer PVD coatings for wear protection. Surface and Coatings Technology 76-77(1), 328-336 (1995).

Kadish K. M. et al., The Porphyrin Handbook, Volume 17/Phthalocyanines: Properties and Materials. ISBN: 0-12-393227-0. Academic Press, Elsevier Science. San Diego, USA (2003).

Karthaus O. et al., Control of Crystal Morphology of Aromatic Electron Donors and Acceptors for Organic Electronics. Japanese Journal of Applied Physics 47(2), 1245–1250 (2008).

Kim R. H. et al., Non-volatile organic memory with sub-millimetre bending radius. Nature Communications 5(3583), (2014).

Knotek O. et al., Process and advantage of multicomponent and multilayer PVD coatings. Surface and Coatings Technology 59(1-3), 14-20 (1993).

Livshits V. A. et al., Semiconductor properties of porphyrins. Journal of Structural Chemistry 8(3), 383-388 (1967).

Liu Y. et al., Aggregation and morphology control enables multiple cases of high-efficiency polymer solar cells. Nature Communications 5(5293), 1-8 (2014).

Lloyd M. T. et al., Photovoltaics from soluble small molecules. Materials Today 10(11), 34-41 (2007).

Lochner C. M. et al., All-organic optoelectronic sensor for pulse oximetry. Nature Communications 5(5745), (2014).

Macías-Montero M. et al Vertically Aligned Hybrid Core/Shell Semiconductor Nanowires for Photonics Applications. Advanced Functional Materials 23(48), 5981–5989 (2013).

Mattox D. M., Handbook of Physical Vapor Deposition (PVD) Processing, 2nd edition. ISBN: 978-0-81-552037-5. Elsevier Inc. Oxford, UK (2010).

Mehmood U. et al., Recent Advances in Dye Sensitized Solar Cell. Advances in Materials Science and Engineering 2014, 1-12 (2014).

Mbenkum Beri M., Selective Growth of Organic 1-D Structures on Au Nanoparticle Arrays. Nanoletters 6(12), 2852-2855 (2006).

Ngô C. & van der Voorde M., Nanotechnology in a Nutshell: From Simple to Complex Systems. ISBN: 978-94-6239-012-6. Atlantis Press (2014).

Ohring Milton. The Materials Science of Thin Films. ISBN: 0-12-524990-X. Academic Press. San Diego, USA (1992).

Parra-Barranco J. et al., Anisotropic In-Plane Conductivity and Dichroic Gold Plasmon Resonance in Plasma-Assisted ITO Thin Films e-Beam-Evaporated at Oblique Angles. ACS Applied Materials and Interfaces 7(20), 10993-11001 (2015).

Pokropivny V.V., Skorokhod V.V., Classification of nanostructures by dimensionality and concept of surface forms engineering in nanomaterial science. Materials Science and Engineering: C 27(5-8), 990-993 (2007).

Romero-Gómez P. et al., Tunable Nanostructure and Photoluminescence of Columnar ZnO Films Grown by Plasma Deposition. Journal of Physical Chemistry C 114(49), 20932–20940 (2010).

Royole corporation, Royole Develops World's Thinnest 0.01 mm Full-Color AMOLED Flexible Display. http://www.prnewswire.com/news-releases/royole-develops-worlds-thinnest-001-mm-full-color-amoled-flexible-display-300010265.html. (2014)

Sajanlal P. R. et al., Anisotropic nanomaterials: structure, growth, assembly, and functions. Nano Reviews 2, 5883 (2011).

Sánchez-Valencia J. R. et al., Selective Dichroic Patterning by Nanosecond Laser Treatment of Ag Nanostripes. Advanced Materials 23(7), 848-853 (2011).

Schubert F. M. et al., Distributed Bragg reflector consisting of high- and low-refractive-index thin film layers made of the same material. Applied Physics Letters 90 (14), 141115 (2007).

Sekitani T. et al., Organic Nonvolatile Memory Transistors for Flexible Sensor Arrays. Science 326(5959), 1516-1519 (2009).

Siegel R. W., Trigg G.L. (ed). Nanophase Materials. Encyclopedia of Applied Physics (11), 173-200. VCH Publishing, Weinheim, Germany (1994).

Silva N. L. et al., Deposition of conductive materials on textile and polymeric flexible substrates. Journal of Materials Science: Materials in Electronics 24(2), 635-643 (2012).

Singh A. K. et al., Unique hydrogenated Ni/NiO core/shell 1D nanoheterostructures with superior electrochemical performance as supercapacitors. Journal of Materials Chemistry A 1(41), 12759-12767 (2013).

Smits E. C. P. et al., Bottom-up organic integrated circuits. Nature Letters 455, 956-959 (2008).

Tamang A. et al., Zinc oxide nanowire arrays for silicon core/shell solar cells. Optics Express 22(103), A622-A632 (2014).

Tiwari J. N. et al., Zero-dimensional, one-dimensional, two-dimensional and three-dimensional nanostructured materials for advanced electrochemical energy devices. Progress in Materials Science 57(4), 724-803 (2012).

Vick D. et al., Growth behavior of evaporated porous thin films. Journal of Materials Research 17(11), 2904-2911 (2002).

Visions for a molecular future. Nature Nanotechnology|Feature 8, 385-38 (2013).

Wang Z. et al., Porphyrin Nanofiber Bundles from Phase-Transfer Ionic Self-assembly and their Photocatalytic Self-Metallization. Advanced Materials 18(19), 2557–2560 (2006).

Wang Z. B. et al., Unlocking the full potential of organic light-emitting diodes on flexible plastic. Nature Photonics 5, 753-757 (2011).

Wasa K., Kitabatake M., Adachi H., Thin film materials technology. ISBN: 0-8155-1483-2. William Andrew Inc., New York, USA (2004).

Wilhelm R., ECR Plasmas for Thin-Film Deposition. Advanced Technologies Based on Wave and Beam Generated Plasmas 67, 111-122 (1999).

Yan P. et al., Self-Organized Perylene Diimide Nanofibers. Journal of Physical Chemistry B 109(2), 724-730 (2005).

Yang P. et al., Semiconductor Nanowire: What's Next? Nano Letters 10(5), 1529-1536 (2010).

Yi H. T. et al., Ultra-flexible solution-processed organic field-effect transistors. Nature Communications 3(1259), 1-7 (2012).

Yijie X. et al., Solution-Processed Metallic Conducting Polymer Films as Transparent Electrode of Optoelectronic Devices. Advanced Materials 24(18), 2436–2440 (2012).

Zang L. et al., One-Dimensional Self-Assembly of Planar π-conjugated molecules: adaptable building blocks for organic nanodevices. Accounts of chemical research 41(12), 1596-1608 (2008).

Zhang C. et al., Synthesis and applications of organic nanorods, nanowires and nanotubes. Annual Reports Section "C" (Physical Chemistry) 109, 211-239 (2013).

Zhao Y.P., Designing Nanostructures by Glancing Angle Deposition, SPIE Proceedings 5219, 59-73 (2003).

Zhao W., Chen F., One-pot Synthesis and its Practical Application in Pharmaceutical Industry. Current Organic Synthesis 9(6), 873-897 (2012).

2. Inorganic nanotubes for DSSCs
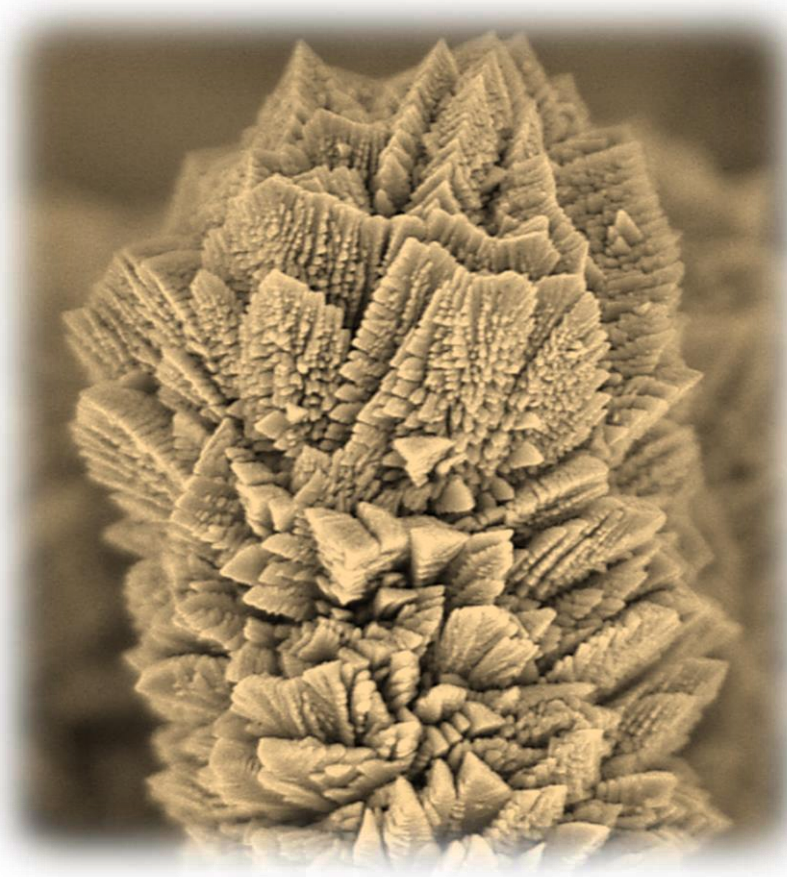
Abstract

Single-shell and multishell ZnO and TiO$_2$ nanotubes are fabricated by PECVD following a template procedure based on ONWs growth by OPVD. The emptying mechanism of the initial 1D nanostructures is evaluated as a function of annealing speed. Their characterization by electron microscopy techniques and implementation in DSSCs is addressed, investigating the effect of wall thickness on the photovoltaic parameters of the cells and the gain in performance when compared to their thin film counterparts.

2.1. Introduction

Since 1883 solar cells have evolved from a laboratory curiosity to a real energy generation alternative [Fritts C. E., Am. J. Sci. 1883]. Moreover, the interest in photovoltaic (PV) technology emerged due to economic reasons after the first oil crisis in 1973, but it has further increased owing to environmental concerns, i.e. pollution related issues associated to conventional power sources (oil, gas, coal, etc.) have further stimulated research and production of solar cells [Armaroli N., Wiley 2011][Palz W., CRC Press 2014]. As seen in Fig.1, PV energy production keeps augmenting, exhibiting a tenfold increase in the period 2008-2014, a remarkable increase in only 6 years. This demonstrates the high level of commitment with PV technology, accompanied by a heavy investment in the field.
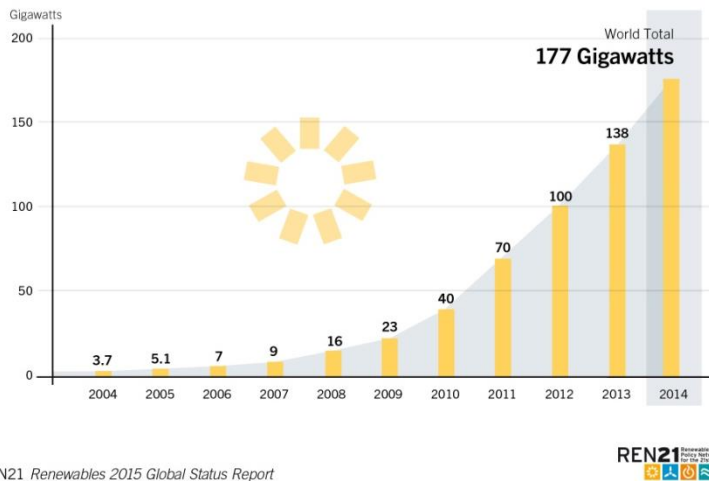
Figure 1. Evolution of global solar PV power capacity in the period 2004-2014 [REN21].

The quest for higher efficiencies and more competitive photovoltaic technologies has led to the development of several classes of solar cells. According to the active materials composing the cells, they may be divided into three groups:

➢ **Inorganic**: They are the most efficient, reliable and long-lasting ones, but also the most expensive both in terms of money and resources consumption (energy payback time is quite high) [Miles R. W., Mater. Today 2007][Espinosa N., Energy Environ. Sci. 2012]. This family comprises several well-established commercial and aerospatial technologies like

amorphous and crystalline Si cells, thin-film (CIGS, CdTe, a-Si:H) and multijunction cells. Third-generation, quantum dot and copper zinc tin selenide (CZTSSe) solar cells are among the novelties in this group and have attracted significant attention [Chuang C. M., Nat. Mater. 2014][Wang W., Adv Energy Mater. 2014][Conibeer G., Mater. Today 2007].

➢ **Organic**: This kind of solar cells rely on the implementation of a small-molecule or polymer, or a combination of both, acceptor and donor for the formation of a proper n-p heterojunction for charge separation. Much effort has been directed towards novel architectures, microstructures and molecular engineering of the organic materials. Organic photovoltaics is a promising field which could ultimately allow for the manufacturing of large-area, cheap and flexible light harvesters, even though the maximum theoretical efficiency of non-tandem organic solar cells has been calculated to be approximately 15% [Li G., Nat. Photonics 2012][Mishra A., Angew. Chem. 2012][Wright M., Sol. Energ. Mat. Sol. C. 2012][Su Y., Mater Today 2012].

➢ **Hybrid**: The combination of organic and inorganic materials in photovoltaics is a route to surpass some of the drawbacks of the individual families, getting the best out of each of them. For example, increasing the efficiency while keeping costs down. The broadly studied dye sensitized solar cells (DSSCs) and the recent organometal halide perovskites belong to this category. The solar cells fabricated during this Thesis are DSSCs, and therefore the ones that will be discussed in further detail here [Fan J., Photon Res. 2014][Heo J. H., Nat. Photonics 2013][Hardin B. E., Nat. Photonics 2012].

Chart 1 summarizes the evolution in certified record efficiencies for different PV technologies.

Best Research-Cell Efficiencies

Chart 1. Best confirmed Research-Cell efficiencies up to March 2015 (up) and a zoomed area of the same chart (down) [NREL 2015].

2.1.1. Brief introduction to semiconductors

A semiconductor is a material which can behave as an insulator or conductor depending on external factors such as temperature, electric field, etc. Intrinsic semiconductors possess a forbidden energy band, the so-called band gap, separating the conduction and valence bands in the solid to which no electronic transitions are allowed. However, electronic transitions from the conduction to the valence band can

occur due to excitation (thermal, electric, etc.), in case the provided energy is larger than the band gap (Fig. 2).
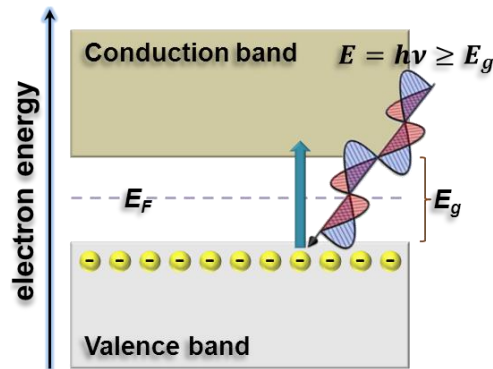

Figure 2. Electronic transitions in an intrinsic semiconductor upon irradiation.

Intrinsic semiconductors may be doped with extremely low quantities of other elements to produce n-type or p-type extrinsic semiconductors. The doping elements are electron donor (pentavalent) or acceptor (trivalent) for n- and p-type extrinsic semiconductors, respectively. Moreover, the presence of defects in the crystal structure of the semiconductor may also confer one of these two behaviors. As observed in Fig. 3, in an n-type semiconductor there are dopant states in the band gap close to the conduction band levels. The energy required to promote an electron from these states to the conduction band (E_d) is much less than the bandgap and at room temperature there is enough energy available for such transitions, partially filling the conduction band and thus increasing the conductivity of the material. In the case of n-type semiconductors, the majority charge carriers are electrons, opposed to holes in p-type ones [Berger L. I., CRC Press 1997].
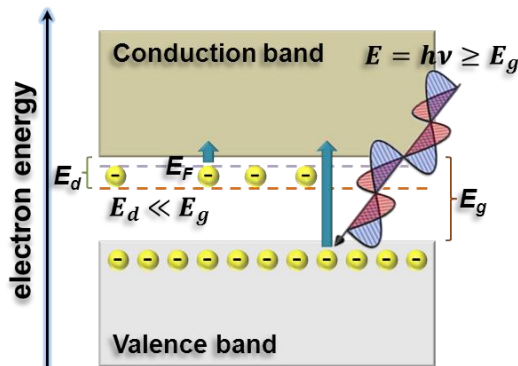

Figure 3. Electronic transitions in an n-type semiconductor upon irradiation.

2.1.2. Operational principles of solar cells

As already mentioned in the General Introduction, solar cells may be split in two different classes according to their working mechanism. On the one hand, conventional solar cells undergo three processes that lead to the generation of a photovoltage:

- ➲ Generation of charge carriers throughout the bulk of the semiconductor due to absorption of electromagnetic radiation. For light absorption to occur, the energy of the incident radiation must be equal or higher the semiconductor bandgap (Fig. 2).
- ➲ Subsequent separation of the charge carriers upon arrival at the cell junction, a pn type for example.
- ➲ Collection of the charge carriers at the electrodes.

On the other hand, in excitonic solar cells such as DSSCs only two processes take place:

- ➲ Simultaneous photogeneration and separation of the charge carriers at the heterointerface.

- ➲ Collection of the charge carriers at the electrodes.

The operational principle of a liquid DSSC is quite simple and can be easily understood looking at Fig. 4. A mesoporous thin film of a wide band gap oxide semiconductor (TiO_2, ZnO, Nb_2O_5, etc.) is generally deposited on a transparent conductive oxide electrode, such as fluorine-doped tin oxide (FTO) on glass, and placed in contact with an electrolyte. A dye (sensitizer), attached to the semiconductor film as a monolayer, is photoexcited and injects an electron into the conduction band of the metal-oxide. The regeneration of the dye is carried out by a redox couple present in the electrolyte (I_3^-/I^- in this case), which is in turn regenerated at the platinum coated counter electrode. Platinum acts as a catalyst for the reaction $I_3^- + 2e^- \rightarrow I^-$, where electrons are supplied through the external load [Grätzel M., Inorg. Chem. 2005].
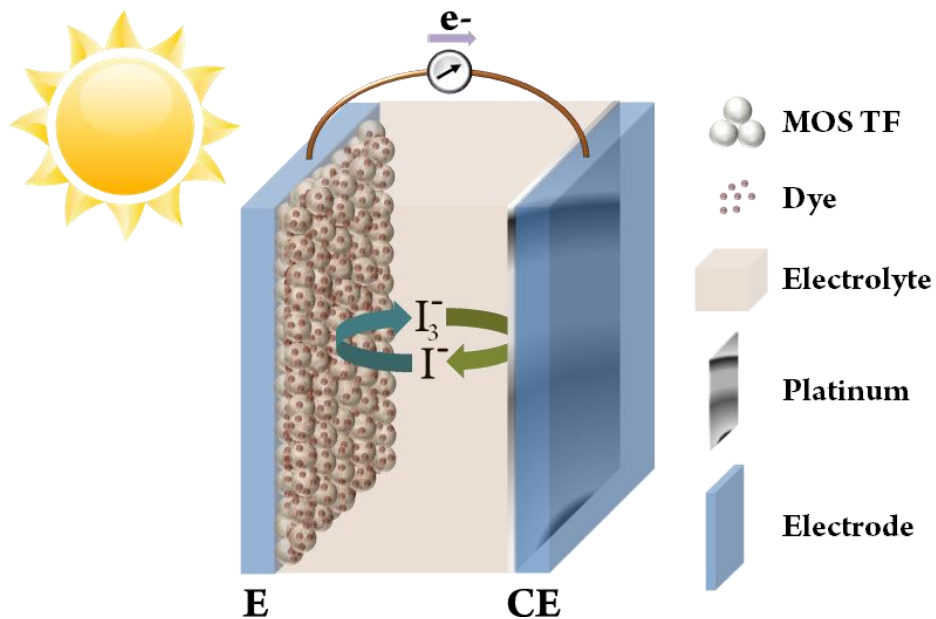
Figure 4. Illustration of a DSSC under operation. E and CE stan for electrode and counter electrode respectively, while MOS TF means Metal-Oxide-Semiconductor thin film (mesoporous in the diagramm).

While the photocurrent in DSSCs depends on the number of dye molecules adsorbed to the oxide, the photovoltage arises from the difference between the Fermi level of the electrons in the semiconductor and the redox potential of the electrolyte. Assuming that the Fermi level is considered to be quite proximate to the conduction band, then for TiO₂ in anatase crystalline form and using I_3^-/I^- as a redox couple, the maximum attainable photovoltage would be $\Delta E = \left| E_{CB\ TiO_2} - E_{I_3^-/I^-} \right| = \left| -4.2\ eV + 4.8\ eV \right| = 0.6\ eV = 600\ mV$. In practice, the immersion of the semiconductor in the electrolyte with redox couple will shift the electron energy levels at the film surface. For example, it has been determined that for anatase, and using I_3^-/I^- as redox couple, the conduction band shifts from -4.2 eV to -3.9 eV, so the maximum possible photovoltage for this DSSC would be 900 mV. Of course, this is an ideal value and is usually lower mainly due to electron recombination in the semiconductor film [Cahen D., J. Phys. Chem. B 2000][Raga S. R., J. Phys. Chem. Lett. 2012].

DSSCs efficiency has slowly improved from 10% to 12.3% in a time lapse of 20 years [Yella A., Science 2011]. New ruthenium-free dyes and combination of dyes have been introduced in order to enhance light harvesting (boosting the photocurrent) while in conjunction with novel Co(II/III) electrolytes favors a parallel increase of the

photovoltage. Moreover, despite the longevity of DSSCs is still inadequate for commercial applications, huge efforts has been made in improving their long term stability, which along with efficiency and low production costs will determine the marketing viability of these cells [Upadhyaya H. M., Sol. Energ. Mat. Sol. C. 2013].

In this work, both ZnO and TiO_2 wide-bandgap semiconductors have been employed as active materials in DSSCs electrodes. Bulk wurtzite ZnO has a direct band gap of 3.44 eV with n-type behavior. Although the causes for such a n-type behavior are still unclear, although it is speculated that the unintended incorporation of impurities such as H would be a possible explanation [Janotti A., Rep. Prog. Phys. 2009]. Bulk TiO_2 has a band gap of 3.2 eV for the anatase phase. It is also an n-type due to oxygen vacancies and the presence of Ti^{+3} cations [Moorthy S. B. K., Springer 2015].

On the one hand, the high electron mobility of ZnO*, μ_e = 200 $cm^2V^{-1}s^{-1}$, and acceptable exciton binding energy of 60 meV make it an attractive candidate for its potential implementation in DSSCs [Look D.C., Sol. State Commun.1998][Xu F., Energy Environ. Sci. 2011][Kosyachenko L. A., Solar Cells – Dye-Sensitized Devices]. On the other hand, its known degradation by many usual dyes limits the overall cell performance and operation lifetime [Soga T., Elsevier 2006]. TiO_2 was the first choice for DSSCs [O'Regan B., Nature 1991] since it is chemically more stable than ZnO and it possesses an injection efficiency[ξ] of 100%, twice than ZnO. The major drawbacks associated with TiO_2 are its low electron mobility, ranging from 1 $cm^2V^{-1}s^{-1}$ for amorphous TiO_2 to 30 $cm^2V^{-1}s^{-1}$ for anatase*, and its relatively low exciton binding energy of 4 meV [Tiwana P., ACS Nano 2011][Forro L., J. Appl. Phys. 1994].

ZnO nanostructures in the form of thin film, nanowires, nanotubes and hierarchical nanostructures have been used as photoanodes in dye sensitized solar cells (DSSC) as an alternative to TiO_2 [Anta J. A., J. Phys. Chem. C 2012]. The record efficiency reported for a DSSC is 7.5% under 1-sun illumination using hierarchical ZnO nanostructures [Memarian N., Angew. Chem. Int. Ed. 2011]. The application of this semiconductor oxide to the emerging field of the perovskite solar cells has also been recently explored [Zhou H., J. Phys. Chem. C 2015]. In fact, nanocolumnar ZnO thin films deposited by PECVD were reported last year as photoanode for both dye-sensitized [Vega-Poot A. G., ChemPhysChem 2014] and perovskite solar cells [Ramos F. J., ChemPhysChem 2014]. In the first work, the electron-transport properties of the highly crystalline and texturized PECVD ZnO film were compared to that of a nanoparticulate layer by means of small-perturbation electrochemical techniques. In this way it was demonstrated that the electron transport in the case of

the texturized film was determined by Fermi-level pining that made voltage independent, in contrast to the nanoparticulate film [Vega-Poot A. G., ChemPhysChem 2014]. On the other hand, a stimulating power conversion of 4.8% was obtained for the solid-state solar cell by depositing $CH_3NH_3PbI_3$ on a porous ZnO nanocolumnar layer [Ramos F. J., ChemPhysChem 2014].

Both TiO_2 amorphous and anatase have also been extensively employed in DSSCs in the form of nanoparticles, nanosheets, nanowires, etc. [O'Regan B, Nature 1991][Chen D., Adv. Mater. 2009][Yu J., Nanoscale 2010][Liao Jin-Yun, Energy Environ. Sci. 2012][Wu Wu-Qiang, Energy Environ. Sci. 2014], achieving remarkable efficiencies by implementing new dyes and electrolytes [Yella A., Science 2011], [Mathew S., Yella A., Nature Chem 2014.]. It has been demonstrated that TiO_2 nanoparticles suffer from higher charge recombination than 1-D nanostructures due to the huge number of grain boundaries in the nanoparticle film. However, 1-D nanostrucutures such as nanorods or nanowires offer much lower surface area compared to nanoparticles, hence dye concentration, and thereby photocurrent, are superior in the latter case [Tan B., J. Phys. Chem. B 2006][Yan X., Phys. Chem. A 2013]. In order to achieve even higher efficiencies with TiO_2 systems, it is therefore required to fabricate structures with low charge recombination and high surface area.

State of the art DSSCs comprising 1D anatase nanostructures have achieved remarkable efficiencies of about 10 % by implementing hierarchical anatase NWs [Wu Wu-Qiang, Energy Environ. Sci. 2014]. In other recent works, efficiencies between 4%-8% have been attained, always exploiting hierarchical 1D nanostructures [Roh D. K., Adv. Funct. Mater. 2014][Liao Jin-Yun, Energy Environ. Sci. 2012][Tan B., J. Phys. Chem. B 2006]. However, not less than 14 μm or even 47 μm of film thickness were needed for such high efficiencies. Here, the maximum attained power conversion efficiency was 4.32% (mean value) with films less than 10 μm thick.

While carbon nanotubes are mainly explored for their use in microelectronic technology and as structural component, inorganic nanotubes (especially metal sulfides or oxides) are mostly fabricated to exploit other material-specific properties, focusing the interest on biomedical, photochemical, electrical, and environmental applications [Patzke G. R., Angew. Chem. 2002][Xia Y., Adv. Mater. 2003][Kolmakov A., Annu. Rev. Mater. Res. 2004][Roy P., Angew. Chem. 2011]. Thus, other materials like ZnO and TiO_2 have been developed and applied in photocatalytic self-cleaning surfaces, piezoelectric devices, chemical sensing, for energy storage and solar energy harvesting applications due to their suitable electrochemical properties, excellent

solution stability, and relatively low toxicity [Pan Z., Science 2001][Wang Z. L., J. Phys. Condens. Matter. 2004][Law M., Nat. Mater. 2005][Nakata K., J. Photochem. Photobiol. C: Photochem. Rev. 2012].

Potential applications of 1D nanostructures have been explored over the past 20 years in devices with increasingly sophisticated photovoltaic, electrochromic, antifogging, or self-cleaning properties or as biomedical coatings, sensors, or smart-surface coatings [Huusko J., Sensor. Actuat. B-Chem. 1993][Satake K., Sensor. Actuat. B-Chem. 1994][Huang S. Y., J. Electrochem. Soc. 1995]. To achieve a maximum overall efficiency for many of these applications, it is crucial to maximize the specific surface area. For this purpose, nanoparticulated materials are usually the first choice, although other nanosize geometries, particularly that of nanotubes, may render a much better control of the chemical or physical behavior. By lowering down dimensions to the nanoscale, not only the specific surface area increases significantly but also the electronic properties may change considerably (owing for example to quantum size effects, strong contribution of surface reconstruction or surface curvature can be obtained). These effects might also contribute to drastically improve the reaction/interaction between a device and the surrounding media, thereby making the system more effective, or even opening entirely novel reaction pathways.

In a general way the methods applied to the fabrication of nanotubes can be divided in four wide groups [Barth S., Prog. Mater. Sci. 2010]: formation of nanotubes due to morphological constrictions by classic VLS, VS and other catalytic methods [Rao C. N. R., Dalton Trans. 2003]; electrospinning [Li L., Electrochem. Commun. 2010]; anodization [Zhu K., Nano Lett. 2007], treatment of solid nanofibres (NFs) and nanowires (NWs) in order to remove the inner part [Elias J., Chem. Mater. 2008][Mancic L. T., Cryst. Growth Des. 2009] and, finally, the use of templates [Cheng F., Chem. Mater. 2008]. There are two principal approaches settled in the last group, namely the use of anodized alumina as hollow 1D template that can be filled through solution-based or vacuum methodologies [Hulteen J., J. Mater. Chem. 1997][Martinson A. B. F., Nano Lett. 2007] and the application of the atomic layer deposition (ALD) of inorganic precursors using as substrate pre-grown 1D nanostructures and fibers [Marichy C., Adv. Mater. 2012][Cho S., Sensor. Actuat. B-Chem. 2012].

The methodology presented herein might be included in the last group of methods above mentioned, with three important particularities:

- Firstly, the nanomaterials used as template are supported single crystalline organic nanowires (ONWs) fabricated by physical vapor deposition of small-molecules on an ample variety of substrates including metal nanoparticles and layers, metal oxide thin films and polymer flexible supports [Briseno A. L., Mater. Today 2008][Oulad-Zian Y., Langmuir 2015].

- Secondly, the metal oxide layers forming the walls of the nanotubes are prepared by PECVD [Macias-Montero M., Adv. Func. Mater. 2013][Gómez-Romero P., J. Phys. Chem. C 2010][Borrás A., J. Electrochem. Soc. 2007].

- Finally, the organic template is removed by annealing of the ONWs at mild temperature.

These characteristics render a full vacuum approach for the fabrication of 3D nanotubes with tunable length, hole dimensions and shapes and tailored wall composition, microstructure, porosity and structure.

Quite recently, the development of hybrid ONW@semiconducting-oxide supported nanowires with application as nanoscale waveguides has been published [Macias-Montero M., Adv. Funct. Mater. 2013]. Critical advantages of the use of PECVD for the formation of such hybrid nanowires are the vertical alignment of the final nanostructures and the formation of the inorganic shell with no damage of the organic structure in the core. Two different amorphous TiO_2 shells have been prepared, labelled as meso and nano attending to their characteristic porosity, columnar and mesoporous in the first case and continuous and microporous in the second one [Borrás A., J. Electrochem. Soc. 2007]. Nano-TiO_2 characterization is included in chapter 3. Moreover, anatase shells have also been successfully fabricated and implemented in DSSCs. The prepared ZnO shows a globular-columnar microstructure in the wurtzite phase.

This chapter is structured as follows: first it is presented the development of the methodology for the formation of TiO_2 and ZnO nanotubes and their characterization. Then, the extension of the technique to a multishell system ZnO NTs@TiO_2 is discussed. Next, the supported ZnO nanotubes are employed as active nanomaterials in the fabrication of a dye sensitized solar cell. Finally, TiO_2 anatase nanotubes, including their characterization and the combination ZnO NTs@TiO_2 (amorphous) and ZnO NTs@TiO_2 anatase are also investigated as active materials in DSSCs.

2.2. Objectives

The following objectives were proposed for this Chapter:

- ❖ Fabrication of single-shell and multi-shell nanotubes made up of ZnO and TiO_2 by PECVD following a template procedure based on ONWs grown by OPVD.
- ❖ Achieve crystalline nanotubes for both ZnO and TiO_2.
- ❖ Structural characterization of the obtained nanostructures. In the case of multi-shell NTs, investigate whether the developed methodology is still suitable for these more complex systems.
- ❖ Apply these nanostructures as active electrodes for dye-sensitized solar cells and characterize the cells.

2.3. Methodology

2.3.1. Fabrication of nanotubes*

There are basically 4 steps involved in the production of 1D hollow nanostructures:

1) Deposition of seeds

The growth of the ONWs is a seed-mediated process. It requires a minimum roughness on the samples which can be obtained by depositing thin films of ZnO, TiO_2, or noble metals, among many others. In the case of the prepared solar cells a thin film of ZnO or TiO_2 (anatase) was first deposited by PECVD on the FTO electrode which act as a hole blocking layer (Fig. 5a).

2) Growth of ONWs

Formation of the ONWs template (Fig. 5b) is a temperature controlled physical vacuum deposition (OPVD) process that allows the growth of squared NWs and nanobelts. As previously mentioned, the organic nanowires are formed on substrates of different chemical nature from metal nanoparticles to polymers including oxide thin films. References [Borras A., Adv. Mater. 2009][Macias-Montero M., Adv. Func. Mater. 2013][Gómez-Romero P., J. Phys. Chem. C 2010][Oulad-Zian Y., Langmuir 2015] gather detailed information on the methodology developed for the controlled fabrication of ONWs. In this work, looking for the final applications of the nanotubes, ONWs have been deposited on

*A general approach to the fabrication and characterization of ZnO and TiO_2 systems will be given, for further details please refer to Dr. Manuel Macías-Montero´s Ph.D. Thesis [Macías-Montero M., Ph.D. thesis 2013]

commercial FTO substrates coated with a thin film of TiO_2 or ZnO. Additional reference substrates like metal nanoparticles and thin films were utilized for specific characterization methods.

3) Formation of a metal oxide semiconductor (MOS) shell

The third step represents the conformal deposition by PECVD of the metal oxide shell on the as-grown ONWs (Fig. 5c).

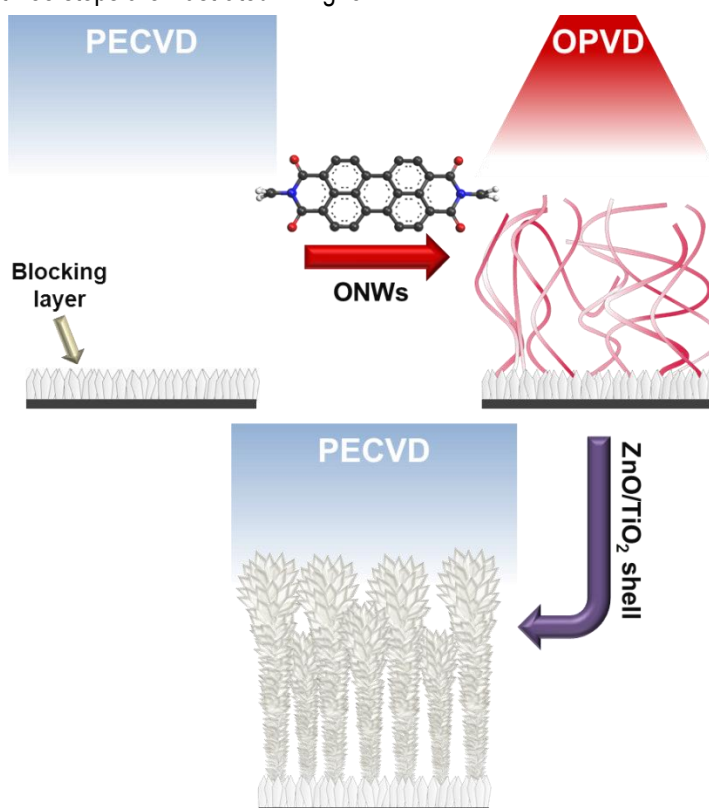These three steps are illustrated in Fig. 5

Figure 5. Formation of 1D ONWs@MOS nanostructures. MePTCDI has been used in the illustration for the growth of the ONWs, but other molecules have been employed as well (see experimental details).

4) Evacuation of the 1D nanostructures

*A general approach to the fabrication and characterization of ZnO and TiO_2 systems will be given, for further details please refer to Dr. Manuel Macías-Montero´s Ph.D. Thesis [Macías-Montero M., Ph.D. thesis 2013]

A simple additional step is performed in order to remove the organic and obtain vertical aligned inorganic nanotubes. This additional step consists on the annealing under vacuum of the hybrid nanowires. In this step, the heating ram is crucial in the final NT microstructure. Increments of the temperature lower than 10 ºC min^{-1} lead to closed nanotubes meanwhile higher temperature ramps result in open nanotubes. Steps ii) and ii') in Fig. 6 depict such a phenomenological conclusion.
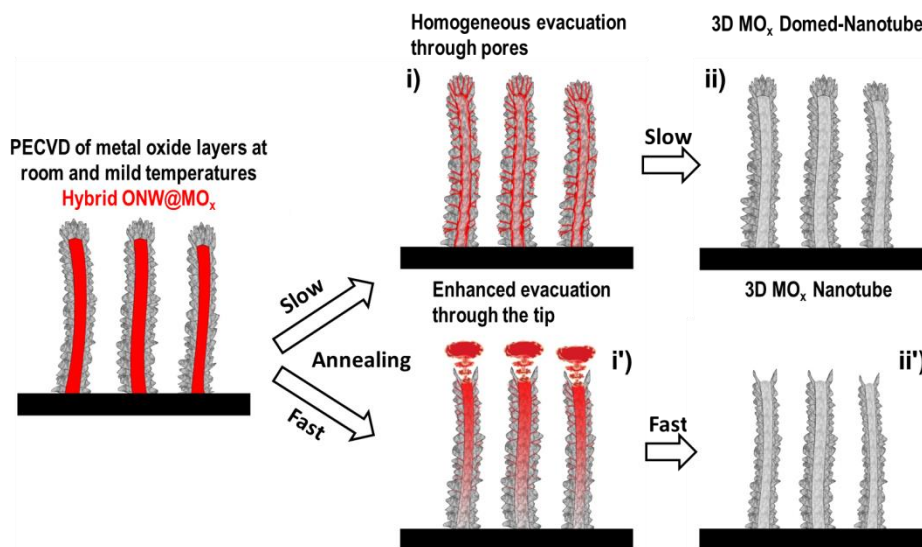

Figure 6. Representation of the steps involved in the formation of the oxide nanotubes.

2.3.2. Experimental details

a) NTs fabrication steps

ONWs by OPVD. The organic precursor perylenediimide (2,9-dimethyl-anthra[2,1-def:6,5,10-d'e'f']diisoquinoline-1,3,8,10-tetrone (Me-PTCDI) was acquired from Sensient Imaging Technologies, and Octaethylporphyrin (OEP), Phthalocyanine (Pc) and Nickel Phthalocyanine (NiPc) were supplied from Aldrich and used as received without further purification. The OPVD procedure for the formation of single crystal ONWs has been fully described in previous references [Borras A., Langmuir 26(8) 2010][Mbenkum Beri M., Nano Lett. 2006]. It consists on the sublimation of the organic molecules from a Knudsen cell at 0.02 mbar of Ar using a growth rate about 0.3 Å/s and controlled substrate temperature. The substrates temperatures were settled at

~175 ºC for the Me-PTCDI; ~130 ºC for the OEP and ~230 ºC for the Pc and NiPc. In DSSCs, the thickness of the NWs was set to 0.65 kÅ which corresponds to NWs 2-3 µm long.

OEP and MEPTCDI have been used for the growth of template NWs in ZnO and multishell DSSCs, while Pc has been employed for the formation of anatase NTs (it withstand higher temperatures). NiPc has been utilized only for mechanistic elucidation purposes.

ZnO and TiO$_2$ layers by PECVD. Both semiconducting oxides, ZnO and TiO$_2$, were fabricated by PECVD in a microwave (2.45 GHz) ECR reactor with a down-stream configuration. The experimental setup for PECVD can be found elsewhere [Macias-Montero M., Adv. Funct. Mater. 2013]. Diethylzinc (ZnEt$_2$) and titanium tetraisopropoxide (TTIP) were utilized as precursors (Sigma Aldrich). Crystalline ZnO was grown at RT with oxygen as plasma gas. Total pressure in the chamber was settled at 1.5 x 10^{-2} mbar and plasma power at 400 W. meso-TiO$_2$ was grown at the same conditions with a slightly lower pressure (8.6 x 10^{-3} mbar). For TiO$_2$, an amorphous thin layer (lower temperature) must be deposited before increasing the substrate temperature to 250 ºC, required for a proper anatase crystalline growth. Although the amorphous layer will certainly act detrimentally to the solar cell performance, it is mandatory since otherwise Pc nanowires will sublimate.

Empty of the 1D nanostructures. Except for anatase nanostructures that loses the organic core during growth, a heating treatment at 350 ºC and 10^{-6} mbar of pressure was applied to these samples for 3 hours to achieve a complete emptying of the inner organic core. No alteration of the vacuum was detected during the process. A cold finger placed in the vacuum system was filled with liquid nitrogen to condensate the sublimated organic material. After the annealing process is performed, the samples are allowed to cool down in high vacuum avoiding water condensation in the highly porous nanotube walls.

b) Solar cells fabrication procedure

Counter electrode. FTO/glass substrates of 2.5 x 2 cm provided by Xop Glass (12-14 Ω/□) were drilled in two points for later electrolyte injection, rinsed with acetone, isopropanol and absolute ethanol and heated to 500 ºC for 1 hour. 12 µL of plastisol (Solaronix) are dispersed on the substrates, dried in air and heated in a furnace for 20' at 400 ºC.

Working electrodes. FTO/glass substrates were cleaned just as the counter electrodes. An active area of 0.7 cm^2 was defined with an aluminum foil mask and a layer of less than 100 nm of ZnO was deposited by PECVD. This ZnO acts as a hole blocking layer and provides the necessary roughness for the growth of ONWs. ZnO 3 NTs with different thicknesses were fabricated by PECVD onto FTO electrode through a mask to delimitate a covered area of 7 x 10 mm^2. Samples were heated up to 80ºC before immersing in the dye solution, 0.5 mM solution of N719 dye (cis-diisothiocyanato-bis(2,20-bipyridyl-4,40-dicarboxylato) ruthenium(II) bis (tetrabutylammonium)) [purchased from Solaronix] in ethanol, to prevent adsorption of air moisture. For cells containing ZnO, immersion time was limited to 1 hour to avoid degradation of the NTs and for anatase the cells were allowed to remain in the dye overnight. Afterwards they were rinsed with an ethanol baker and dried in air.

Polished n-type Si(100) purchased from Topsil and fused silica from Sico Technology GmbH were used in each preparation for later characterization.

The electrolytic solution. Prepared by addition of 0.6 M 1,2-dimethyl-3-propylimidazole iodine (DMPII), 0.1 M LiI, 0.5M 4-tertbutyl-pyridine (TBP), 0.05 M I2 and 0.1 M guanidinium thiocyanate (GuSCN) to a mixture of acetonitrile/valeronitrile (85/15).

Sealing of the cells. A frame of a thermoplastic polymer (Surlyn, Solaronix) was placed on the perimeter of the active area and then sandwiched with the counterelectrode. The whole cell was heated to 140 ºC under slight pressure to ensure a proper sealing. After that the electrolyte was injected and the holes on the counterelectrode sealed with Surlyn and a cover slide glass.

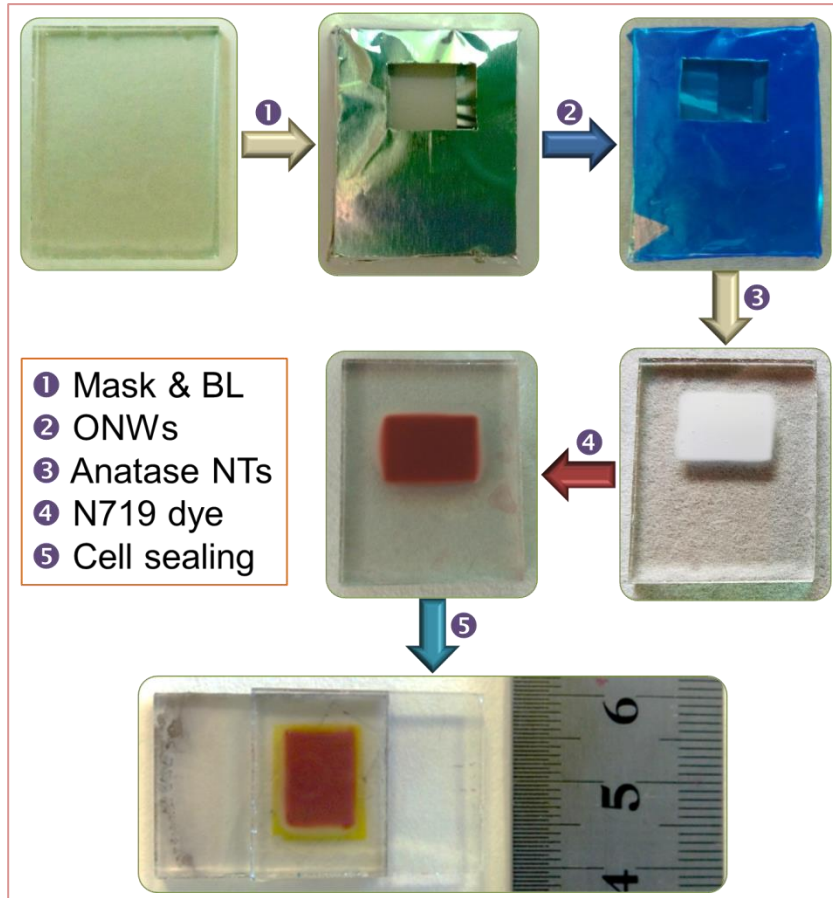The whole fabrication process of a DSSC is depicted in chart 1.

Chart 1. Steps involved in the production of a DSSC.

Characterization of DSSCs. The solar-cell devices were characterized using a solar simulator with an AM1.5G filter (ABET). A reference solar cell with temperature output (Oriel, 91150) was used for calibration. EIS measurements were performed under light with perturbations in the 10^5-10^{-3} Hz range and the IMPS measurements in the same Hz range. For all the small perturbation techniques, a LED LUXEON collimated (540 nm) source and an Autolab/PGSTAT302N potentiostat were used. Zview equivalent circuit modelling software (Scribner) was used to fit the EIS data, including the distributed element DX11 (transmission line model). The NOVA 1.7 software was used to analyze the IMPS data.

c) Dye N719 concentration determination

A calibration curve was constructed by measuring the absorbance between 200 and 900 nm of four solutions of dye N719 in KOH 1M in MeOH, being the molar

concentration of the dye in each case 1×10^{-6}, 5×10^{-6}, 5×10^{-5} and 1×10^{-4}. By taking the absorbance at 515 nm and by using the Lambert-Beer´s law, the absorption coefficient ε ($M^{-1}cm^{-1}$) can be calculated. This law is usually expressed as $A = \varepsilon cl$, where A is the absorbance, c the concentration (M) and l the light path (cm). In this case, a straight line with $R^2 = 0.997$ was obtained by linear regression, estimating a value of 11331 ± 276 for ε. With this value and a known value of 1 cm for the light path, the molar volume concentration was calculated for each sample.

The total number of moles for each film was calculated by multiplying the obtained concentration by the volume of solution employed (2 ml). Then, the surface concentration was calculated by dividing this value by the area of the sample (1.875 cm^2). Finally, the normalized surface concentration is simply this value divided by the thickness of the layer.

A precision quartz cell from Hellma with a light path of 1 cm and a Cary 100 spectrometer from Varian were used for these experiments.

d) Characterization of samples

SEM micrographs were acquired in a Hitachi S4800 working at 2 kV. The samples were dispersed onto Holey carbon films on Cu or Ni grids from Agar scientific for TEM characterization. EDX maps were acquired with a FEI Tecnai Orisis TEM/STEM 80-200 working at 200 kV. Post-processing of EDX data was performed with the open source Hyperspy software: hyperspy.org. EDX raw data was post-processed in order to obtain more accurate compositional maps of the multishell system. The main reason for this post-treatment is an inadequate description of the Ti spatial distribution arising mainly from the fact that the microscope software mixes the signal of Ti Lα with O Kα and it does not allow selection of other emission lines or any further spectral refinement, which is critical in this nanosized structures. HAADF STEM and HRTEM were carried out with both Osiris and FEI Tecnai G2F30 S-Twin STEM microscope also working at 200 kV. The crystal structure was analyzed by XRD in a Siemens D5000 spectrometer operated in the θ - 2 θ configuration and using the Cu Kα (1.5418 Å) radiation as an excitation source. UV-Vis analysis of the samples was done in a Cary 100 spectrometer from Varian.

2.3.3. Solar cells characterization techniques

a) IV curves measurements

By performing a linear sweep voltammetry to an illuminated solar cell, i.e. the external applied potential is increased linearly in time while recording the photocurrent, key photovoltaic parameters of the cell can be obtained (Fig. 7).
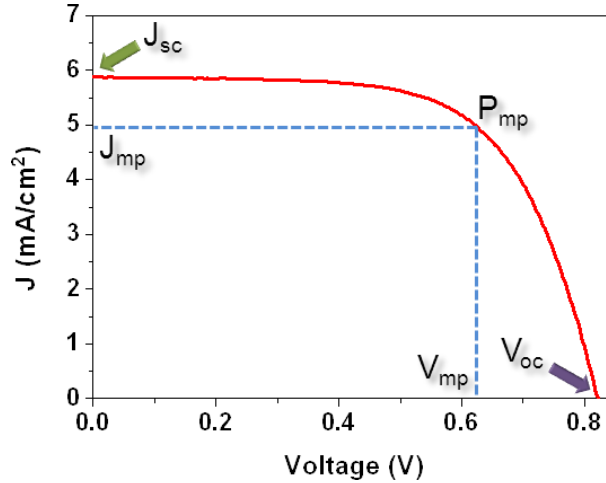

Figure 7. Example of an IV curve and the most relevant photovoltaic parameters associated to the cell.

The power conversion efficiency of a cell is generally defined as

$$\eta = \frac{J_{SC} \times V_{OC} \times FF}{P_{sun}}$$

Where J_{SC} is the short-circuit photocurrent per unit of active area of the solar cell (mA/cm^2) and it represents the maximum attainable current flow at closed circuit (zero resistance). V_{OC} is the open-circuit photovoltage, achieved under no current flow conditions (infinite resistance). P_{sun} is the power of the incident light and FF stands for the fill factor of the cell, a parameter representing the ease of extraction of the photogenerated carriers out of the photovoltaic device. The FF is mathematically expressed as

$$FF = \frac{J_{mp} \times V_{mp}}{J_{sc} \times V_{OC}}$$

$J_{mp} \times V_{mp} = P_{mp}$ is the maximum power output of the cell, while $J_{SC} \times V_{OC}$ is the so-called 'dummy' power output of the device (see Fig. 7). The fill factor is mainly

influenced by the series resistance of the cell and the non-ideality factor *m* of still uncertain origin.

In order to study the response of the solar cells, a standard spectral distribution of light corresponding to an Air Mass parameter of 1.5G (AM 1.5G) is normally used, but the irradiance is set to 1000 W/m^2 (1 sun illumination).

Shor-circuit voltage (V_{sc}) measurements

The electron quasi-Fermi level in dye-sensitized semiconductors may be estimated using this technique. It consists on illuminating the cell under short-circuit conditions, suddenly turning the light off and simultaneously switching the cell to open-circuit condition.

b) Frequency-domain small-perturbation analysis techniques

In this family of techniques, a tiny sinusoidal modulation in light intensity or voltage is superimposed to a DC component while recording the phase and magnitude. Frequencies in the range mHz-MHz are swept, which correspond to timescales of crucial photoelectrochemical processes in DSSCs.

b1) Electrochemical Impedance Spectroscopy (EIS)

The basis of EIS is to apply a small amplitude sinusoidal modulation to the voltage of the cell and to register the sinusoidal current response as a function of the modulation frequency. The impedance is given by the expression

$$Z = Z_0 e^{-j\phi} = Z_0 \cos\varphi - Z_0\, j \sin\varphi$$

Where Z_0 is the characteristic frequency of the system and ϕ is the phase shift. By varying the frequency of the applied signal, the impedance of the system as a function of frequency may be obtained. The data can be represented either as a Bode plot (magnitude of Z and phase vs frequency) or as a Nyquist plot (Re(Z) vs Im(Z)). A Nyquist representation is shown in Fig. 8 along with the potential information obtainable from each frequency zone. Note that not all features will be present or distinguishable for a particular DSSC, e.g. for low viscosity electrolytes the third semicircle will be absent or negligible.
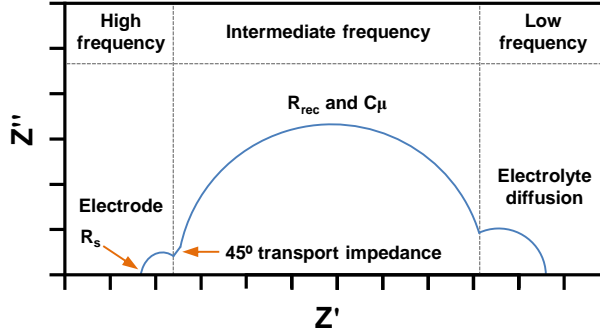
Figure 8. Nyquist impedance spectrum of a common DSSC.

To extract useful information about the charge transfer and to a less extent the transport processes of the cell, it is often necessary to implement an equivalent circuit model made up of common electrical elements such as resistors, capacitors and inductors placed in series or parallel. The equivalent circuit employed in this work is depicted in Fig. 9.
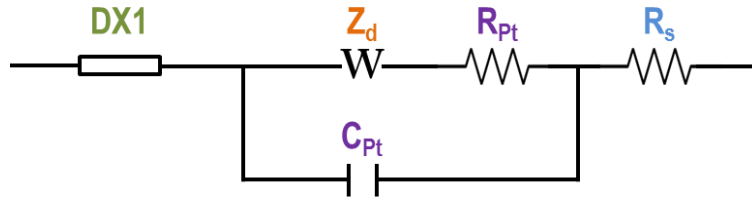

Figure 9. Equivalent circuit model employed to fit the impedance spectra.

DX1 represents the distributed element accounting for the diffusion-recombination transmission line, which is generally used to model the various processes occurring in the oxide film. R_{Pt} and C_{Pt} arise from the charge transfer resistance and the double layer capacitance at the platinized FTO (counter electrode), while R_s symbolizes the series resistance of the electrode plus any other elements that might be in series with cell circuit. Finally, a finite-length Warburg element is used to model the diffusion impedance (Z_d) of the redox species present in the electrolyte.

By applying the diffusion-recombination model of Bisquert and coworkers to a DSSC where electron trapping is dominant, the chemical capacitance ($C\mu$) and recombination resistance (R_{rec}) present at the oxide/electrolyte interface may be calculated according to

$$C_\mu^{-1} = \frac{\partial E_F}{\partial n} = C_{\mu,0}^{-1} exp\left(\frac{-\alpha(E_F - E_F^0)}{k_B T}\right)$$

$$R_{rec}^{-1} = \frac{\partial J_R}{\partial E_F} = R_{rec,0}^{-1} exp\left(\frac{-\beta(E_F - E_F^0)}{k_B T}\right)$$

where α is a dimensionless parameter related to the mean energy of the exponential distribution of localized states in the oxide, β is a dimensionless parameter which can be related to the reaction order of the recombination reaction with respect to free electrons, T is the temperature (ºK), k is the Boltzmann constant and the term $E_F - E_F^0$ accounts for difference in Fermi levels in the oxide and electrolyte, respectively, and is equal to the voltage applied to the cell.

Moreover, the electron lifetime can be extracted from the intermediate frequency semicircle using the relationship

$$\tau_n^{EIS} = R_{rec} \times C_\mu = \omega_{max}^{-1}$$

The small amplitude diffusion length may be determined from the transfer and transport resistances,

$$\frac{L_n}{d} = \sqrt{\frac{R_{rec}}{R_t}}$$

where *d* is the thickness of the film.

Zview software (Scribner) has been used to fit the EIS spectra along with the above mentioned equivalent circuit.

b2) Intensity-modulated spectroscopies

These techniques comprise a small amplitude sinusoidal modulation in light intensity, instead of in voltage as in EIS, superimposed to the steady-state illumination level. Photocurrent (IMPS) response and the phase-shift of this response to the applied modulation are recorded.

A 530 nm LED from LUXEON capable of moving backwards and forward to regulate the light intensity was employed as illumination source for all three frequency response techniques.

Intensity modulated photocurrent spectroscopy (IMPS): carried put under short-circuit conditions. It provides information about the transport processes in the cell (electron

recombination is negligible due to short-circuit conditions). The time constant in IMPS is related to the effective diffusion coefficient (D_n) through equation:

$$\tau_{IMPS} = \frac{1}{\omega_{min}} = \frac{d^2}{\gamma D_n}$$

Where d is the layer thickness and γ is a numerical factor dependent on the layer thickness, absorption coefficient and illumination direction. Here it has been given a value of 2.5.

2.4. Results and Discussion

2.4.1. Fabrication and characterization of TiO₂ and ZnO nanotubes

a) Single-shell NTs

Figures 10 and 11 summarize representative FESEM and HAADF-STEM results obtained after the post-annealing of MePTCDI@meso-TiO₂ (Fig. 10), and MePTCDI@ZnO (Fig. 11) nanowires. It is important to remark that controlling the annealing ramp, the nanotubes either keep the original domed shape with rounded tip (Fig. 10) or appears open on the top (Fig. 11 a-d).

ONWs composition working as template is an element of choice. In this case octaethyl porphyrin (OEP) and red perylene (MePTCDI) have been preferentially employed because of their low sublimation temperature (below 300 ºC at 10^{-2} mbar) facilitates their sublimation through the inorganic walls porous microstructure. Results on metal phthalocyanine as ONWs are also included in the section regarding the emptying mechanism of the nanotubes in order to follow the metal in the molecule as trail of the evacuation pathway.

In Figures 10 and 11 it is possible to appreciate that the original morphology of the hybrid nanowires, even their preferential vertical orientation (Fig. 10b), is preserved after the evacuation process. Moreover, the NTs do not collapse or get deformed after this annealing treatment. Thus, the NTs remain supported on the substrates (Fig. 10b) where the original cores, i.e. the ONWs, were grown. This result is of special relevance since it opens the way for a straightforward growth of these 1D nanostructures on electrodes, processable substrates and devices.
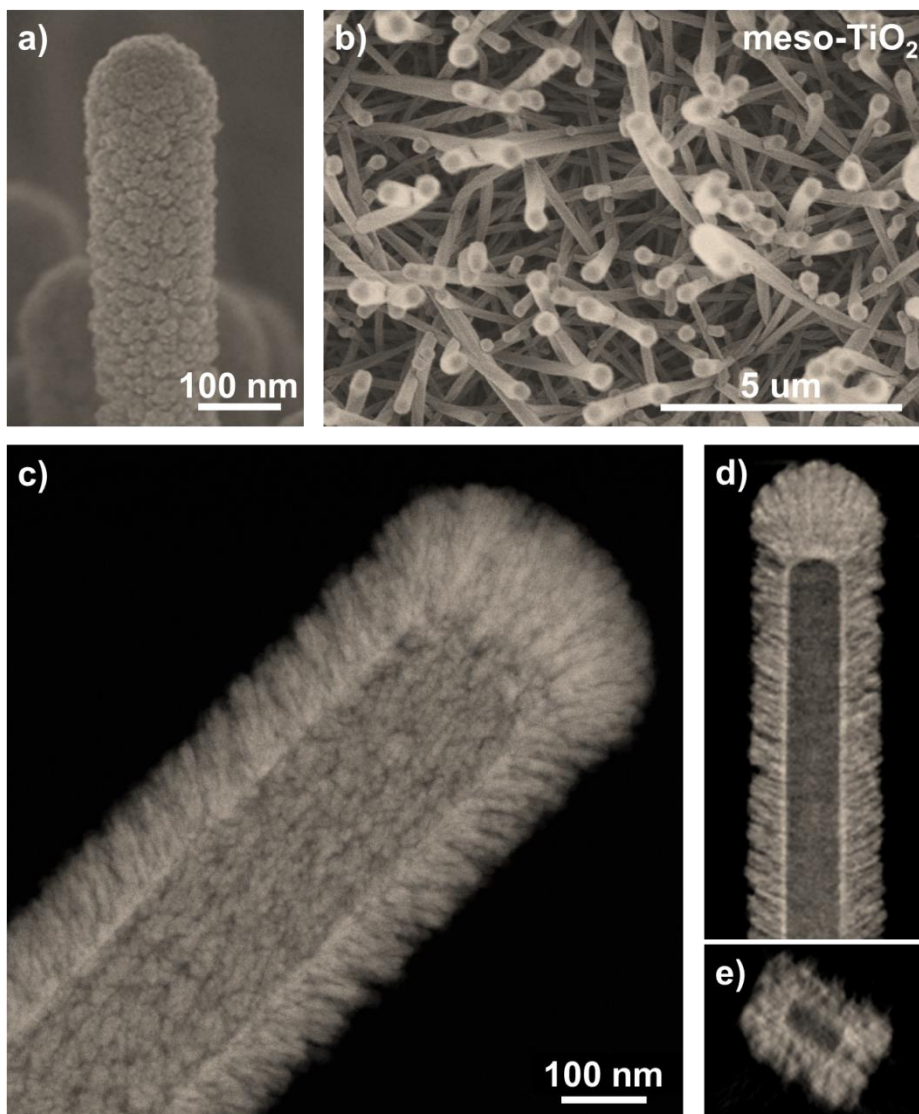
Figure 10. Meso-TiO$_2$ nanotubes. SEM (a-b) and HAADF-STEM (c-e) characterization of nanotubes formed by columnar TiO$_2$ walls. Panel (a) shows the globular surface characteristic of the meso-TiO$_2$ fabricated by PECVD at RT under oxygen plasma. Micrograph in (c) demonstrates the mesoporous microstructure of the wall with columns growing radially from the evacuated core. d) and e) gather snapshots of the HAADF-STEM 3D reconstruction were the rectangular cross section of the tube is clearly appreciable (e) along with a continuous interface between the empty core and the TiO$_2$ columns (d).

Regarding the formation of tailored porous TiO_2 shells, Fig. 10a shows that the TiO_2-mesoporous NTs (see Methodology) depict a rough and globular surface in good concordance with a columnar microstructure radially distributed along the nanowire length (Fig. 10c-d). These columns present a diameter distribution between 5 and 20 nm with pores comprised in both the mesopores ($2 < d < 50$ nm columnar interdistance) and the micropores range ($d < 2$ nm inherent to the distribution of the material forming the columns). It is worth of mention that the HAADF-STEM reconstruction in Fig. 10d demonstrates the formation of a continuous interface between the columns and the empty core in the order of the tens of nanometers that is likely the responsible for the good mechanical stability of the samples. These shells are amorphous since the fabrication process has been carried out at room temperature. Formation of the anatase crystalline thin films is obtained by increasing the substrate temperature up to 250 ºC as it will be described below.

On the other hand, Figure 11 gathers representative SEM, HAADF-STEM and HRTEM images of the ZnO shells. The shell is formed by globular-columnar features growing from a granular interface (Fig. 11a-d). PECVD ZnO thin films are crystalline even deposited at room temperature [Gómez-Romero P., J. Phys. Chem. C 2010]. Figure 11d shows a low magnification STEM micrograph of a ZnO nanotube where it is possible to appreciate an inner hollow core surrounded by ZnO globular grains. Electrical conductivity of the ZnO nanotubes is a key property for many different applications, but it is especially important for the purposes of this Thesis such as solar cells or piezoelectric devices [Wang Z. L., J. Phys. Condens. Matter. 2004][Aricò A. S., Nat. Mater. 2005]. Grain boundary and crystal orientation has been investigated by HR-STEM, since they are critical microstructural features that control the conductivity. This technique provides high resolution images revealing the crystal planes that appear as parallel stripes. Fig. 11e shows the outer side of a nanotube wall formed by ZnO single crystalline columns. The symmetries of the crystal planes are observed by performing a fast Fourier transformation (FFT) of the image in the stripped areas (see insets in e and f). The interplanar distances obtained from the selected area are 2.6 and 2.45 Å which correspond to the typical distances between the (002) and (101) planes, respectively. Fig. 11f presents a high resolution micrograph of the inner nanotube where it is possible to assess the porous size, crystal planes and grain boundaries. At first glance, the material shown in this figure is heavily packed with narrow spaces between grains. However, it also reveals the presence of open porous of about 2-3 nm width that are connecting the inner hollow with the exterior. It will be discussed below that this porosity is crucial to empty the organic core and determinant

in the electron transport properties of the NTs. The FFT analyses in regions A and B yield plane distances of 2.6 and 2.8 Å that correspond to the (002) and (100) planes respectively. The FFT of the C zone results in both distances supporting that both planes are simultaneously observed. These results are in good agreement with the XRD spectra in Figure 12, where peaks corresponding to the planes (100), (002) and (101) were present.
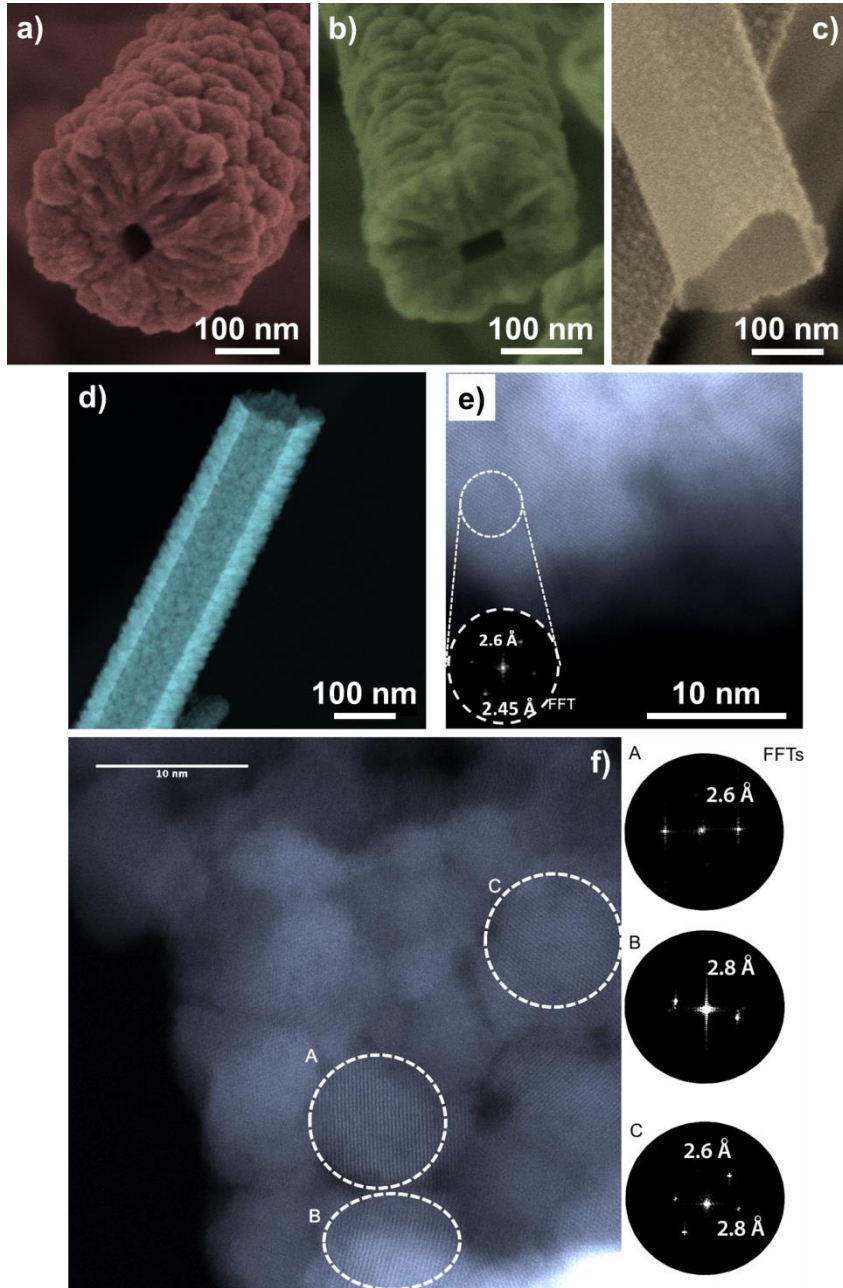
Figure 11. ZnO Nanotubes. a-c) SEM characterization of different nanotubes formed by ZnO of thickness 250 nm a), 80 nm b) and 20 nm c). Details of the columnar microstructure and different shape and lateral sizes of the cavity in open nanotubes are appreciated in (e-g). d) STEM micrograph of a ZnO nanotube, e) and f) HR-STEM micrographs of a ZnO nanotube where the outer and inner wall are correspondingly exposed and analyzed. The insets show the FFTs of the marked areas in the images.

However, analyzing the XRD diagram of supported ZnO nanotubes and comparing them with the reference ZnO thin film, i.e. the layer deposited under the same experimental conditions on a Si(100) substrate, there are some interesting differences. An important feature is the non-texturized character of the supported NTs as evidenced by the presence of an intense (002) peak along to the (100) and (101) in comparison with the XRD diagram corresponding to the thin film that is dominated by the (101) peak (Fig. 12).
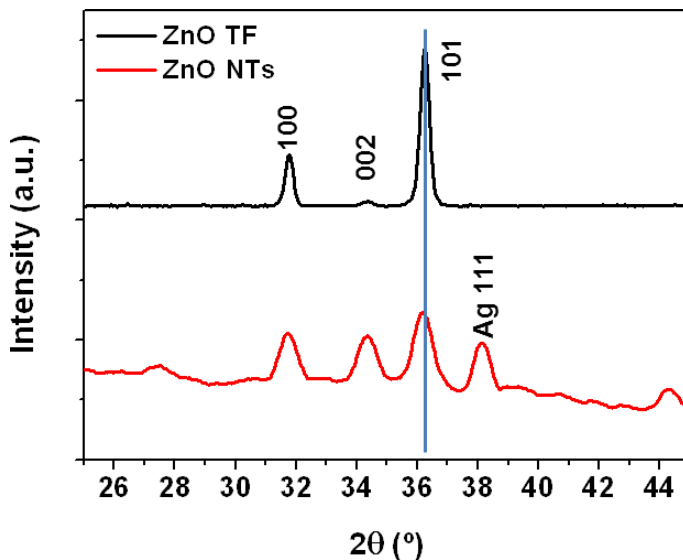

Figure 12. XRD diagrams of ZnO thin film (black) and nanotubes (red). Note that the Ag(111) peak originates from the Ag nanoparticles used as seeds for the ONWs growth.

Also important to notice is that the ZnO nanocrystals present some internal stress as evidenced by a left-shift on the diffraction peaks. From previous studies regarding the growth of nanocrystalline plasma materials it is well known that thinner films present a higher level of stress [Gómez-Romero P., J. Phys. Chem. C 2010] and a low degree of texture development. The smaller deposited thickness on the 1D nanostructure is result of a much larger effective area to be covered in this case. In addition, using Sherrer equation, the wider shape of the diffraction peaks of the nanotubes sustains a smaller crystallite size of ~ 21 nm.

It is also interesting to address several additional features of this method. In one hand, the thickness of the 3D nanotubes is easily controlled and defined by the deposition time. The SEM images in Figure 11a-c show examples of open ZnO nanotubes with

wall thicknesses of 200 nm, 80 nm and 20 nm respectively where the empty core is clearly visible. The wall thickness tends to be thicker at the tips of the NTs (Fig. 10d) due to a self-shadowing effect during the inorganic shell growth by plasma deposition. This effect is more pronounced for thicker nanotubes and is directly linked to their vertical alignment [Macias-Montero M., Adv. Func. Mater. 2013].

The NTs synthesis is carried out at low temperature and in remote plasma deposition conditions, being compatible with temperature-sensible and delicate substrates. On the other hand, the created hollow core replicates the shape of the organic nanowires, characterized by squared (Fig. 11a) or rectangular (Fig. 10e and 11b) inner walls. It is also worth noting the flatness of the inner face (e.g. Fig. 10d). Thus, the outer parts present the typical surface roughness of the TiO_2 or ZnO thin films meanwhile, the interface between the empty core and the shell keeps memory of the smooth molecular surface of the single-crystal wire template. The length of the NTs is as well easily tunable by the deposition time applied in the formation of the ONWs, ranging between the 500 nm and several tens of micrometers.

b) Multishell oxide nanotubes

The PECVD technique allows the formation of multilayer systems of metal oxides by simply alternating the metalorganic or organometallic precursors within the reactor without the need to expose the interfaces to air. This concept has been applied to the fabrication of multishell nanotubes, i.e. nanotubes with 3D walls formed by layers of different metal oxides. Figure 13 gathers two examples of multishell nanotubes of ZnO and TiO_2. In the Figure 13 a)-b) it is shown the formation of a ZnO@nano-TiO_2 multishell (see chapter 3 for nano-TiO_2 information), where the crystalline ZnO layer were first deposited on the ONWs template and the nano-TiO_2 subsequently fabricated on the ONW@ZnO system
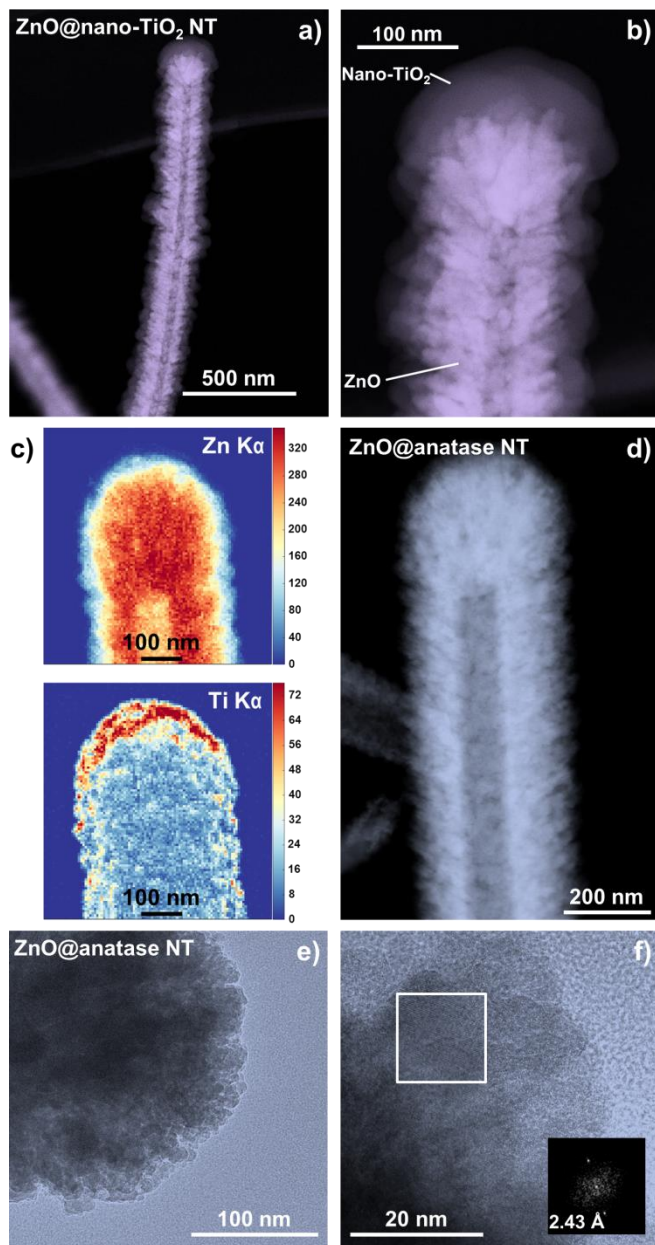
Figure 13. Multishell Nanotubes. a-b) HAADF-STEM micrographs of a ZnO@nano-TiO$_2$ nanotube at two magnification scales showing the homogeneous coverage of TiO$_2$ along the ZnO nanotube length (a) and a detail of this complex nanostructure (b). c-f) Formation of an anatase layer on top of a ZnO nanotube. Distribution of Zn (up) and Ti (down) in the resulting EDX maps (c) obtained from the ZnO@anatase nanotube (d). Bright field TEM (e) and HRTEM (f), the inset showing the FFT of the selected area.

After evacuation of the organic compound the final nanostructure is defined as a ZnO@nano-TiO$_2$ nanotube as seen in the EDX analyses from Fig. 14.
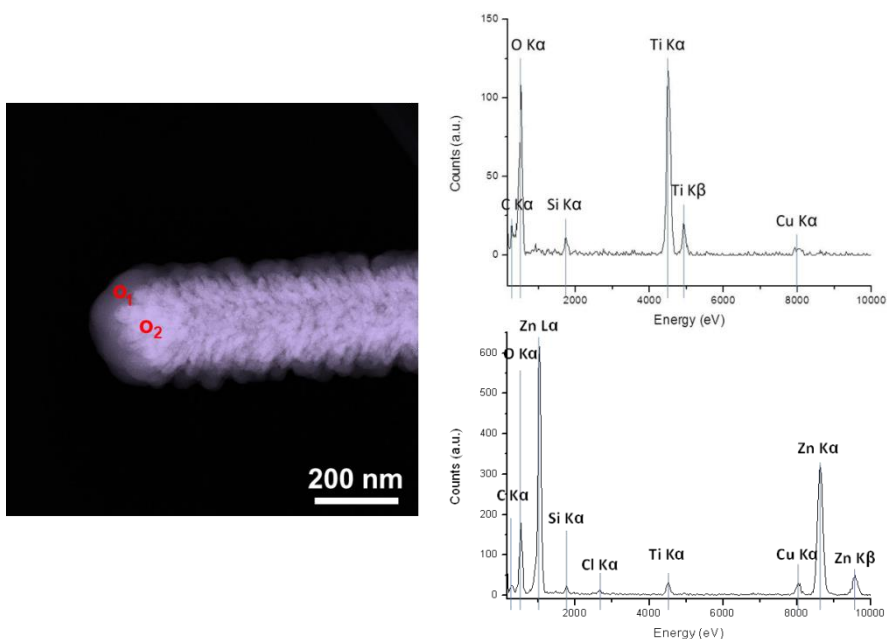

Figure 14. EDX (right) spectra of the selected points in the HAADF-STEM micrograph on the left) showing the different composition of the shells in good agreement with the sequential deposition of ZnO (inner shell) and TiO$_2$ (outer shell).

The HAADF-STEM image in Figure 13 a) demonstrates the homogeneous deposition of the second layer on top of the ZnO shell. The microstructure of the TiO$_2$ shell remains continuous and microporous. Moreover, it conformally follows the roughness of the ZnO surface (Fig. 13b). The method is also extendable to the fabrication of two crystalline shells. As an example, Figure 13 c-f shows the formation of TiO$_2$ anatase grains as external shell on the top of the wurtzite ZnO layer. It is noticeable in the EDX maps (Fig. 13c) that even for such a low thickness (20 nm), the anatase phase is covering the whole ZnO shell. The FFT analysis of the selected area in Fig. 13 f) is in good agreement with the preferential formation of (004) planes as previously published for PECVD polycrystalline TiO$_2$ thin films [Borras A., Crys. Growth. Des. 2009]. Although the results reported here were obtained with TiO$_2$ and ZnO NTs, the methodology is straightforwardly applicable to other oxides deposited by PECVD deposition like SiO$_2$, SiO$_x$C$_y$H$_z$, Al$_2$O$_3$, Ta$_2$O$_5$, oxynitrides, doped oxides, etc. and even to metal (Au, Ag) layers deposited by sputtering. The virtually universal character of the developed procedure and the variety of possible synthesized materials opens the

way to the fabrication of multishell 1D nanostructures with potential applications as single-wire devices.

c) Core-emptying mechanism of hybrid ONW@MOx nanowires

An important characteristic of the NTs microstructure is their tailored porosity. The microstructures presented in this chapter, the meso-TiO_2 and ZnO, possess open pores connecting the inner channel with the exterior. Such porosity contributes positively to the evacuation of the organic template after annealing under vacuum. EDX (Fig. 14), XPS (not-shown) and UV-Vis spectroscopy results (Fig. 15) support that after the evacuation step ii) in Fig. 6, the organic core is completely removed. Figure 15 compares the UV-Vis spectra of PtOEP@ZnO NWs with the corresponding ZnO nanotubes after the vacuum annealing at 280 ºC during 60 minutes at 10^{-6} mbar. The spectrum of the as-prepared samples shows a high absorption in the visible range, due to the absorption of the PtOEP molecules, combined with light scattering. However, after the emptying process, the UV-Vis spectrum changes, resulting in a considerable increment of transparency. At an intermediate stage of annealing it can be seen how the spectrum still presents some features of the absorption bands of PtOEP. In all cases where ZnO shell is present, the spectra are significantly dominated by light scattering effects related with the size and distribution of the 1D supported nanostructures.
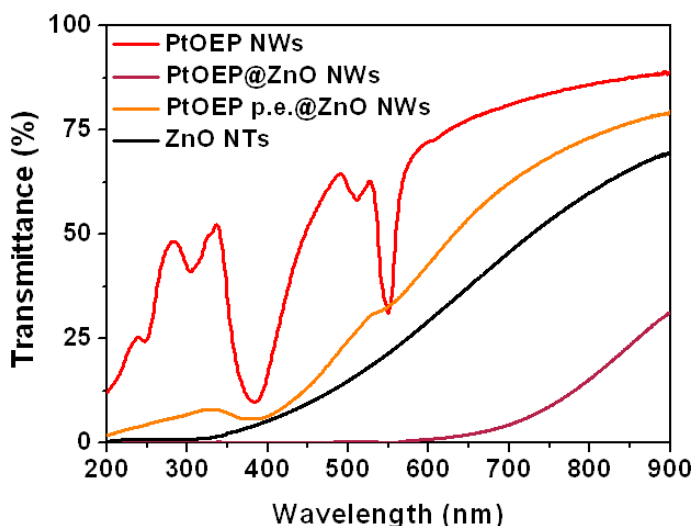

Figure 15. UV-vis spectra of PtOEP NWs, PtOEP@ZnO NWs (hybrid nanowires), PtOEP@ZnO partially evacuated (p.e.) NWs and ZnO nanotubes (fully evacuated) on a fused silica substrate previously coated with a GLAD-SiO_2 thin film.

Further information on the evacuation mechanism was obtained after characterization of different nanowires (Fig. 16) in intermediate stages of post-annealing, i.e. before the organic molecules were completely removed from the inorganic shell. Figure 16 a)-c) gathers characteristic SEM micrographs of the emptying process. The organic compound segregates to the surface of the nanotube in the form of thin stripes (Fig. 16 a). Because of the columnar microstructure of the shells (ZnO and meso-TiO_2) it is possible to observe how some porous channels weaken, provoking the detachment of small grains (e.g. Fig. 16 c). Such effect is more important on the tips of the wires leading to tip detachment under appropriated annealing conditions as schematized in Fig. 6 from the methodology section.

To have access to the interior of the nanostructure during the emptying process, a HAADF-STEM analysis was carried out for partially evacuated samples (Fig. 16d-f). Experiments were performed with NiPc@meso-TiO_2 as starting hybrid nanowire in order to enhance the contrast between the organic compound and the inorganic shell. In good agreement with SEM results, by HAADF-STEM it is possible to appreciate that the remaining organic material redistributes in the form of long and irregular stripes that lay close to the inner walls (brighter regions in Fig. 16 d). Besides, the porous structure appears well defined, evidencing a pore size distribution of a few nanometers. Looking closer to these pores (Fig. 16 e) it is possible to observe low contrast halos surrounding them. These may be attributed to the leftover organic material precipitated during the evacuation through the pores. To verify this, EDX analysis was performed on areas marked in Figure 16 f) as **1** (brighter region) and **2** (darker region). The resulting spectra are compared in Figure 16 g) showing that zone **2** has an important amount of titanium, while zone **1** presents nickel and carbon as main components. It is also important to remark that after completing the emptying process there is no trace of the small-molecules forming the original ONW template.
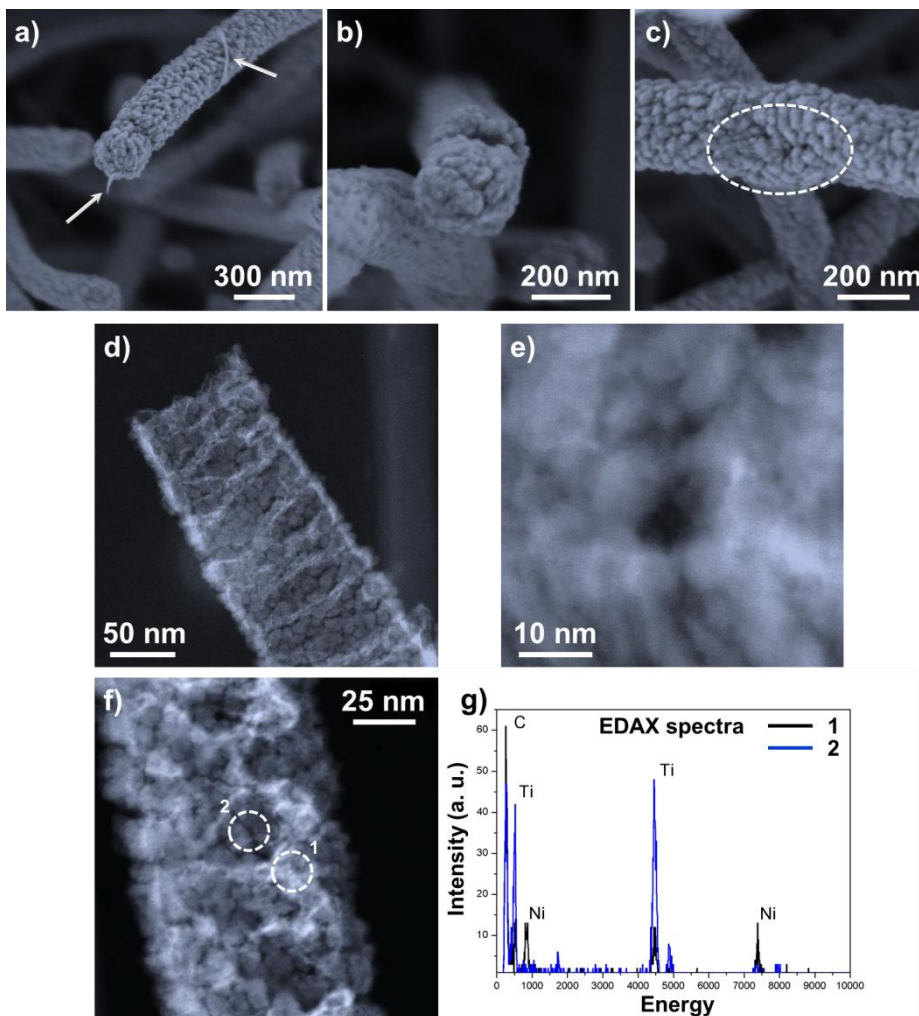
Figure 16.Characterization of the emptying process. a-c) SEM micro-graphs of hybrid MePTCDI@ZnO after heating for 30 min in high vacuum, where the emptying process is clearly observable: arrows in a) indicate the accumulation of the organic molecule; c)shows one of the leaking points of the nanostructure. d-f) HAADF-STEM micrographs of hybrid NiPc@TiO$_2$ after a partially completed emptying process where the brighter regions correspond to the Ni in the NiPc molecule as it is corroborated by the EDX comparison in g) between the areas marked as **1** and **2** in (f).

Therefore, these results conclude that the organic core molecules are released through the connected porosity on the inorganic shells without decomposition. In the cases analyzed in Figure 16, the final situation of the nanotubes is open but similar results were found for the domed nanotubes. Figures 6i and 6i' in the methodology

section intend to illustrate the intermediate steps. The increased pressure created in the interior of the inorganic shell by partial sublimation of the organic core would be released by diffusion of the organic part through the porous structure in a continuous and homogeneous way. This takes place when the hybrid nanowires temperature is slowly increased to the organic molecule sublimation temperature, which leaves the unmodified inorganic shell microstructure (Fig. 6i). For higher temperature ramps, the overpressure conditions inside the nanowire drive to the detachment of the tip, likely due to a different grain or columnar orientation (Fig. 6i').The last route makes accessible the inner hollow of the nanotube as presented in Fig. 11a-d.

In the previous subsections, a full vacuum approach for the fabrication of supported 3D nanotubes with tailored composition, microstructure and porosity have been presented. The aim now is to demonstrate that the developed procedure allows the implementation of functional oxide NTs as active component in a particular application, namely as photoanode in dye sensitized solar cells.

2.4.2. ZnO Nanotubes-Based Dye Sensitized Solar Cells

In this section, the fabrication of a complete and functional DSSC based on supported NTs is presented. The main goal of this study is to demonstrate the capability of the ZnO nanostructures to act as photoanodes and to study their charge transfer and electron transport properties. Moreover, for the first time the influence of NT wall thickness on DSSCs performance is introduced and analyzed. The length of the NTs was kept constant owing to prior studies of its impact in DSSCs [Bi D., J. Phys. Chem. C. 2010]. It is important to note that no efforts have been carried out to optimize the efficiency, as this requires to look for the appropriate dye, sensitization procedure and choice of electrolyte, which is out of the scope of this study.

The analysis of the electron dynamics transport in the NTs is especially important since its results are extendable to the performance of the NTs in other devices such as the already mentioned perovskite solar cells, piezoelectric nanogenerators, gases and UV sensors. Three different types of samples have been chosen for this study with a similar NT density and length but different NT wall thicknesses: 20 nm, 80 nm and 250 nm.

To avoid recombination at the bare zones of the electrode, a ZnO thin film of 200 nm, covering completely the FTO substrate, has been deposited prior to the nanotube growth (see Fig. 18a). Additional details about device fabrication are included in the methods section. Figures 17 and 18 and Table 1 gather selected photovoltaic

parameters for the solar cells fabricated by using the three photoelectrodes. An 800 nm ZnO porous thin film electrode has also been included in the study as a reference to compare the performance of the nanotubes with respect to porous thin films. This reference sample was grown under the same experimental conditions that the NTs but a longer deposition period and without the ONW-template.

Significant changes are observed in the IV curves as a function of the NT wall thickness. The first difference is that the open circuit voltage decrease for thicker NTs. This parameter depends on the recombination rate from the ZnO electrode to acceptors in the electrolyte (I_3^- in Fig. 18b). Its lower value for 250 nm electrodes indicates that thicker NTs present higher surface area for electron transfer to the electrolyte. An inverse effect is observed in the generated photocurrent, a parameter that is larger for thicker NTs. This is likely due to the amount of dye absorbed on the surface. The observed tendency can be accounted for by the increment of the effective surface available in thicker nanotubes that should result in a higher dye load.
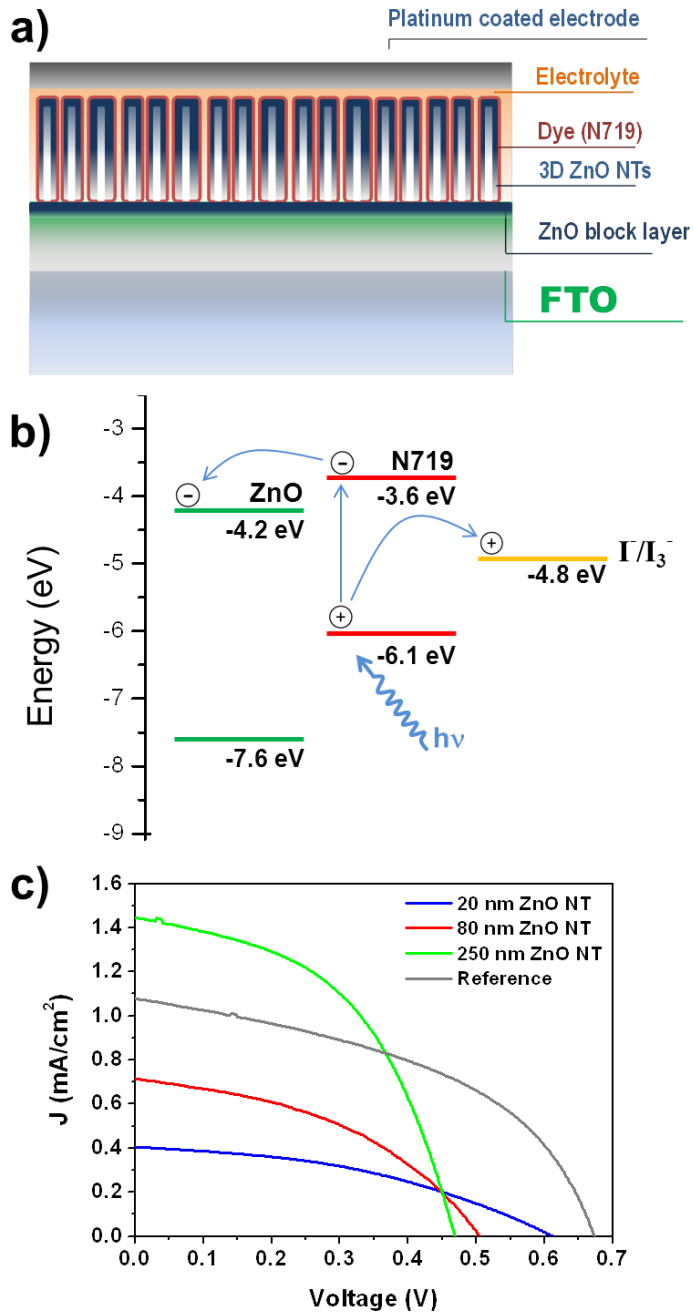
Figure 17. Schematics of the DSSC device based on ZnO NTs (a) and energy levels (b) [Liu J., Nanotechnology 2010] c) I-V curves for the DSSCs assembled with NTs of three wall thickness and a 900 nm thick ZnO thin film as a reference [Macías M., Ph.D. thesis 2103].

The best efficiency reached by the DSSCs implementing the electrode with 250 nm is 0.3% (c.f., Table 1). In order to contextualize the results obtained for the ZnO NTs, a reference DSSCs incorporating a PECVD porous ZnO thin film as electrode has been fabricated. It is apparent that although the highest nanotube DSSC efficiency is lower than the one obtained for the reference thin film, the photocurrent measured is larger for the NT electrode. This result is very significant since the nanotubes are more than three times thinner than the reference thin film. The increment of dye adsorbed might be related to the high specific surface area achieved with the nanotubes configuration and the smaller crystal size developed in these systems (Fig. 11).

Table 1. Photovoltaic parameters for ZnO-based DSSCs as a function of the wall thicknesses. - Mean photovoltaic parameters values and estimated errors have been obtained from data of three devices with the same configuration. A device fabricated with an 800 nm thin film is used as reference.

Cell	J_{sc}(mA/cm^2)	V_{oc}(mV)	FF(%)	η(%)
20 nm ZnO NT	0.39$\pm$0.21	610$\pm$25	40$\pm$1	0.10$\pm$0.05
80 nm ZnO NT	0.73$\pm$0.15	500$\pm$30	44$\pm$2	0.20$\pm$0.05
250 nm ZnO NT	1.48$\pm$0.25	460$\pm$20	50$\pm$1	0.30$\pm$0.05
Reference	1.05$\pm$0.30	670$\pm$15	45$\pm$1	0.50$\pm$0.1

Further information about the charge transfer and electron transport processes of the cell can be obtained by Electrochemical Impedance Spectroscopy (EIS) and Intensity Modulated Photocurrent Spectroscopy (IMPS). The EIS spectra exhibited the typical shape of the current response of a DSSC under small Fermi level perturbations, with a semicircle at intermediate frequencies attributed to the charge transfer between semiconductor and electrolyte (recombination reaction) [Fabregat-Santiago F., Sol. Energ. Mat. Sol. C. 2005][Guillén E., J. Phys. Chem. C. 2011]. Fitting these spectra by using the transmission line model accounting for transport and recombination in the semiconductor electrode provides specific data for the recombination resistance and the capacitance of the system as a function of the applied bias. The variation of these parameters as a function of the Fermi level (voltage) is presented in Figure 18 a)-c). The recombination resistance presents the usual exponential behavior with respect to the applied bias, while the exponential behavior of the experimental capacitance for the two ZnO textured electrodes (reference and NT) suggests that it corresponds to a chemical capacitance [Bisquert J., Phys. Chem. Chem. Phys. 2003]. Moreover, the lifetime of accumulated electrons in the semiconductor electrode is higher for the reference DSSC, a result that explains the larger V_{oc} obtained for this electrode.
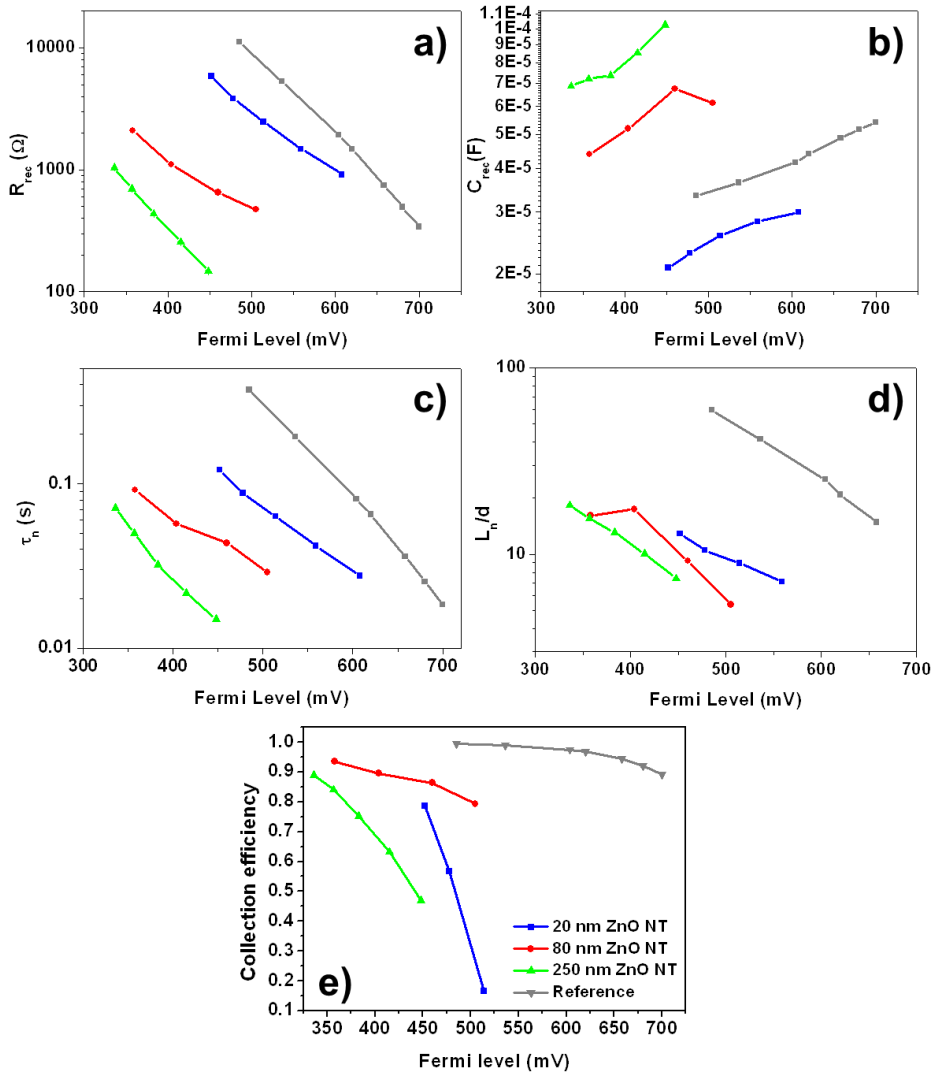
Figure 18. a-c) Impedance spectroscopy results of DSSCs fabricated with ZnO nanotubes. Impedance parameters extracted from the fitting of the EIS spectra at various applied potentials: a) Recombination resistance. b) Capacitance. c) Lifetime. Collection efficiency: d) electron diffusion length, estimated as the ratio of recombination and transport resistances, normalized to the ZnO thickness (L_n/d). e) Collection efficiency calculated as 1 - τ_{IMPS}/τ_n.

The IMPS measurements provide useful information about the electron transport properties of the electrodes. The calculated time constants (τ_{IMPS}) are in the order of tens of milliseconds and present two different behaviors. An exponential dependence is found for the DSSCs fabricated with the thinnest nanotubes (20 nm), while for the

80 nm and 250 nm NTs, τ_{IMPS} remains approximately constant. A similar constant behavior is found for the reference thin film. Such a constant value of τ_{IMPS} can be related with the absence of an electron multiple trapping behavior in the ZnO electrode as previously reported [Vega-Poot A. G., ChemPhysChem 2014]. The diffusion length, defined as the average distance that electrons can travel in the photoanode before recombination, provides information about charge collection processes in photoanodes. For small perturbations of the Fermi level, a small-perturbation diffusion length L_n is defined, which can be obtained by combining EIS lifetime and IMPS transport time. Figure 18 d) presents the calculated values for this magnitude, showing values around ten times larger than the ZnO wall thickness and values for the reference thin film cell one order of magnitude higher than those found for the nanotubes DSSCs. A diffusion length much longer than the film thickness indicates that electron collection is quantitative, so this is not an issue for the performance of the cell.

Joining the information provided by the EIS and IMPS analysis it is possible to approximately estimate the collection efficiency as $1 - \tau_{IMPS}/\tau_n$ (Fig. 18e) where τ_n corresponds to the lifetime of accumulated electrons. Due to the relatively long diffusion lengths observed, this equation can be expected to be reasonably valid with an acceptable level of inaccuracy. Moreover, given the possible deviations of the calculated collection efficiencies from real ones, for values < 90%, focus is made on the trends and not on the absolute values. The graph shows clear differences between the efficiencies calculated for the different nanotubes devices, although in all the cases they converge to a maximum efficiency situation for low Fermi level energies (short-circuit conditions).
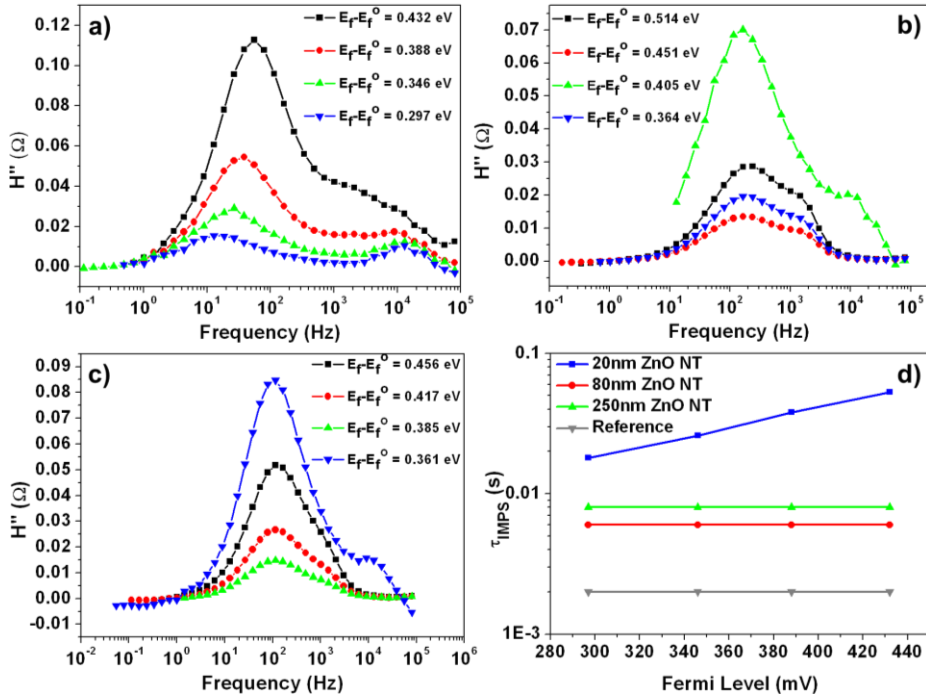
Figure 19. IMPS of DSSCs implementing ZnO nanotubes - a-c) Imaginary IMPS component plotted versus the frequency at different light intensities for NTs 20 nm wall thickness. d) τ_{IMPS} plotted versus the Fermi level for the different DSSCs, including the ZnO porous thin film device as a reference.

Taking into account all this information, the mechanism shown in Figure 20 for the electron transport in ZnO NTs is proposed. The nanotube wall is formed by ZnO globular columns (see Fig. 11) growing from the interface with the core. The photoelectrons are mainly generated in the outer shell of the ZnO wall and then migrate till the FTO substrate across the shell. The transport of electrons is effective within the column as such is the case in the columnar thin film and in good agreement with the single-crystalline condition (see Fig. 11e). However, while in the porous thin film configuration the columns are directly connected to the FTO electrode, in the NT architecture the path between the column where the photoelectron was generated and the electrode is more tortuous due to the grain boundaries between the columns and at their bases (i.e., in the inner face of the wall), involving as well the interface between the NT and the 200 nm ZnO blocking layer. This explains the shorter lifetimes and diffusion lengths and lower recombination resistances observed in NTs of increased thickness and when compared with the reference.
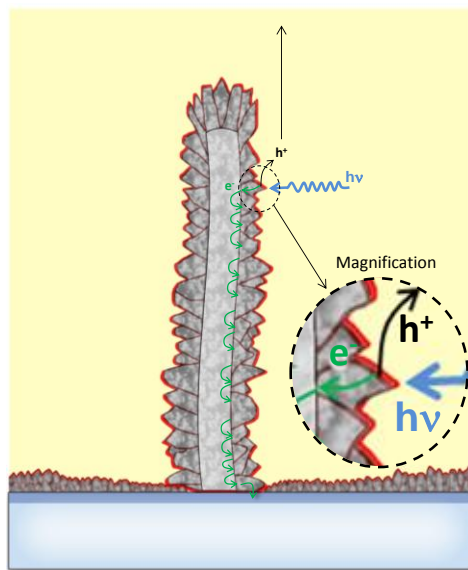
Figure 20. Scheme of electron conduction along a ZnO NT by an electron hopping mechanism.

2.4.3. TiO$_2$ Nanotubes-Based Dye Sensitized Solar Cells

Hollow 1-D nanostructured anatase NTs DSSCs were also fabricated. Three different anatase nanotubes were produced with increasing thickness so as to study the evolution of photovoltaic performance. The equivalent thin film thickness for each cell was: 660 nm, 1.6 µm and 6.6 µm. A 200 nm anatase thin film (blocking layer) was deposited on the FTO prior to the growth of the NTs (for further details see the methodology section). At the same time, reference thin films directly grown on the bare FTO substrate were also fabricated for comparison.

Figure 21 a) presents a complete anatase TiO$_2$ NT, where it can be appreciated a great number of crystalline facets arising radially and axially (at the tip). These crystals are present along the whole body of the NTs as observed in Figure 21 b). The microstructure of the NTs resembles that of anatase thin films grown directly on Si substrates, as already reported [Borras A., Crys. Growth. Des. 2009].
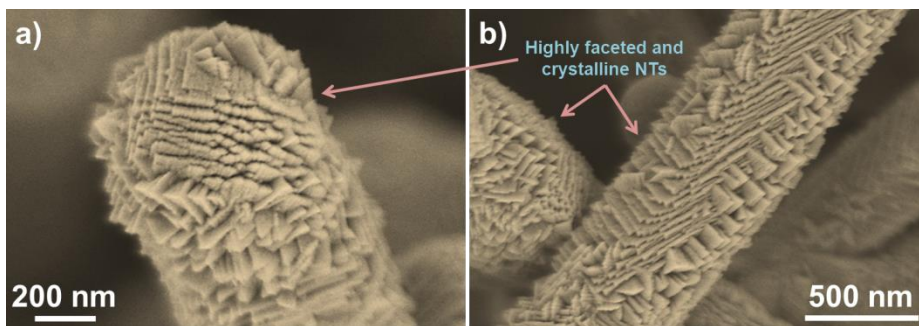
Figure 21. SEM normal view of a 660 nm anatase NT tip (a) and its "body" (b).

By augmenting the thickness of the NTs to 1.6 μm, the crystal habits develop even further to the extent of conferring a rose-like shape to the NTs (when observed from the top) as seen in Figure 22 a). As already discussed for ZnO NTs, the thickness is not uniform along the whole structure. The thickness matches with the analogue thin film at the very top of the nanotube and it gradually becomes thinner towards the base (Fig. 22 b). It is also evident from the SEM cross-section that there is still plenty of unoccupied space between NWs which will not contribute to the cell performance. However, by a close inspection to Fig. 22 d), it may be noted that each crystal emerging from the NT is decorated with numerous sub-crystals, resembling a feather. These features will increase even more the surface area of the NTs, which in turn should boost dye loading.
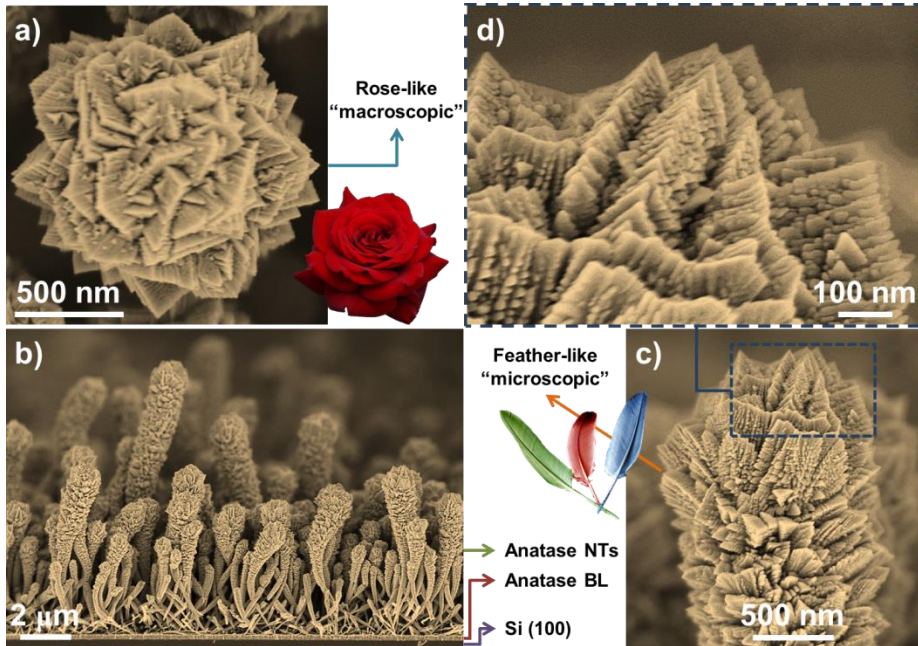
Figure 22. SEM images of 1.6 μm NTs. normal view (a) and cross sections (b-c). (d) zoomed area of (c).

The anatase feathers growing radially from the axis of the NTs retain some degree of individuallity with some empty space between as evidenced by STEM in Fig. 23, even though they are welded at the bottom forming the cavity walls. This axial cavity is formed as a consequence of the organic template evaporation.
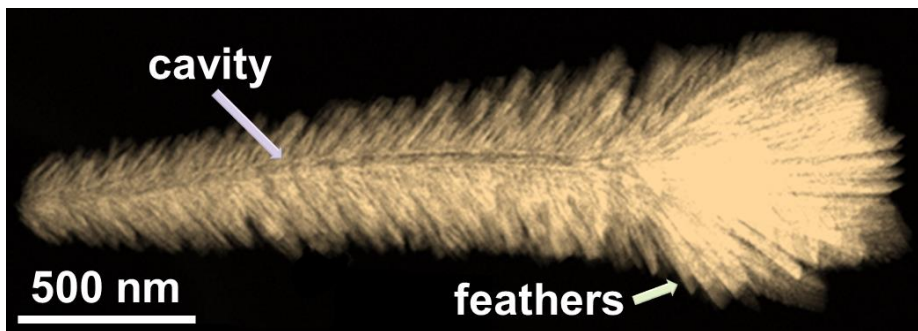

Figure 23. HAADF STEM image of a 1.6 μm NT with some features indicated.

If the thicknees of the anatase shell is increased even further up to 6.6 μm, the shape of the NTs heads change from "roses" to "artichokes" (Fig. 24 a-d). A few more observations can be made by inspection of the SEM images in Fig. 25: the gaps between adjacent structures has been reduced dramatically (Fig. 24 c-d), to the extent

* In a feather, the barb consists of the small filaments growing from the shaft (center of the feather).

of notiaceable percolation at the top with some voids as evidenced in Fig. 24 a-b). Cross-section micrographs (Fig. 24 c-d) also reveal that the initial small crystals (Fig. 21-22) have evolved into "huge" structures, changing from barbs* to feathers. Moreover, it is worth mentioning that these structures present a high degree of interconnection at the bottom, visible in Figure 24 d) where an island of these structures has detached from the substrate. On the other hand, anatase TiO$_2$ thin films exhibit a vertical growth of feather-like crystals as shown in Figure 24 e). Compared to 1D NTs, thin film are more compact, even when they possess both micro and mesoporosity [Borrás A., Micropor. Mesopor. Mat. 2009].
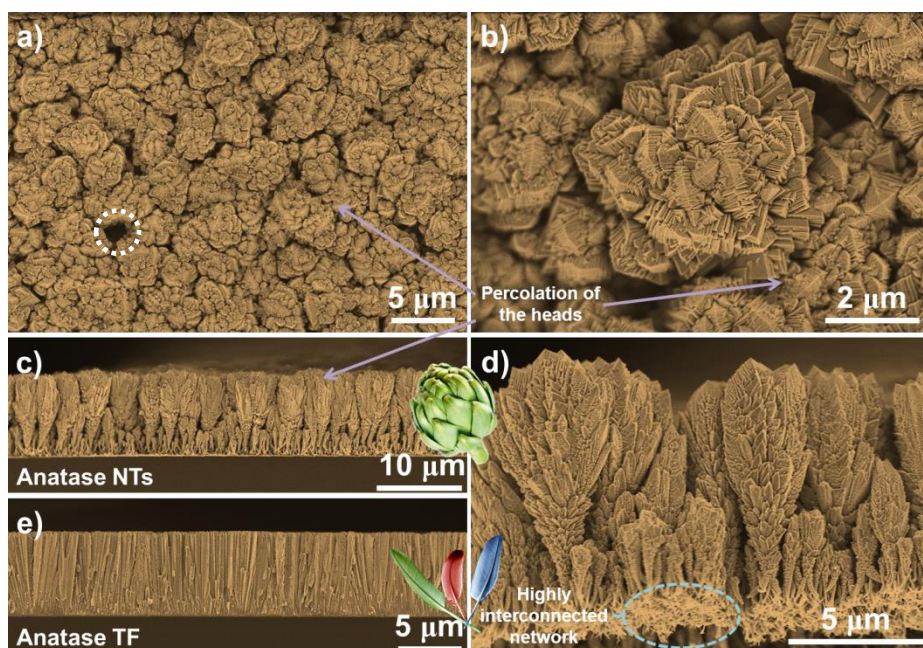

Figure 24. SEM images in normal view of 6.6 µm anatase NTs (a) and (b). Cross sections of NTs (c)-(d) and thin film (e).

Furthermore, some interesting changes are readily observed in anatase thin films used as reference when the thickness is increased ten times. As it can be observed in Figure 25, the first noticeable difference is the interspacing between adjacent anatase columns. For 660 nm there exist clear gaps between columns (Fig. 25a-b), while for 6.6 µm the empty space has been drastically reduced, giving the sensation of more closed-packed structures (Fig. 25c-d). Secondly, the size of the columns has evolved from less than 100 nm to more than 200-300 nm, which certainly explains the reduction of free space.
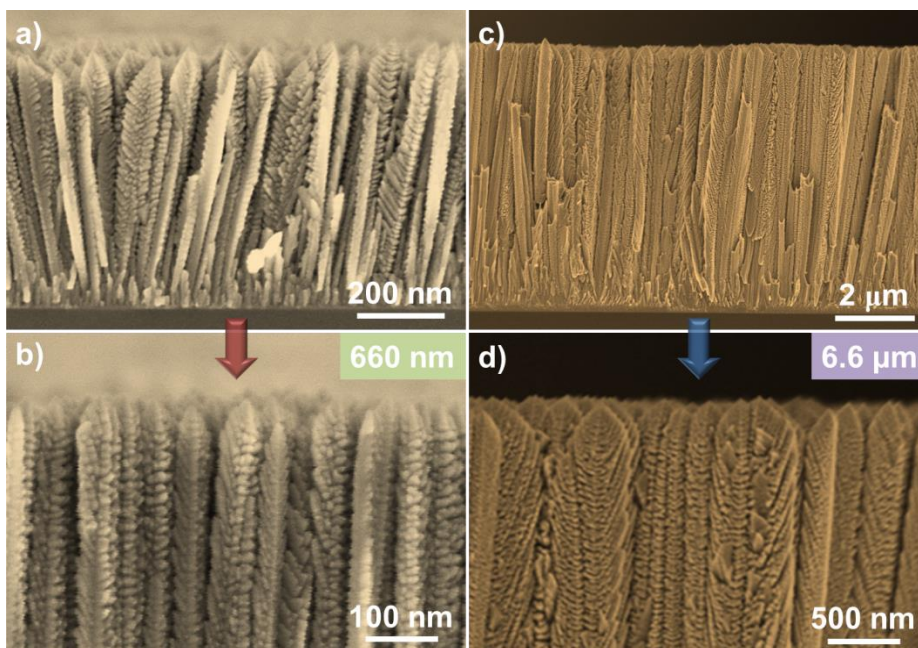
Figure 25. SEM cross sections of 660 nm (a-b) and 6.6 μm (c-d) anatase thin films.

The XRD diagramms for the anatase NTs are presented in Figure 26, where it is clear the crystalline nature of the as prepared samples. Just as in the case for ZnO, NTs did not presented a preferential orientation while thin film samples were texturized [Borras A., Cryst. Growth Des. 2009].
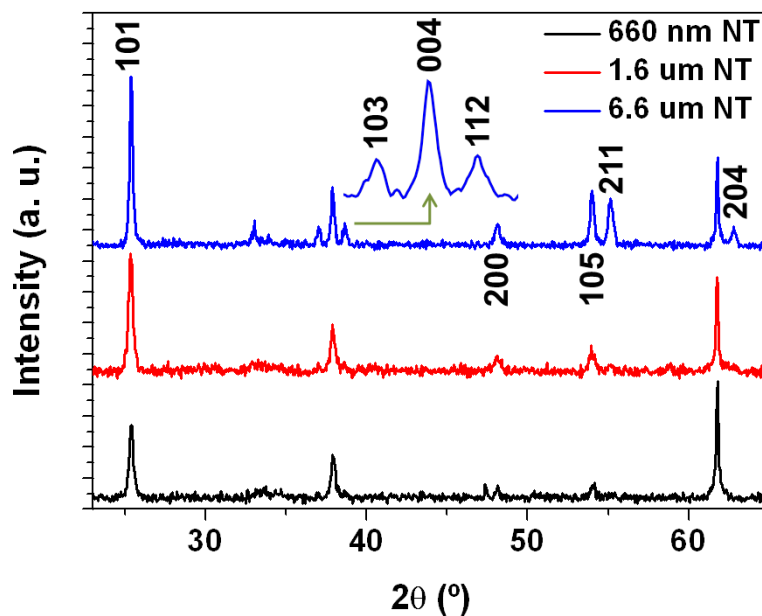
Figure 26. XRD diagramms of anatase NTs for a TiO_2 thickness of 660 nm, 1.6 μm and 6.6 μm.

The optical properties of these samples were also investigated. As it can be observed In Figure 27, thin film samples were relatively transparent presenting low scattering, which became more apparent for thicker samples. On the other hand, NTs exhibited always a whitish appearance due to important scattering effects.
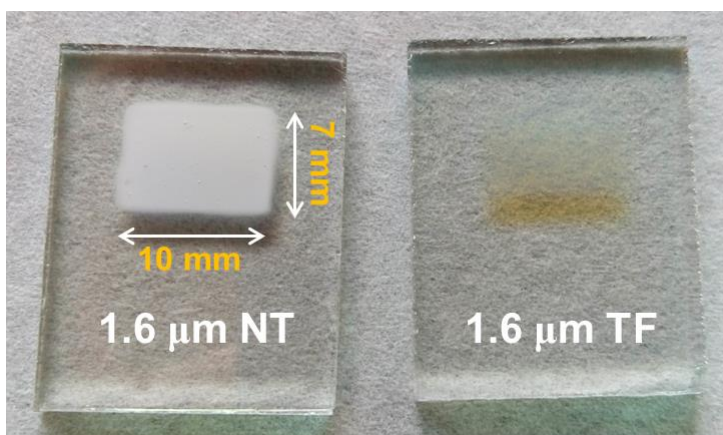
Figure 27. Photograph of 1.6 μm thick anatase thin film (right) and NTs (left) samples prepared on FTO coated glass.

Figure 28 presents the UV-Vis-NIR transmission spectra of a 3 μm thick anatase thin film and the corresponding NTs samples. NTs strongly scatter the light in the whole visible and NIR range, whereas the thin films present significantly less scattering. It is important to note that the strong absorption bands in the region 1400-2500 nm are due to the FTO/glass substrate.
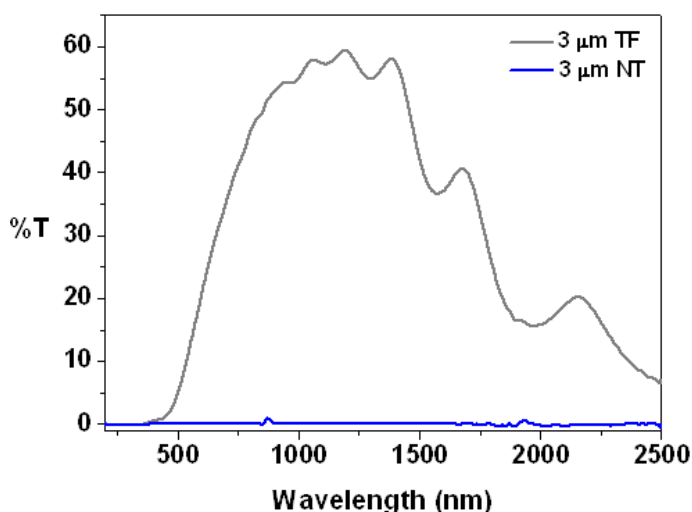

Figure 28. UV-Vis-NIR transmission spectra of 3 μm thick anatase thin film and NTs on FTO/glass.

The mean NT length can be calculated performing statistics on cross-section SEM images. The mean values for the three NT samples are presented in table 2, where it can be observed that even for the thickest sample the average NT length stays below 10 μm.

Table 2. Mean NT length obtained from SEM micrographs.

Sample	Mean length (μm)
660 nm	2.67 (extrapolated)
1.6 μm NT	3.14±1.26
6.6 μm NT	5.62±3.34

A second type of anatase with a different microstructure was grown just for comparison with the as-grown anatase in DSSCs. This second version of anatase

consisted in meso-TiO$_2$ which was post-annealed to 450 ºC to induce the crystallization to anatase. Furthermore, an hiperbranched anatase variant of meso-TiO$_2$ (nanotree) has also been prepared and implemented in DSSCs (For further details about nanotrees formation please refer to Chapter 4). Meso-TiO$_2$ exhibited the typical columnar nanostructure, but due to the high thickness (3.72 μm), the tips were rounded and smooth like a baseball bat (Fig. 29a-b). However, the nanotree version retained the columnar character even at the tip, probably due to a smaller diameter of the nanostructures. This last fact is a consequence of a higher density of template NWs (see Chapter 4), which in turn gives rise to a major distribution of TiO$_2$ and hence thinner nanostructures (Fig. 29c-d).
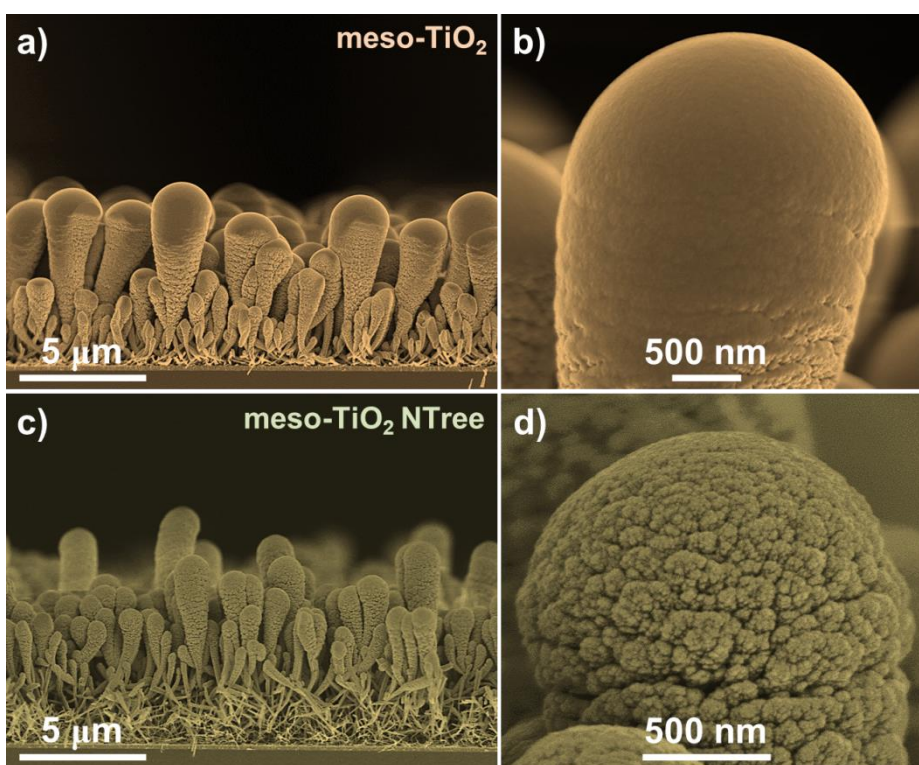

Figure 29. SEM cross sections of meso-TiO$_2$ post-heated samples (a-b) and the corresponding nanotree (NTree) version (c-d).

In order to evaluate the dye loading on the samples, integrating sphere measurements were performed. Unfortunately, due to the high light scattering of the NTs samples which increased significantly with the thickness, the results were not coherent. Instead of that, to illustrate the dye loading the Figure 30 presents both NT and thin film samples with the three different anatase thicknesses after the dye adsorption. It is

clear that the thicker the anatase layer the greater the amount of dye adsorbed. Moreover, NT samples exhibited always a more intense pigmentation than their equivalent thin film.
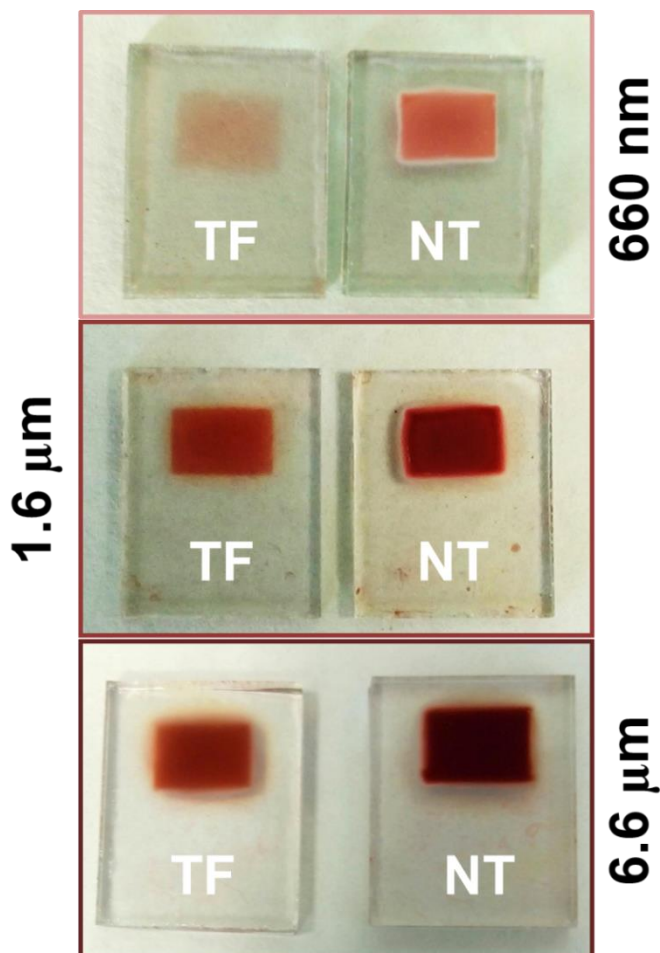

Figure 30. Photographs of real DSSCs electrodes after overnight immersion in dye N719. The anatase layer thickness was 660 nm (up), 1.6 μm (middle) and 6.6 μm (down).

Anatase DSSCs were constructed just as ZnO ones: on the electrode side, a thin anatase blocking layer (see methodology) was deposited on FTO/glass followed by the growth of a nanostructured film (thin film or 1D). The rest of the cell, i. e. counterelectrode, electrolyte and dye remained unchanged. A scheme of a complete cell is shown in Figure 10 a) together with the energy level diagramm of the cell, Figure 31 b). The I-V curves of four different thicknesses of anatase in NTs and thin films are presented in Figure 31 c).
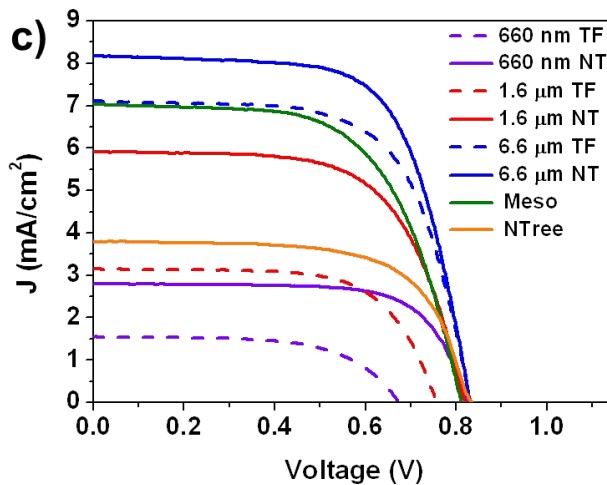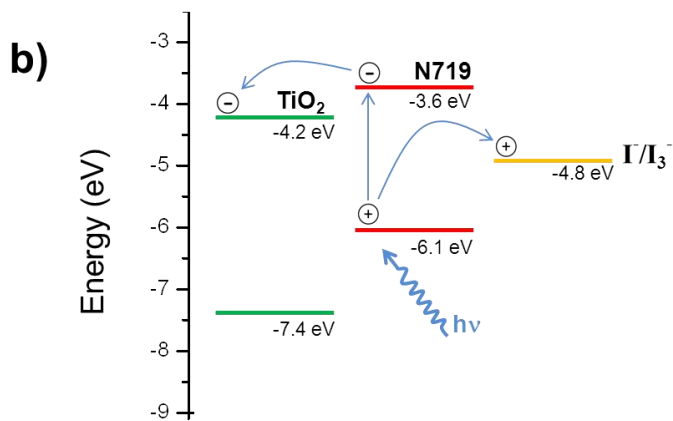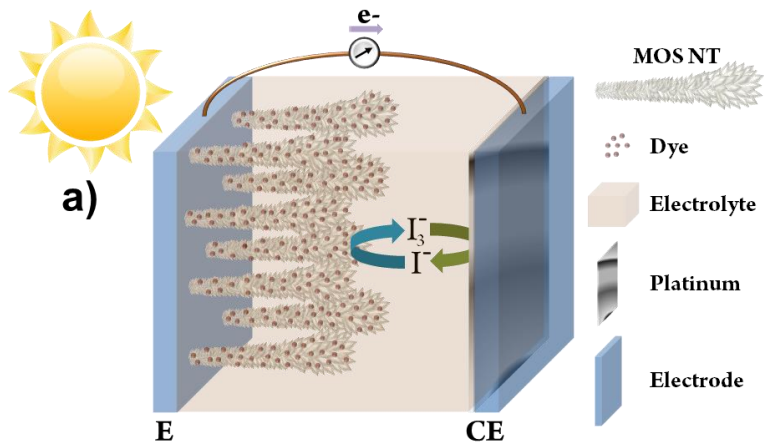
Figure 31. a) Scheme of a DSSC with anatase NTs (blocking layer not shown), b) energy levels of the cell [Cao G., World Scientific Publising 2010] and c) I-V curves for the DSSCs assembled with NTs and TFs of three wall thicknesses (best cells shown). Mesto-TiO_2 and meso-TiO_2 NTree curves are also shown.

The photovoltaic parameters of a DSSC are directly linked to the thichkness of the mesoporous layer for a given semiconductor material. Usually, by increasing the thickness of the active area, more dye is adsorbed as a consequence of a higher surface area, which in turn translates in a higher photocurrent (J_{SC}), but the photovoltage (V_{OC}) drops as a consequence of a higher recombination rate. [Ref paper Jesús]

According to Table 4, an increase in anatase thickness effectively produced higher photocurrents, but interstengly, the photovoltage does not drop as expected for the thickest samples. On the other hand, the fill factor presented a mixed behavior depending on the kind of film present, i.e. thin film or nanotubes.

- As already mentioned, the photocurrent increases with the thickness of anatase. Moreover, for the same thickness NTs exhibited always a higher photocurrent than TF, probably due to their superior surface area. This is in perfect agreement with noticeable more dyed NT samples compared to their TF counterparts (Fig. 30). Furthermore, the superior optical dispersion of NTs compared to TF is probably contributing to a higher photocurrent. This effect is well known to be beneficial for the cell performance due to an increase in light harvesting [Cheol S., Adv. Pow. Tech. 2012][Wu Wu-Qiang, Energy Environ. Sci. 2014].

- Unexpectedly, the photovoltage of the cells generally did not decrease for thicker layers of anatase. Thin film cells showed an improved behavior when the the thickness of TiO_2 was increased reaching a maximum of 831±1 mV for 6.6 μm. A feasible explanation may be found in Table 3 where the size of the crystalline domains have been calculated for some samples. When the thickness is increased beyond 660 nm up to 2 μm, the size of the crystals is incremented, and considering that the crystal size for TFs is larger than that for equivalent NTs cells, then for a 6.6 μm the size of the crystalline domains should surprass 80-90 nm, which in turn should translate into a smaller recombination rate and higher photovoltage, as observed.

  The photovoltage of NTs cells was more or less constant with thickness, but generally much larger than that of equivalent thin film cells. An unattended diference between NTs and TF cells is the presence of a blocking layer in NTs. According to Table 3, a blocking layer of 200 nm should posses a crystal size of aorund 80-90 nm, while for a thin film of 660 nm the crystalline domains are around 49 nm, giving rise to a higher recombination

and lower photovoltage. So, the thickness of the blocking layer seems to play an important role due to recombination a at the electrode level.

Table 3. Sizes of the crystalline domains determined by the Scherrer method after the XRD patterns in Figure 27 and reference [Borras A., Cryst. Growth Des. 2009]*.

Sample	Crystal size (nm) (101)
150 nm TF*	80.2
295 nm TF*	90.6
660 nm TF*	49.1
2 µm TF*	57.6
660 nm NT	42.9
1.6 µm NT	39.1
6.6 µm NT	86.6

The photovoltaic parameters extracted from the I-V curves are gathered in Table 4. The most important observations from the Table 3 are the following:

- Anatase was considerably more efficient than ZnO, at least for the thin film case. By comparing a 800 nm ZnO thin film vs a 660 nm anatase one, it can be noticed that ZnO yielded lower photocurrent, photovoltage and fill factor. It has been determined that ZnO-based cells posses worse electron injection rate and dye regeneration, contributing to a poorer performance against TiO_2 [Idígoras J., J. Phys. Chem. C 2015].
- The fill factor does not seem to have changed much for TFs, while for NTs there has been a drop of this value when the thickness of anatase was increased. Interestingly, NTs possessed a higher FF than thin films.
- For higher thickness, 6.6 µm, the efficiency of the thin film cell nearly triplicated, whereas for NTs it augmented by a factor of 1.5. Looking at the photovoltaic parameters of NTs and thin film, it can be noticed that there are no big differences between them, with a slightly higher photocurrent generated by NTs. A possible explanation for this behavior is based on the high level of (undesired) percolation reached for such a thick deposit (Fig. 24a-d), i. e. the advantage of a higher surface area is lost. Taking this fact into consideration, it is reasonable to think that there might be a maximum in

efficiency for NTs between 1.6 μm and 6.6 μm, althgugh it has not been reached in this work.

- 3.7 μm meso-TiO$_2$ performed reasonably well, exhibiting a high photocurrent and photovoltage, although the fill factor was somewhat lower compared to anatase thin films (see Fill Factor for 1.3 and 6.6 μm TF). The nanotree sample, which has the same thickness, was expected to present a higher photocurrent due to an increase in the surface area and a lower photovoltage (higher recombination). However, it turned out that the photocurrent was appreciably lower than for regular meso-TiO$_2$. A probable explanation might be the extremely low covearge at the base of the NTs (most of the material accummulates at the body and tip owing to the high density of initial template NWs), as it can be observed in Figure 29 c). If the NTs are not properly linked to the anatase blocking layer, then a higher dye load will not translate into photocurrent.

Table 4. Photovoltaic parameters for TiO$_2$ (anatase)-based DSSCs as a function of the wall thicknesses. - Mean photovoltaic parameters values and estimated errors have been obtained from data of three devices with the same configuration, except for the devices marked with a * where statistics were performed with only two cells due to malfunction of the third one. Thin films of the same thickness as their NTs counterparts are used as references.

Cell	J_{sc} (mA/cm^2)	V_{oc} (mV)	FF (%)	η (%)
660 nm TF	1.52±0.05	670±7	62.7±1.9	0.64±0.05
1.6 μm TF*	2.86±0.30	698±58	64.9±1.4	1.31±0.27
6.6 μm TF	7.12±0.15	831±1	63.6±1.6	3.76±0.17
660 nm NT	2.48±0.30	833±9	71.4±0.8	1.47±0.10
1.6 μm NT*	5.39±0.53	819±2	66.6±2.4	2.93±0.18
6.6 μm NT	7.87±0.58	835±6	65.7±0.2	4.32±0.30
3.7 μm meso-TiO$_2$	6.63±0.60	830±22	60.9±3.4	3.34±0.18
3.7 μm meso-TiO$_2$ NTree*	3.90±0.05	811±35	61.5±1.6	1.95±0.15
800 nm ZnO TF	1.05±0.30	670±15	45±1	0.50±0.1

It must be stressed that the active area of the cells used in this work is 0.7 cm², in contrast with the typical areas of ca. 0.2 cm². The utilization of smaller areas assures a more reliable and more efficient solar cell performance due to inhomogeneities in the samples and lower series resistance [REF??]. In this work we have taken a higher active area that, under our consideration, is more representative of the fabricated solar cells, even if it is detrimental for the overall cell performance. In addittion, the mean thickness of the film always remains below 10 μm in contrast with other works which uses significantly higher thicknesses [Roh D. K., Adv. Funct. Mater. 2014][Liao Jin-Yun, Energy Environ. Sci. 2012][Tan B., J. Phys. Chem. B 2006].

By means of Electrochemical Impedance Spectroscopy (EIS) and modelling, some process parameters may be quantified as already seen for ZnO. Again, focus will be made on the trends, not on the absolute values. In addition, EIS and IMPS measurements were done only for the best cells of each series due to the fact that these are considerably time-consuming techniques and it is out of the scope of this work. The different parameters obtained by EIS are plotted in Figure 32.
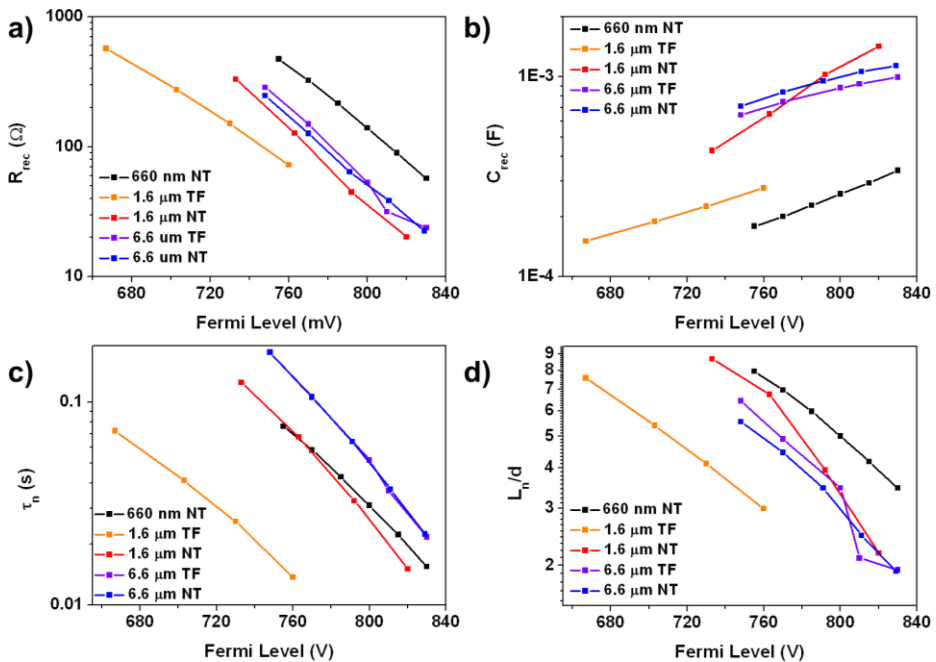

Figure 32. a-d) Impedance spectroscopy results of DSSCs fabricated with anatase nanotubes and thin films. Impedance parameters extracted from the fitting of the EIS spectra at various applied potentials: a) Recombination resistance, b) Capacitance, c)

93

Lifetime, d) electron diffusion length, estimated as the ratio of recombination and transport resistances.

In order to correctly compare the parameters extracted from EIS and IMPS, it is generally necessary to take into consideration the band shifts occasioned by the additives and solvent composing the electrolyte. In this case, the electrolyte is the same for all samples so in principle, there is no such shift between different cells. Nevertheless, still a correction must be applied so as to compare all cells at the same value of the total electron density stored in the semiconductor oxide. This is done by shifting the potential so that the capacitance lines overlap (in a vertical axis) and then this shift in potential is equally applied to the other parameters extracted from EIS and IMPS [Idígoras J., J. Phys. Chem. C 2014].

Figure 33 presents the corrected EIS parameters from Figure 32. It can be noticed that the recombination resistance (Fig. 33 a) was larger for the thinner anatase cells, whereas it got smaller when the thickness was increased as expected due to a higher specific area. The effect of the area on the recombination resistance is also evident for low thicknesses where a much thinner film of NTs (1.6 μm) exhibited more or less the same values as a thin film of 1.6 μm. Interestingly, for higher anatase thicknesses the resistance appears to be quite similar.

The capacitance (Fig. 33 b) showed an opposite behavior, being larger for thicker films and smaller for the thinner ones, again this is expected due to surface area effects. The exponential behavior resembles a chemical capacitance [Azaceta E., J. Mater. Chem. A 2013].

The electron lifetime (Fig. 33 c) was in line with the obtained potentials in the I-V curves, the higher the electron lifetime the higher the V_{OC} and vice versa. Finally, the normalized diffusion length (Fig 33 d) shows that all cells had a diffusion length larger than their mean thickness, which means that the photovoltaic performance is still not constrained by the thickness and could be increased even further.
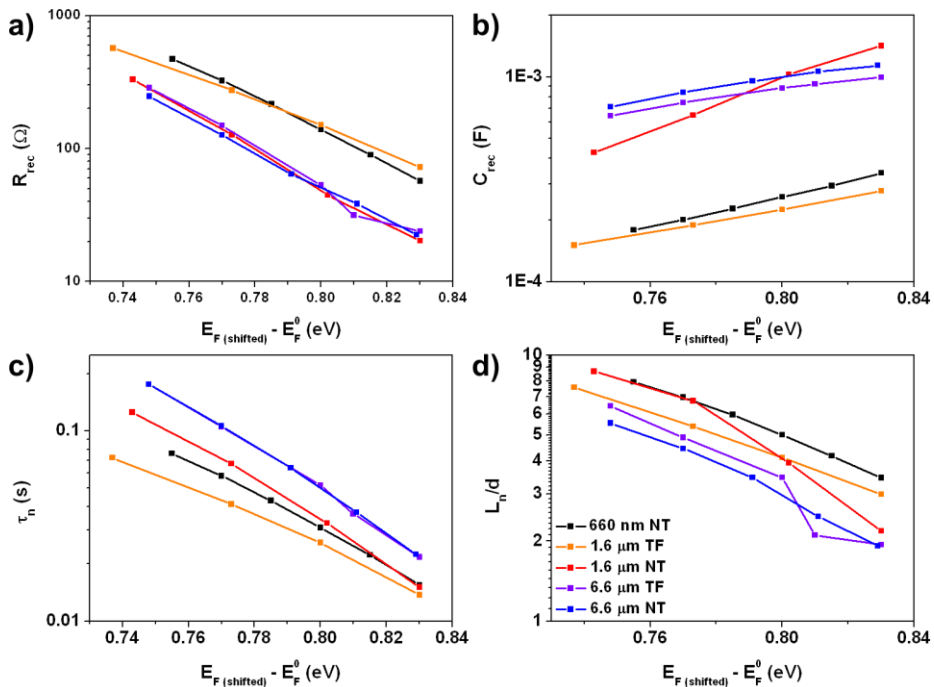
Figure 33. a-d) Corrected Impedance spectroscopy results of DSSCs fabricated with anatase nanotubes and thin films. Impedance parameters extracted from the fitting of the EIS spectra at various applied potentials: a) Recombination resistance, b) Capacitance, c) Lifetime, d) electron diffusion length, estimated as the ratio of recombination and transport resistances.

IMPS technique was also used to extract the time constant of the diffusion process (Fig. 34 a) and diffusion coefficient (Fig. 34 b). The time constants were larger for thicker thin films, even though for NTs of 660 nm and 1.6 μm they were quite similar, whereas the diffusion coefficients are quite similar, except for the 6.6 um TF sample which exhibits significantly higher values.
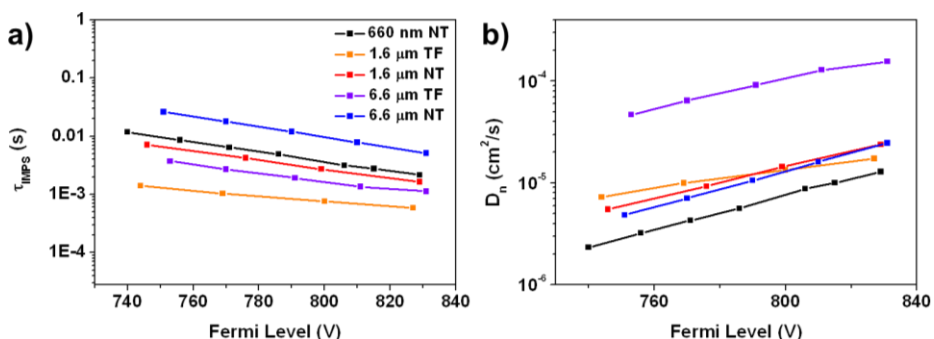
Figure 34. Corrected τ_{IMPS} (a) and diffusion coefficient (b) plotted versus the Fermi level for various antase thicknesses in both thin film and nanotubes.

In spite of the fact that the efficiencies reached in this work do not come close to the best reported ones for anatase 1D nanostructures, the results are certainly encouraging. Two possibilities are proposed to push even further the light harvesting capabilities of these cells:

> ➢ To deposit even thicker films of anatase in the form of thin films. There is still margin to improve the efficiency with this architecture, and it seems that by adding more material to NTs will only result in an even more percolated structure, thus diminishing its advantage with respect to thin film.

> ➢ To produce a stack of NTs. This is a much more tempting attempt to increase the surface area, dye load and cell efficiency. The idea behind this approach is quite simple, it just requires the production of NTs as usual with an anatase thickness between 1.6 and 6.6 μm, and repeat the entire growth process of NTs on top. This last step may be repeated until a maximum in efficiency is reached. In this way, percolation is avoided and surface area can still be maintained high.

> ➢ Longer NTs will not improve the solar cell performance due to preferential accumulation of TiO_2 on the tip, i. e. the base of the NTs could probably receive far less material than the body and tip, suffering from the same issues as meso-TiO_2 NTree.

2.4.4. Multi-shell Nanotubes-Based Dye Sensitized Solar Cells

Despite possessing remarkable electron mobility, the already mentioned poor chemical stability of ZnO certainly limits its use in DSSCs. In an attempt to hinder its degradation, 1-D multishell based DSSCs comprising ZnO NTs covered with a TiO_2 shell have been fabricated. In order to investigate the effect of the outer shell in the chemical stability of the ZnO, both meso-TiO_2 amorphous and anatase were produced. Moreover, three different shell thicknesses have been tested to examine the influence of thicker TiO_2 layers. The multi-shell samples are named as "inner shell"@"outer shell", for example ZnO@meso-TiO_2. Within this section, the analogue multi-layer (i.e a multilayer of ZnO and then TiO_2) have also been studied to compare the performance in thin film architecture (named TF1/TF2, for example ZnO/meso-TiO_2). For the sake of simplicity, ZnO wurtzite will be called just ZnO.

The thickness of the ZnO NT was maintained at 250 nm, while three different TiO_2 shells thicknesses were chosen: 5 nm, 20 nm and 50 nm. The general aspect of a ZnO NT@TiO_2 has already been presented in Figure 13 (d) for the case of anatase. The kind of TiO_2 (meso or anatase) or its thickness do no change the appearance of the nanostructure (for such low thicknesses involved), just a small increase in the NT walls is noticed (especially on the top).

Figure 35 shows the evolution of TiO_2 coverage. With a layer only 5 nm thin, the intensity of Ti in the EDX maps is extremely low, revealing deposit preferentially at the top. Owing to this poor coverage by TiO_2, most of the ZnO is expected to be exposed to its surround. In the case of 20 nm, there are only a few regions approaching deep blue in the color scale, meaning that almost no ZnO will be directly exposed. For 50 nm a continuous layer of TiO_2 is formed, hindering the direct contact between ZnO and its surroundings. Please note that both meso-TiO_2 and anatase are porous materials, so it is expected that the electrolyte and dye can diffuse to and into ZnO, but the negative effect of the solvent is diminished.
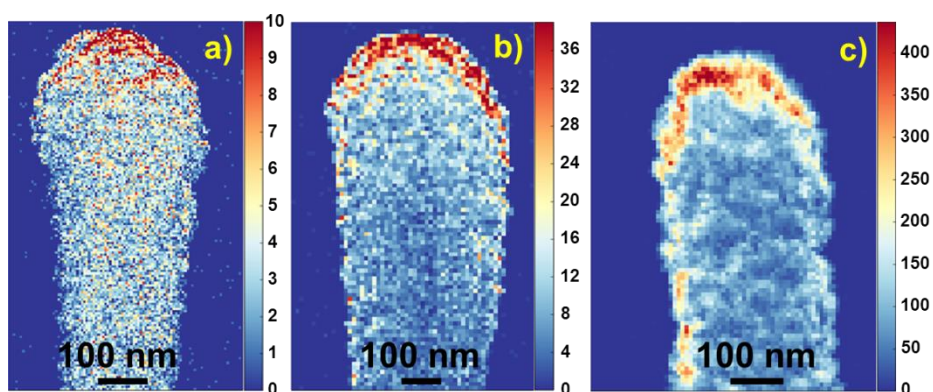

Figure 35. Intensity of Ti Kα at 4.51 keV in the resulting EDX maps obtained from the ZnO@meso-TiO_2 nanotube for a TiO_2 thickness of a) 5 nm, b) 20 nm and c) 50 nm.

In order to investigate the influence of the multi-shell in the adsorption capacity, several adsorption-desorption experiments were conducted in the corresponding single layers on ZnO, meso-TiO_2 and anatase. The experiments consisted in the immersion of the thin film samples in N719 followed by desorption of the dye in KOH 1M in MeOH and collection of the UV-Vis spectra of the resulting dye solutions. Figure 36 shows the UV-Vis spectra in the region of one of the absorption bands of N719 for ZnO, meso-TiO_2 and anatase. Note that the absorbance has been normalized by the corresponding thin film thickness.
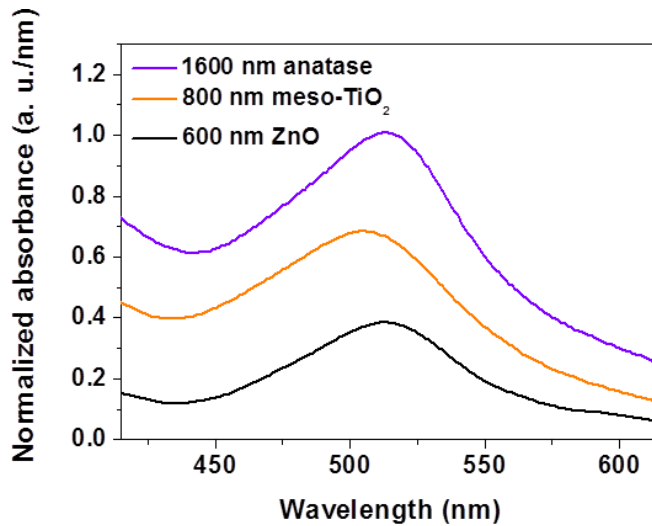
Figure 36. UV-Vis spectra of N719 in KOH 1M in MeOH after desorption from ZnO, meso-TiO$_2$ and anatase thin films.

It is clear that the dye intake ability of ZnO is limited, perhaps due to the low permissible immersion time for this material. Meso-TiO$_2$ performs much better, but it is greatly surpassed by anatase. Please note that even though anatase and meso-TiO$_2$ films are thicker, these conclusions will still be valid thinner films since the absorption has been normalized to the thickness of each sample.

The addition of a TiO$_2$ shell to 250 nm ZnO enhances significantly the dye loading capability of the films. Moreover, the effect was found to be more pronounced in anatase (Fig. 37a) than in amorphous meso-TiO$_2$ (Fig. 37b).
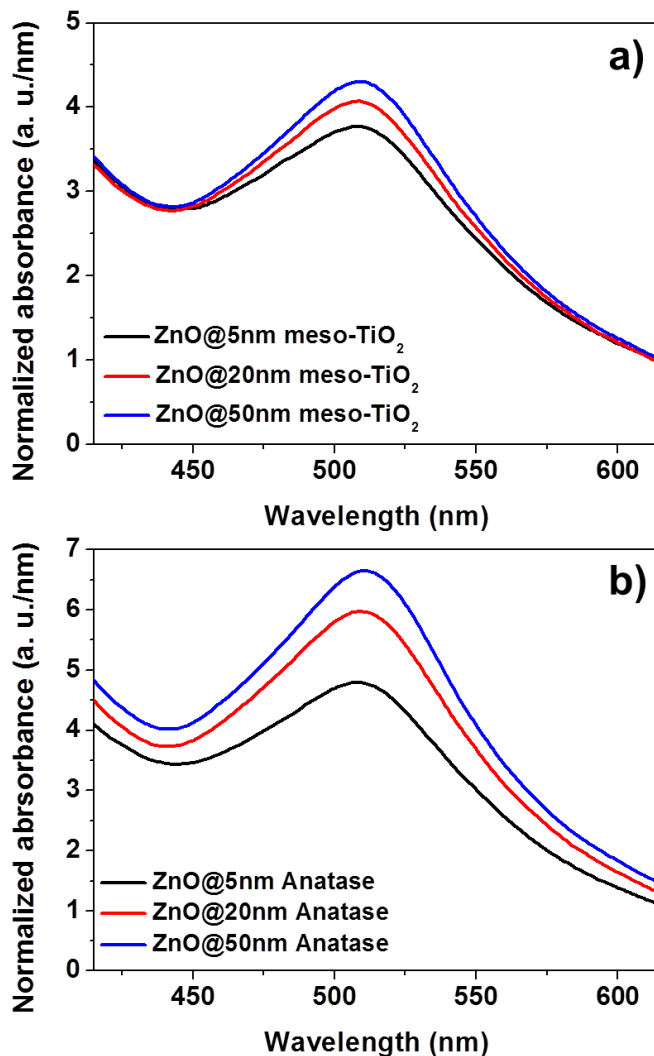
Figure 37. UV-Vis spectra of N719 in KOH 1M in MeOH after desorption from (a) ZnO/meso-TiO$_2$ and (b) ZnO/anatase.

Table 5 gathers the obtained concentrations for ZnO, meso-TiO$_2$, anatase and the different multilayers (please, refer to the methodology section for the concentration determination procedure).

Note that the normalized surface concentration is just the surface concentration divided by the thickness of the film. It is remarkable that the combination of ZnO and TiO$_2$ boosts the dye load in the films. Looking at the obtained concentrations in the table, three observations can be made. First, all ZnO/TiO$_2$ films are able to adsorb more dye than even anatase. Secondly, anatase seems to work better than meso-TiO$_2$

in the ZnO/TiO$_2$ system. Lastly, an increase in the thickness of the TiO$_2$ films (amorphous or anatase) gives rise to an increment in dye surface concentration, which may be due to microstructural transitions of TiO$_2$.

Table 5. N719 dye concentration for the studied samples obtained from adsorption-desorption experiments

Sample	Absorbance at 515nm	Surface concentration ($x10^{-10}$ moles/cm^2)	Normalized surface concentration ($x10^{-12}$ moles/nm.cm^2)
600nm ZnO	0.0220	20.7 ± 0.5	3.45 ± 0.08
800nm TiO$_2$	0.0547	51.5 ± 1.3	6.44 ± 0.16
1600nm anatase	0.1605	1510.8 ± 3.7	9.44 ± 0.23
ZnO 250nm/5nm meso-TiO$_2$	0.0773	727.6 ± 1.8	28.53 ± 0.69
ZnO 250nm/20nm meso-TiO$_2$	0.0896	843.4 ± 2.1	31.24 ± 0.76
ZnO 250nm/50nm meso-TiO$_2$	0.1075	1011.9 ± 2.5	33.73 ± 0.82
ZnO 250nm/5nm anatase	0.0983	925.3 ± 2.3	36.29 ± 8.83
ZnO 250nm/20nm anatase	0.1314	1236.9 ± 3.0	45.81 ± 1.11
ZnO 250nm/50nm anatase	0.1662	1564.5 ± 3.8	52.15 ± 1.27

Due to severe limitations in the desorption of N719 from NTs (the films did not release all the dye), integrating sphere measurements were successfully performed in ZnO samples covered with 50 nm of anatase to compare qualitatively the dye load in thin film and nanotubes. It is clear from Figure 38, that NTs can increase substantially the dye loading by offering a much higher surface area as already observed for pure anatase systems. Moreover, this difference in dye concentration is readily noticeable at the naked eye as in Figure 38 b): the thin film samples possess a barely appreciable color whereas in NTs the dyed film was pretty apparent.
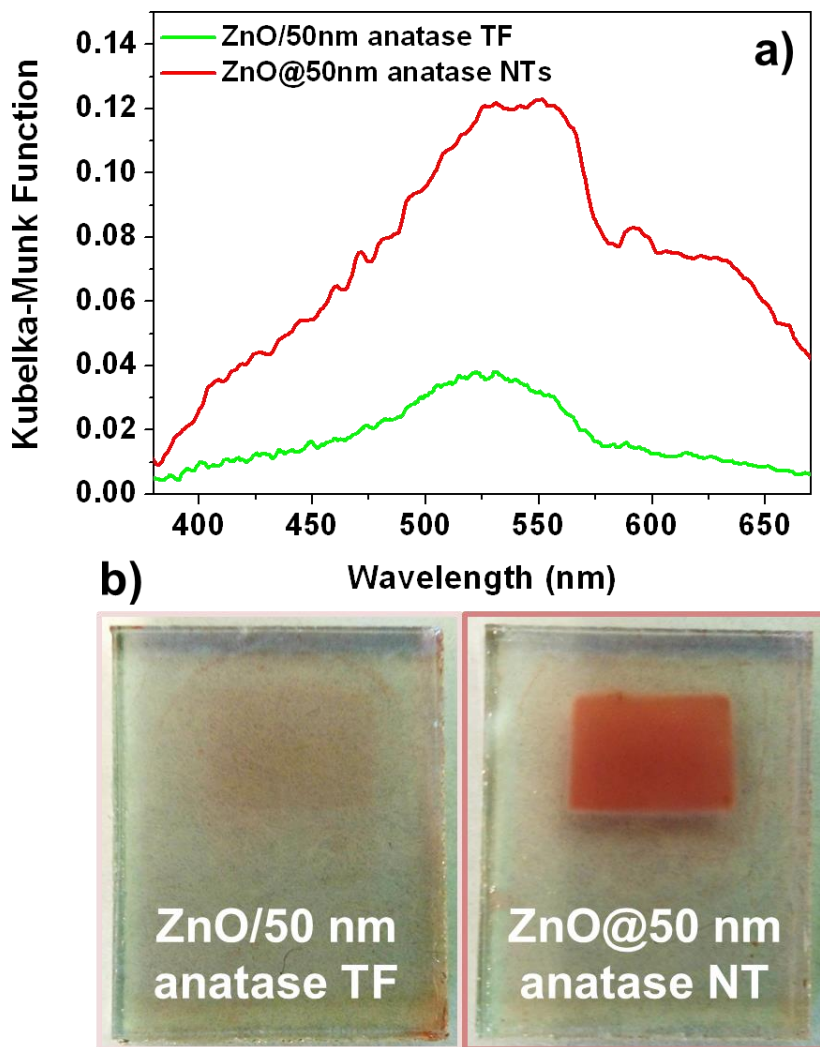
Figure 38. a) Comparison of the Kubelka-Munk function for a multi-shell NT (ZnO@50 nm anatase) cell and its multi-layer analogue. b) electrodes for DSSCs comprising ZnO/TiO$_2$ TF (left) and ZnO@TiO$_2$ NT (right) as active materials

Table 6 collects the most relevant photovoltaic parameters for the prepared multi-shell and multilayer cells. At first glance, the incorporation of a TiO$_2$ shell is detrimental for the cell performance. Photocurrents are remarkable lower, in spite of the fact that multi-shells show a more promising dye adsorption capacity (table 5). Moreover, fill factors generally exhibit a poorer behavior as well, only the highest thickness of meso-TiO$_2$ shows a fill factor close to uncovered ZnO NTs. In contrast, the photovoltage is superior to that of pure ZnO NTs, especially for the thickest anatase shell.

Table 6. Photovoltaic parameters for ZnO@TiO2 NT-based DSSCs as a function of the TiO2 (meso or anatase) wall thicknesses. - Mean photovoltaic parameters values and estimated errors have been obtained from data of three devices with the same configuration. ZnO NT without TiO_2 has been included for comparison.

Cell	J_{sc}(mA/cm^2)	V_{oc}(mV)	FF(%)	η(%)
250 nm ZnO NT	1.48±0.25	460±20	50±1.0	0.30±0.05
ZnO 250nm@meso-TiO$_2$ 5nm NT	0.81±0.05	540±5	43.8±0.5	0.20±0.05
ZnO 250nm@meso-TiO$_2$ 20nm NT	0.79±0.05	542±5	47.3±1.0	0.20±0.05
ZnO 250nm@meso-TiO$_2$ 50nm NT	0.77±0.05	529±7	49±1.0	0.20±0.05
ZnO 250nm/meso-TiO$_2$ 50nm TF	043±0.05	573±13	39.9±8.0	0.10±0.05
ZnO 250nm@anatase 5nm NT	0.87±0.14	579±13	38.3±0.5	0.20±0.05
ZnO 250nm@anatase 20nm NT	0.99±0.13	588±8	43.4±5.3	0.20±0.05
ZnO 250nm@anatase 50nm NT	0.96±0.17	635±15	32.3±0.5	0.20±0.05
ZnO 250nm/anatase 50nm TF	0.64±0.16	615±1	37.9±2.0	0.15±0.05

Apparently, the electronic transfer between TiO_2 and ZnO is hindered due to a small energy barrier [Manthina V., J. Phys. Chem. C 2012], despite their conduction bands and thus their respective Fermi levels are generally considered to be aligned, just as in Figure 39.
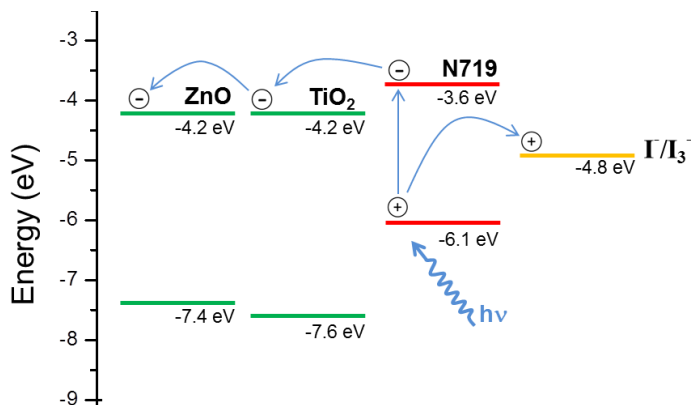
Figure 39. Energy levels diagram for a ZnO/TiO$_2$ system [Cao G., World Scientific Publising 2010][Liu J., Nanotechnology 2010].

Owing to this lack of electronic transfer between TiO$_2$ and ZnO, the photovoltaic response seems to be proceeding primarily from the ZnO cores at least for the thinnest TiO$_2$ shells, where the clusters of TiO$_2$ are not percolated yet and cannot contact the substrate directly. Once full percolation of the TiO$_2$ shell is achieved and the ZnO core is completely covered, the response should switch to that of TiO$_2$ (again, due to negligible electronic transfer between ZnO and TiO$_2$). The photovoltaic response of the cells was different depending on the crystallinity of TiO$_2$:

- Meso-TiO$_2$ shells improved the fill factor, but the photocurrent got worse when the thickness was increased probably due to severe electron trapping [Soga T., Elsevier 2006]. The potential remained more or less constant, with a slight decrease for the thickest meso-TiO$_2$ shell.
- Anatase shells did improve the photovoltage, but contrary to meso-TiO$_2$, an intermediate stage seems to be present. For 20 nm, the fill factor and photocurrent have reached a maximum, which could suggest contribution from both ZnO and antase. On the other hand, a 50 nm anatase shell produced and obvious drop of the fill factor while the photocurrent remained the same. This could indicate a still poor percolation of the final anatase shell.

Thin Films with 50 nm of meso-TiO$_2$ and anatase have been measured as references. Compared to their 1D counterparts, these cells offered higher photovoltages probably due to a lower recombination rate and lower photocurrents as a consequence of a lower surface area.

As mentioned above, in the studied 1D multishell system, the addition of a TiO_2 shell to ZnO nanotubes demonstrated to be detrimental for the performance of the cells. No further electrochemical studies were carried out due to the poor results obtained.

2.5. Conclusions

A reliable full vacuum methodology for the fabrication of semiconducting nanotubes made of ZnO and TiO_2 with single and multishell configurations has been presented. The versatility of the plasma techniques such as PECVD and dc-sputtering for the growth of metal nanoparticles and metal oxide layers has been exploited here for the formation of nanostructured nanotubes with tailored shells in terms of microstructure, porosity, structure and thickness on an ample variety of substrates ranging from FTO supports to metal nanoparticles.

The procedure provides hollow's cross sections in the form of square or rectangle keeping memory of the flat surface of the organic single crystal used as templates. The performance of the ZnO and anatase nanotubes as photoanodes in DSSC has been analyzed as a function of the shell thickness, finding an increase of efficiency with this parameter. In the case of multi-shell nanotubes, mixed results were obtained for amorphous and crystalline TiO_2, however, it has been found that the addition of a thin TiO_2 shell turned out to be detrimental for the performance of the cells.

2.6. References

Anta J. A. et al., ZnO-Based Dye-Sensitized Solar Cells. Journal of Physical Chemistry C 116(21), 11413-11425 (2012).

Aricò A. S. et al., Nanostructured materials for advanced energy conversion and storage devices. Nature Materials 4, 366-377 (2005).

Armaroli N., Balzani V., Energy for a sustainable world. ISBN: 978-3-527-32540-5. WILEY-VCH Verlag & Co. Weinheim, Germany (2011).

Azaceta E. et al., ZnO–ionic liquid hybrid films: electrochemical synthesis and application in dye-sensitized solar cells. Journal of Materials Chemistry A 1(35), 10173—10183 (2013).

Barth S. et al., Synthesis and applications of one-dimensional semiconductors. Progress in Materials Science 55(6), 563-627 (2010).

Berger L. I., Semiconductor materials. ISBN: 0-8493-8912-7. CRC Press, Inc. Boca Raton, USA (1997).

Bi D. et al., Device Performance Correlated with Structural Properties of Vertically Aligned Nanorod Arrays in Polymer/ZnO Solar Cells. Journal of Physical Chemistry C 114(32), 13846-13852 (2010).

Bisquert J., Chemical capacitance of nanostructured semiconductors: its origin and significance for nanocomposite solar cells. Physical Chemistry Chemical Physics 5(24), 5360-5364 (2003).

Borrás A. et al., Type of Plasmas and Microstructures of TiO_2 Thin Films Prepared by Plasma Enhanced Chemical Vapor Deposition. Journal of The Electrochemical Society 154(12), P152-P157 (2007).

Borras A. et al., Growth of Crystalline TiO_2 by Plasma Enhanced Chemical Vapor Deposition. Crystal Growth & Design 9(6), 2868-2876 (2009).

Borrás A. et al., Porosity and microstructure of plasma deposited TiO_2 thin films. Microporous and Mesoporous Materials 118(1-3), 314-324 (2009).

Borras A. et al., One-Step Dry Method for the Synthesis of Supported Single-Crystalline Organic Nanowires Formed by π-Conjugated Molecules. Langmuir 26(8), 5763–5771 (2010).

Briseno A. L. et al., Introducing organic nanowire transistors. Materials Today 11(4), 38-47 (2008).

Cahen D., Hodes G. et al., Nature of Photovoltaic Action in Dye-Sensitized Solar Cells. Journal of Physical Chemistry B 104(9), 2053-2059 (2000).

Cao G., Zhang Q., Brinker C. J., Annual Review of Nano Research, Vol. 3. ISBN: 978-981-4280-51-8. World Scientific Publishing Co. Pte. Ltd., Singapore (2010).

Chen D. et al., Mesoporous Anatase TiO_2 beads with High Surface Areas and Controllable Pore Sizes: A Superior Candidate for High-Performance Dye-Sensitized Solar Cells. Advanced Materials 21(21), 2206-2210 (2009).

Cheng F. et al., Template-Directed Materials for Rechargeable Lithium-Ion Batteries. Chemistry of Materials 20(3), 667-681 (2008).

Cheol S. et al., Effects of light scattering TiO_2 surface- modified by dual oxide coating in dye-sensitized solar cells. Advanced Powder Technology 23(6), 866-871 (2012).

Cho S. et al., Ethanol sensors based on ZnO nanotubes with controllable wall thickness via atomic layer deposition, an O_2 plasma process and an annealing process. Sensors and Actuators B: Chemical 162(1), 300-306 (2012).

Chuang C. M. et al., Improved performance and stability in quantum dot solar cells through band alignment engineering. Nature Materials 13, 796-801 (2014).

Conibeer G., Third-generation photovoltaics. Materials Today 10(11), 42-50 (2007).

Elias J. et al., Conversion of ZnO Nanowires into Nanotubes with Tailored Dimensions. Chemistry of Materials 20(21), 6633-6637 (2008).

Espinosa N. et al., Solar cells with one-day energy payback for the factories of the future. Energy & Environmental Science 5, 5117-5132 (2012).

Fabregat-Santiago F. et al., Influence of electrolyte in transport and recombination in dye-sensitized solar cells studied by impedance spectroscopy. Solar Energy Materials and Solar Cells 8(1-4), 117-131 (2005).

Fan J. et al., Perovskite-based low-cost and high-efficiency hybrid halide solar cells

Forro L. et al., High mobility n-type charge carriers in large single crystals of anatase (TiO_2). Journal of Applied Physics 75(1), 633-635 (1994).

Fritts C. E., On a New Form of Selenium Photocell. American Journal of Science 26, 465 (1883).

Grätzel M., Photoelectrochemical cells. Nature 414, 338-344 (2001).

Grätzel M., Solar Energy Conversion by Dye-Sensitized Photovoltaic Cells. Inorganic Chemistry 44(20), 6841-6851.

Guillén E. et al., Electron Transport and Recombination in ZnO-based Dye Sensitized Solar Cells. Journal of Physical Chemistry C 115(45), 22622-22632 (2011)

Hardin B. E. et al., The renaissance of dye-sensitized solar cells. Nature Photonics 6, 162-169 (2012).

Heo J. H., Efficient inorganic–organic hybrid heterojunction solar cells containing perovskite compound and polymeric hole conductors. Nature Photonics 7, 486–491 (2013).

Huang S. Y. et al., Rocking Chair Lithium Battery Based on Nanocrystalline TiO_2 (Anatase). Journal of The Electrochemical Society 142(9), L142-L144 (1995).

Hulteen J. C. and Martin C. R., A general template-based method for the preparation of nanomaterials. Journal of Materials Chemistry 7(7), 1075-1087 (1997).

Huusko J. et al., TiO_2 thick-film gas sensors and their suitability for NO_x monitoring. Sensors and Actuators B: Chemical 16(1-3), 245-248 (1993).

Idígoras J. et al., The Redox Pair Chemical Environment Influence on the Recombination Loss in Dye-Sensitized Solar Cells. Journal of Physical Chemistry C, 118(8), 3878-3889 (2014).

Idígoras J. et al., The Impact of the Electrical Nature of the Metal Oxide on the Performance in Dye-Sensitized Solar Cells: New Look at Old Paradigms. Journal of Physical Chemistry C 119(8), 3931-3944 (2015)

Janotti A., Van de Walle C. G., Fundamentals of zinc oxide as a semiconductor. Reports on Progress in Physics 72(12), 126501 (2009).

Kolmakov A. and Moskovits M., CHEMICAL SENSING AND CATALYSIS BY ONE-DIMENSIONAL METAL-OXIDE NANOSTRUCTURES. Annual Review of Materials Research 34, 151-180 (2004).

Kosyachenko L. A. (Ed.). Comparative Study of Dye-Sensitized Solar Cell Based on ZnO and TiO_2 Nanostructures. Solar Cells - Dye-Sensitized Devices. ISBN: 978-953-307-735-2. Intech (2011).

Law M. et al., Nanowire dye-sensitized solar cells. Nature Materials 4, 455-459 (2005).

Li G. et al, Polymer solar cells. Nature Photonics 6, 153-161 (2012).

Li L. et al., Electrospun porous SnO_2 nanotubes as high capacity anode materials for lithium ion batteries. Electrochemistry Communications 12(10), 1383-1386 (2010).

Liao Jin-Yun et al., Oriented hierarchical single crystalline anatase TiO_2 nanowire arrays on Ti-foil substrate for efficient flexible dye-sensitized solar cells. Energy & Environmental Science 5(2), 5750-5757 (2012).

Liu J. et al., Enhanced photoconduction of free-standing ZnO nanowire films by L-lysine treatment. Nanotechnology 21(48), 485504-1–485504-7.

Look D.C. et al., ELECTRICAL PROPERTIES OF BULK ZnO. Solid State Communications 105(6), 399-401 (1998).

Macias-Montero M. et al., Vertically Aligned Hybrid Core/Shell Semiconductor Nanowires for Photonics Applications. Advanced Functional Materials 23(48), 5981–5989 (2013).

Macías-Montero M., Ph.D. thesis: New Plasma-based synthesis procedures and applications of 1D nanostructures. Universidad de Sevilla, España (2013).

Marichy C. et al., Atomic Layer Deposition of Nanostructured Materials for Energy and Environmental Applications. Advanced Materials 24(8), 1017-1032 (2012).

Mancic L. T. et al., Precursor Particle Size as the Key Parameter for Isothermal Tuning of Morphology from Nanofibers to Nanotubes in the $Na_{2-x}H_xTinO_{2n+1}$ System through Hydrothermal Alkali Treatment of Rutile Mineral Sand. Crystal Growth & Design 9(5), 2152–2158 (2009).

Manthina V. et al., ZnO−TiO_2 Nanocomposite Films for High Light Harvesting Efficiency and Fast Electron Transport in Dye-Sensitized Solar Cells. The Journal of Physical Chemistry C 116(45), 23864-23870 (2012).

Martinson A. B. F. et al., ZnO Nanotube Based Dye-Sensitized Solar Cells. Nano Letters 7(8), 2183-2187 (2007).

Mathew S., Yella A. et al., Dye-sensitized solar cells with 13% efficiency achieved through the molecular engineering of porphyrin sensitizers. Nature Chemistry 6, 242-247 (2014).

Mbenkum Beri M., Selective Growth of Organic 1-D Structures on Au Nanoparticle Arrays. Nanoletters 6(12), 2852-2855 (2006).

Memarian N. et al., Hierarchically Assembled ZnO Nanocrystallites for High-Efficiency Dye-Sensitized Solar Cells. Angewandte Chemie International Edition 50(51), 12321-12325 (2011).

Miles R. W. et al., Inorganic photovoltaic cells. Materials Today 10(11), 20-27 (2007).

Mishra A., Bäuerle P., Small Molecule Organic Semiconductors on the Move: Promises for Future Solar Energy Technology. Angewandte Chemie 51(9), 2020-2067 (2012).

Moorthy S. B. K., Thin Film Structures in Energy Applications. ISBN: 978-3-319-14773-4. Springer International Publishing Switzerland (2015).

Nakata K. and Fujishima A., Journal of Photochemistry and Photobiology C: Photochemistry Reviews 13(3), 169-189 (2012).

NREL, National Center for Photovoltaics, http://www.nrel.gov/ncpv/.

O'Reagan B., Grätzel M., A low-cost, high-efficiency solar cell based on dye-sensitized colloidal TiO_2 films. Nature 353(6346), 737-740 (1991).

Oulad-Zian Y. et al., Ultraviolet Pretreatment of Titanium Dioxide and Tin-Doped Indium Oxide Surfaces as a Promoter of the Adsorption of Organic Molecules in Dry Deposition Processes: Light Patterning of Organic Nanowires. Langmuir 31(30), 8294-8302 (2015).

Palz W., Solar Power for the World: What You Wanted to Know about Photovoltaics. ISBN: 978-981-4411-88-2. CRC Press, Boca Raton, USA (2014).

Pan Z. et al., Nanobelts of semiconducting oxides. Science 291(5510), 1947-1949 (2001).

Patzke G. R., Oxidic Nanotubes and Nanorods—Anisotropic Modules for a Future Nanotechnology. Angewandte Chemie International Edition 41(14), 2446-2461 (2002).

Raga S. R. et al., Analysis of the Origin of Open Circuit Voltage in Dye Solar Cells. Journal of Physical Chemistry Letters 3(12), 1629-1634.

Ramos F. J. et al., Perovskite Solar Cells Based on Nanocolumnar Plasma-Deposited ZnO Thin Films. ChemPhysChem 15(6), 1148-1153 (2014).

Rao C. N. R. and Nath M., Inorganic nanotubes. Dalton Transactions (1), 1-24 (2003).

REN21, Renewable Energy Policy Network for the 21st Century, http://www.ren21.net/status-of-renewables/global-status-report/.

Roh D. K. et al., High Efficiency Solid-State Dye-Sensitized Solar Cells Assembled with Hierarchical Anatase Pine Tree-like TiO_2 Nanotubes. Advanced Functional Materials 24(3), 379-386 (2014).

Romero-Gómez P. et al., Tunable Nanostructure and Photoluminescence of Columnar ZnO Films Grown by Plasma Deposition. Journal of Physical Chemistry C 114(49), 20932-20940 (2010).

Roy P. et al., TiO_2 Nanotubes: Synthesis and Applications. Angewandte Chemie International Edition 50(13), 2904-2939 (2011).

Satake K. et al., Titania NO_x sensors for exhaust monitoring. Sensors and actuators B: Chemical 20(2-3), 111-117 (1994).

Soga T., Nanostructured Materials for Solar Energy Conversion. ISBN: 978-0-444-52844-5. Elsevier. Oxford, UK (2006).

Su Y. et al., Organic Photovoltaics. Materials Today 15(12), 554-552 (2012).

Tan B., Wu Y., Dye-Sensitized Solar Cells Based on Anatase TiO2 Nanoparticle/Nanowire Composites. Journal of Physical Chemistry B 110(32), 15932-1938 (2006).

Tiwana P. et al., Electron mobility and injection dynamics in mesoporous ZnO, SnO_2 and TiO_2 films used in dye-sensitized solar cells. ACS Nano 5(6), 5158-5166 (2011).

Upadhyaya H. M., Recent progress and the status of dye-sensitised solar cell (DSSC) technology with state-of-the-art conversion efficiencies. Energy Materials & Solar Cells 119, 291-295 (2013).

Vega-Poot A. G. et al., Mechanisms of Electron Transport and Recombination in ZnO Nanostructures for Dye-Sensitized Solar Cells. ChemPhysChem 15(6), 1088-1097 (2014).

Wang W., Device Characteristics of CZTSSe Thin-Film Solar Cells with 12.6% Efficiency. Advanced Energy Materials 4(7), 1301465 (2014).

Wang Z. L., Zinc oxide nanostructures: growth, properties and applications. Journal of Physics: Condensed Matter 16(25), R829 (2004).

Wright M., Uddin A., Organic—inorganic hybrid solar cells: A comparative review. Solar Energy Materials and Solar Cells 107, 87-111 (2012).

Wu Wu-Qiang et al., Ultra-long anatase TiO_2 nanowire arrays with multi-layered configuration on FTO glass for high-efficiency dye-sensitized solar cells. Energy & Environmental Science 7(2), 644-649 (2014).

Xia Y. et al., One-dimensional nanostructures: synthesis, characterization, and applications. Advanced Materials 15(5), 353-389 (2003).

Xu F., Su L., Solution-derived ZnO nanostructures for photoanodes of dye-sensitized solar cells. Energy & Environmental Science 4(3), 81-841 (2011).

Yan X. et al., Controllable synthesis of anatase TiO_2 crystals for high-performance dye-sensitized solar cells. Journal of Materials Chemistry A 1(17), 5347-5352 (2013).

Yella A. et al., Porphyrin-Sensitized Solar Cells with Cobalt (II/III)-Based Redox Electrolyte Exceed 12 Percent Efficiency. Science 334(605), 629-634 (2011).

Yu J. et al., Anatase TiO_2 nanosheets with exposed (001) facets: improved photoelectric conversion efficiency in dye-sensitized solar cells. Nanoscale 2(10), 2144-2149 (2010).

Zhou H. et al., Low-Temperature Processed and Carbon-Based $ZnO/CH_3NH_3PbI_3/C$ Planar Heterojunction Perovskite Solar Cells. Journal of Physical Chemistry C 119(9), 4600-4605 (2015).

Zhu K. et al., Removing Structural Disorder from Oriented TiO_2 Nanotube Arrays: Reducing the Dimensionality of Transport and Recombination in Dye-Sensitized Solar Cells. Nano Letters 7(12), 3739–3746 (2007).

3. 1D and 2D transparent platinum nanoelectrodes by plasma processing of platinum porphyrin nanocolumns and thin films
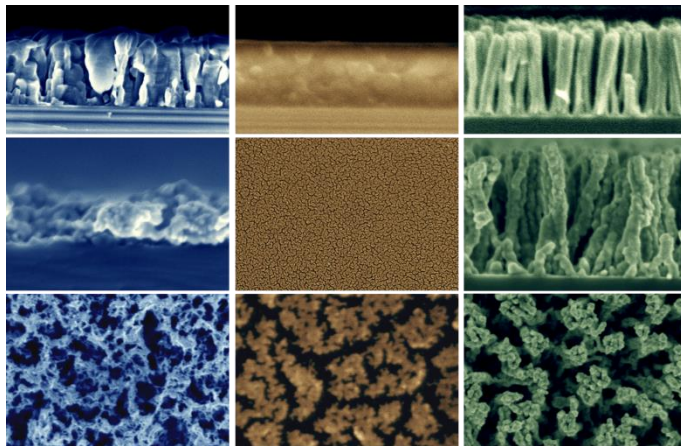
Abstract

The fabrication of platinum nanoelectrodes in the form of higly porous layers (2D) and nanocolumns (1D) by dry processing of platinum octaethylporphyrin (PtOEP) nanomaterials is presented. Transparency as high as 70% with about 750 Ω.cm ohms are achieved by controlling the deposition of the PtOEP precursor materials by organic physical vapor deposition and remote plasma assisted plasma deposition and posterior oxydation-reduction plasma treatments. The catalytic properties of the nanoelectrodes are further demonstrated by their implementation as counter electrode in a solar cell. The expansion of the protocol to the fabrication of porous materials of different compositions by tuning the metal porphyrin or phthalocyanine used as precursor is as well explored. Finally, it is included the application of organic nanowires as supported template of the developed material giving rise to a new family of hierarchical heterostructured core@shell nanowires.

3.1. Introduction

Development of new fabrication methods for transparent and semitransparent conductive nanoelectrodes compatible with different processable substrates and high mass production is extremely important in fields like nanoelectronics/photonics and solar energy harvesting.[Hu-MRSBulletin.2011, Angmo-JAP.2013] The urgency to replace the highly and rising cost indium in the current ITO technology has motivated an intensive research to fabricate high density nanoelectrodes with high transparency along to a high active area. Looking to these requirements, the use of tailored porous conductive nanostructures appears as a promising route because of their inherent high surface area [Hu-MRSBulletin.2011; Chen-ACS2013; Langley-Nanotechnol2013; Hu-PNAS2009]. Most of the recent results on the literature reports in the use of silver nanomesh and nanowires or metal decorated carbon nanotubes networks.[Langley-Nanotechnol.2013; Hu-MRSBulletin.2011, Angmo-JAP.2013] However, the use of platinum nanostructures present an added value related with the simultaneous function as transparent counter electrode and catalyst layer in dye sensitized solar cells.[Kim-ACS.2013; Jang-ChemMater.2013] In this chapter we will approach to this issue from the point of view of the fabrication of supported transparent and porous Pt in form of thin layers and nanocolumns, i.e., Pt nanoelectrodes in 2D and 1D architectures respectively. The method consists in a combination of vacuum and plasma procedures applied to the deposition and posterior decomposition of platinum octaethylporphyrin (PtOEP) acting as precursor for the formation of highly porous platinum nanoelectrodes. Two different methodologies have been utilized in the deposition of the precursor materials, namely physical vapour deposition of small molecules (PVD)[Borras-Langmuir.2009] and remote plasma assisted vapour deposition (RPAVD)[Aparicio-JMC.2014] both of them scalable up to wafer level and carried out at room temperature. In addition, these methods have been proved to be compatible with an ample range of processable substrates including polymers, Si, ITO, metal electrodes and photonic architectures.[Macias-Montero-AFM-2013; Aparicio-AM2011] The post-processing of the PtOEP precursor layers to form the metal nanostructures is achieved by soft plasma etching (SPE)[see also Chapter 4; Alcaire-Nanoscale.2011; Alcaire-PPP2015] under different combinations of oxygen, argon and hydrogen gases in the plasma and for temperatures ranging from RT to 280 ºC.

PVD is a well stablished methodology for the fabrication of two dimensional organic and metal-organic layers also extended in the last years to the formation of supported

small-molecule organic nanowires.[Borras-Langmuir2010; Briseno-MT2008] The main parameters controlling the formation of organic thin films and nanowires from evaporable molecules are the substrate surface composition and microstructure, temperature of the substrate in relation with the sublimation temperature of the molecules, pressure, growth rate and thickness.[Borras-Langmuir2010; ChemMater2008] In previous chapters, PVD has been applied to the fabrication of single crystalline organic nanowires, herein, we have utilized this method for the formation at room temperature of polycrystalline PtOEP thin films.

On the other hand, we have also explored the growth of PtOEP layers by remote plasma assisted vacuum deposition (RPAVD). This methodology has been developed in recent years for the formation of nanocomposite organic films showing an advanced performance in applications as UV and gases sensors. In those previous references the precursor materials utilized comprises photonic functional organic molecules as rhodamines, flavonols and perylenes. In this chapter we include the first results on the fabrication by RPAVD of metal-organic small molecules. In a brief description, the protocol consists in the evaporation of the organic molecules in the afterglow region of a microwave plasma with the substrates facing the evaporation source and back to a microwave plasma discharge, i.e. in a downstream configuration (see details in Methods and Chapter 1). This procedure provides the formation of nanocomposite thin films where the functional molecules appear embedded in a polymeric matrix consisting on the molecular fragments formed by interaction with the plasma species. In this chapter we have extended this protocol, usually working under pure Ar plasmas, to the application of oxygen rich plasma gases in order to further control the microstructure and composition of the nanocomposite thin films.

Microstructure, structure, composition and optical and electrical properties of the samples deposited and treated under different conditions have been thoroughly analysed.

In situ XPS experiments have been included in order to study the mineralization of the PtOEP precursor films and oxidation state of the platinum outcome layers.

As a proof of concept, the metallic Pt layers and nanocolumns have been tested as counter electrode in the fabrication of dye synthetized solar cells.

3.2. Objectives

The specific objectives of this chapter appear detailed in the following list:

❖ Fabrication and characterization of nanocomposite PtOEP thin films by remote plasma assisted vacuum deposition under Ar (RPAVD-Ar) and Ar/O_2 (RPAVD-O_2) plasmas.

❖ Analysis of the soft plasma etching conditions required for the formation of Pt layers and columns.

➢ Realization of XPS in situ experiments under different SPE conditions following the conversion from PtOEP to Pt layers.

❖ Formation of Pt electrodes with desirable high transparency and conductivity.

➢ UV-Vis and UV-VIS-NIR characterization of thin films and nanocolumns.

➢ Electrical characterization of thin films and nanocolumns.

❖ Implementation of the Pt layers and nanocolumns as counter electrode in a DSC and comparison with commercial available Platisol standard electrodes.

3.3. Methodology

3.3.1. Fabrication of the nanostructured platinum films

PtOEP was purchased in Frontier Scientific and used as received. The compound was deposited by PVD and RPAVD on several substrates as n-doped Si (100), fused silica, ITO and FTO thin films on glass (CASA). The substrates were place in a vacuum chamber, previously pumped until reaching a base pressure of 2 x 10^{-5} mbar. PVD was carried out at 2 x 10^{-2} mbar of Ar, nominal growth rate settled in the QCM at 0.35 Å/s and substrates at room temperature. Similar conditions were applied for the RPAVD-Ar, operating the plasma ECR-MW discharge at 300 W, and keeping fixed the plasma-to-substrate distance at 10 cm. RPAVD-O_2 experiments with a gas mixture of 80 % O_2 / 20 % Ar were carried out at 600 W and growth rate 0.6 Å/s in the same conditions of pressure, temperature and sample-plasma distance. The post-treatment of the samples by soft plasma etching was produced in the same reactor with the samples facing down the plasma glow discharge. Treatment duration, substrate temperature and plasma composition were varied in order to obtain the full mineralization of the PtOEP and reduction of the platinum films. SPE (O_2+Ar) label

corresponds to etching under 0.02 mbar (20% Ar / 80 % O_2) at 400 W and SPE (O_2+H_2) to treatments at 0.02 mbar (50 % O_2 / 50 % H_2) at 600 W. A second post-treatment consisting in annealing under constant gas flow of a mixture 95% Ar / 5% H_2 was carried out in a furnace. The temperature was set to 135ºC for 2 hours.

In order to facilitate the exposition of results the labels of the samples specifically address the main experimental parameters varied during their fabrication. As an example:

PVD (550nm) + SPE (O_2+Ar) 180ºC 120min + Anneal (H_2+Ar)

Where (550nm) indicates the nominal thickness in the QCM, 180ºC and 120min the substrate temperature and treatment duration of the soft plasma etching step. Since the annealing conditions were always the same for simplicity the label not always includes this step and it is only expressed when comparing samples previous and after post-annealing.

High-resolution SEM images of the samples deposited on silicon wafers were obtained in a Hitachi S4800 microscope, working at different acceleration voltages (1-5 kV). Cross sectional views were obtained by cleaving the Si(100) substrates. XPS characterization and in situ XPS experiments were performed in a Phoibos 100 DLD X-ray spectrometer from SPECS. The spectra were collected in the pass energy constant mode at a value of 50 eV using a Mg Kα source. C1s signal at 284.5 eV was utilized for calibration of the binding energy in the spectra. The assignment of the BE to the different elements in the spectra corresponds to the data in reference 34. In situ XPS experiments were performed in a VG ESCALAB 210 spectrometer with a prechamber where all PtOEP depositions and treatments were carried out. The plasma source used for these experiments consisted of a quartz tube where the plasma was excited by means of a resonant cavity connected to a microwave generator. The power was 70 mW and the oxygen was supplied to the tube up to a pressure of about 2 x 10^{-1} mbar.

3.3.2. Charactezitation

X-ray Diffraction (XRD) and Glancing Angle X-ray Diffraction (GAXRD) were carried out in a Panalytical X'PERT PRO diffractometer. For GAXRD the incident angle was 0.2 º. UV-Vis transmission spectra of samples deposited on fused silica slides were recorded in a Cary 100 spectrophotometer in the range from 190 to 900 nm. Electrical characterization was carried out following different procedures. In the first case, the

samples were grown on commercial available Pt electrodes (Figure 1a). These electrodes present an interdigitated array with 10 um separation and electrode thickness of 10 um. Conducting Atomic Force Microscopy (C-AFM) characterization was also carried out in the columnar films in the contacting mode in Pico Plus instrument from Molecular Imaging. DLC-cover tips with a diameter below 70 nm (Nanosensors) were utilized with the BIAS applied to the sample. In addition, four probes measurements (Figure 1 b) were also applied in particular cases in order to overcome plasma sheath issues in the deposition on the commercial electrodes (see Section 4.2). The contact between the electrically conductive tip and the sample was produced through a silver paste droplet cured in air during 20 minutes at room temperature. In these characteristics V_M indicates the voltage measured by meter. Because sense current is negligible, $V_M = V_R$ and the measured resistance is obtained through Equation 1.

$$R = \frac{V_M}{I} = \frac{V_R}{I} \quad \textbf{Eq. 1}$$
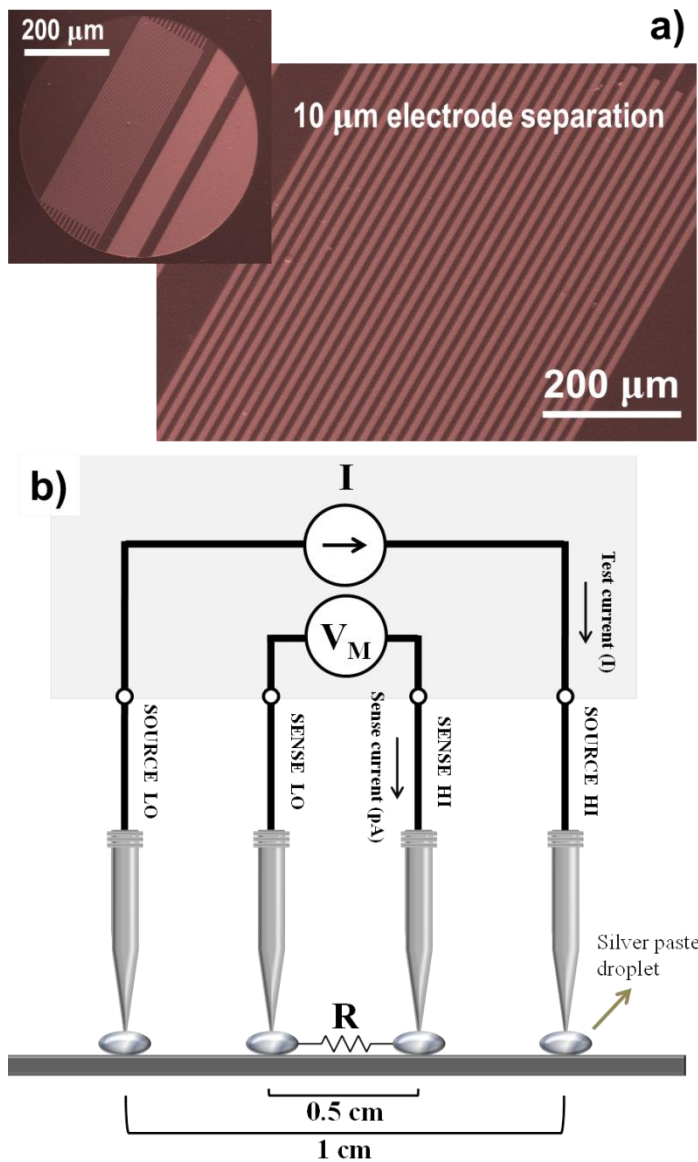
Figure 1. a) Normal view SEM micrograph of the interdigitated electrodes utilized for the electrical characterization of the samples. b) Schematics on the four probe measurements where V_M indicates voltage measured per meter.

In both cases the measurements were made with a 2635A system sourcemeter working in sweep voltage mode under ambient conditions.

3.3.3. DSSCs fabrication, assembly and characterization

Working electrodes. Prior to any deposition, the substrates were rinsed with acetone, isopropanol and absolute ethanol, and heated to 500 ºC for 1 hour. A blocking layer

was deposited on the FTO/glass substrates (Xop Glass, 12-14 Ω/cm^2) by immersion in a $TiCl_4$ (40 mM) solution at 70 ºC for 30 minutes and then dried in air. The active area consisted of 12 µm thick films made up of a layer of 8 µm of 20 nm TiO_2 nanoparticles (Dyesol© paste) and a layer of 4 µm of 400 nm TiO_2 particles (scattering layer), both deposited by the screen printing technique on the conducting glass substrates This electrodes were slowly heated up to 500 C (with a plateu of 15 minutes) and then immersed in a solution of TiCl4 (40 mM), heated to 70 ºC for 30 minutes and dried in air. A final heating cycle was performed at 500 ºC during 30 minutes and then allowed to cool down in air. The active area of the cells was 0.16 cm^2 [Idígoras J., Phys. Chem. Chem. Phys. 2014]. The working electrodes were left overnight in a 0.5 mM solution of N719 dye in ethanol. Afterwards they were rinsed with an ethanol baker and dried in air.

Counter electrodes. A small hole was drilled on them to allow for electrolyte injection at the end of the process. Later, they were cleaned just as the working electrodes.

Platisol® Counterelectrodes. Distributed 6 µl of Platisol® all over the counterelectrode area and once dried added 6 µl more. Then, the counterelectrodes were put into the furnance at 400 ºC during 5 minutes with a 15 minutes heating ramp.

Electrolyte solutions. Two different electrolytes were tested. AN50 was purchased from Solaronix and used as received. 100% Pyr has the following formulation: 0.1M I2, 0.05M LiI, 0.5M TBP, 0.1M GuSCN, 1M BMII, 1-butyl-00 ºC during 5 minutes with a 15 minutes heating ramp. 1-methylpyrrolidiniumbis(trifluoromethanesulfonyl)imide (Pyr). Pyr was purchased from Solvionic.

Nanostructured electrodes. Two types of nanoelectrodes were tested: "RPAVD-Ar (420nm) SPE (Ar+O_2) 210ºC 240 min + Anneal (O_2+H_2)" and "RPAVD-O_2 (500nm) SPE (Ar+O_2) 210ºC 240 min +Anneal (O_2+H_2)".

Sealing of the cells. A frame of a thermoplastic polymer (Surlyn, Solaronix) was placed on the perimeter of the active area and then sandwiched with the counterelectrode. The whole cell was heated to 140 ºC under slight pressure to ensure a proper sealing. After that the electrolyte was injected and the hole on the counterelectrode sealed with Surlyn and a cover slide glass.

Characterization of DSSCs. The solar-cell devices were characterized using a solar simulator with an AM1.5G filter (ABET). A reference solar cell with temperature output (Oriel, 91150) was used for calibration. EIS measurements were performed under light

with perturbations in the 10^5-10^{-3} Hz. A LED LUXEON collimated (540 nm) source and an Autolab/PGSTAT302N potentiostat were used for EIS measuremets. Zview equivalent circuit modelling software (Scribner) was used to fit the EIS data, including the distributed element DX11 (transmission line model).

3.4. Results and Discussion

3.4.1. Microstructure, optical properties and chemical composition

a) In situ plasma etching experiments.

In order to state optimum conditions for the mineralization of the PtOEP into Pt we carried out preliminary in situ experiments by XPS. In these experiments a thin layer of PtOEP was sublimated and plasma post-treated in a prechamber attached to the XPS analysis chamber. Figure 2 gathers the main XPS peaks acquired during the experiments. In first place a nominal thickness of PtOEP was sublimated onto Si(100) substrates at room temperature (black line). This precursor layer was treated with an Ar/O_2 plasma (see Methods) during different times at 175 ºC. Full decomposition of the platinum porphyrin is achieved after vanishing of the N1s peak (Fig. 2 c) for treatments longer than 20 minutes. Fig. 2 a) shows the corresponding Pt4f peaks appear with binding energies values in good agreement with the formation of Pt(0).[nist] Interestingly, for short treatment periods (green line), the position of the Pt4f peak is also compatible with the partial oxidation of platinum. We will go back to these results in the following section.
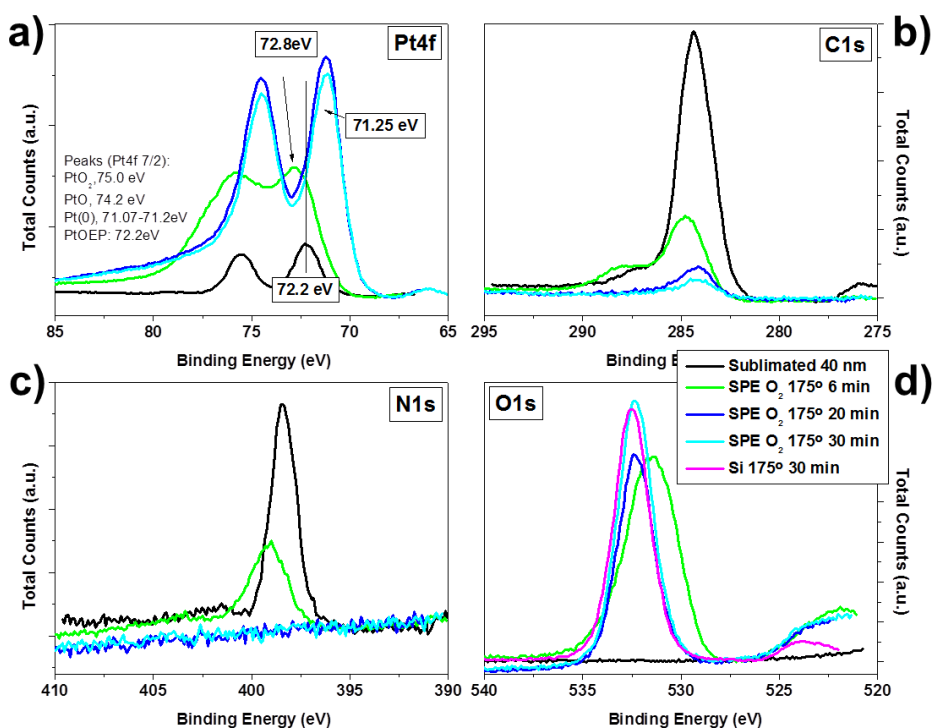
Figure 2. In situ experiments following the soft plasma etching in O_2+Ar (300W) at 175ºC on 40 nm PtOEP sublimated film. Surface was sequentially exposed to plasma.

In summary, the porphyrin is completely decomposed after oxygen plasma treatment at mild temperature giving rise to the formation of platinum metal clusters. However, equivalent experiments at room temperature demonstrated that prolonged treatment did not effectively oxidize the organic counterpart.

The chemical composition of the samples as grown and after several post-treatments was evaluated by means of ex situ XPS (Table 1). The three first lines on Table 1 correspond to the as-grown samples comparing the PVD layers with those formed under Ar and O_2 plasma.

Table 1. Atomic percentage obtained from the XPS peaks corresponding to the elements presented.

Sample	% Pt(0)	% Pt(+2)	% O	% N	% C
PVD (550nm)	-	2.7	5	6.8	85.5
RPAVD-Ar (280nm)	-	2.4	18.8	7.1	71.7

RPAVD-O$_2$ (200nm)	6.4	8.3	52.6	1.9	30.8
RPAVD-Ar (280nm) +SPE (O$_2$+Ar) 180ºC 120min	8.1	5.0	65.3	1.3	20.3
RPAVD-Ar (280nm) +SPE (O$_2$+Ar) 180ºC 120min + Anneal (H$_2$+Ar)	13.5	-	58.8	1.8	25.9
RPAVD-O$_2$ (200nm)+SPE (Ar+O$_2$) 180ºC 140min + Anneal (H$_2$+Ar)	14.2	-	44. 7	1.9	39.2

Results in Table 1 indicate that after the SPE treatments the metal organic molecule layers got enricher in metallic platinum as the percentage of nitrogen and carbon decreases. Oxygen contribution might be split by the silicon oxide substrate exposed after the SPE treatments and partial oxidation of the platinum under RPAVD-O$_2$ conditions.

b) Microstructure and structure.

Figure 3 to 7 present the ample variety on microstructure of PtOEP and Pt containing thin films layers obtained for the different deposition conditions and post-treatments. Fig. 3 gathers cross sectional and planar views of characteristics samples with the aim of showing an overview of the available microstructures.

Samples fabricated by PVD conditions (Fig. 3a) grow as stacked columns of inhomogeneous shapes and thickness that increase in length with the increment in the deposition time. The microstructure of the PVD PtOEP layers is equivalent for the different reference substrates utilized in this research (Si(100) wafers, fused silica and commercial available FTO thin films on glass) for the experimental conditions selected.

Samples formed under RPAVD-Ar experiments present a homogeneous and continuous cross section with a low roughness surface (Fig. 3 b) meanwhile samples deposited under oxygen plasma, i.e. RPAVD-O$_2$, develops a 1D microstructure characterized by the formation of vertical columns of constant diameter (<100nm). The normal view of these samples (Fig. 7 a-b) show the columns are forming nanometer-scale arrays by agglomeration of several columns in one clusters.
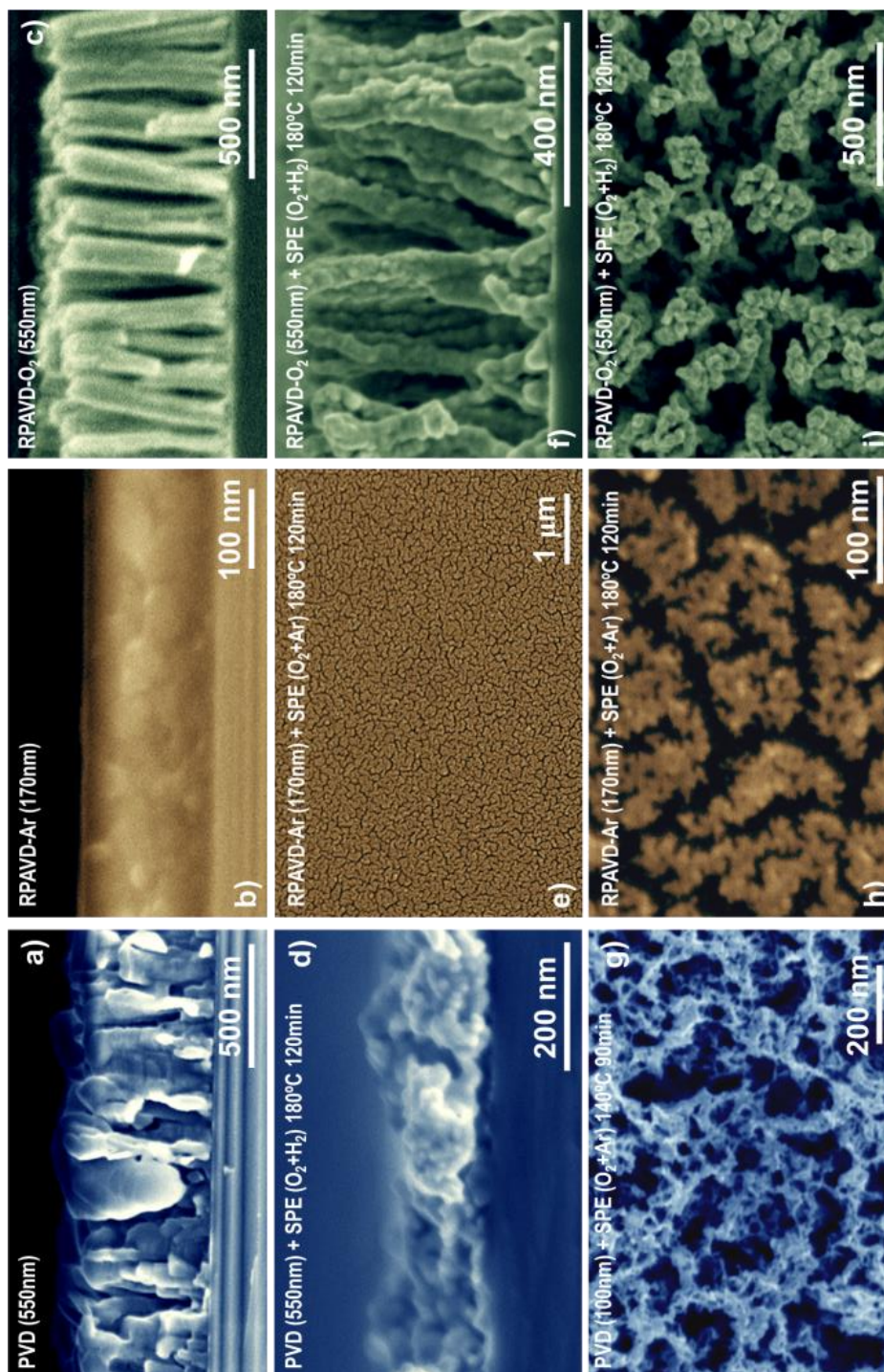
Figure 3. Cross section (a-c, d, f) and planar views (e, g-i) of characteristics samples as labelled.

Although same driving forces are far to be acting herein it is worth to mention that this behavior is similar to the obtained by nanocarpet effect, as consequence of capillarity forces induced by evaporation of a liquid droplet.[Macias-Montero-Langmuir2012]

Microstructure of the samples is drastically affected by all the SPE treatments carried out. Fig. 4 shows the evolution of the PVD samples for several sample thicknesses after SPE(O_2+Ar) treatments (see Fig. 3 d) and g) for results on SPE(O_2+H_2). The polycrystalline films have been converted into a highly porous of partially interconnected Pt particles. Samples present different coverage area dependently on the initial sample thickness and plasma treatment duration.
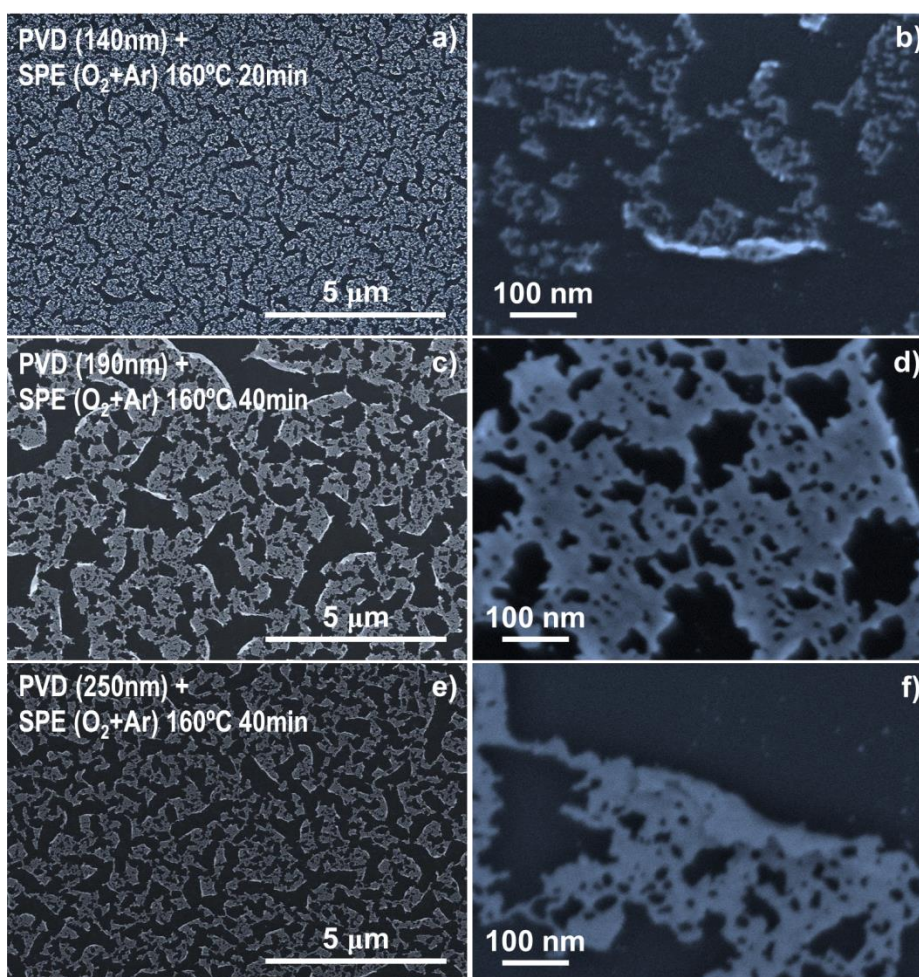
Figure 4. Planar view SEM images at different magnifications of the Pt porous layer obtained after soft plasma etching of PtOEP films deposited by PVD with different thicknesses between 140 and 250 nm as labelled.

Thus, for thinner samples (140 nm), low magnification images present high coverage area (Fig. 4 a) meanwhile empty micrometer-size areas appear for thicker samples (Fig. 4 c and e). However, a closer look by high magnification SEM reveals the lower connectivity between the metal grains in the thinner samples. The percolation of the layers increases with the thickness of the precursor layers, showing anyhow mesopores of different sizes even for the thicker deposited sample (Fig. 4 d-f).

A similar behavior is depicted by RPAVD-Ar post-treated samples (Fig. 3 e) and h), Fig. 5 and 6) with an important difference in the level of percolation of the platinum. In this case, even for thin layers (140 nm) the SPE produces highly interconnected dendritic features. Size of these grains increases with the thickness of the precursor layers producing platinum porous sheets extended in the plane with sizes in the order of several microns. These sheets percolate leaving also pores in the range of the micron for intermediate thickness (Fig. 5 b) and even below for thick samples (Fig. d). The cross section images in Fig. 5 c) and e) and high resolution SEM image in Fig. 6 addresses the yet highly porosity of the percolated layers showing pores in the range of the mesopores (2nm < d < 50 nm).

RPAVD-O_2 samples keep their columnar microstructure after the SPE treatments but increasing enormously the roughness of the surface of such columns due to the formation of platinum nanoparticles.

It is worth to mention the reduction in thickness of all the post-treated samples when compared with the as-grown layers. This reduction is more accused for PVD and RPVAD-Ar samples and for O2+Ar treatment than for O_2+H_2 treatments.
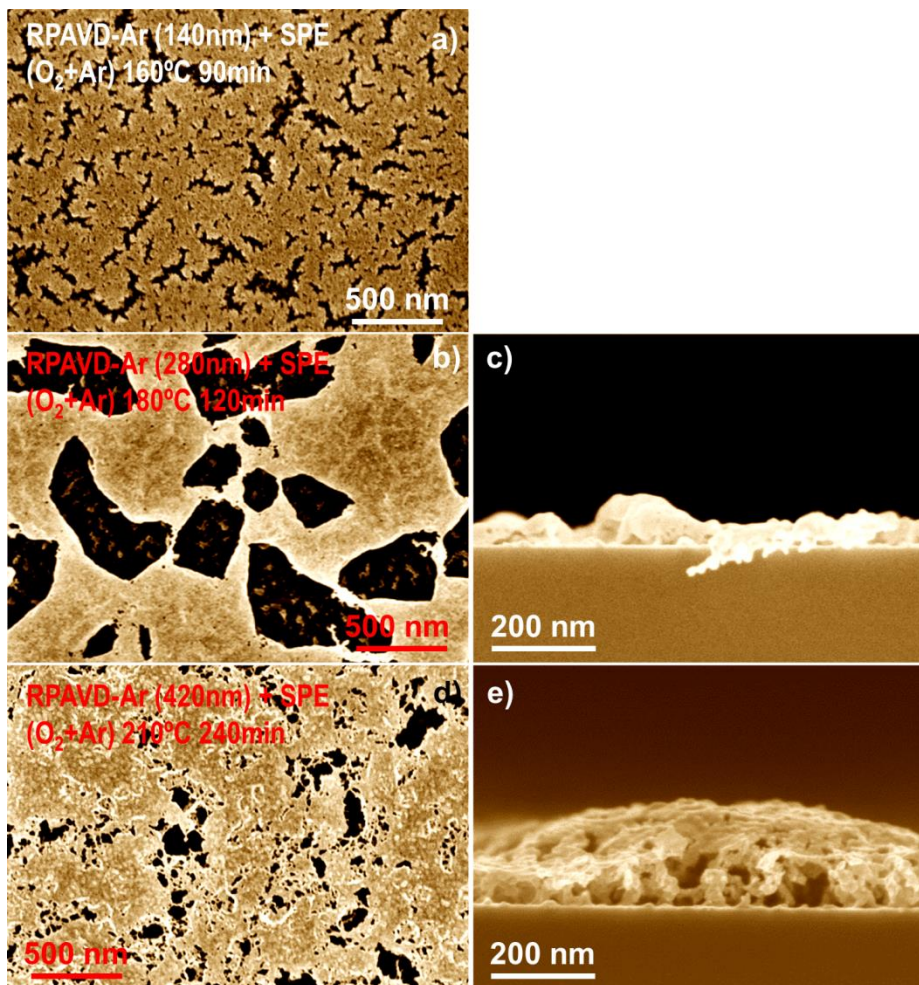
Figure 5. Planar view (left) and cross section (right) SEM images of the Pt porous layer obtained after soft plasma etching of continuous PtOEP films deposited with different thicknesses between 140 and 420 nm as labelled.
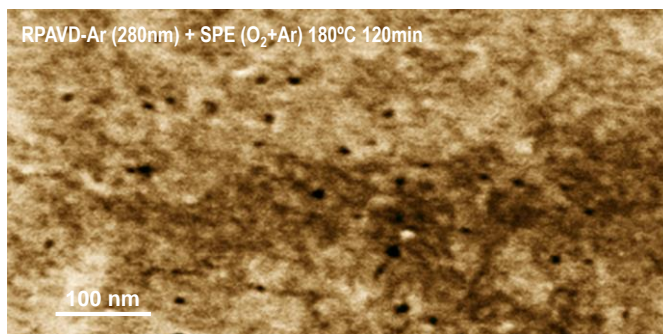
Figure 6. High magnification SEM image of the Pt porous layer obtained after soft plasma etching of a continuous PtOEP precursor film showing the mesoporous with diameters in the range of ten nanometers.
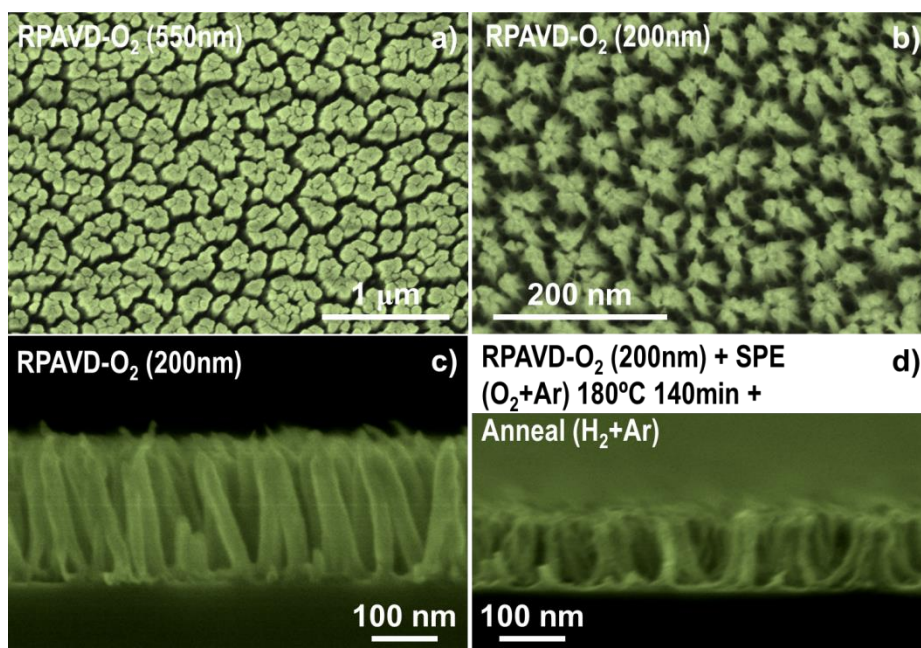

Figure 7. Planar view (top) and cross section (bottom) SEM images of the columnar PtOEP precursor layers obtained by remote plasma assisted vacuum deposition in presence of oxygen for a 200 nm precursor layer as grown (a-c) and after a complete treatment of oxidation-reduction (b-d).

GAXRD and XRD analyses were performed in order to inquire about the crystalline condition of the samples. Figure 8 Top) gathers GAXRD patterns from the precursor layers, showing a pronounced peak at low angles alongside lower intensity peaks between 15º and 30º for the sublimated thin film (PVD (550nm)) according to its polycristalline character.[Borras Langmuir 2010]
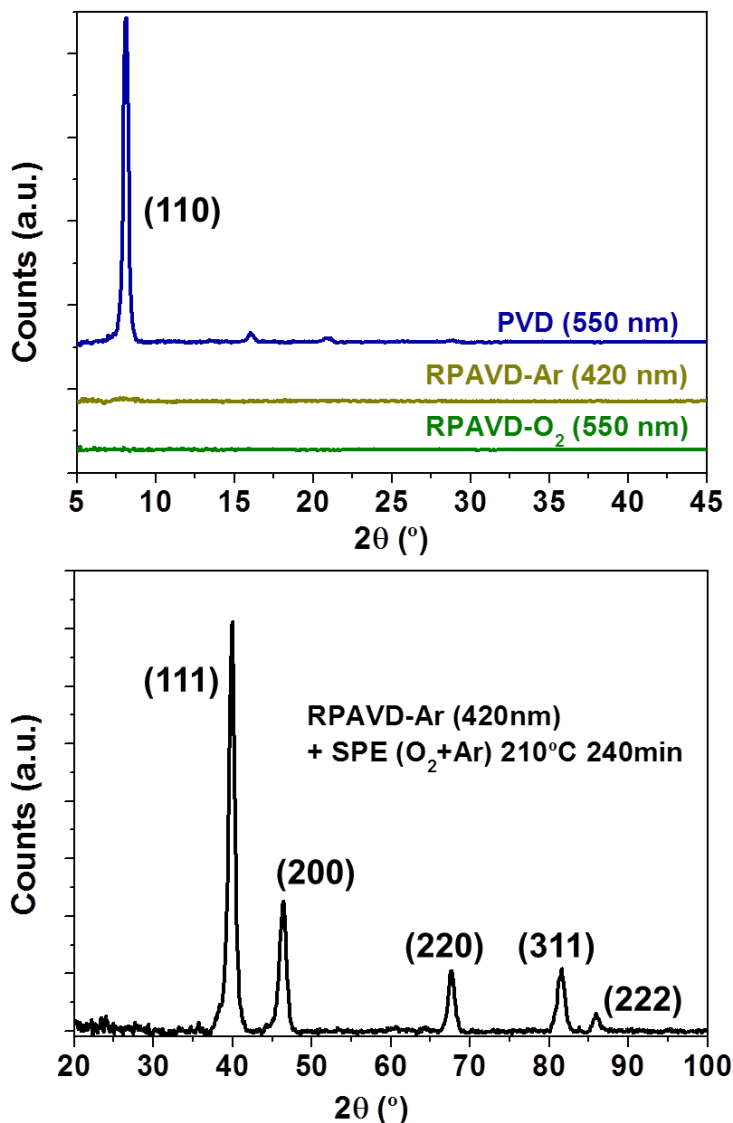
Figure 8. Top) GAXRD of the precursor layers formed by PVD and RPAVD under argon and oxygen plasma gases conditions. Bottom) XRD pattern of a platinum layer formed after plasma etching of a RPAVD-Ar (420nm) precursor film.

Patterns acquired for the samples grown by RPAVD presented no peaks independently on the plasma gas composition. This result is in good agreement with the smooth and homogeneous microstructure depicted by the samples RPAVD-Ar similar to the standard nanocomposite organic thin films deposited by this technique.[Aparicio-Adv.Mater.2011] In contrast, the post-treated samples all show well defined peaks corresponding to the planes (111), (200), (220), (311) and (222), which are characteristic of the FCC structure of Pt.[Leontyev-RSCAdv.2014; Mi-ChemMater.2015] An average particle size of 12 nm was estimated from XRD pattern in Fig. 8 Bottom).

c) Optical properties.

One of the main motivations of this chapter is the fabrication of transparent and semitransparent nanoelectrodes based on platinum nanostructures. Figures 9 – 12 show the UV-VIS-NIR (Fig. 9) and UV-VIS (Figs. 10-12) transmittance spectra of the samples deposited on fused silica substrates and post-treated under different conditions. Fig. 9 presents an overview of characteristics samples demonstrating the variety in the transmittance depending on the experimental conditions.

In general, samples SPE treated present an almost constant transmissivity along the UV-VIS-NIR spectrum, with lower transmission values for thicker films. Annealing in H_2+Ar gases does not significantly affect the optical properties of the samples, therefore, from now on we will discuss the results on annealed samples even though this label is not attached to all the samples denotations. Only in those cases where comparison between annealed and not-annealed samples is worthy, the label would indicate that post-treatment.

It is interesting to stress the strong difference between the RPAVD-Ar and RPAVD-O_2 samples. In the first case, the spectra (black line in Fig. 9) yet depicts characteristic absorption band due to the presence of partially decomposed PtOEP molecules as we will demonstrate below. However, sample deposited under oxygen plasma present a strong absorption below 400 nm but not porphyrin related bands.

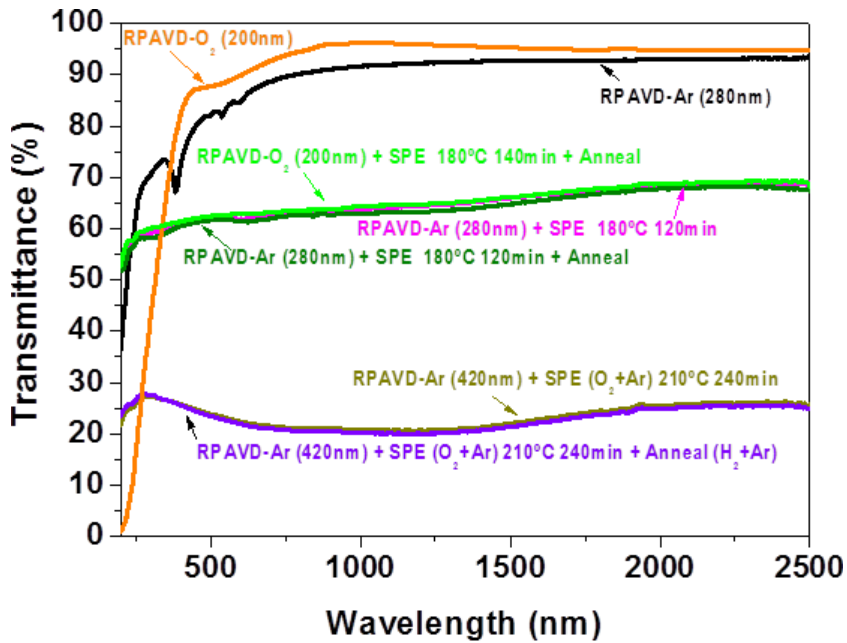Figure 10 – 12 show the comparison of samples as a function of the deposition method.

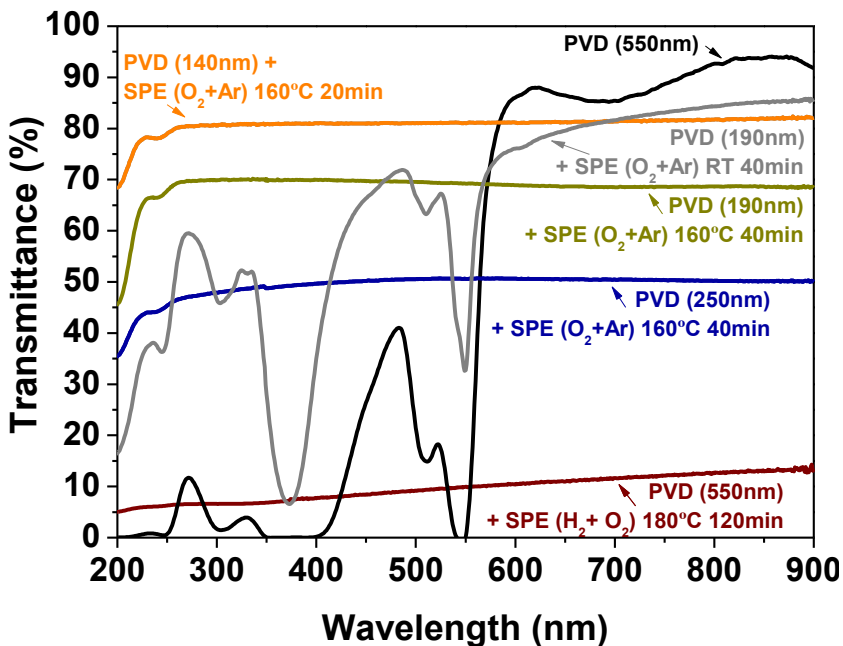**Figure 9.** UV-VIS-NIR spectra of characteristic samples as labelled.

Figure 10. UV-VIS spectra of PVD and PVD plasma treated samples as labelled. All the treated samples had undergone post-annealing in H_2/Ar at 135 ºC.

Thus, Fig. 10 gathers the UV-VIS spectra of PVD as grown and post-treated samples. PVD samples present several strong absorption bands, the first one in the UV region at about 300 – 400 nm (Soret band) and the second double one in the visible part of the spectrum around 475 – 550 nm (Q and Q´bands). Soret band arises from the deeper π-levels → LUMO transition meanwhile the Q bands are attributed to the π – π* transition from the highest occupied molecular orbital (HOMO) to the lowest unoccupied molecular orbital (LUMO) of the of the pi resonant system of the phthalocyanine.[Zhang-RSCAdv.2014]

It is easily visible that SPE (O$_2$+Ar) treatment at room temperature of the PVD samples (see gray line in Fig. 10) does not decompose the porphyrin efficiently as already mentioned regarding the in situ XPS experiments, even for thin layers with thickness below 190 nm. The corresponding line yet depicts the strong absorption bands related to the PtOEP molecules. The increment of the treatment temperature up to 160 ºC drastically affects to the layers composition. In fact, highly flat transmission curves are obtained for the SPE (O$_2$+Ar) treatments at such temperature with transmission decreasing as a function of the sample thickness (compare orange, dark yellow and royal lines). It is worthy to mention again the extremely constant reflectivity of these samples that are comparable to results presented in the literature for complex metal and metal/CNTs networks.[Hu-MRSBulletin.2011] Transmission drops for the thicker sample treated under SPE (H$_2$+O$_2$) – 180 ºC conditions. In all these samples the small absorption below 250 nm is related to the fused silica substrate properties.

Figure 11 summarizes main results regarding RPAVD-Ar as-grown and post-treated samples. As expected from previous results of RPAVD of organic molecules, [Aparicio-Adv.Mater2011, Aparicio-JMC-C.2014] samples deposited under this plasma conditions contain integer PtOEP molecules along with fragments formed after partial plasma etching of the molecule. For thinner layers the characteristic bands present a weaker absorption (comparison between black and orange lines). In good agreement with results extracted for PVD samples, SPE (O$_2$+Ar) treatments of the samples induce the mineralization of the PtOEP vanishing the organic-related bands and giving rise to constant transmission spectra. In this case, treatment temperature needs to be higher than 160 ºC in order to produce the full decomposition of the molecule (see royal and green lines), even higher than 180 ºC for thicker samples (dark yellow line). Increasing the treatment duration and sample thickness also increases the reflectivity of the samples (compare blue and purple lines and purple and dark yellow lines). For similar thicknesses of the precursor layers, SPE (H$_2$+O$_2$) treatments provoke a fall in the transmission in comparison of equivalent SPE (O$_2$+Ar) treatments (see gray and

wine lines). On the other hand, this figure shows the ample variety in light constant transmissivity of the sample that can be easily tuned by selecting the experimental parameters.
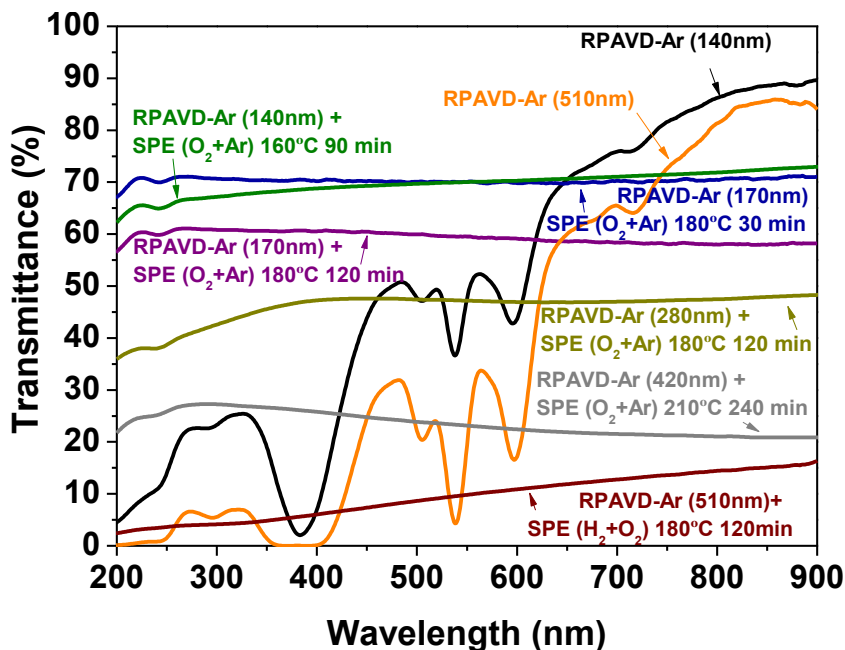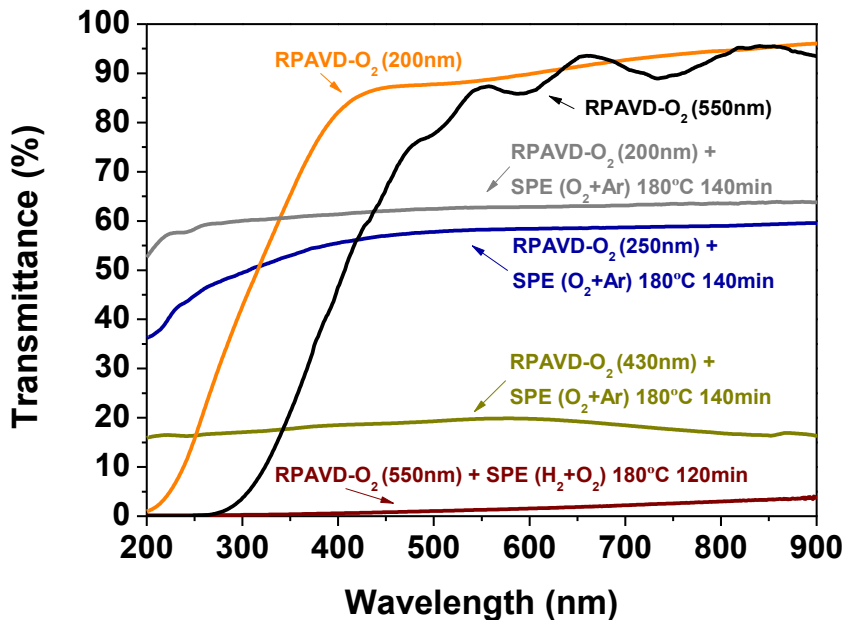

Figure 11. UV-VIS spectra of RPAVD-Ar and RPAVD-Ar plasma treated samples as labelled. All the treated samples had undergone post-annealing in H_2/Ar at 135 ºC.

Figure 12 presents the UV-VIS spectra corresponding to as-grown and post-treated RPAVD-O_2 samples. It is important to stress the peculiar behavior of the as-grown RPAVD-O_2 in contrast to PVD and RPAVD-Ar samples. In this case, the spectra for the as-grown sample present a band-gap below 400 nm that strongly depends on the sample thickness (see orange and black lines). The presence of such a band-gap is in concordance with the XPS data regarding the formation of platinum oxide embedded nanoparticles. Although these results might be of highly relevance in the catalytic performance of these nanocolumns, in this chapter we cannot accomplish a full analysis of such properties due to time limitations.

Figure 12. UV-VIS spectra of RPAVD-O$_2$ and RPAVD-O$_2$ plasma treated samples as labelled. All the treated samples had undergone post-annealing in H$_2$/Ar at 135 ºC.

Once the SPE treatments are carried out on the samples, the transmittance spectra present a similar behavior than for the PVD and RPAVD-Ar post-treated samples. In this case, a substrate temperature about 180 ºC permits the conversion into platinum of the metal-organic porphyrin. It is worth to mention that the SPE (H$_2$+O$_2$) sample (wine line) presents the lowest transmittance of all the analyzed samples, i.e. transmission below 5 % in the full UV-VIS range.

3.4.2. Electrical characterization

Figure 13 shows typical IV characteristics obtained for different as-grown and post-treated samples measured by the four probe method (Fig. 13 a-b) and on the layers deposited onto commercially available electrodes separated 10 um (Fig. 13 c-f). The comparison between Ar+H_2 annealed and as prepared samples (Fig. 13 a) show an improvement of twice the conductivity of the samples, therefore in the rest of the panels the sample represented were annealed. As-grown samples present high resistivity even that increases and the sample thickness decrease. Best results regarding conductivity of the samples correspond to thick samples post-treated under H_2+O_2 oxygen, and, in general, the resistance decreases with the thickness of the samples. Table 2 summarizes the resistance and sheet resistance measure for the different samples.

It is also interesting to mention that measurements carried out on the 10 um interdigitated electrodes shall present worse interconnection results because of the existence of zones of plasma shadow in close vicinity to the electrode itself. Thus, Fig. 14 show SEM micrograph of the different precursor layers deposited onto the interdigitate electrodes evidence the inhomogeneities in the growth below the electrode. This issue is more pronounced in thin and in columnar layers. In order to circunvent such handicap we procedded to the evaluation of the resistance by four probe method in the case of the RPVAD-Ar samples and by conducting-AFM in the columnar layers (Figure 15).
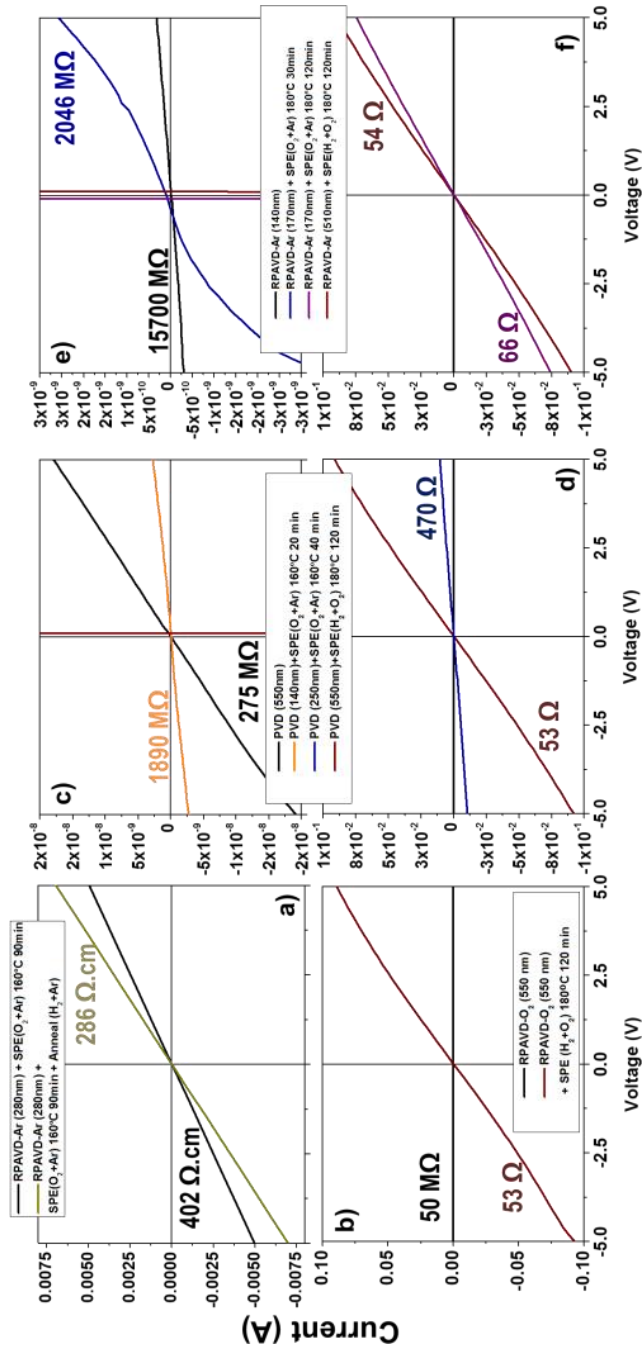
Figure 13. IV characteristics of representative samples as labelled. a) Characteristics measured by the four probes method comparing the sample before and after annealing. b)-f) Curves obtained for the samples deposited on de interdigitated electrodes (10 um). In all the panels but a) the treated samples had undergone a posterior annealing in H₂/Ar at 135 ºC.

Table 2. Resistance measured for characteristic samples in the interdigitated electrodes (ID) and for the four probe method in the case of the RPAVD-Ar samples. Note that all the post-treated samples presented herein were annealed in H_2+Ar at 135 ºC during 2 hours.

Sample	10 um ID	Four probes
PVD (550nm)	275 MΩ	
PVD (140nm) + SPE (O_2+Ar) 160ºC 20min	1890 MΩ	
PVD(250nm) + SPE (O_2+Ar) 160ºC 40min	470 Ω	
PVD(550nm) + SPE (H_2+O_2) 180ºC 120min	53 Ω	
RPAVD-O_2 (550nm)	50 MΩ	
RPAVD-O_2 (200nm)	86 MΩ	
RPAVD-O_2 (550nm) + SPE (H_2+O_2) 180ºC 120min	53 Ω	
RPAVD-Ar (140nm)	15.7×10^3 MΩ	
RPAVD-Ar (140nm) + SPE (O_2+Ar) 160ºC 90min	54 Ω	752 Ω.cm
RPAVD-Ar (170nm) + SPE (O_2+Ar) 180ºC 30min	2046 MΩ	
RPAVD-Ar (170nm) + SPE (O_2+Ar) 180ºC 120min	66 Ω	
RPAVD-Ar (280nm) + SPE (O_2+Ar) 180ºC 120min	63 Ω	286 Ω.cm
RPAVD-Ar (420nm) + SPE (O_2+Ar) 210ºC 240min	54 Ω	24 Ω.cm
RPAVD-Ar (510nm) + SPE (H_2+O_2) 180ºC 120min	54 Ω	
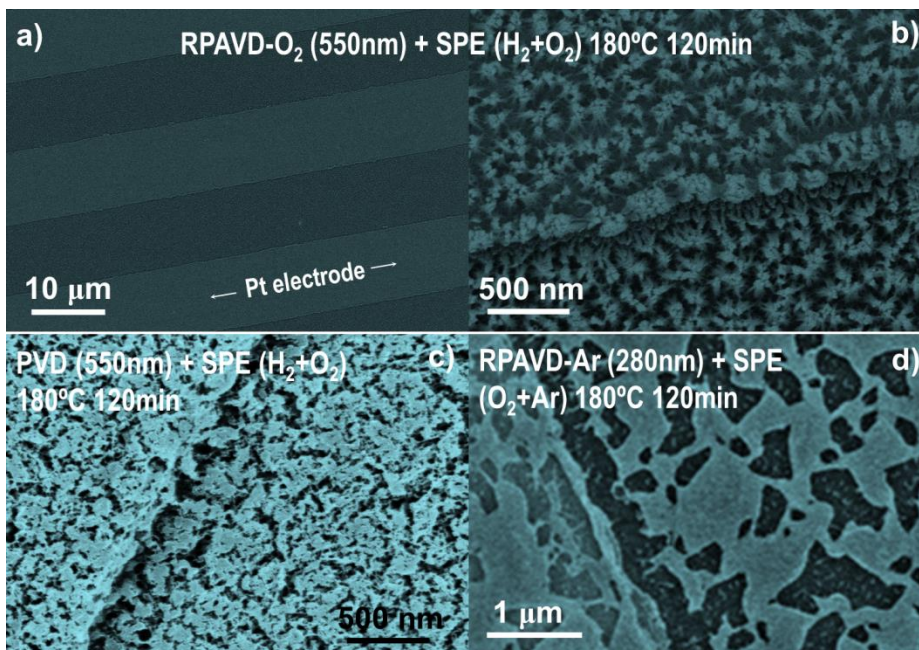
Figure 14. SEM micrographs of different samples deposited on interdigitated Pt electrodes as labelled; panel a) presents a low magnification view of the nanocolumns deposited showing the high homogeneity in the coverage; panels b-d) gather characteristic images of the growth at the boundary with the metal electrode, bringing out the important discontinuities formed under RPAVD-Ar conditions.

Conducting-AFM characterization was carried out on the columnar samples deposited on commercial available ITO substrates. Main results on these analyses are presented in Fig. 5. The topography of the sample forming by clusters of columns is also visible by AFM. Bias applied to the tip produce an increment in the current emmited by the sample (Fig. 15 a-b). When a bias is applied between sample and tip, the sample ignitiates a current signal (recorded in Fig. 15 c-d). Conductivity maps in this figure were acquired for two different bias showing an increment in the top current of an order of magnitude by increasing the bias voltage from 0.01V (Fig. 15 c) and (0.035V). It is as well possible to address the conducting properties of individual nanocolumns by situating the conductive tip on the top of the column and performance an IV curve. Fig. 15 e) and f) presents curves obtained in the brighter and darker spots in Fig 15 d) correspondently. Current conducted by one of these columns is in the order of several nanometers.
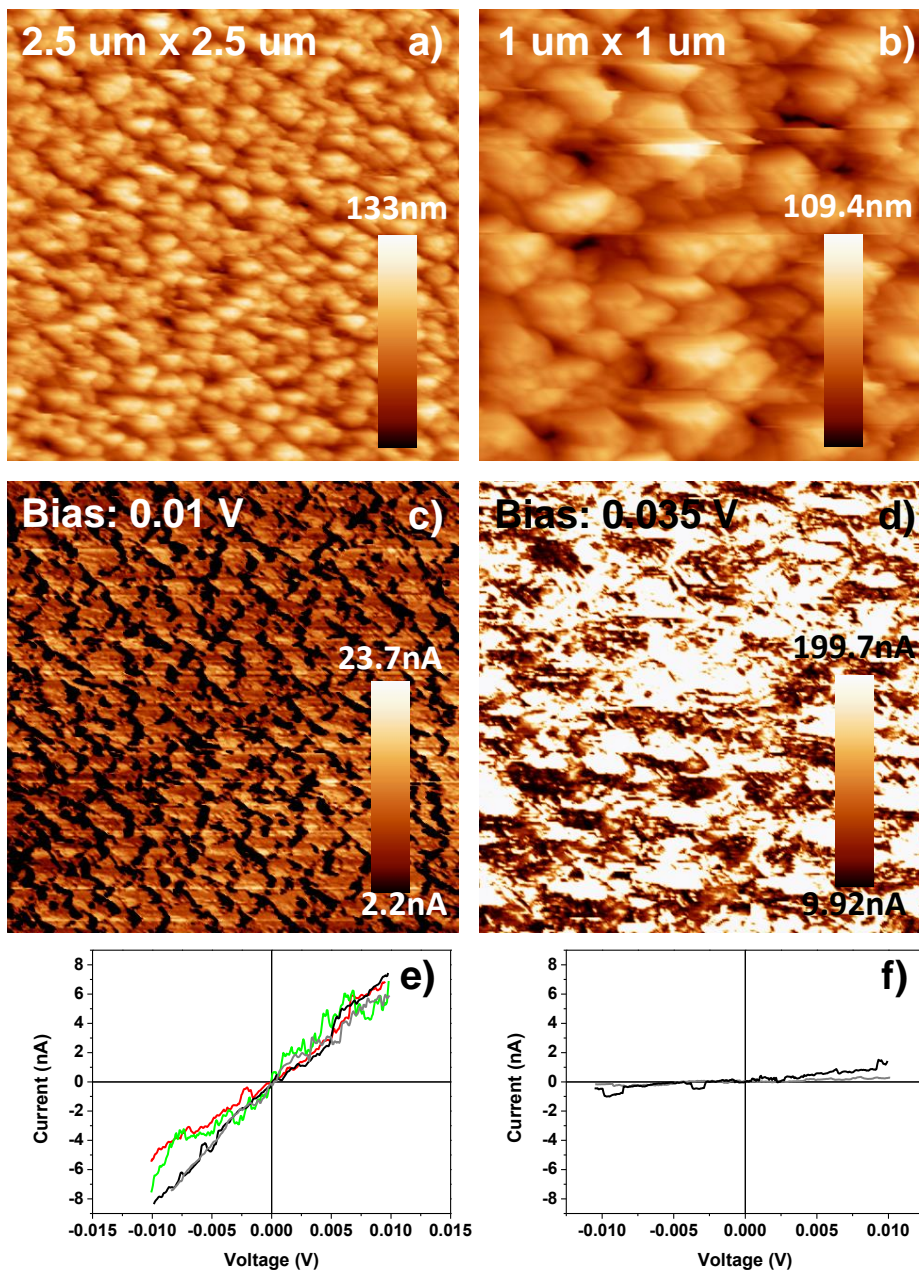
Figure 15. Topography AFM (a-b) and Conducting AFM (c-d) images acquired at two different scales and sample bias on the "RPAVD-O_2 (200nm) + SPE(Ar+O_2) 180ºC 140min" columns; I−V curves measured with the AFM tip placed on a position with a maximum (e) and minimum (f) conductivity.

3.4 .4. 1D and 2D transparent Platinum layers as counter electrode in a Dye Sensitized Solar Cell.

Towards the implementation of both 1D (nanorods) and 2D (membrane) configurations in real devices, DSSCs using counter electrodes with vacuum deposited platinum have been fabricated and compared to classical FTO counter electrodes coated with commercial Platisol (Solaronix). In order to gather additional information of the influence of these platinum electrodes on the performance of DSSCs, A commercial low-viscosity electrolyte, namely AN50 (Solaronix), and a high-viscosity one made of pure ionic liquid (Pyr 100%) were tested. Fig. 15 shows the I-V curves for the three kinds of counter electrodes used in the study and for the two distinct electrolytes employed. For the low-viscosity electrolyte (AN50), a remarkable difference in the photovoltaic behavior was observed by altering the nanostructure of the deposited platinum. Both platinum nanorods and membrane outperform Platisol in terms of the generated photocurrent and photovoltage, although the grid electrode had a noticeable superior performance. In the case of the high-viscosity electrolyte, all three counter electrodes behaved quite similarly, except for a higher photocurrent observed in the columnar one.
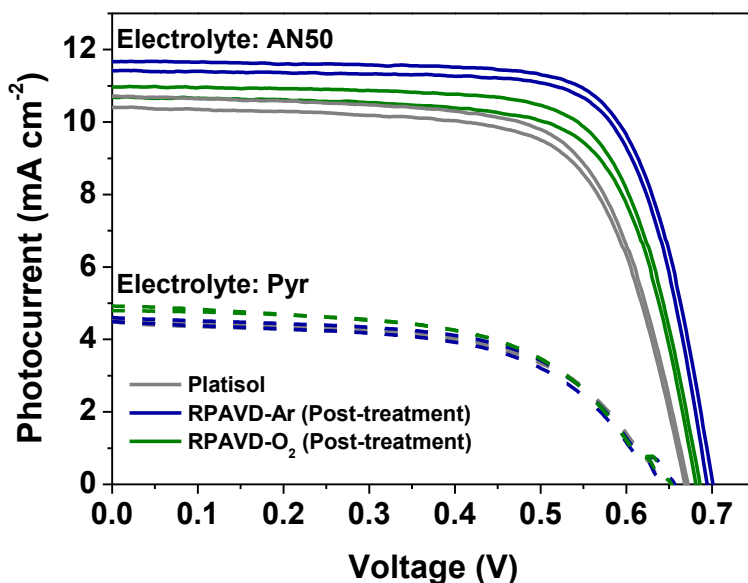
Figure 16. I-V curves for the different counter electrodes and electrolytes employed.

Table 3 presents the different parameters obtained for the fabricated solar cells with electrolyte AN50. Along with the higher photocurrent and photovoltage given for the vacuum deposited platinum as mentioned above, a higher fill factor was observed for

these cells compared to the Platisol ones. These facts suggest that our electrodes allowed for a faster regeneration of iodide ions at the counterelectrode/electrolyte interface.

Table 3. Characteristic photovoltaic parameters for the electrolyte AN50.

AN50 (Solaronix)	J_{sc} (mA·cm^{-2})	Voc (mV)	Fill Factor	η (%)
Platisol A	10.4	668	69	4.8
Platisol B	10.7	671	68.9	5.0
RPAVD-Ar (post-treatment) A	11.4	694	74.3	5.9
RPAVD-Ar (post-treatment) B	11.6	700	73.8	6.0
RPAVD-O$_2$ (post-treatment) A	10.4	681	71.4	5.1
RPAVD-O$_2$ (post-treatment) B	10.9	685	72.2	5.4

For the high-density electrolyte, the photovoltaic parameters are much more similar to each other than for the case of the low-viscosity electrolyte. Only the nanorods counter electrodes exhibited a slight superior efficiency (on average) due to a higher photocurrent. The smaller efficiencies observed for Pyr are expected for such a higher-viscosity formulation.[Kubo-JPCB.2003; Kuang-AdvMater20017] The potential faster reduction of tri-iodide by our electrodes is expected to be more noticeable in cells with a higher photocurrent, since in this case a more rapid regeneration is required. Hence, if tri-iodide cannot diffuse fast enough to the counter electrode, it really does not matter whether its reduction rate is further increased.

Table 4. Characteristic photovoltaic parameters for the electrolyte Pyr.

100% Pyr*	J_{sc} (mA·cm^{-2})	Voc (mV)	Fill Factor	η (%)

Platisol A	**4.5**	**644**	**57.4**	**1.7**
Platisol B	**4.6**	**644**	**58.0**	**1.7**
RPAVD-Ar (post-treatment) A	**4.6**	**652**	**58.1**	**1.8**
RPAVD-Ar (post-treatment) B	**4.5**	**644**	**57.0**	**1.7**
RPAVD-O_2 (post-treatment) A	**4.7**	**647**	**57.6**	**1.8**
RPAVD-O_2 (post-treatment) B	**4.9**	**649**	**56.1**	**1.8**

Electrochemical Impedance Spectroscopy (EIS) was carried out to get a further insight of the behavior of the electrodes. Fig. 17 presents the Nyquist plots for the DSSCs fabricated with AN50 (a) and Pyr (b). It can be seen in Fig. 2(a) that Platisol gives rise to the lowest series resistance (onset of the impedance curve) and the platinum membrane originates the largest one, but the width of the first semicircle, corresponding to the Pt/electrolyte interface, decreases in the order Platisol > nanorods > membrane. This is indicative of a decreasing charge transfer resistance at the Pt/electrolyte interface and is in agreement with the faster regeneration of the redox couple suggested and the higher photocurrents observed. It also contributes to a decrease of the voltage drop occurring at the same interface, which would explain the larger V_{oc}.
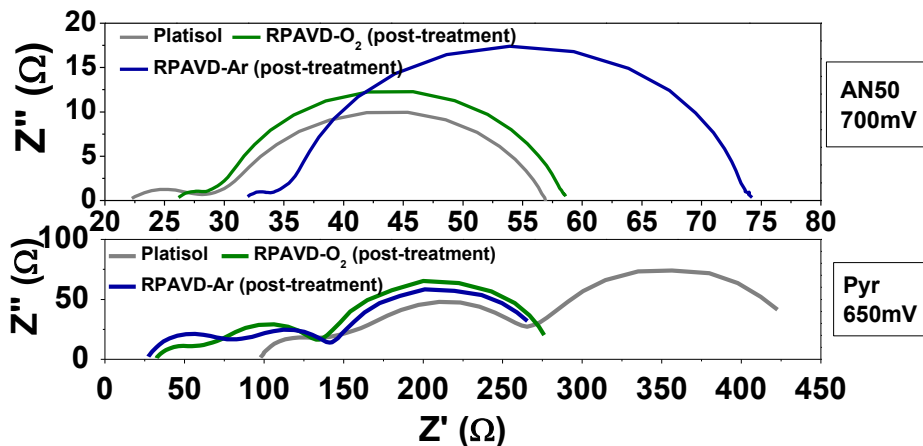
Figure 17. Nyquist plot of DSSCs with AN50 (a) and Pyr (b) electrolytes. The voltages used for the measurements are indicated in the respective figure.

By applying the transmission line model to the EIS data of the cells fabricated with AN50, different cell parameters were obtained (Fig. 18). Recombination resistances (Fig. 18 a) are slightly higher for the platinum grid and lower for Platisol. Electron lifetimes and capacitances are very similar, as expected, for all electrodes.
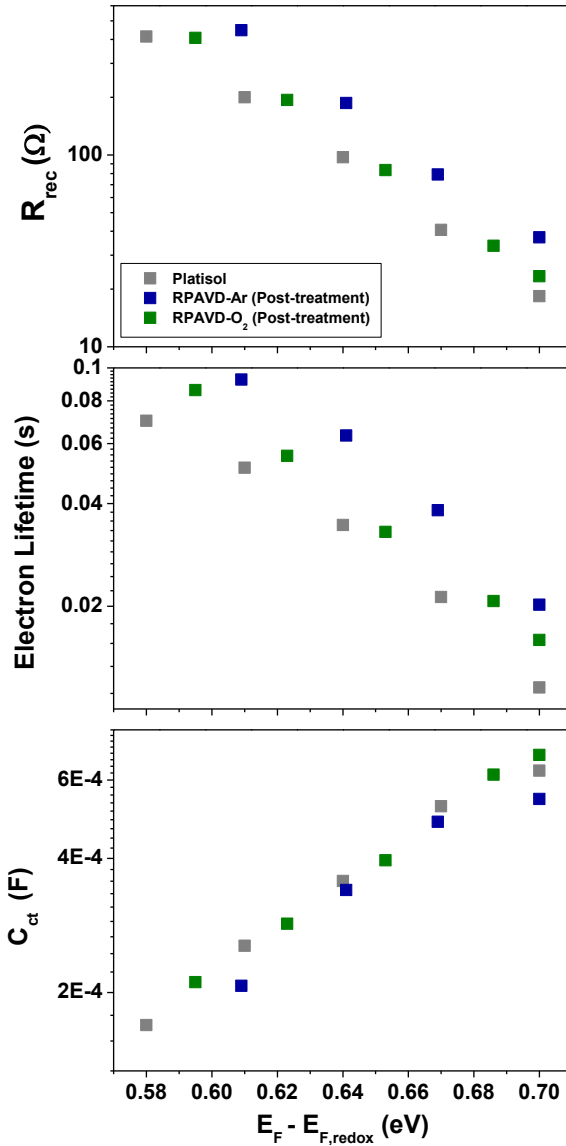
Figure 18. Impedance spectroscopy results of DSSCs fabricated with commercial TiO$_2$ nanoparticles (Dyesol© paste) and AN50 electrolyte. Impedance parameters extracted from the fitting of the EIS spectra at various applied potentials: (a) Recombination resistance, (b) Electron lifetime and (c) Capacitance.

All in all, platinum nanorods and columnar counter electrodes exhibited superior photovoltaic performance and parameters compared to the Platisol normally used in DSSCs when a low-viscosity electrolyte was employed. An additional advantage of

these vacuum deposited electrodes is the easy of production scalability, which could potentially reduce their overall cost .
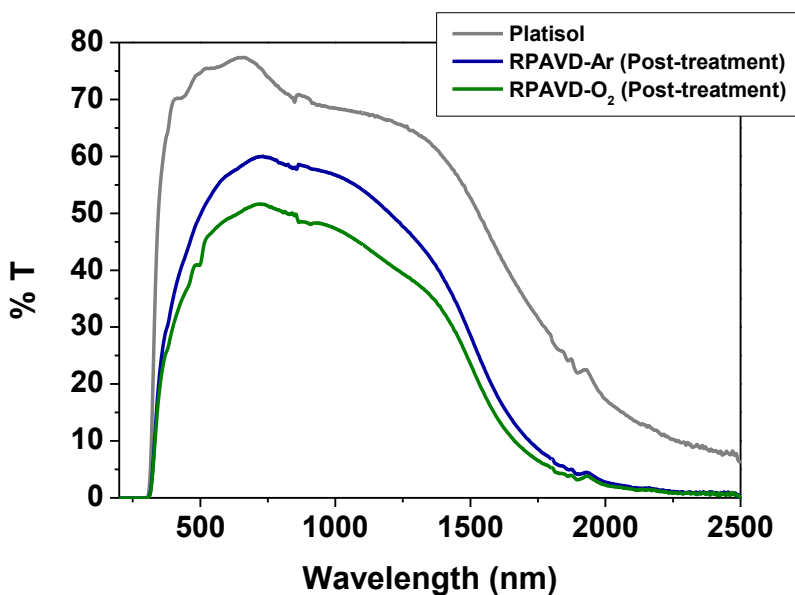
Figure 19. UV-Vis-NIR spectra of the different nanostructured Pt on real FTO/glass substrates.

3.5. Conclusions

A new plasma assisted methodology for the fabrication of transparent metallic electrodes has been developed. One- and two-dimensional metallic structures has been fabricated. *Remote Oxygen Plasma Etching decomposes the PtOEP molecule providing the formation of metallic Pt structures. *Thermal mobilization of the PtOEP molecules improves homogeneity and density of the Pt structures, reducing the SPE treatment duration.

*Transmittance of the Pt layers and nanocolumns depends strongly on the thickness and post-treatment. UV-VIS and UV-VIS-NIR characterization reveals highly homogeneous transmittance in these wavelengths with an ample variety in the transmission range (from 10 % to 70 %).

*Samples prepared under RPAVD conditions are amorphous meanwhile the post-treatment yields crystallization of the Pt. *Deposition conditions of the sacrificial PtOEP layers drastically affect to the final Pt nanoelectrode porosity

and microstructure UV-Vis transmission and XPS results indicated the total decomposition of the organic counterpart and formation of metallic Pt.

*The Current vs Voltage current shows the high conductivity of the films able to drive stable currents of around 0.1 A.

*Transparency and conductivity in 2D nanoelectrodes has been related with the thickness and microstructure of the sacrificial PtOEP.

3.6. References

Alcaire M. et al.; Soft plasma processing of organic nanowires: a route for the fabrication of 1D organic heterostructures and the template synthesis of inorganic 1D nanostructures. Nanoscale 3(11), 4554-4559 (2011).

Alcaire M. et al.; Highly porous ZnO thin films and 1D nanostructures by remote plasma processing of Zn-phthalocyanine. Minor revision Plasma Processes and Polymers.

Angmo, D. et al.; Flexible ITO-Free Polymer Solar Cells. J. Appl. Polym. Sci. 1-14 (2013), DOI: 10.1002/APP.38854.

Aparicio F. J. et al.; Transparent nanometric organic luminescent films as UV active components in photonic structures. Adv. Mater. 23, 761-765 (2011)

Aparicio F. J. et al., Luminescent 3-hydroxyflavone nanocomposites with a tuneable refractive index for photonics and UV detection by plasma assisted vacuum deposition. Journal of Materials Chemistry 2(32), 6561-6573 (2014).

Borras A. et al.; Synthesis of Supported Single-Crystalline Organic Nanowires by Physical Vapor Deposition. Chem. Mater. 20, 7371–7373 (2008).

Borras A. et al., One-Step Dry Method for the Synthesis of Supported Single-Crystalline Organic Nanowires Formed by π-Conjugated Molecules. Langmuir 26(8), 5763–5771 (2010).

Briseno A. L. et al., Introducing organic nanowire transistors. Materials Today 11(4), 38-47 (2008).

Chen, J. et al.; Highly Conductive and Flexible Paper of 1D Silver-Nanowire-Doped Graphene. ACS Appl. Mater. Interfaces 5, 1408−1413 (2013).

Hu, L. et al.; Highly conductive paper for energy-storage devices. PNAS 106, 21490-21494 (2009).

Hu, L. et al.; Metal nanogrids, nanowires, and nanofibers for transparent electrodes. MRS Bulletin 36, 760-766 (2011).

Jang, H. J. et al.; Fabrication of Metallic Nanomesh: Pt Nano-Mesh as a Proof of Concept for Stretchable and Transparent Electrodes. Chem. Mater. 25, 3535−3538 (2013).

Kim, J. et al.; Catalytic, Conductive, and Transparent Platinum Nanofiber Webs for FTO-Free Dye-Sensitized Solar Cells. ACS Appl. Mater. Interfaces 5, 3176−3181 (2013).

Kuang, D. B. et al.; High-Efficiency and Stable Mesoscopic Dye-Sensitized Solar Cells Based on a High Molar Extinction Coefficient Ruthenium Sensitizer and Nonvolatile Electrolyte. Adv. Mater., 2007, 19, 1133–1137.

Kubo, W. Photocurrent-Determining Processes in Quasi-Solid-State Dye-Sensitized Solar Cells Using Ionic Gel Electrolytes. J. Phys. Chem. B, 2003, 107,4374–4381.

Langley, D. et al.; Flexible transparent conductive materials based on silver nanowire networks: a review. Nanotechnology 24, 452001 (2013).

Layani, M. et al.; Transparent conductors composed of Nanomaterials. Nanoscale 6, 5581 (2014).

Lee, P. et al.; Highly Stretchable and Highly Conductive Metal Electrode by Very Long Metal Nanowire Percolation Network. Adv. Mater. 24, 3326–3332 (2012).

Leontyev, I. N. et al.; Size dependence of the lattice parameters of carbon supported platinum nanoparticles: X-ray diffraction analysis and theoretical considerations. RSC Adv. 4,35959 (2014).

Macias-Montero M. et al.; Following the wetting of one-dimensional photoactive surfaces. Langmuir 28, 15047-15055 (2012)

Macias-Montero M. et al., Vertically Aligned Hybrid Core/Shell Semiconductor Nanowires for Photonics Applications. Advanced Functional Materials 23(48), 5981–5989 (2013).

Mi, J. L. et al.; Pulsed-Flow Near-Critical and Supercritical Synthesis of Carbon-Supported Platinum Nanoparticles and In Situ X‑ray DiffractionStudy of Their Formation and Growth. Chem.Mater. 27, 450−456 (2015).

NIST X-ray Photoelectron Spectroscopy Database. http://srdata.nist.gov/xps/Default.aspx

Zhang, Q.G. et al.; Facile fabrication and optoelectronic properties of platinum octaethylporphyrin microsheets. RSC Adv. 4, 47325-47328 (2014).

Zhu, R. et al.; Fused Silver Nanowires with Metal Oxide Nanoparticles and Organic Polymers for Highly Transparent Conductors. ACS Nano 5, 9877–9882 (2011).

4. 1D core@shell piezoelectric nanogenerators
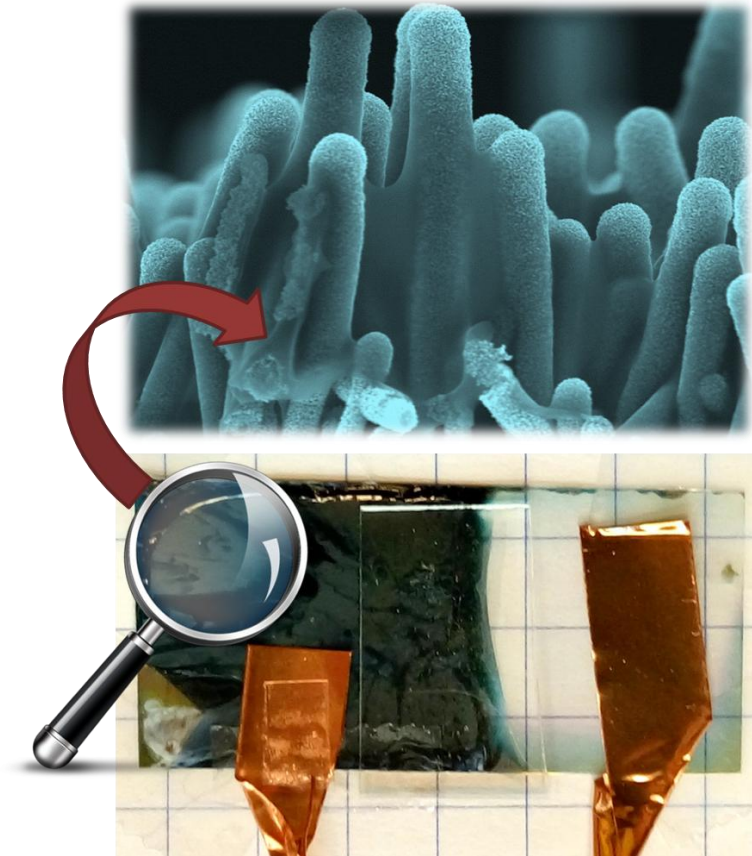
Abstract

Multishell 1D nanogenerators based on crystalline ZnO are fabricated by means of a combination of techniques: magnetron sputtering, OPVD, RPAVD, PECVD and spin coating. The characterization of these systems is performed by a variety of techniques such as SEM, High-resolution TEM, HAADF-STEM and 3D EDX maps. The electrical behavior is evaluated as well and the piezoelectric effect of 1D and thin film systems is investigated.

4.1. Introduction

4.1.1. Description of the piezoelectric effect

A dielectric material is said to be piezoelectric if it can be polarized by both the application of an electric field or mechanical stress. Piezoelectric materials can be divided into two categories, polar (ferroelectrics) and non-polar. The main difference between these groups is that the former presents spontaneous polarization, i.e. they possess a non-zero dipole moment per unit volume. One singular and useful characteristic of the piezoelectric effect is its reversible nature: when a piezoelectric is placed under mechanical stress, an external electric field is generated (direct piezoelectric effect), and if subjected to an external electric field, mechanical strain appears on the material (inverse or converse piezoelectric effect).

When a piezoelectric is physically deformed, it undergoes a forced charge shifting and unbalance process, and depending on certain parameters like the dielectric capacity and crystal structure (orientation and symmetry*), charge separation may happen at the surface leading to the establishment of an electric field across the material boundary.

The relationship between induced charges per unit area (Polarization) and the applied stress is usually considered to be linear and reversible within certain limits, and may be mathematically expressed as $d = P/\sigma$, where P is the polarization vector, σ the stress tensor and d is the so-called piezoelectric coefficient which is a measure of the piezoelectricity of a given material. The full electromechanical behavior of a piezoelectric is given by the coupled equations:

$$S = sT + d^t E$$

$$D = dT + \varepsilon E$$

Where s is the compliance, ε the permittivity, d the piezoelectric coefficient and d its matrix-transpose (converse piezoelectric effect). This constitutive matrix equations define the way in which a material´s strain (S), stress (T), charge-density displacement (D) and electric field (E) interact [Leprince-Wang Y., John Wiley & Sons 2015][Dakua I., Nanomater. Nanotechnol. 2013].

ZnO is an increasingly popular piezoelectric material, mainly because unlike other regular piezoelectrics like PZT, it can be easily and cheaply produced by a wide variety of techniques and it does not represent a threat for human health or the environment []. Furthermore, while PZT has a much larger piezoelectric coefficient compared to several other piezoelectrics, ZnO has the highest piezoelectric tensor among tetrahedrally bonded semiconductors, which is of utmost importance in that technological applications requiring large electromechanical coupling [Lee J., Phys. Chem. Chem. Phys. 2015].

The most stable and common crystal structure of ZnO is hexagonal wurtzite, which belongs to the space group P63mc and lacks an inversion center, a condition that is necessary, but not sufficient, for a material to be piezoelectric. Fig.1 shows the crystal structure of ZnO as hexagonal wurtzite.
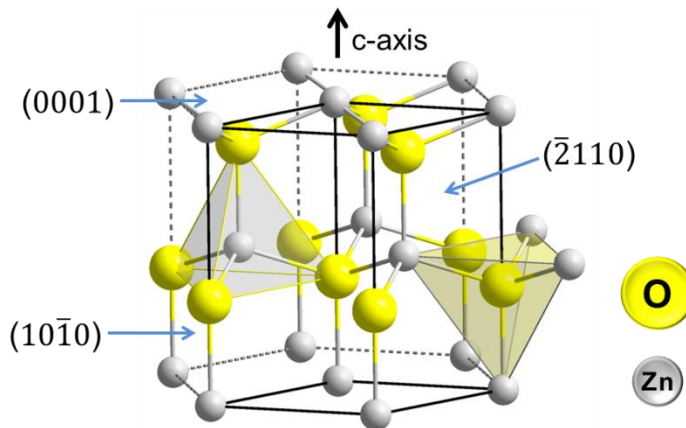
Figure 1. Representation of the crystal structure of ZnO as hexagonal wurtzite. Adapted from [Zinc oxide, Wikipedia].

It can be observed in Fig. 1 that positively charged Zn ions are located in one plane, (0001), alternating with negatively charged O planes, (0001). In contrast to these polar planes, lateral ones such as (1010) and (2110) are non-polar planes. This leads to an intrinsic polarization along the so-called c-axis*, which combined with the absence of central symmetry of the hexagonal wurtzite structure originates the piezoelectric characteristics of ZnO.

One of the fundamental parameters associated to a piezoelectric material, and hence to a nanogenerator, is the piezopotential. The origin of this potential can be better

* As mentioned below, the **net** polarization of an unstrained ZnO crystal is zero.

understood looking at Fig. 2: when a crystal of ZnO wurtzite is in an unstrained state, the charge center of the cations and ions in the structure coincide with each other leading to a null **net** polarization. However, when subjected to mechanical stress, such as compression along the c-axis, the structure is deformed shifting the charge-center of the ions and thus giving rise to an electric dipole and net surface polarization. As long as the strain is maintained and due to the fact that ions are fixed (cannot move freely to compensate this effect), the piezoelectric field and potential are preserved.
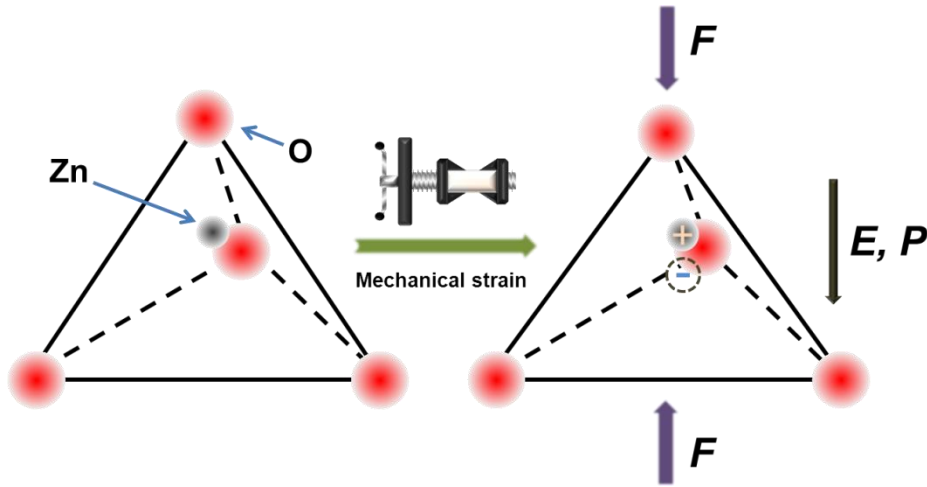
Figure 2. Scheme of the atomic origin of the piezopotential in ZnO showing the effect of dynamic strain onto a ZnO wurtzite tetrahedral.

To build a functional piezoelectric device it is necessary to at least incorporate the following elements: the piezoelectric material, metal contacts to collect the generated current, and a support.

The electrical contact between semiconductor and a conductor can be of two types: Ohmic and Schottky. If the current-voltage characteristic (I-V curve) of the junction is linear, then the contact is ohmic. In this case, electron transport is symmetric at either forward or reversal bias due to a lack of potential barrier at the metal/semiconductor interface. In contrast, when a potential barrier is present at the interface, the metal-semiconductor junction presents a rectifying behavior, making the device a Schottky diode. The Schottky-Mott rule helps to predict the kind of contact it will be form when joining a metal and a semiconductor together:

$$\varphi_{sb} = \varphi_m - \chi_s$$

φ_M is the work function of the metal, while χ_s is the electron affinity of the semiconductor. φ_{sb} represents the Schottky barrier height and its sign determines approximately the type of contact. If $\varphi_{sb} < 0$, then the contact may be ohmic, otherwise it may be Schottky ($\varphi_{sb} > 0$).

It is generally considered that a piezoelectric nanodevice must be constituted of at least one rectifying Schottky contact in order for these devices to operate correctly because such a junction acts as a switch for unidirectional current output [Wang Z. L., Science 2006][Shao Z., Physica E 2010]. However, the generation of piezoelectric potential has been demonstrated in ohmic-like contacts, but the piezoelectric response turned out to be noticeably weaker [Comjani F. F., Appl. Phys. Lett. 2014].

A lot of effort has been made to reduce the size of electronic or electromechanical devices, giving rise to unprecedented levels of energy efficiency and miniaturization of individual components which in turn opens up the possibility for the fabrication and implementation of fully functional highly-integrated systems [Manz A., Pure Appl. Chem. 2001][]. This has led to the development of portable or even wearable and wireless electronics, sensors or more complex and versatile Lab on a chip for chemical and biochemical analysis, microreactors, biomedical applications such as real-time health monitoring and life support, nanorobotics and micro-electromechanical systems, etc. [Cavallini A., Ieee Sens. J. 2015][Dagdeviren C, PNAS 2014][deMello A. J., Nature 2006][Hu Y., Adv. Mater. 011]. Even though the progress made in microelectronics and nanotechnology has helped to greatly cut down the power consumption of these devices, they still require a small amount of energy to fulfill their function. This energy can be effectively provided by a piezoelectric generator integrated in the same chip, exploiting the movement of animals, humans, plants (due to wind), blood, muscles, organs, wind, water currents, sound, etc. and thus creating self-powered devices [Wang Z. L., Georgia I. T. 2011]. Among several nanostrucutres fabricated and studied, ZnO NWs seem to stand out due to superior piezoelectric properties, in addition to an effective increase of surface area compared to thin film ZnO; The piezoelectric coefficient of bulk (0001) ZnO value was reported to be 9.93 pm/V, while that of NWs has been found to be two orders of magnitude higher, 1200 pm/V [Wang Z. L. Adv. Func. Mater. 2008][Yang R., Nano Lett. 2009][Wang Z. L., Sci. Am. 2008][Lee J., Phys.Chem.Chem.Phys. 2015].

Long and more or less ordered ZnO NWs are usually synthetized by solution-phase (template-free) procedures, such as electrochemical deposition and hydrothermal methods [Elias J., J. Electroanal. Chem. 2008][Tian J., Nanotechnology 2011][Baruah

S., Sci. Technol. Adv. Mater. 2009][Hu H., Mater. Chem Phys. 2007]. High quality ZnO NWs have also been extensively produced by dry methods governed by VLS or VS mechanisms like thermal chemical deposition (CVD), metal-organic chemical vapor deposition (MOCVD), pulse-laser-deposition (PLD), etc. [Singh D. P., Sci. Adv. Mater. 2010]. In line with Chapter 2, here unique ZnO NWs have been grown by PECVD using ONWs as a template.

In chapter 3, the fabrication of platinum in thin film from a metalorganic precursor by RPAVD was addressed. RPAVD technique is essential to obtain much more conformal samples compared to standard platinum evaporation when nonplanar substrates are used. The optical and electrical properties of the electrodes were explored towards their implementation in piezoelectricity and counter electrodes in DSSCs. In this chapter, the focus will be made in the fabrication of 1D Pt nanowires, using as a basis the acquired knowledge by the group in the field of production of Co NPs in CoPc NWs (Fig. 3).
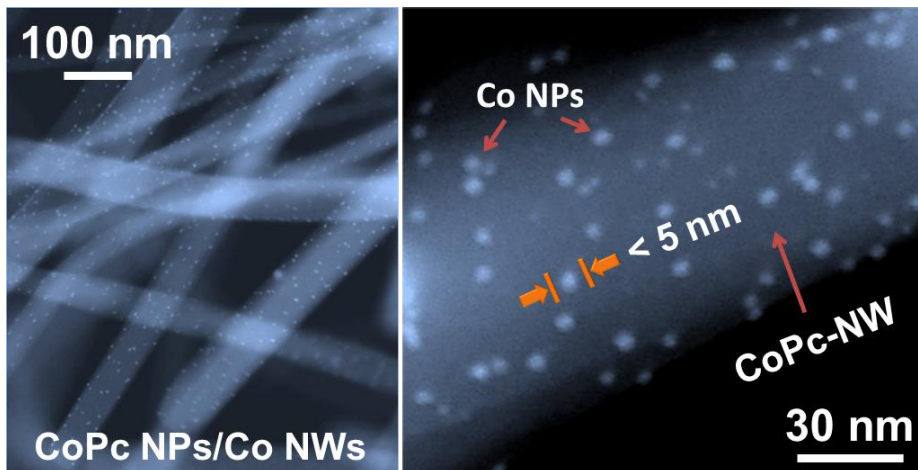
Figure 3. STEM micrograph of hybrid (a) Co NPs/CoPc NWs fprmed by oxygen plasma treatment and (b) magnified view of a decorated NW. [Alcaire M., Nanoscale 2011].

In order to increase the power output (per cm^2) of the piezoelectric devices, the detailed fabrication of 1D nanogenerators is presented, placing special emphasis in their characterization. Finally, it is shown how to successfully transfer the entire fabrication process from rigid to flexible substrates.

4.2. Objectives

The objectives pursued in this chapter are:

❖ Development of the methodology for the preparation of 1D core@shell nanostructures compromising noble metals (Au and Pt) and ZnO. This includes the fabrication of full working devices on flexible substrates and infiltration of Poly(methyl methacrylate) for improved mechanical stability.

❖ Electrical and structural characterization of the 1D nanostructures in order to gain knowledge about the influence of the different fabrication stages.

4.3. Methodology

4.3.1. Lateral Piezo

PET coated with 130 nm ITO from Sigma-Aldrich was cut into pieces of 4.5 cm x 1 cm. HCl 8% was used to remove the ITO layer from half of the substrate surface and then rinsed with milli-Q water and absolute ethanol. By applying a mask with aluminum foil, gold was deposited on the clean side of the substrates leaving a gap of 2 mm between the ITO and Au. Next, masks were applied onto a portion of the Au and ITO contacts and 400 nm of ZnO was deposited by PECVD.

4.3.2. 1D piezoelectric Pt@ZnO@Au

The whole production procedure of 1D piezoelectrics can be splitted in two distinct stages:

1) Fabrication of metallic nanowires.

a) Deposition of metallic seeds by magnetron sputtering at 0.1 mbar employing and Emitech K550 sputter coater equipped with a gold target; 12.5 mA 15 s yielded adequate Au NPs both in density and size.

b) Growth of Pc NWs by OPVD. The base pressure of the chamber was ~ 10^{-5}-10^{-6} mbar, the total pressure during deposition was 0.02 mbar of Ar, deposition rate of 0.45 Å/s (measured by QCM), substrates temperature of 200-210 ºC and a sample-to-evaporator distance of 6.5 cm. The thickness of the primary NWs was set to 3 kÅ (QCM). The evaporation source consisted of point source evaporator deposition source model LTE 01 supplied by Kurt J. Lesker.

The formation of nanotrees consisted in the growth of secondary and tertiary Pc NWs by successive soft plasma etching and depositions. After the primary NWs were

grown, a first oxygen plasma treatment of 40 minutes at 300 W was applied. The total pressure was 0.02 mbar, the substrates were held at room temperature and the sample-to-plasma distance was set to 10 cm. The oxidative treatment was followed by the growth of secondary NWs just as in (b) but reducing the deposition time to 1 kÅ. The etching-NW growth cycle was repeated, reducing the time of plasma treatment to 20 minutes.

c) Formation of a PtOEP shell by RPAVD. Identical conditions to the NWs growth except that the deposition rate was reduced to 0.3 Å/s and a plasma is switched on during the entire process. An ECR microwave plasma source working at 2.45 GHz and 300 W of power output was used for the conformal deposition of PtOEP. The sample-to-plasma distance was fixed at 10 cm and the substrates were kept at room temperature.

d) The oxidation of the shell was performed in the same chamber following the deposition of the PtOEP shell. Treatment time, substrates temperature, sample-to-plasma distance and plasma power were adjusted to control the degree of oxidation of the shell. Gas pressure was maintained at 0.02 mbar using a gas composition of 80% O_2 and 20% Ar. To obtain Pt NPs, 30 minutes at room temperature and 300 W of power were sufficient, while for the complete formation of Pt NWs treatment time ranged from 100 minutes for 1 kÅ thick PtOEP shells to 280 minutes for 3 kÅ shells. Moreover, the substrates had to be heated to 180 ºC and the plasma power increased to 600W to obtain Pt NWs. It must be stressed that the substrates were always facing down towards de evaporator and not directly bombarded by the plasma.

The obtained Pt NWs were then reduced by soft H_2 treatment in a furnace at 135 ºC, with a constant flux of 5% H_2/Ar during 2 hours.

A scheme with the different steps involved in the first stage is presented in Figure 4 (excluding the reductive treatment).
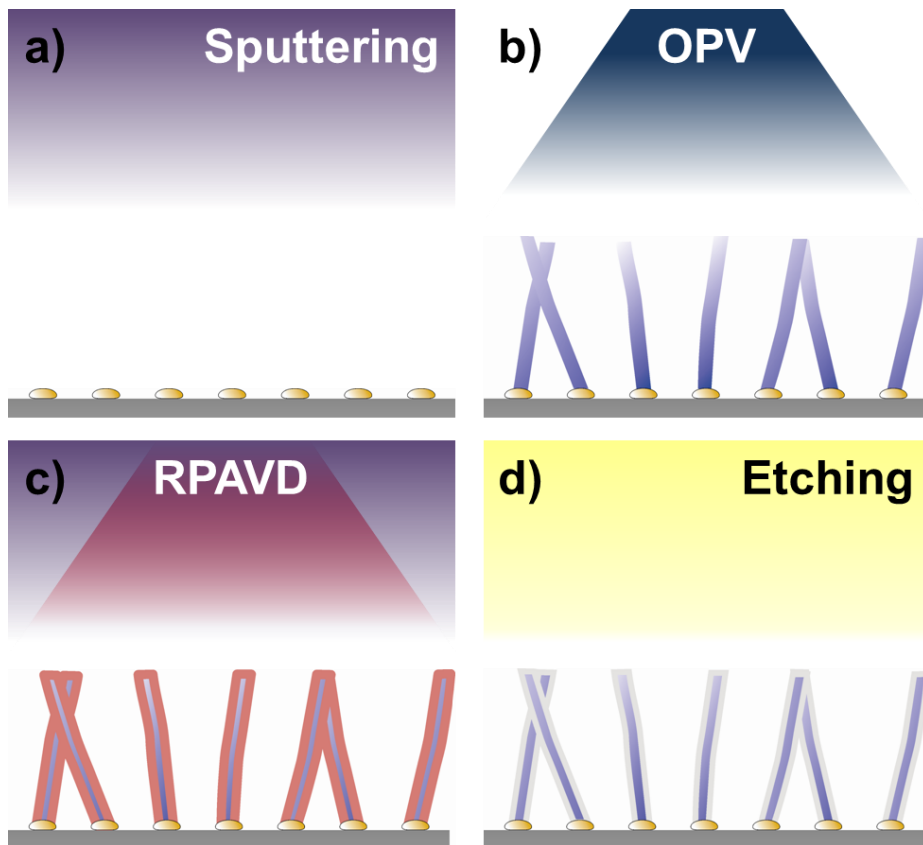
Figure 4. a) Deposition of Au or Ag seeds by magnetron sputtering. b) Growth of the NWs. c) Formation of the shell by RPAVD. d) Formation of the metallic shell by plasma oxidation.

2) Formation of the ZnO shell and deposition of the outer electrode.

a) The deposition of a conformal ZnO is achieved by means of PECVD at room temperature. $ZnEt_2$, purchased at Sigma-Aldrich and used as delivered, is employed as ZnO precursor and dozed into the chamber by means of a mass flow controller. The plasma is generated with a 2.45 GHz microwave ECR source working in a down-stream configuration. At 8 sccm of ZnO flux and 400 W of plasma power, the deposition rate was around 4.2 nm measured by SEM. Oxygen was utilized as reactive gas.

b)-d) Deposition of Au by magnetron sputtering (same equipment as in 1(a)). Different conditions were swept in order to achieve full Au shell percolation: 12.5mA 15s (a),

25mA 30s (b) and 25mA 45s (c). Figure 5 schematizes the distinct gold coverage stages.
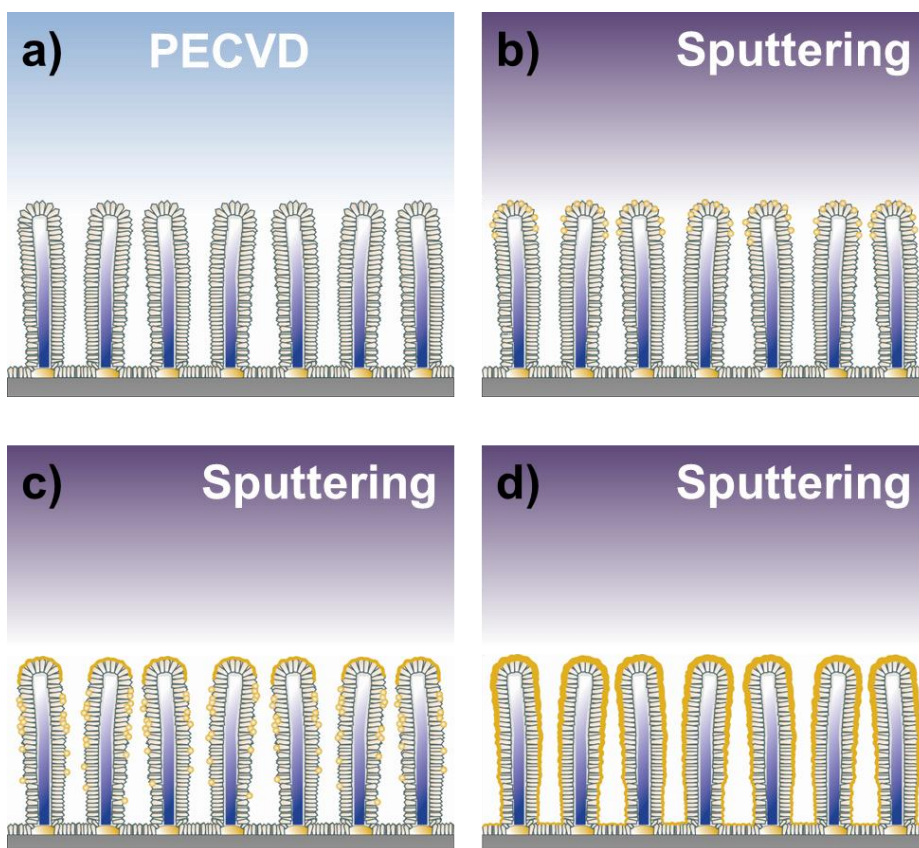
Figure 5. a) Growth of the ZnO shell by PECVD. Deposition of gold by magnetron sputtering: b) 12.5mA 15s, c) 25mA 30s, and d) 25mA 45s.

Polished n-type Si(100) purchased from Topsil and fused silica from Sico Technology GmbH were used in each preparation for characterization.

4.3.3. Characterization of the nanostructures

Characterization: SEM micrographs were acquired in a Hitachi S4800 working at 2 kV, while STEM (SEM) micrographs were acquired in a Hitachi S5200 working at 30 kV. The samples were dispersed onto Holey carbon films on Cu or Ni grids from Agar scientific for TEM characterization. HAADF STEM and HRTEM were carried out with both FEI Tecnai Orisis TEM/STEM 80-200 and FEI Tecnai G2F30 S-Twin STEM microscope also working at 200 kV. EDX maps were acquired with the former microscope working at 200 kV. Post-processing of EDX data was performed with the

open source Hyperspy software: hyperspy.org. EDX raw data was post-processed in to order to obtain more accurate compositional maps of the multishell system. The main reason for this post-treatment is an inadequate description of the Pt spatial distribution arising mainly from the fact that the microscope software mixes the signal of Pt Lα with Au Lα and it does not allow selection of other emission lines or any further spectral refinement, which is critical in this nanosized structures

The crystal structure was analyzed by XRD in a Siemens D5000 spectrometer operated in the θ - 2 θ configuration and using the Cu Kα (1.5418 Å) radiation as an excitation source.

UV-Vis analysis of the samples was done in a Cary 100 spectrometer from Varian.

Electrical characterization of the piezoelectric devices

I-V curves were recorded with a 2635A system sourcemeter working in sweep voltage mode.

4.4. Results and discussion

4.4.1. 1D nanogenerators

Gold seeds produced by magnetron sputtering provided the required roughness for the growth of NWs in several substrates. This deposition technique is highly convenient for the fast, easy and controllable production of gold nanoparticles which act as nucleation sites. Using 12.5mA and 15s, irregular NPS with a mean area of 135.5 nm^2 and a maximum distribution between 50-100 nm_2 were obtained (histogram in Fig. 6). By increasing the deposition time and current, Au thin films were readily obtained (Fig. 6). Furthermore, at 25mA 30s percolation was already achieved.
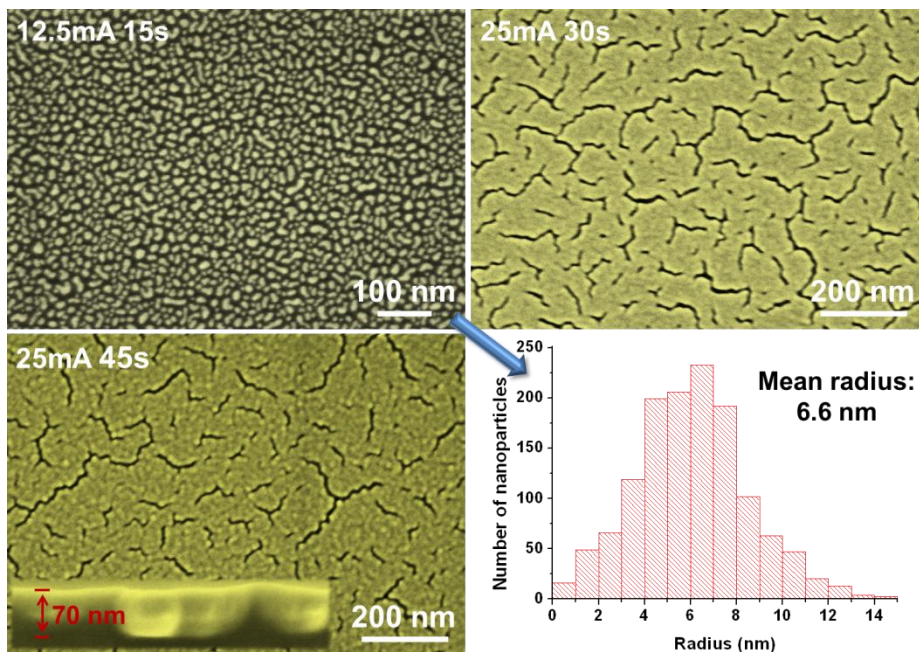
Figure 6. SEM images of several Au sputtering depositions. An histogram is attached for the Au NPs case and a cross section for the thickest film is shown as inset.

Metal-free phthalocyanine (H$_2$Pc) was chosen as the construction block molecule of the NWs due to its relatively high sublimation temperature (above 280 ºC) and lack of central metal cation, which may lead to an undesired source of contamination. By optimizing the deposition conditions, a high-density of H$_2$Pc NWs was readily attained (Fig. 7).
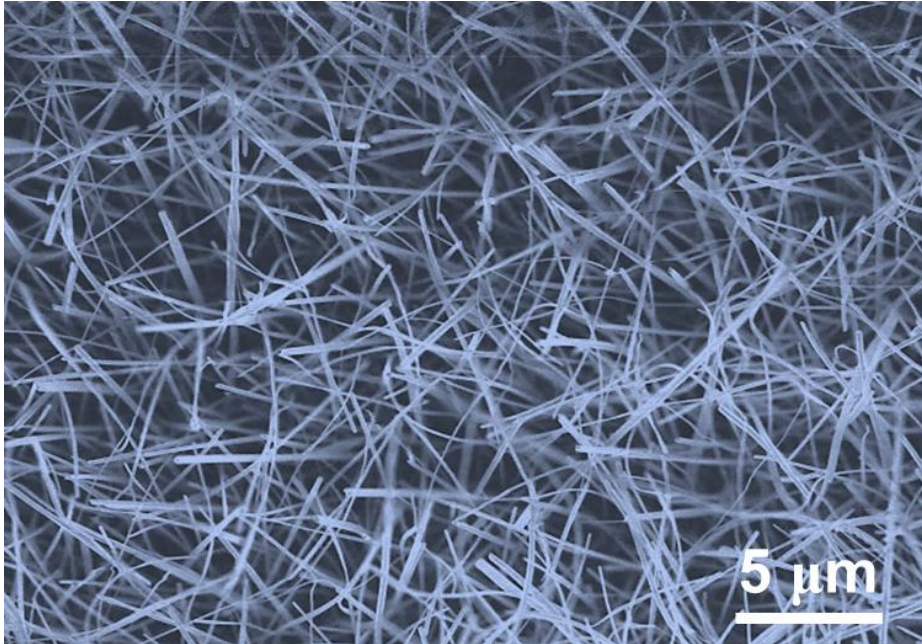
Figure 7. SEM image of approximately 10-12 μm long Pc NWs (3 kÅ in QCM).

Nanotrees of H_2Pc were also fabricated to study the feasibility of 1-D hyperbranched nanogenereators production and its potential implementation in piezoelectric devices; In theory, an increase in the active surface area of such a device should boost its power output. Figure 8 reveals the high degree of interconnection between NWs 10 μm close that can be achieved with the nanotree concept.
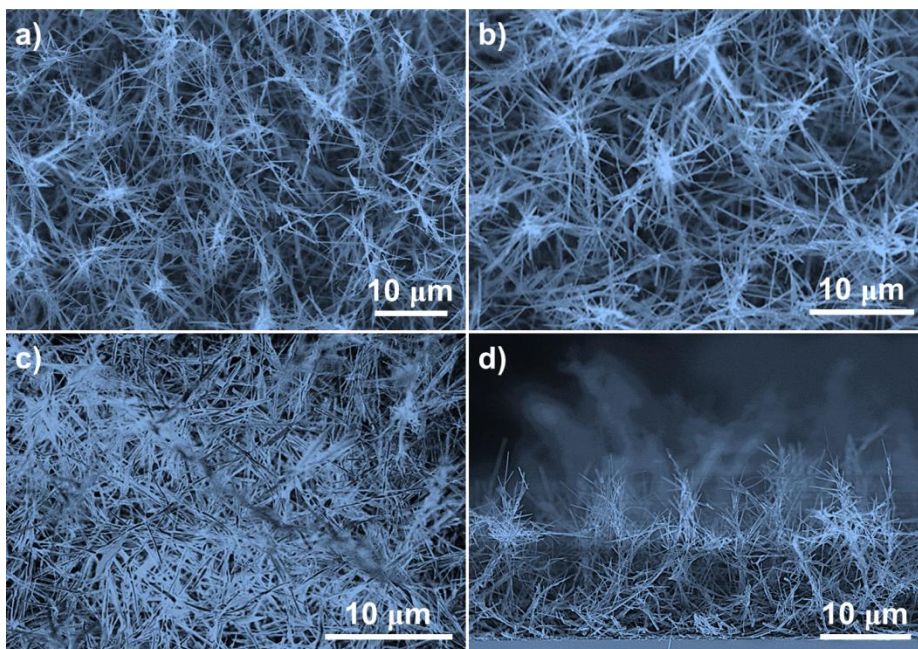
Figure 8. SEM images in normal view of of Pc nanotrees ramified twice, 3 kÅ+1 kÅ+1 kÅ. Low-magnification image of the nanotrees (a), and further magnified views (b-c). SEM cross section of the nanotrees (d).

In order to fabricate nanotrees, it is mandatory to generate enough surface roughness on the primary NWs for the growth of secondary and subsequent NWs. This roughness can be effectively produced by soft plasma etching after the initial growth of NWs and may be regulated by varying the plasma parameters and substrate temperature. In Fig. 9 a roughened H_2Pc NW is shown, this is the appearance of a NW after 40 minutes of oxidative plasma treatment.
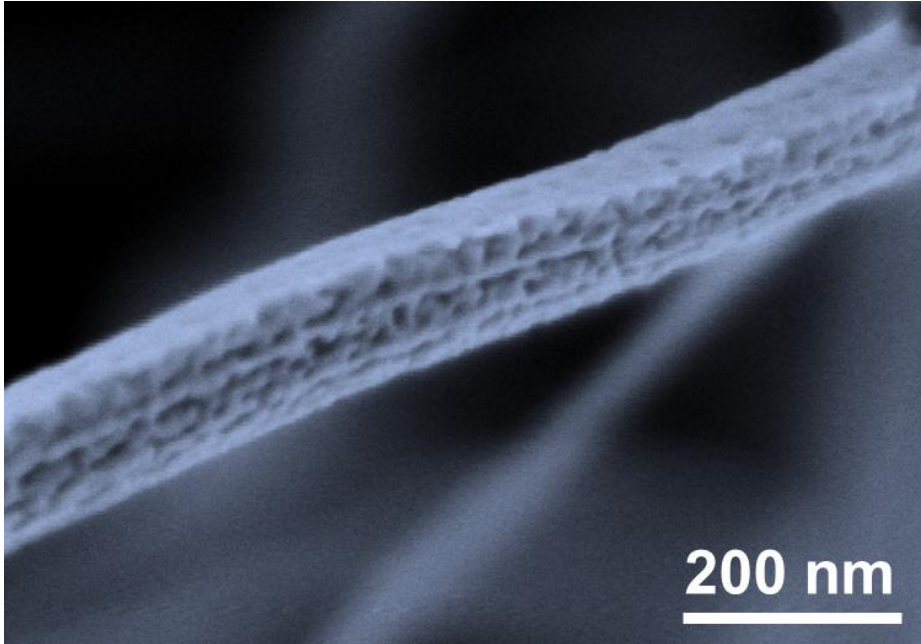
Figure 9. SEM image of a H$_2$Pc NW subjected to an oxidative plasma treatment.

The next step was the production of a PtOEP shell by RPAVD as conformal as possible, aiming to the fabrication of platinum nanoelectrodes. As observed in Fig. 10 a), the achieved PtOEP shells are rounded at the tip and cylindrical along the along the axis, losing the squared shape of the Pc core. In addition, in Fig. 11 b) the homogeneity and conformality of the PtOEP shell is highly noticeable, even for such considerably small shell thicknesses (0.6 kÅ in QCM). Quite remarkably, the thickness of the shell only varies two nanometers in 1.5 μm of NW length.
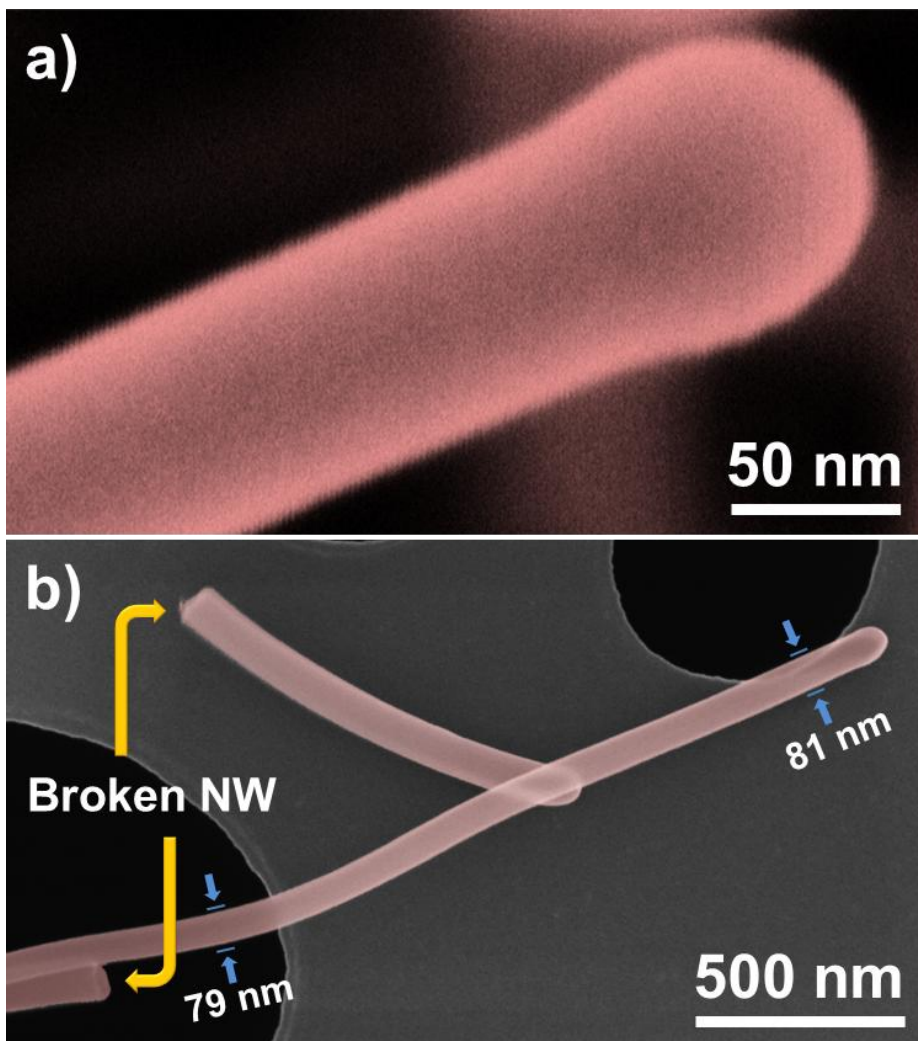
Figure 11. (a) SEM image of PtOEP shell of thickness 0.6 kÅ and (b) STEM micrograph of two Pc@PtOEP NWs.

The thickness of the shell can be estimated from SEM working in BSE-STEM mode. For a 0.6 kÅ (QCM) PtOEP deposit, a shell of approximately 30 nm is formed (Fig. 12).
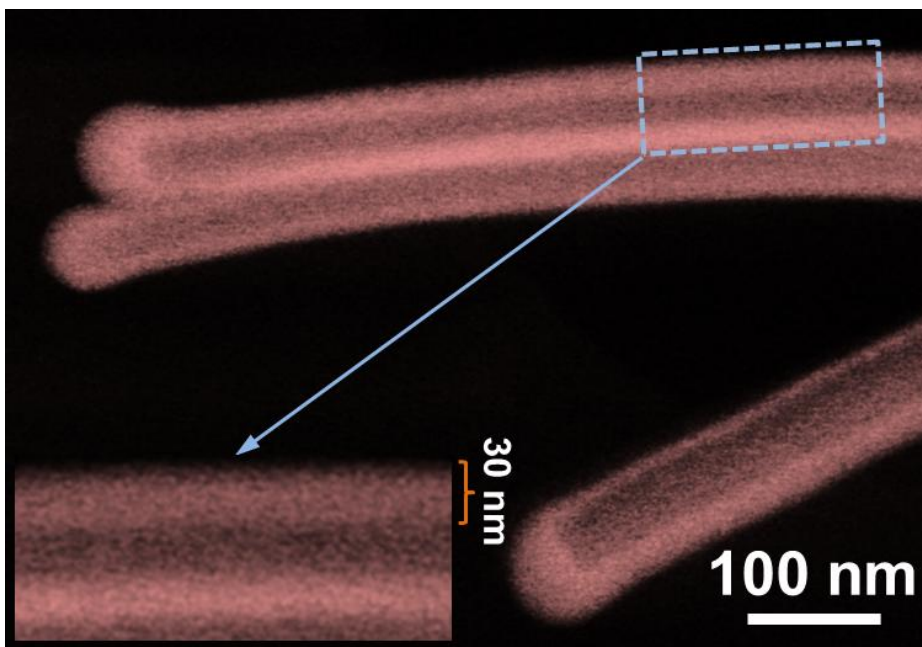
Figure 12. BSE (STEM) image of H_2Pc NWs@PtOEP. The difference in contrast arising from different organic materials, H_2Pc and PtOEP molecules, allows for the estimation of organic shell thicknesses.

Using the information from Chapter 3, the thickness of the resulting Pt shell after plasma etching may be approximately calculated. For a 30 nm wall thickness, a Pt layer of 16 nm would be expected, which is certainly quite thin and might not be enough to support a NW. With this in mind, thicker PtOEP were produced and treated.

An increase in the shell thickness did not produce any morphological change in the nanostructure, just a substantial gain in diameter as observed in Figure 13 for the 3 kÅ case.
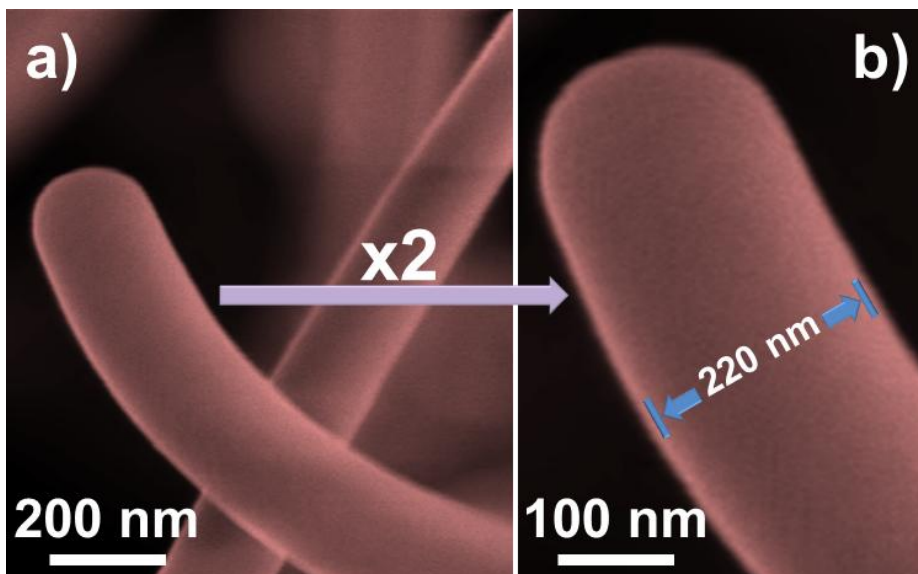
Figure 13. SEM image of 3 kÅ PtOEP shell (a) and a NW tip magnified by a factor of two (b).

Depending on the thickness of the PtOEP layer and the conditions of the plasma etching, the post-treatment may be adjusted to be soft enough so as to yield unpercolated NPs. With only 30 minutes of treatment at room temperature, highly decorated NWs were achieved as observed in Figure 14. High-resolution TEM reveals the crystalline nature of the Pt NPs formed (inset in Fig. 14 a)), whilst carefully focusing the core, the original Pc molecular planes are still observable (Fig. 14 b)), proving that this soft etching condition has not compromised the integrity of the inner core. The Pt NPs had a mean diameter of 1.54 ± 0.019 nm according to Figure 14 b) and (c). It seems that much more NPs and smaller ones were formed in (c), but it is only due to the scale difference (the NW in (c) is much thicker). The NPs in (a) had a mean diameter of 2.18 ± 0.41 nm, noticeable bigger than in (b) and (c), but this might be explained by the smaller diameter of the NW, which adjacent NPs to joint more easily into smaller ones, or the High-resolution acquisition which can cause severe beam damage and NP growth.
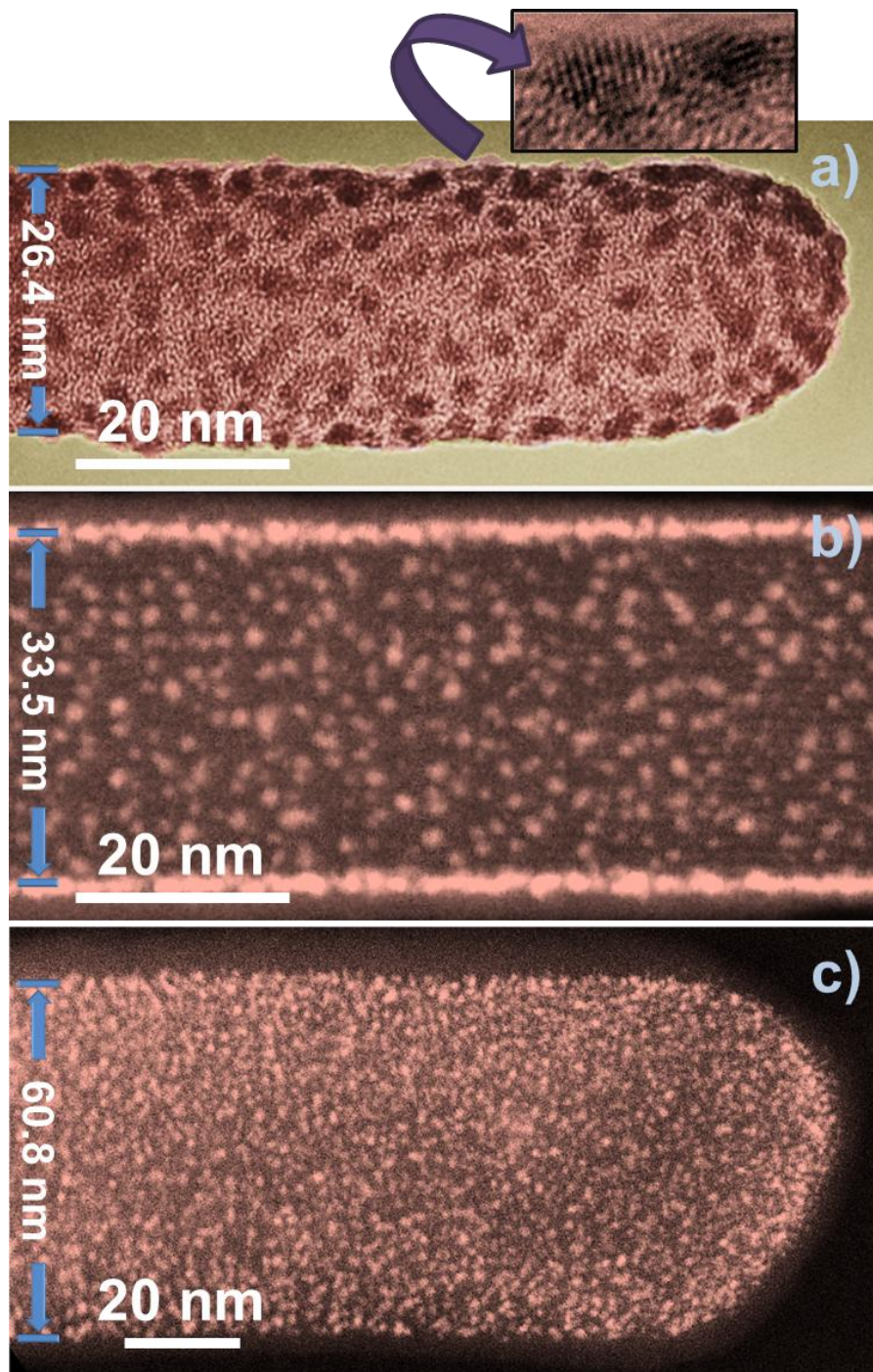
Figure 14. High-resolution TEM (a) and HAADF STEM (b-c) images of a PtOEP NW@PtOEP/Pt NPs. The thickness of the shell was 0.6 kÅ and the plasma treatment was limited to 30 minutes.

When the etching process was prolonged to 60 minutes, i.e. twice the time for generating NPs, a semi-percolated Pt grid was obtained (Fig. 15).
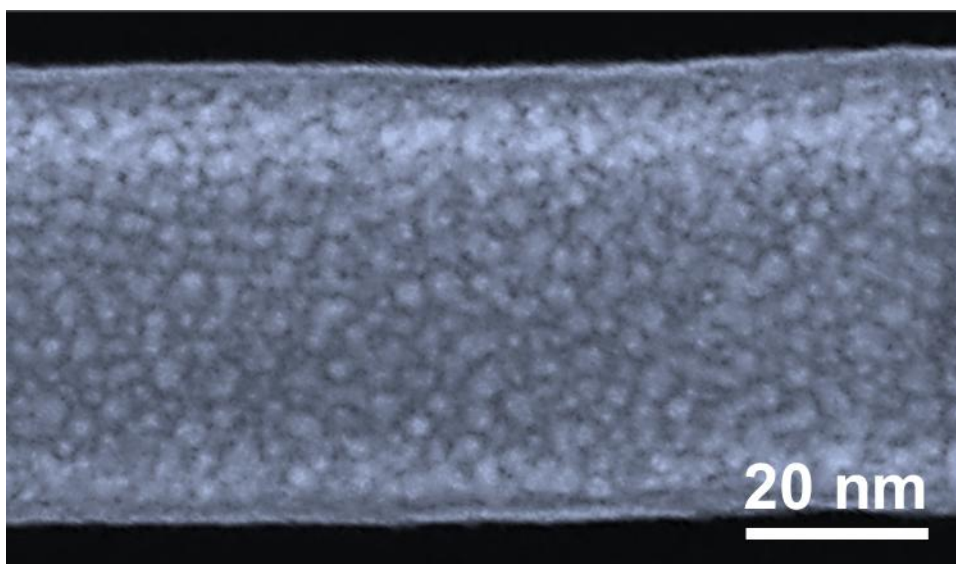

Figure 15. HAADF STEM image of a 0.6 kÅ PtOEP shell after undergoing 60 minutes of treatment.

Highly porous and percolated platinum shells were also obtained by increasing the thickness of the PtOEP shell and by implementing a more severe etching treatment. 1 kÅ Pt NWs (Fig. 16 a)) presented a great number of interconnections already, although the many of the NWs did not survive the treatment or just broke off due to their tiny diameter. In contrast, 3 kÅ NWs have withstood the whole process and their density and diameter certainly were much higher (Fig. 16 b)).
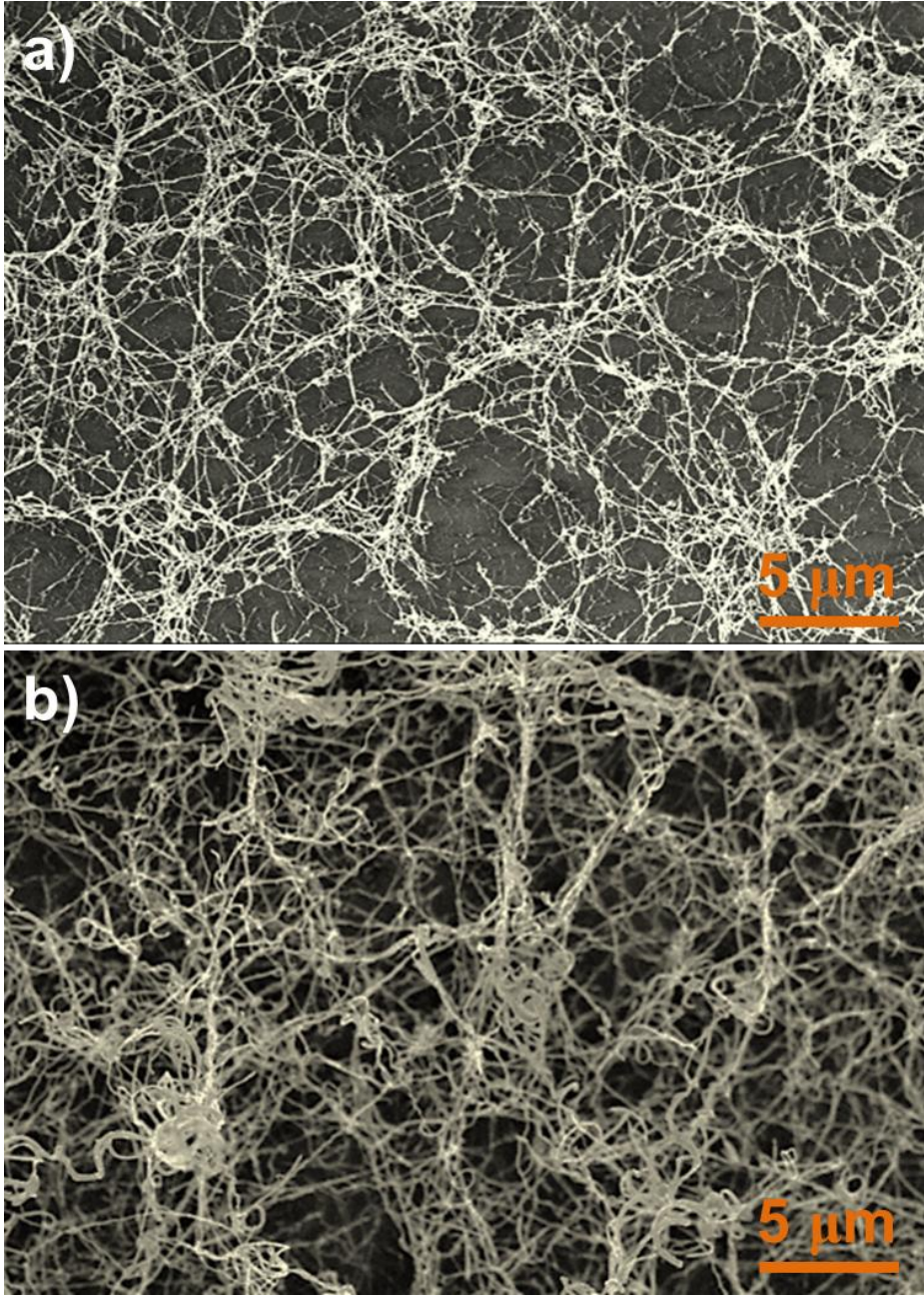
Figure 16. SEM images of highly interconnected Pt nanotrees, (a) 1 kÅ and (b) 3 kÅ.
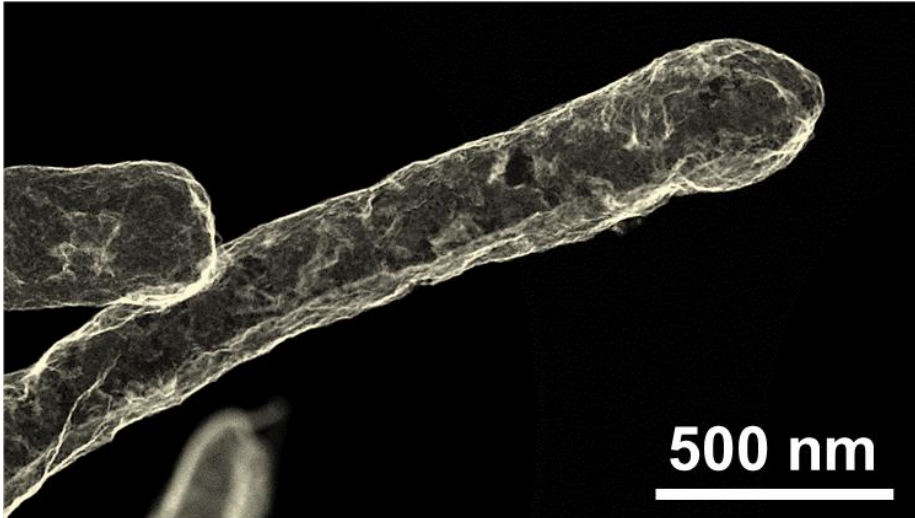
Figure 17. HAADF STEM image of a Pt NW, obtained from a 3 kÅ PtOEP shell.

It must be mentioned that the formation of nanoparticles was carried out at relatively low plasma power (300 W), room temperature and short treatment time (1 hour maximum), while the formation of a platinum layer requires higher power (600 W), temperature (180-190 ºC) and treatment time.

The obtained platinum nanoparticles or shell are highly crystalline as confirmed by HRTEM in Figure 18.
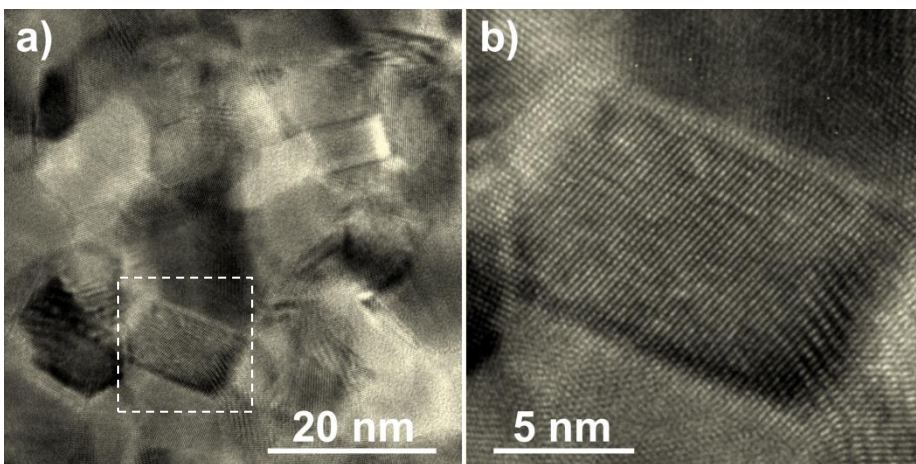
Figure 18. a) HRTEM image of a 3 kÅ Pt NW. b) Magnified view of the region selected in (a).

In the case of the magnified zone in Fig 19 b), two families of planes can be perfectly distinguished: (111) and (200), shown in Fig. ppt.
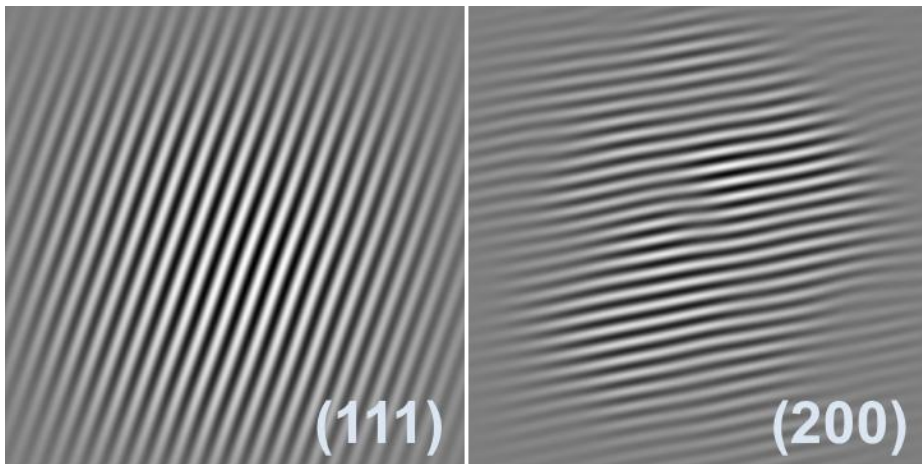

Figure 19. Families of planes present in Figure 18 b) extracted from the digital diffractogram pattern.

The formation of the metallic core was followed by the deposition of a conformal ZnO shell by PECVD. The fabrication and characteristics of this particular shell was already discussed in Chapter 2, but it is worth mentioning that by this particular method polycrystalline ZnO was obtained at room temperature (Fig. 20 b)).
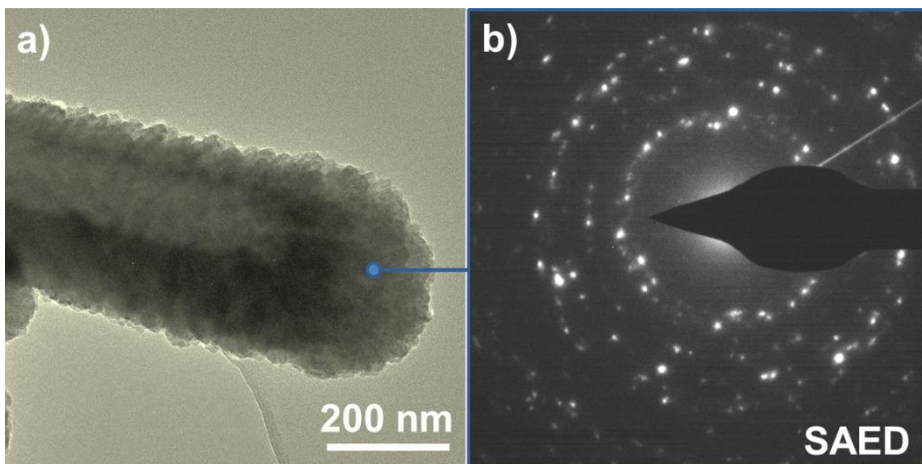

Figure 20. (a) Bright field TEM image of a Pt@ZnO NW. (b) SAED of the ZnO shell.

In order to build a complete 1-D piezoelectric nanogenerator, it is mandatory to deposit a second electrode. In this case, gold was chosen for the outer electrode because it possesses an adequate work function when platinum is employed in the piezoelectric

device. Magnetron sputtering was used with that purpose in mind, mainly due to the speed of the technique (see Methodology) and ability to control quite precisely the quantity of deposited gold. Three different gold coverage stages were explored and are presented in Figure 21. For 12.5 mA 15 s, gold nanoparticles mainly localized on the top of the nanowire were obtained (Fig. 21 a) and b)), whereas by increasing the deposition time and current to 25 mA 30 s, a thin porous layer of gold was formed around the ZnO (Fig. gld (c) and (d)). Finally, with 25 mA 45 s a rather continuous gold shell was achieved (Fig. 21 e) and f)).
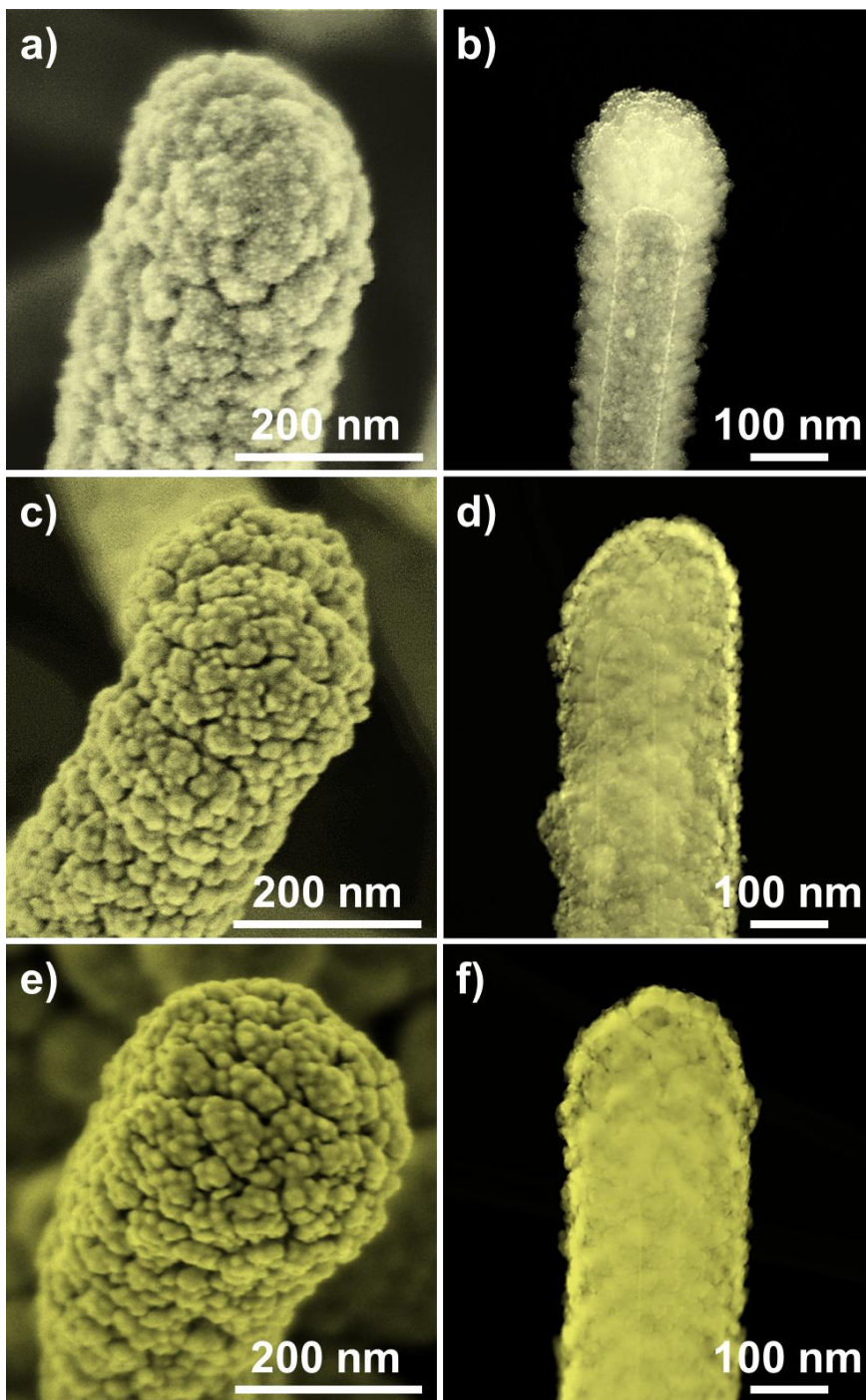
Figure 21. SEM (left) and HAADF STEM (right) images of Pt@ZnO@Au NWs with increasing quantities of gold deposited by magnetron sputtering: (a) and (b) 12.5 mA 15 s, (c) and (d) 25 mA 30 s, (e) and (f) 25 mA 45 s.

To verify the extent of gold percolation observed by microscopy techniques, EDX was carried out on single nanowires. By performing the methods PCA/ICA on EDX data using Hyperspy software, it was possible to obtain the distribution of Au on single 1-D nanostructures, as shown in Figure 22. It is clear that with 25 mA 45 s of gold deposition, full percolation has been accomplished and the resulting gold layer turned out to be greatly conformal, which was not expected from a technique such as magnetron sputtering. Hyperspy was required to correctly isolate the signals of platinum and gold, otherwise identical for ordinary software at this scale.
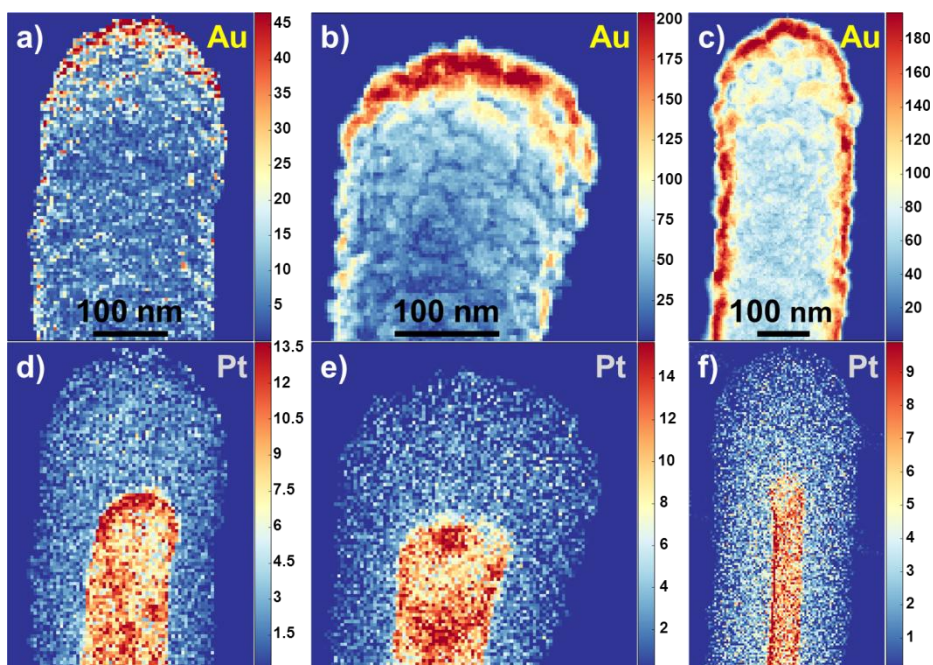

Figure 22. (Up) Intensity of Au Mα signal for deposition condition: a) 12.5mA 15s, b) 25mA 30s and c) 25A 45s. (Down) Intensity of Pt Mα signal.

UV-Vis.Near IR properties

Depending on the thickness of the platinum shell, transparent to semi-transparent samples were obtained. Unlike common transparent conductors such as ITO and FTO, Pt NWs do no present strong absorptions in the UV and near IR regions. Moreover, the transmittance of these systems is relatively smooth in a wide range of wavelengths (Fig. 23).
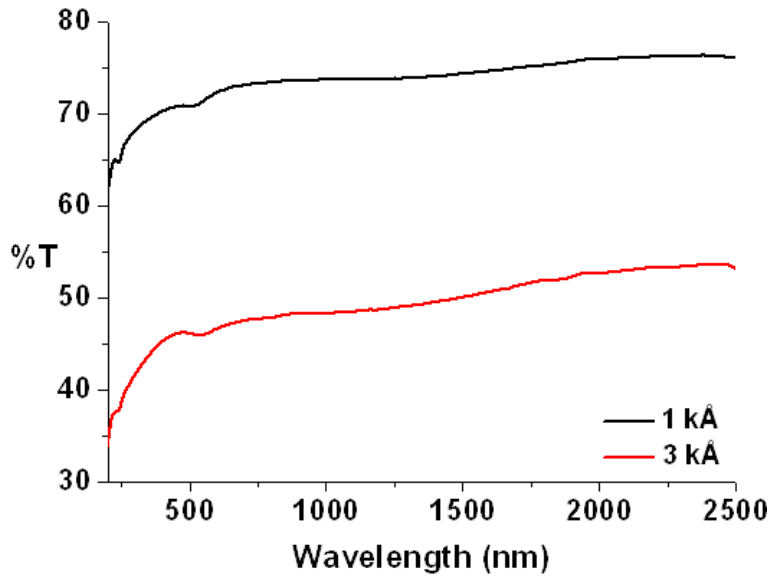
Figure 23. Transmittance UV-Vis-near IR spectra for Pt NWs samples of different thickness.

Electrical properties

Four-point probe resistivity measurements were performed on samples fabricated on fused silica so as to check the degree of interconnection in nanotrees. In Fig. 24 a) it can be seen again that a soft H_2 treatment dramatically decreases the resisitivity of the samples, while increasing the thickness of the PtOEP layer by three, and hence multiplying platinum content by three, produces a reduction of the resisitivy by a factor of 2.4. Despite 297.6 Ωcm seems somewhat high, it must be stressed that the electrical conduction in this samples is due to numerous contact points between NWs, which are not fused one to the other. Moreover, the resistivity of these systems does not scale linearly with length (see below). If lateral conduction is that good, vertical conduction (along the axis of the NWs) is expected to be excellent.
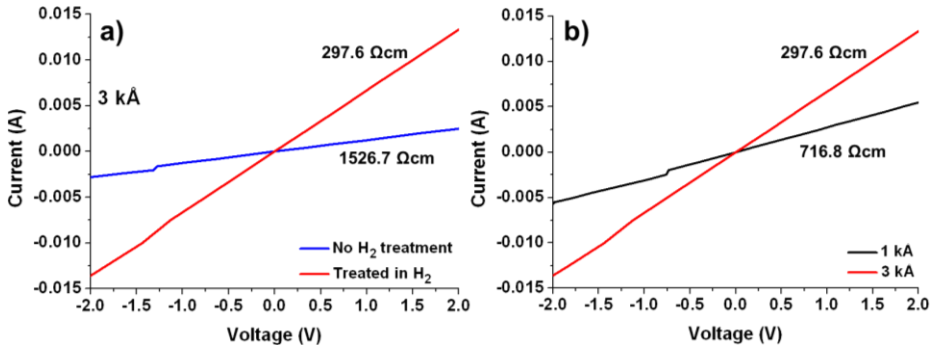
Figure 24. Four-point probe I-V graphs of a) as prepared and H_2 treated 3 kÅ Pt NWs and b) 1 and 3 kÅ H_2 treated NWs.

Electrical measurements were also performed on commercial Pt electrodes separated by 10 μm (interdigitated) and 100 μm. Table 1 gathers the resistance values subtracted from the correpsonding I-V curves.

Table 1. Resistivity of Pt NWs for different thicknesses and treatments. The values are in Ohms per length informed (10 μm or 100 μm).

Treatment	1 kÅ		2 kÅ		3 kÅ	
	10 μm	100 μm	10 μm	100 μm	10 μm	100 μm
As prepared	2.67E9	4.04E10	-	-	-	-
Plasma etching	52	127	86	91	70.8	100.4
Annealing in H_2	51.7	118.8	60	125.5	54.9	102.8

The untreated samples presented an immense resistance, as expected for an organic semiconductor such as PtOEP. Once fully oxidized, Pt NWs showed relatively low resistance values with no obvious trend at these scales, but it can be concluded that at such low lengths the amount of Pt does not change the electrical properties dramatically, the H_2 treatment seems effective only in the 10 μm case but not for 100 µm and that the resistance does not increase linearly with length. This last observation is further corroborated when comparing these values against the ones obtained for 1 cm.

In order to study the conductive and piezoelectric capabilities of PECVD ZnO, a first prototype was fabricated. 400 nm ZnO was laterally sandwiched between a gold and ITO electrodes (Fig. 25) and its I-V curve was recorded. Note that the measurements

correspond to lateral electrical characteristics of ZnO films, i.e. perpendicular to the ZnO crystals axis.
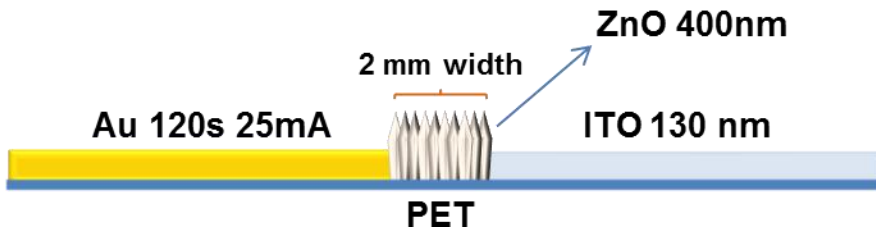

Figure 25. Scheme of the lateral piezoelectric device

The corresponding I-V curve for the lateral piezo can be observed in Fig. For the applied range of voltage, currents turned out to be significantly low, but the values were reasonable considering the fact that charge was passing through 2 mm of material and that in the lateral configuration employed electrons were forced to hop from crystal to crystal (inset in Fig. 26). Of outmost importance is that despite having chosen one of the toughest experimental conditions for the measurement, ZnO exhibited conductivity and rectifying behavior, validating the prepared PECVD ZnO.
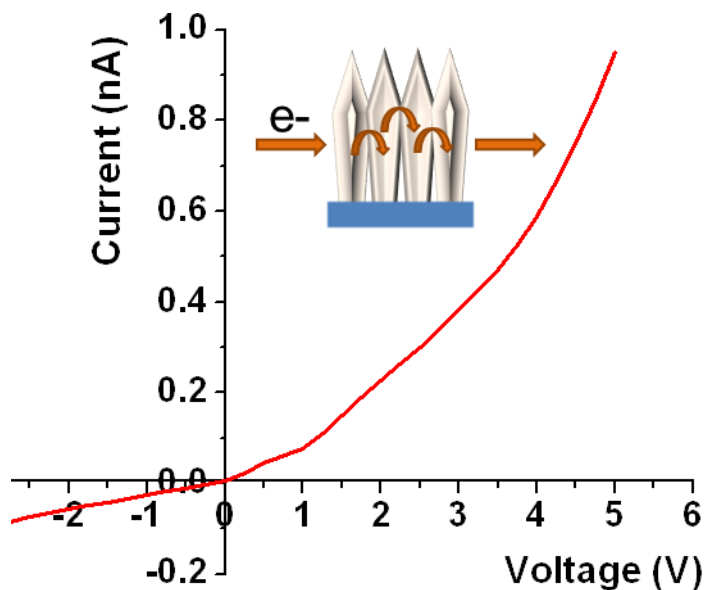

Figure 26. I-V curve of 400 nm ZnO measured in a lateral configuration. The inset represents the hopping mechanism responsible of conduction.

The next step was to check the presence of piezoelectric effect in the as prepared polycrystalline ZnO thin films.

Finally, a full piezoelectric device was fabricated consisting of 4 electrodes as shown in Fig. 27. The idea behind this design was to test in a single device the conductivity between Au-Au and Pt-Pt electrodes and electrical behavior between Au-Pt electrodes.
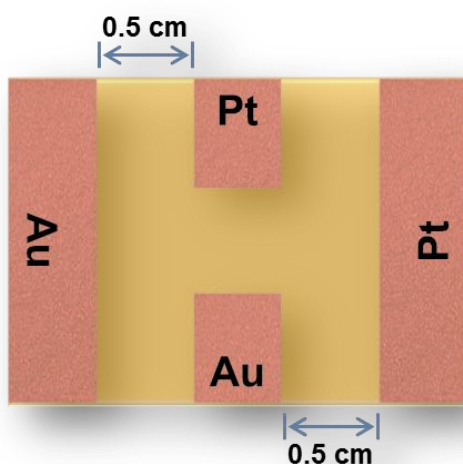

Figure 27. Scheme of the 4-electrode piezoelectric prototype.

SEM images reveal that the nanostructures were not vertical but rather a tangle (Fig. 28). This is mainly due to the formation of the 1D Pt electrodes from nanotrees and the etching of the inner Pc core, making the resulting nanostructures rigid. It does not mean that the inner core and flexibility cannot be preserved, just that the experimental conditions must be more carefully controlled if the integrity of the Pc core wants to be maintained. Furthermore, despite the non-verticality of the nanowires, ZnO has grown with an impressive degree of conformality, Figure 28 (down).
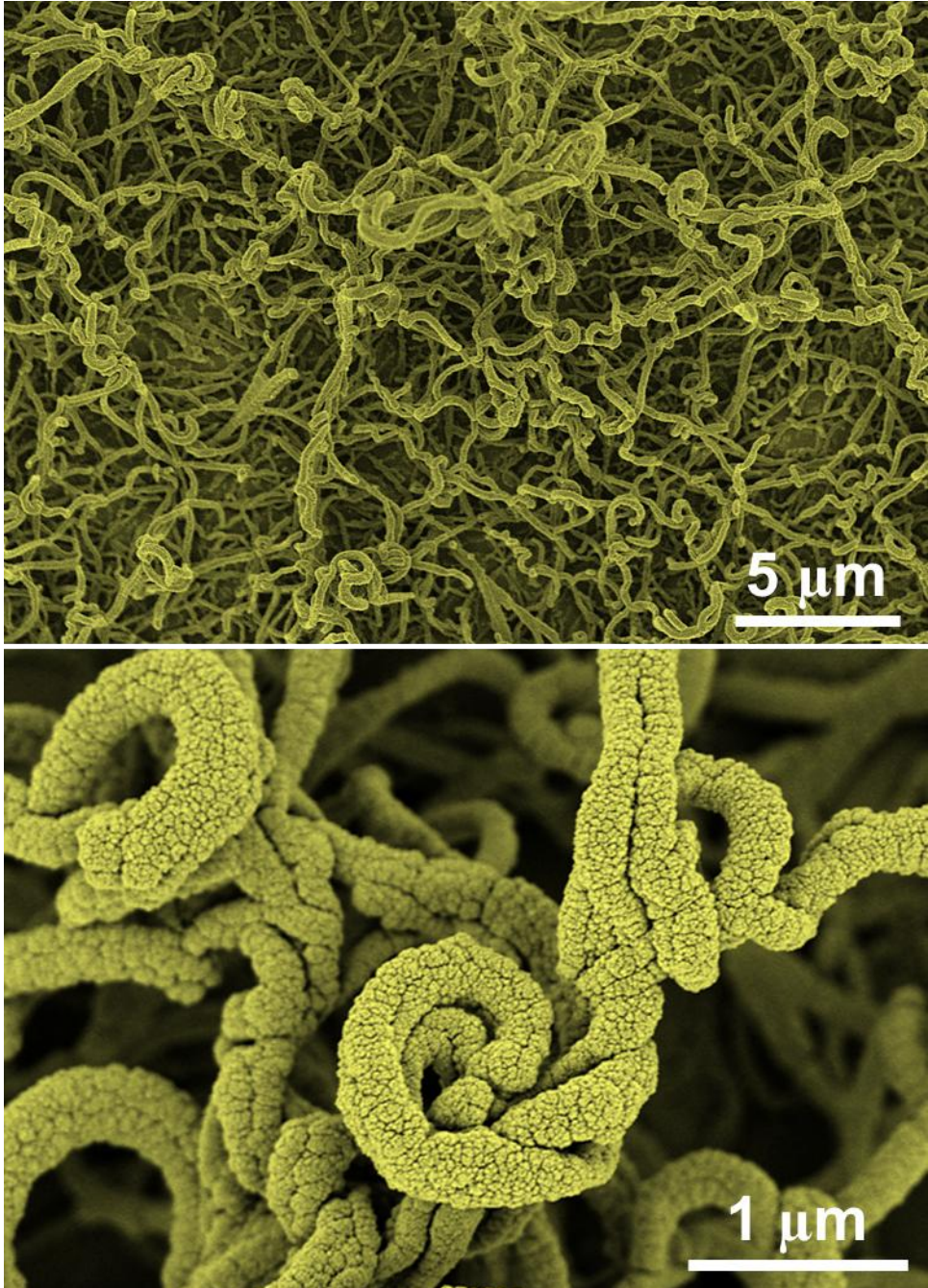
Figure 28. SEM Images of the piezo Pt@ZnO@Au. Formation of a tangle (up) and extreme conformality of ZnO (down).

The I-V curves for the Au-Au, Pt-Pt and Au-ZnO-Pt are presented in Figure 29. At first glance, Pt exhibited the highest conductivity, while Au a noticeable lower conductivity

probably due to the low amount of material deposited. The conduction between Au and Pt did not show any rectifying characteristics and was considerably high, which indicates a short circuit in the device. The high diffusivity of sputtered Au added to a highly porous ZnO, is among the principal responsible for this undesired effect.
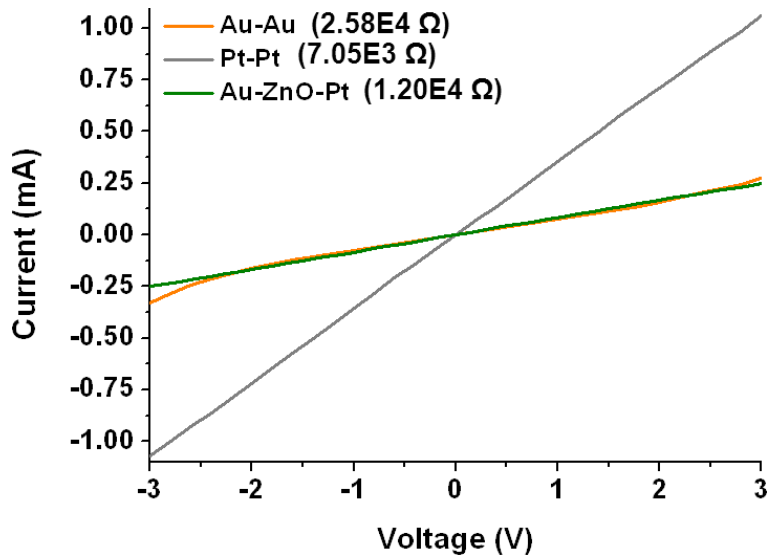

Figure 29. I-V curves for contacts Au-Au, Pt-Pt and Au-ZnO-Pt.

In order to address the issue of short circuits due to gold diffusion, six different devices with increasing complexity were fabricating, beginning with thin film ones until reaching 1D piezoelectrics.

Device I

It comprised a relatively thick ZnO film of 2.4 μm (Fig. 30 a)) deposited on PET coated with ITO. The purpose of such a thick layer of ZnO was to avoid as far as possible any short circuit between the ITO and a copper tape placed on the ZnO. Another piece of copper tape was located at the ITO to ensure a better electrical contact (Fig. 30 b)). As shown in Figure 30 b), the device did present rectifying characteristics, besides, it is a good indication of absence of short circuits.
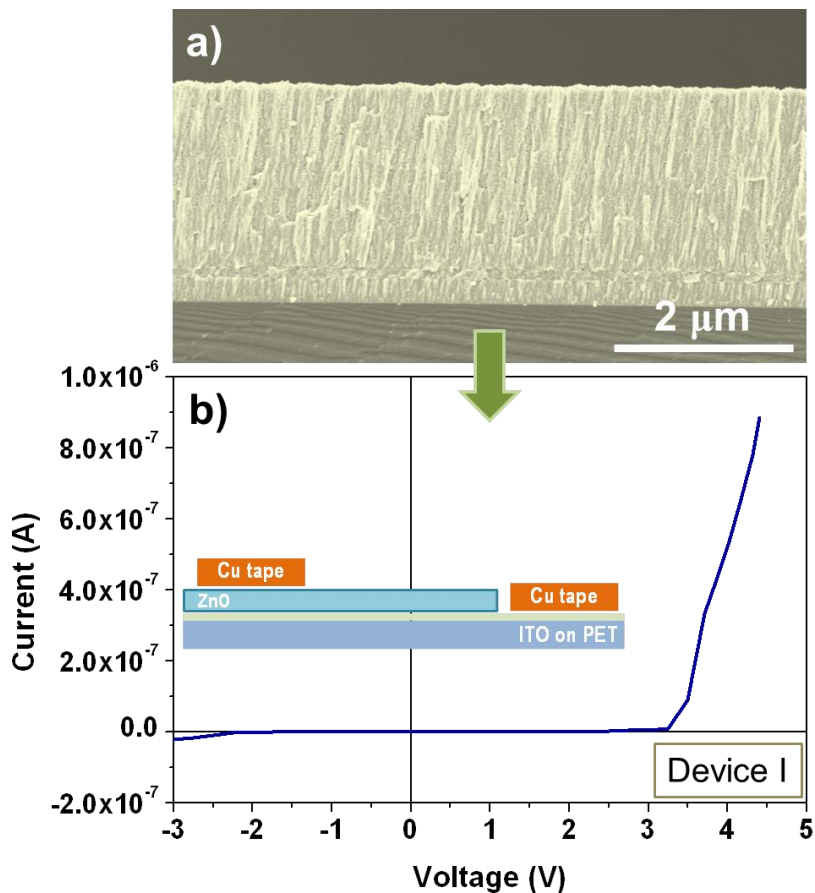
Figure 30. (a) SEM cross section of the ZnO thin film. (b) I-V characteristic measured between the Cu tapes located following the schematic in the inset for a ZnO thin film (2.4 μm) deposited at room temperature on FTO/PET substrates.

The generation of piezoelectricity was verified by placing a slide of PDMS below the device and one on top of the copper contact attached to ZnO, and by exerting intermittent pressure with the index finger on top of the contact. It has been estimated that the maximum pressure was roughly 3 kg/cm^2. It is clear from Figure 31 that the device indeed functioned as a piezoelectric (the spikes correspond to the moment when force was applied).
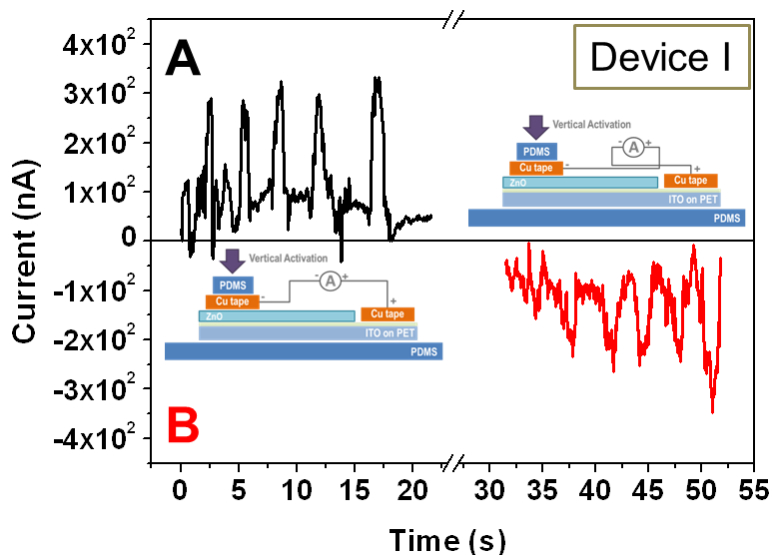
Figure 31. Output current obtained after vertical activation of the device through a PDMS button, situation A. Red line has been obtained by switching the polarity as represented in the schematics, situation B.

To discard that the current response was due to an electrical artifcat arising from the force applied to the electrode, the PDMS section was moved from the copper contact to over the ZnO film (lateral position) and pressure was applied on it. As a result, current peaks were obtained again confirming that the previously observed response was not an artifact. However, by comparing the height of the current peaks in Figures 31 and 32, it may be noticed that in the lateral configuration the peaks got smaller, probably due to the better electrical contact in te vertical configuration. Moreover, a replica peak arose a few seconds after the applied force ceased (Fig. 32 b)), which could possibliy originate from the relaxation of the flexible device.
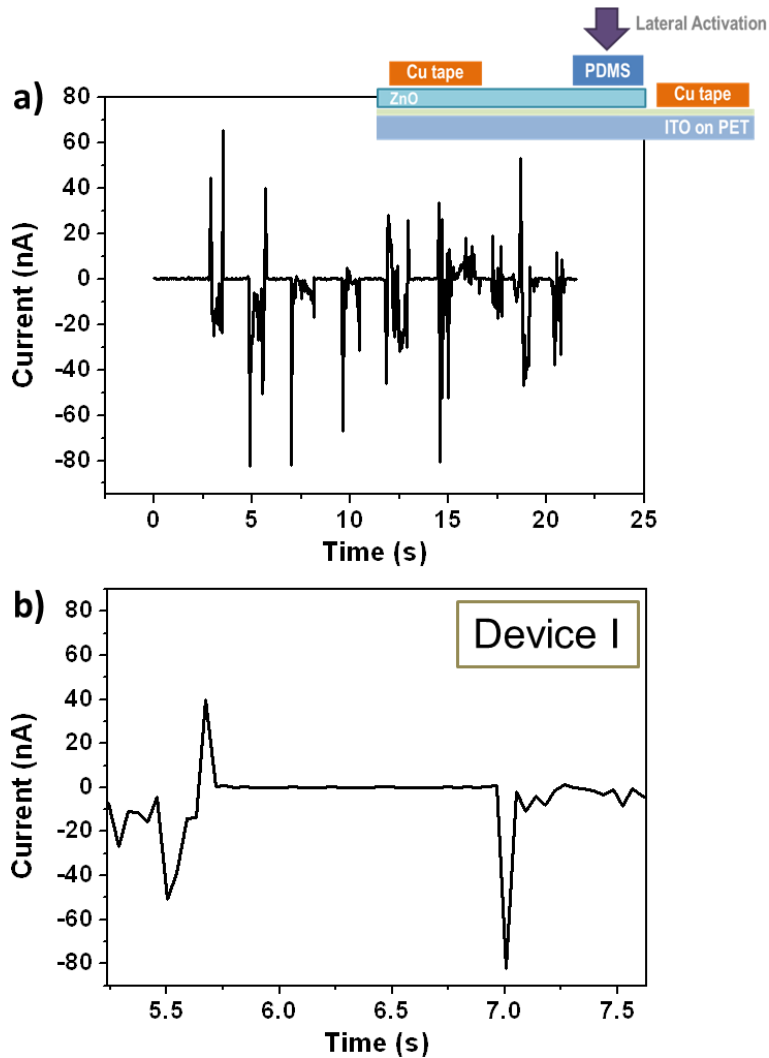
Figure 32. Output current obtained after lateral activation of the device through a PDMS button. Curve in b) is a zoom in showing a detail of the measured signal.

The influence of applied pressure on the piezoelectric response was qualitatively studied by means of a mechanical oscillator which periodically touched the surface of the device generating an electrical response (Fig. 33 (Top)). While no efforts were made to quantify the force exerted by the oscillator on the surface, at least it was possible to observe qualitatively that a higher pressure gave rise to higher currents and ultimately to higher power outputs (Fig. 33 (Bottom)). The replica peaks were again present, but this time they looked much more symmetric with respect to original current response.

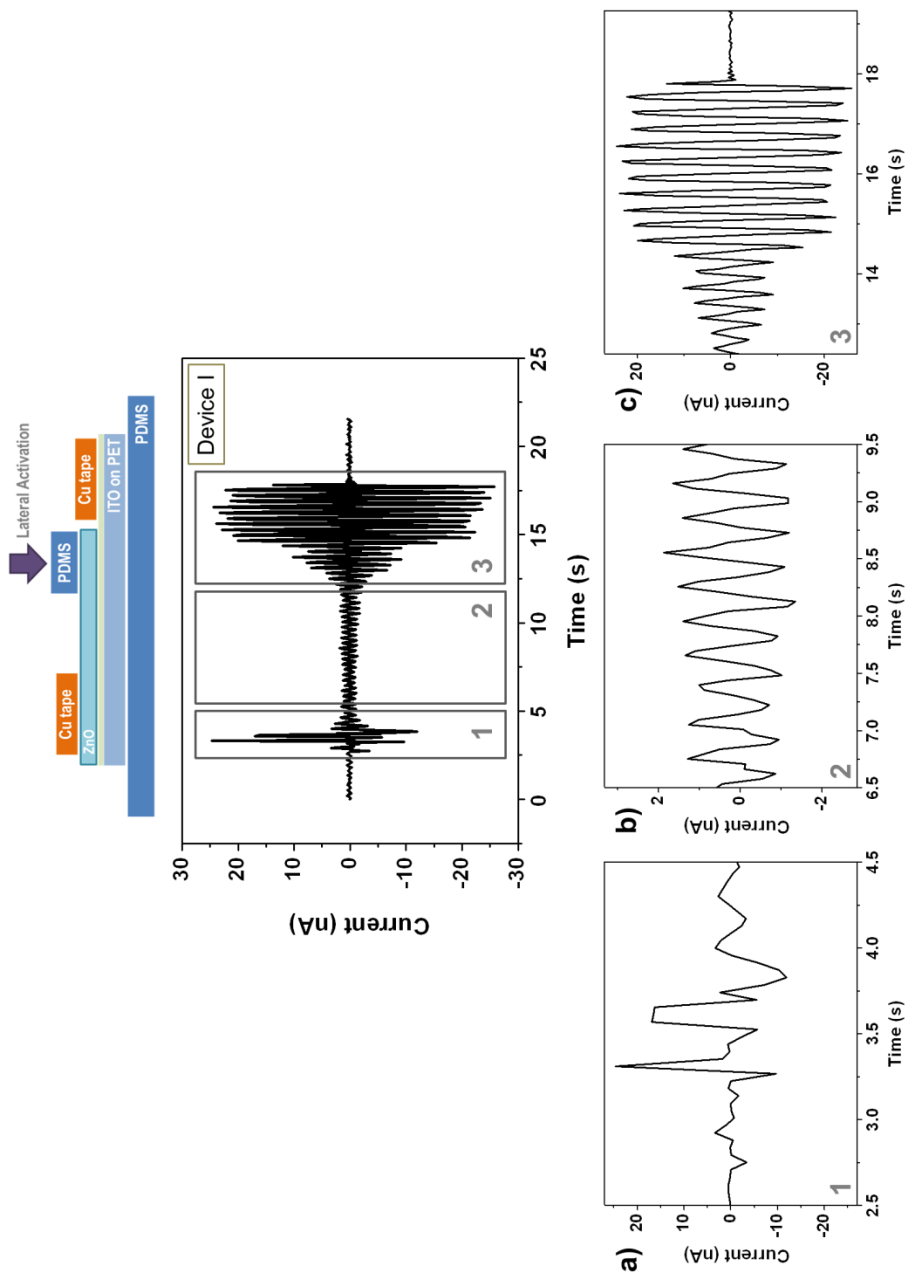**Figure 33**. **Top**. Schematic of the measured device and output current obtained after lateral activation of the device by a mechanical oscilator with constant frequency and different loads. **Bottom**. Zoom in of each of the different zones: a) initial positioning of

the activator; b) output for mild load at ?? Hz; c) increment in load and deactivation of the vibration.

Devices II and III

In a second stage, the thickness of the ZnO layer was reduced to 900 nm (ZnO II) so as to check if the device could still work or if short circuits were evidenced. In the device labeled as II, the configuration was exactly the same as in the device I (inset in Fig. 34 a)), with the PDMS included, whereas in device III the ZnO layer was directly grown on copper tape. A piece of copper tape was used for the top contact and PDMS was also included as in device II (inset in Fig. 34 d)). In both cases the devices were tested in a lateral configuration.

The I-V curves for devices II and III showed rectifying behavior (Fig. 34 a) and d)) with no evidence of short circuits. The I-V curve under a pressure of roughly 3 kg/cm^2 (denoted as load in Fig. 34 a)) demonstrated an increase in current for the same value of voltage as in the stress-free case. The piezoelectric response in both devices was quite similar (Fig. b-c) and e-f)), although a decrease in peak height was observed with respect to device I owing to a considerable thinner ZnO layer.
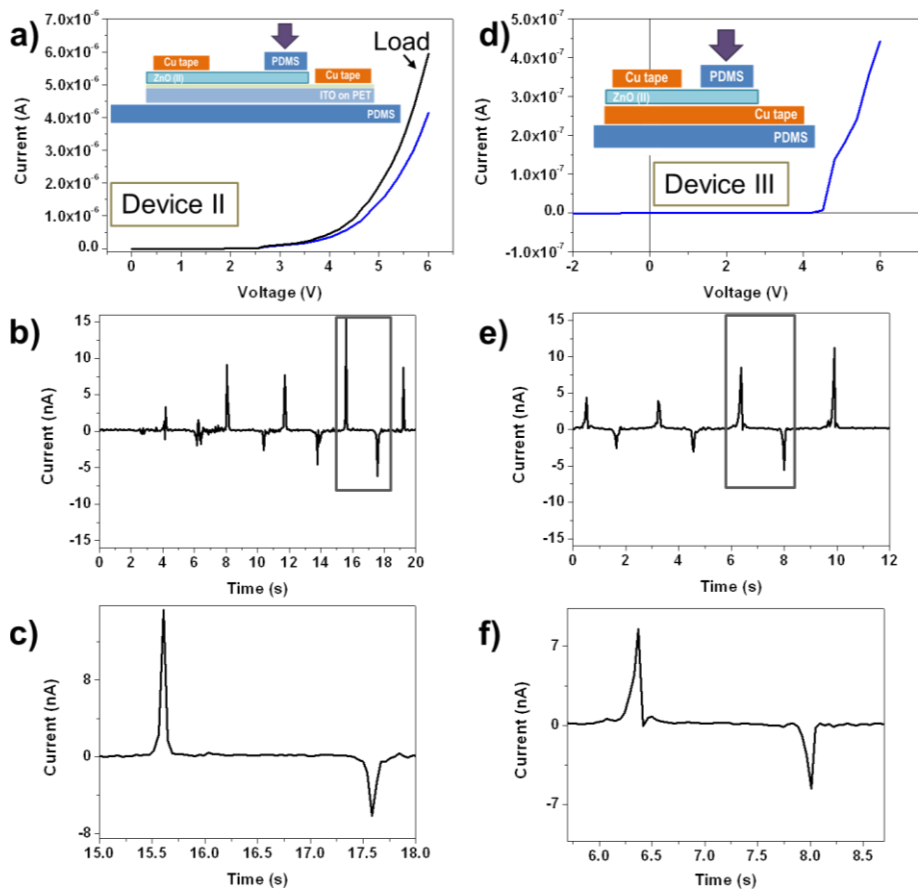
Figure 34. I-V characteristics (a, d) and output current for lateral activation (b, c, e, f) for two different devices as schematized in the inset with a piezo film of 900 nm deposited on ITO/PET (a-c) and on a Cu tape (d-f). The black line in panel a) corresponds to the characteristic acquired for a constant load.

Device IV

A lateral piezo was again fabricated but this time on paper. It consisted of two evaporated contacts, one of Au and the other of Au/Al, on 400 nm ZnO (Fig. 55 b)). Paper is a substrate with a high natural roughness due to the cellulose fibers which made up the material, but the conformallity of the deposition technique allows for the coverage of the very same fibers (inset in Fig. 55 a)). The I-V characteristics of the piezo reveal once more a Schottky contact, just as in the precious devices. Once more, the piezoelectric effect was observed, but this time by pressing, bending or stretching the paper (Fig. 55 e-f)). The highest power output was achieved in pressing mode.
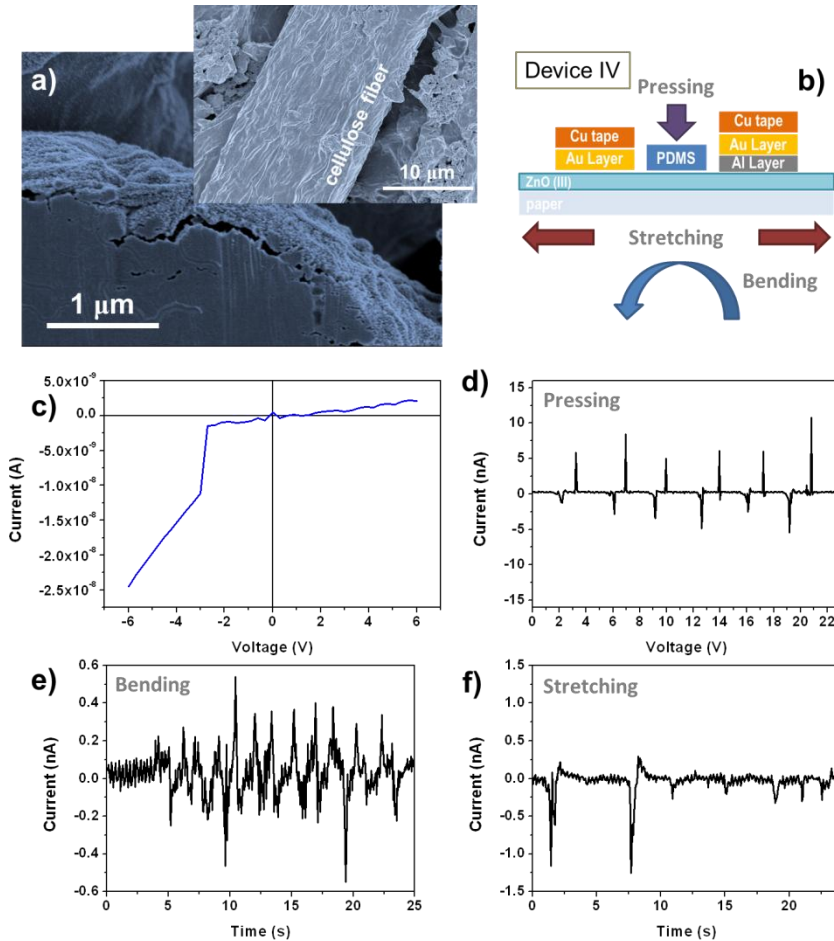
Figure 55. a) SEM micrographs of the ZnO layer (400 nm) deposited on paper; b) Schematic of the mechanical activation and device architecture. Gold and Aluminum layers were deposited by magnetron sputtering and thermal evaporation correspondently on top of the ZnO thin film. c) IV curve showing the Schottky/Ohmic characteristic; d-f) Output current obtained by the different mechanical activation tests (pressing, bending, and stretching) as labeled.

Devices V-VI

The maximum level of complexity was achieved with the fabrication of 1D core@shell piezoelectric devices embedded in PMMA. Two variants were fabricated:

➢ Device V: H_2Pc core covered with a shell of ZnO.
➢ Device VI: H_2Pc core cover by a first shell of gold (inner shell) and a second shell of ZnO (outer shell).

In both cases a seed layer of 900 nm of ZnO was deposited previous to the growth of the NWs. In Figure 56 the whole system H$_2$Pc@Au@ZnO may be appreciated, note that for the device V (without the gold shell) the aspect would be exactly the same. The inner gold shell can be perfectly distinguished (Fig. 56 d-e)) and the ZnO deposition oriented the nanostructures in a vertical fashion as already discussed in Chapter 2 (Fig. 56 a-c)).
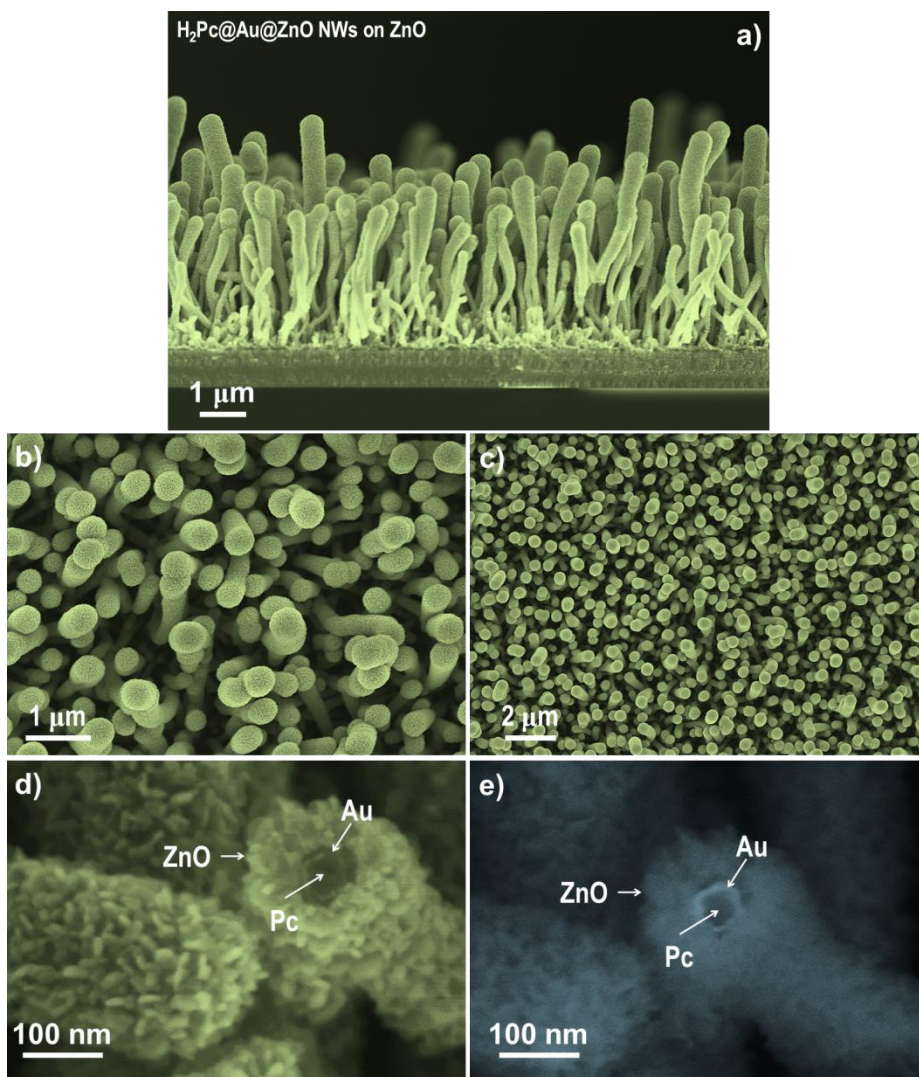
Figure 56. SEM (a-d) and BSE-SEM (e) micrographs of H$_2$Pc@Au@ZnO nanowires deposited on a ZnO (900 nm) layer. a) Cross section showing the vertical alignment of the core@multishell nanowires as well as the seed layer. It is worthy to indicate the deposition of the gold shell provoked a short circuit of this piezo film. b)–c) Planar

views at different magnifications demonstrating the tips of the NWs. d-e) High magnification micrographs revealing the cross section of an individual NW where the core and two shells were easily addressable.

The incorporation of PMMA to the samples was probably the most critical step in the preparation of the devices. There was no certainty that the solvent employed during the process (see methodology) would not attack the ZnO or if the PMMA would be able to diffuse towards the bottom of the samples. By inspection of Figure 57 a) and b) it can be concluded that PMMA effectively embedded the nanostructures, although not homogeneously in the case of the silicon substrate (Fig. 57 a)).
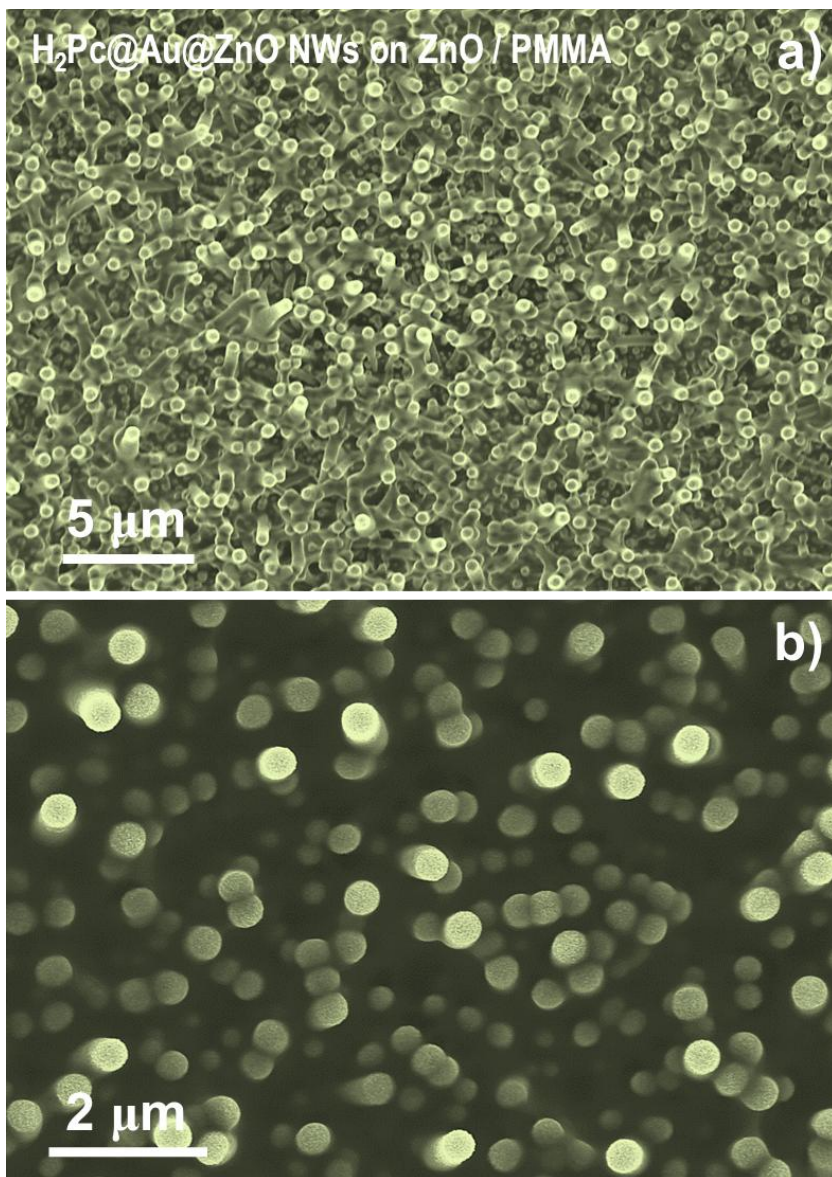
Figure 7. SEM normal view at different magnifications of H$_2$Pc NWs@Au@ZnO embedded in PMMA (5% w/w) after annealing during 1 hour at 80 ºC; image in panel a) corresponds to the NWs deposited on ZnO/Si(100) and panel b) to the deposition on ZnO/ITO/PET.

Finally, a rather short oxygen plasma treatment released the heads of the nanostructures from PMMA as seen in Figure 58. The duration and/or power of the plasma source may be varied in order to increase or decrease the exposed polymer-free ZnO area, but this study has not been carried out in this work. It is worth

mentioning that the exposed ZnO seems reasonably intact, without obvious vestiges of degradation (Fig. 58 a)).
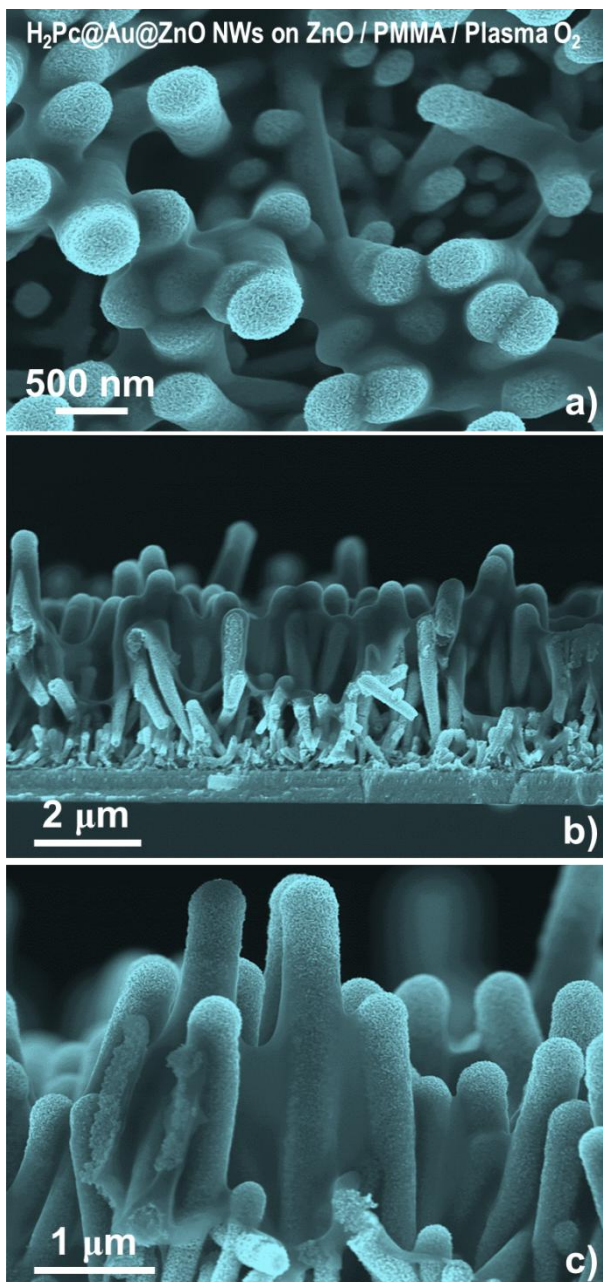
Figure 58. Normal (a) and cross section (b-c) SEM views showing the effect of the oxygen plasma treatment at room temperature of the Pc@Au@ZnO deposited on ZnO/Si(100) and embedded in PMMA. As it is demonstrated only part of the NWs were released of the polymeric sheath after the plasma treatment. The PMMA matrix improved the mechanical stability and distribution of the load.

The I-V characteristics of devices V and VI were remarkably symmetric for the positive and negatove bias. It is obvious that the device with a gold shell exhibited a much lower resistance compared to the one without it, which may be reasonably atributted to the fact that gold diffused throw the ZnO seed layer and contacted the ITO. In this particular case this turned out to be an advantage, besides, the contribution of the ZnO seed layer is cancelled (because it is short circuited).
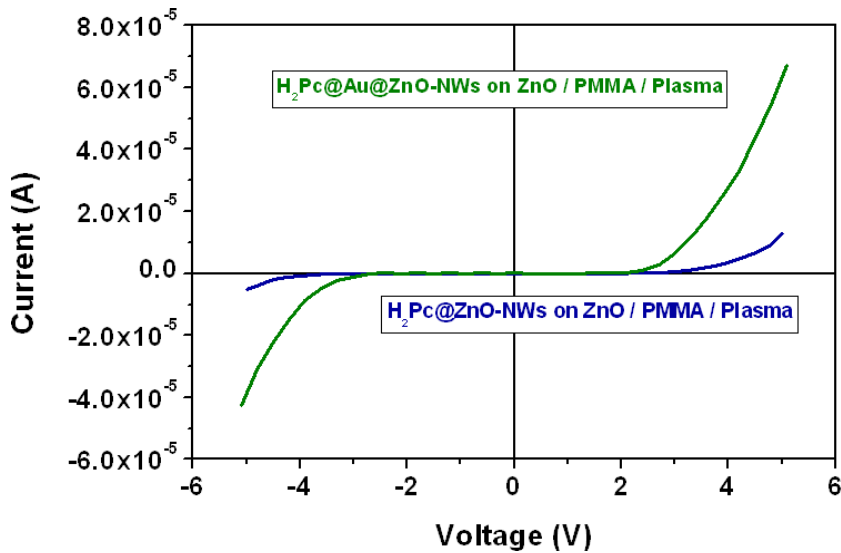
Figure 59. I-V characteristics measured for the two NWs devices deposited on ZnO/ITO/PET and contacted through Cu tapes.

The piezoelectric behaviour of devices V and VI was quite similar, except for its magnitude. Interestingly, for the vertical configuration no replica current peaks were observed, but they did appear in the lateral configuration. Moreover, it seems that the power output was higher for device VI in vertical configuration, while in the lateral configuration the difference was much more apparent. This is in agreement with the previous result of the I-V characteristics.
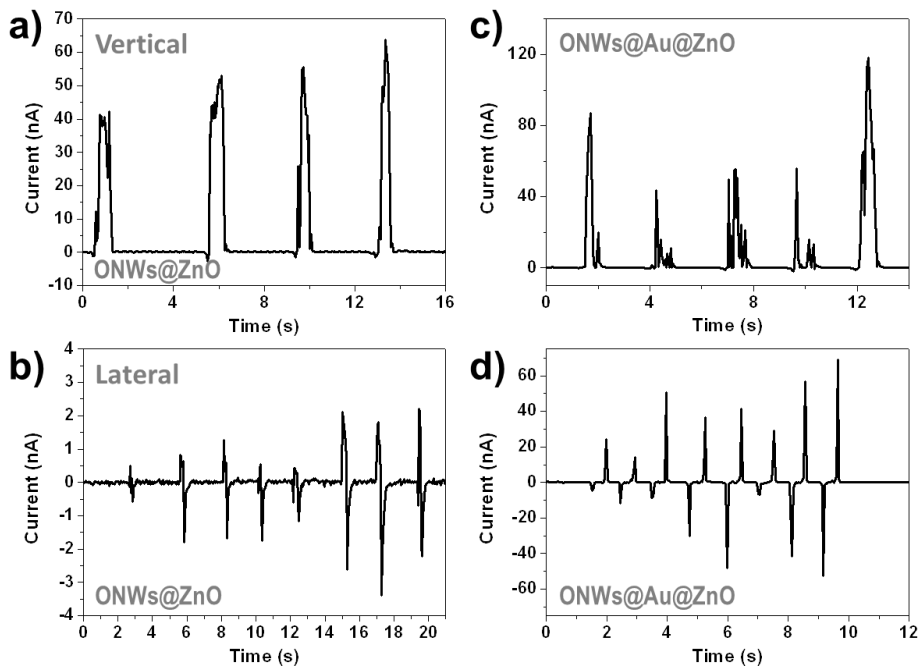
Figure 60. Output current obtained from the NWs devices deposited on ZnO/ITO/PET after vertical (a-c) and lateral (b-d) mechanical activation through a PDMS button.

4.5. Conclusions

The ZnO grown at room temperature by PECVD has proven to exhibit adequate electric and piezoelectric characteristics.

The development of 1D core@shell nanostructures with application in the field of piezoelectricity has been addressed. It has been possible to generate and thoroughly characterize complete nanogenerators with the structure Pt NWs@ZnO@Au following a full vacuum fabrication approach. In spite of the fact that the fabricated device was short circuited, it does not mean that the system is not appropriate for its implementation in piezoelectric generators, but just that more care must be taken to avoid that issues (PMMA infiltration for example). Moreover, these nanostructures have proven to be excellent samples for the development and refinement of more powerful EDX mapping and analysis techniques, as exemplified in Appendix B.

Thin film and 1D piezoelectrics have been successfully fabricated on flexible substrates. Despite not having performed quantitative studies, it has been demonstrated that the fabricated devices truly work as piezoelectrics, paving the way for more detailed studies.

4.6. References

Alcaire M. et al., Soft plasma processing of organic nanowires: a route for the fabrication of 1D organic heterostructures and the template synthesis of inorganic 1D nanostructures. Nanoscale 3(11), 4554-4559 (2011).

Baruah S., Dutta J., Hydrothermal growth of ZnO nanostructures (topical review). Science and Technology of Advanced Materials 10(1), 013001 (2009).

Cavallini A. et al., A Subcutaneous Biochip for Remote Monitoring of Human Metabolism: Packaging and Biocompatibility Assessment. Ieee Sensors Journal 15 (1), 417-424 (2015).

Comjani F. F. et al., Influence of the metal-semiconductor contact by energy harvesting from vertically aligned zinc oxide nanowires. Applied Physics Letters 104(14), 143113- 143113-5 (2014).

Dagdeviren C., Yang B.D., Su Y. et al., Conformal piezoelectric energy harvesting and storage from motions of the heart, lung, and diaphragm. Proceedings of the national academy of sciences 111(5), 1927–1932 (2014).

Dakua I., Afzulpurkar N., Piezoelectric Energy Generation and Harvesting at the Nano-Scale: Materials and Devices. Nanomaterials and Nanotechnology 3(21), 1-16 (2013).

deMello A. J., Control and detection of chemical reactions in microfluidic systems. Nature 442, 394-402 (2006).

Elias J. et al., Electrochemical deposition of ZnO nanowire arrays with tailored dimensions. Journal of Electroanalytical Chemistry 621(2), 171-177 (2008).

Hu H. et al., Hydrothermal synthesis of ZnO nanowires and nanobelts on a large scale. Materials Chemistry and Physics 106(1), 58-62 (2007).

Hu Y. et al., A Nanogenerator for Energy Harvesting from a Rotating Tire and its Application as a Self-Powered Pressure/Speed Sensor. Advanced Materials 23 (35), 4068–4071 (2011).

Janasek D. et al., Scaling and the design of miniaturized chemical-analysis systems. Nature 442, 374-380 (2006).

Lee J. et al., Atomic-scale origin of piezoelectricity in wurtzite ZnO. Physical Chemistry Chemical Physics 17(12), 7857-7863 (2015).

Leprince-Wang Y., Piezoelectric ZnO Nanostructure for Energy Harvesting, Vol. 1. ISBN: 978-1-84821-718-8. John Wiley & Sons. New Jersey, USA (2015).

Manz A., Eijkel J. C. T., Miniaturization and chip technology. What can we expect? Pure and Applied Chemistry 73(10), 1555-1561 (2001).

Shao Z. et al., Pt/ZnO Schottky nano-contact for piezoelectric nanogenerator. Physica E 43(1), 173-175 (2010).

Singh D. P., Synthesis and Growth of ZnO Nanowires. Science of Advanced Materials 2(3), 245-272 (2010).

Tian J. et al., Improved seedless hydrothermal synthesis of dense and ultralong ZnO nanowires. Nanotechnology 22(24), 245601 (2011).

Wang Z. L, Jinhui S., Piezoelectric Nanogenerators Based on Zinc Oxide Nanowire Arrays. Science 312(5771), 242-246 (2006).

Wang Z. L., Towards Self-Powered Nanosystems: From Nanogenerators to Nanopiezotronics. Advanced Functional Materials 18(22), 3553-3567 (2008).

Wang Z. L., Self-powered Nanotech. Scientific American (January), 82-87 (2008).

Wang Z. L., ZnO nanowire and nanobelt platform for nanotechnology. Materials Science and Engineering R 64(3-4), 33-71 (2009).

Wang Z. L., Nanogenerators for Self-powered Devices and Systems. ISBN: 978-1-4507-8016-2. Georgia Institute of Technology. Atlanta, USA (2011).

Yang R. et al., Converting Biomechanical Energy into Electricity by a Muscle-Movement-Driven Nanogenerator. Nano Letters 9(3), 1201-1205 (2009).

Zinc Oxide, Wikipedia. https://en.wikipedia.org/wiki/Zinc_oxide.

5. Laser induced enhancement of dichroism in supported silver nanoparticles deposited by evaporation at glancing angles
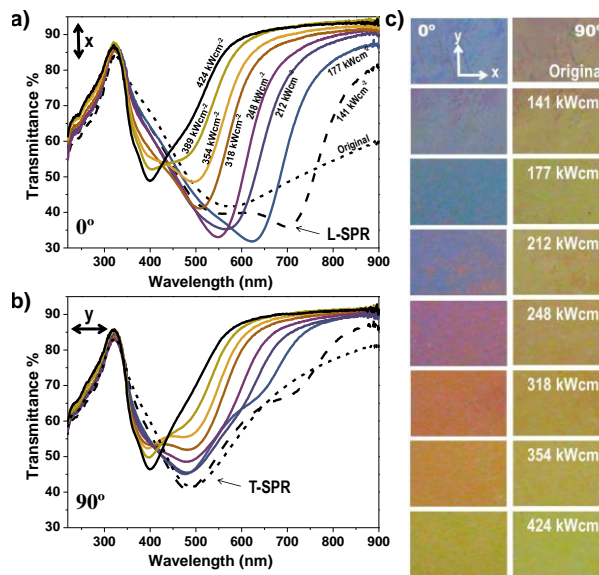
Abstract

Silver nanoparticles (NP) depicting well defined Surface Plasmon Resonance (SPR) absorption are deposited on flat substrates by physical vapor deposition in a glancing angle (GLAD) configuration. The particles are then characterized by Scanning electron Microscopy (SEM) and Atomic Force Microscopy (AFM) and their optical properties examined by UV-Vis absorption spectroscopy using linearly polarized light. It is found that, depending on the amount of deposited silver and the evaporation angle, part of the "as prepared" samples present NPs characterized by an anisotropic shape and a polarization dependent SPR absorption and

different colors when using polarized white light at 0º and 90º. Low power irradiation of these materials with an infrared Nd-YAG nanosecond laser in ambient conditions produce an enhancement in such dichroism. At higher powers, the dichroism is lost and the SPR bands shift to lower wavelengths as a result of the reshaping of the silver NPs in the form of spheres. The possible factors contributing to the observed changes in dichroism are discussed.

These NPs deposited on melted silica are finally employed as substrates for Surface enhanced Raman scattering (SERS) to detect Rhodamine 6G in solution. The effect of laser treatment on SERS effect is also evaluated [Chapter 6].

5.1. Introduction

Metal nanoparticles (NPs) with Surface Plasmon Resonance (SPR) activity have been widely studied because of their applications for the fabrication of optical devices such as filters, non-linear optical components, Raman enhancers and others [Mertens H., Appl. Phys. Lett. 2006][Liang H. Y., Adv. Mater. 2009][Giannini V., Chem. Rev. 2011][Rycenga M., Chem. Rev. 2011]. The dichroic activity of anisotropic metal aggregates has been exploited for the development of optical filters, new encryption processes, the fabrication of polarized light emitters or materials with enhanced IR luminescence [Fort E., Nano Lett. 2003][Suzuki M., J. Appl. Phys. 2005][Camelio S., Phys. Rev. B 2009][Cavallini M., Adv. Mater. 2009]. Dichroism, usually achieved by managing the shape and distribution of the metal aggregates along a preferential direction, can be produced by different methods. For example, by manufacturing assemblies of parallel stripes of NPs onto preformed surfaces presenting 1D periodic roughness [Fort E., Nano Lett. 2003][Suzuki M., J. Appl. Phys. 2005] or by more sophisticated approaches consisting of the application of soft lithographic techniques to accurately tailor the nanostructure of the materials according to asymmetric patterns [Camelio S., Phys. Rev. B 2009]. A well-known soft lithographic technique widely used to modify the shape and structure of NPs relies on the use of laser scanning [Wenzel T., Appl. Phys. B 1999][Kaempfe M., Appl. Phys. Lett. 2001][Link S., Phys. Chem. B 1999][Zijlstra P., Nature 2009][Sanchez-Valencia J. R., Plasmonics 2010] either by in situ [Wenzel T., Appl. Phys. B 1999] or ex situ [Kaempfe M., Appl. Phys. Lett. 2001][Link S., Phys. Chem. B 1999][Zijlstra P., Nature 2009][Sanchez-Valencia J. R., Plasmonics 2010] treatments.

Not long ago, memebers of the *Nanotechnology on Surfaces* group have prepared dichroic structures of silver by sputtering of this metal onto SiO_2 thin films consisting of bundled arrangements of SiO_2 nanocolumns (i.e., Ag/SiO_2 systems) prepared by glancing angle deposition (GLAD) and a posterior treatment with nanosecond laser [Sanchez-Valencia J. R., Adv. Mater. 2011][Nouneh K., Alloys and Comp. 2011]. In that case an anisotropic distribution of silver in the form of stripes was induced by a surface template effect of the nanocolumns bundles existing in the SiO_2 GLAD thin films. The anisotropy was enhanced by the partial melting and agglomeration of the silver aggregates under the action of laser irradiation. Principal achievements of that work were the tuning of the SPR along the visible range and the demonstration of the applicability of system for optical nano-patterning applications. Enhancement of dichroism by laser irradiation in deposited silver by laser is rather unusual since most

common behaviour of deposited NPs consists of the agglomeration of the smaller particles into spherical and bigger ones [Ebothé J., Mat. Chem. Phys. 2009][Cattaruzza E., Appl. Surf. Sci. 2011][Tawfick S., Adv. Mater. 2012].

In the present work, the preparation of silver NPs by direct evaporation at glancing angles (GLAD-PVD) by evaporation of silver in high vacuum conditions from a punctual source has been essayed. As it will be demonstrated below the technique provides a straightforward way to the formation of asymmetric nanoparticles with different plasmon-wavelengths associated to their shape. The growth of such particular NPs is due to the specific geometry of the deposition. Different experiments shown in this work demonstrate the relation between the geometry of the deposition and the morphology and, therefore, optical properties of the nanoparticles. Meanwhile in the previous references [Sanchez-Valencia J. R., Adv. Mater. 2011][Nouneh K., Alloys and Comp. 2011] the silver deposition was carried out by a plasma related technology, sputtering dc from a silver thread in Ar pressure. The isotropic character of the DC sputtering produces at low thickness rounded nanoparticles. On other hand, references [Sanchez-Valencia J. R., Adv. Mater. 2011] and [Nouneh K., Alloys and Comp. 2011] show the formation of elongated silver nanoparticles using a SiO_2 template fabricated by GLAD. Therefore, main differences between this protocol and the previous ones are: 1) methodology for the preparation of the nanoparticles; 2) this new methodology allows us to further control the optical properties of the starting material, i.e. before the laser treatment; 3) this is a template-free protocol, meaning the interesting results on control of the dichroism and plasmon resonance wavelength that has been previously demonstrated can be applied in a one-step routine.

This technique has been widely used for the preparation of nanocolumnar porous thin films of metals [Messier R., J. Vac. Sci. Technol. 2000][Gonzalez-Garcia L., Mater. Chem. 2010] oxides [Hawkeye M. M., J. Vac. Sci. Technol. A 2007][Sanchez-Valencia J. R., Langmuir 2009][Alvarez R., J. Phys. D: Appl. Phys. 2011] or semiconductor [Van Kranenburg H., Mater. Sci. and Eng. R 1994][Hodkinson I., Adv. Mater. 2001][Chaney S. B., Appl. Phys. Lett. 2006] materials. Silver nanocolumnar films have been also obtained by this method [Bloemer M. J., Phys. Rev. B 1998][Liu Y., Appl. Phys. Lett. 2006][Zhao Y. P., J. Appl. Phys. 2006][Horcas I., Rev. Sci. Instrum. 2007]. Herein, the deposition process has been stopped before the development of the nanocolumns and obtained discrete silver NPs at the initial stages of growth. It is shown that these metal nuclei have an elongated shape and present a dichroic optical behaviour that can be enhanced by laser irradiation. Besides dealing with the preparation of the silver deposits and studying their optical behaviour before and after the laser treatment, the

implications of the GLAD geometry for the fabrication of anisotropic silver NPs on flat substrates and the factors that contribute to increase their anisotropy by laser irradiation are discussed.

5.2. Methodology

Silver evaporation was carried out in an electron bombardment evaporator by using a crucible with silver as a target. Pieces of a Si (100) wafer with a size of 2.5 x 2.5 cm^2 were used as substrates for the SEM characterization of the as-grown samples. Simultaneous evaporation was also carried out on glass and quartz plates that thereafter were examined by UV-Vis absorption spectroscopy and underwent the laser treatments. Deposition was performed at room temperature in vacuum (i.e., 10^{-6} Torr) by placing the substrates at different glancing zenithal angles α from 60 to 85º. The layer thickness was controlled by monitoring the evaporation process with a quartz crystal monitor (QCM) previously calibrated by comparing its response with the thickness of Ag films prepared at normal geometry. When the text refers to the amount of evaporated silver, the data always indicate the nominal thickness measured by the (QCM) place at normal geometry. Therefore, the typical cosine rule should be applied to estimate the amount of silver actually deposited on the substrates placed at glancing angles with respect to the source. For comparative purposes, samples were also prepared at normal configuration (α=0º) or at glancing angle while rotating the substrate. In the text, samples will be named by indicating their nominal thickness followed by the deposition angle (e.g., 50nm/85º means a sample with a nominal thickness of 50 nm prepared at 85º zenithal evaporation angle). The samples were fabricated at deposition rates comprised between 0.5 and 1.5 Å/s in all cases. The as-prepared samples were kept in a desiccator under controlled conditions until their use.

Laser post-treatment was performed at room temperature with a 20 W diode-pumped Nd:YAG (Powerline E, Rofi n-Baasel Inc.) unpolarized laser emitting at 1064 nm with a 100 ns pulse width and a 20 kHz repetition rate. The samples were scanned with a 60 ꭥm spot, measured by analyzing the laser marks on a silver thick film at the working distance (Fig. 1), at 100 mm s^{-1} speed with one pulse per spot fired into the material. The maximum energy fluence applied in these experiments is 21.2 Jcm^{-2} and was calculated as the ratio energy per pulse to area. Full width of the beam at half its maximum intensity (FWHM) supplied by the constructor is 10 nm. UV-Vis absorption spectra were recorded at normal incidence in a Cary 100 spectrophotometer at normal incidence and in the [220 – 900 nm] range with a 1 nm monochromator step spectrometer by using linearly polarized light at 0º and 90º.
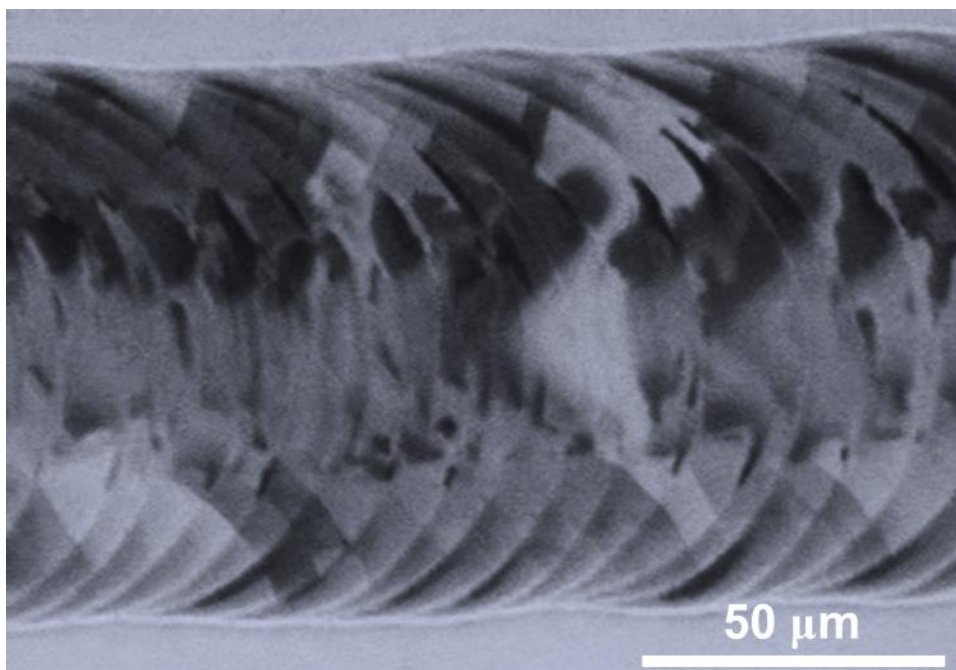
Figure 1. SEM image used for the estimation of the laser mean diameter measured at the working distance on a silver thick layer ($\sim$ 750 nm).

The particle size and shape of the silver NPs evaporated on a silicon wafer was analysed by Field Emission Scanning Electron Microscopy (FESEM) in a Hitachi S4800 microscope by examining both their surfaces and cross sections. The surface topography of the deposited particles was analysed by Atomic Force Microscopy (AFM) in a Dulcinea microscope from Nanotec (Madrid, Spain) working in tapping mode and using high frequency cantilevers. AFM images, taken on a 1 x 1 μm^2 surface area, were processed with the WSxM free available software from Nanotec [Ferraris M., Mater. Chem. Phys. 2010]. Besides to a conventional analysis of the surface topography, Fast Fourier Transforms (FFTs) of the images were calculated to assess both the shape and particle size distribution of the deposited silver.

5.3. Results and Discussion

5.3.1. Evaporation of silver at glancing angles

Evaporation of silver at glancing angles on a glass or any other transparent substrate leads to the formation of optical layers characterized by either a wavelength widespread mirror reflectance or a localized SPR feature. The transition from one

regime to the other depended on the amount of evaporated silver and on the zenithal evaporation angle. Figure 2 illustrates this behavior for silver deposits of 10 and 50 nm nominal thickness prepared at zenithal angles α=0º, 65º, 70º, 80º, 85º. It is apparent in this figure that the layers fabricated at the higher zenithal angles depict a defined absorption band located between 500 and 600 nm that it is attributed to the SPR absorption of silver NPs [Mertens H., Appl. Phys. Lett. 2006][Liang H. Y., Adv. Mater. 2009][Giannini V., Chem. Rev. 2011][Rycenga M., Chem. Rev. 2011]. At low zenithal evaporation angles, particularly at normal evaporation (i.e., α=0º), the layer behaves as a mirror without any defined absorption feature.
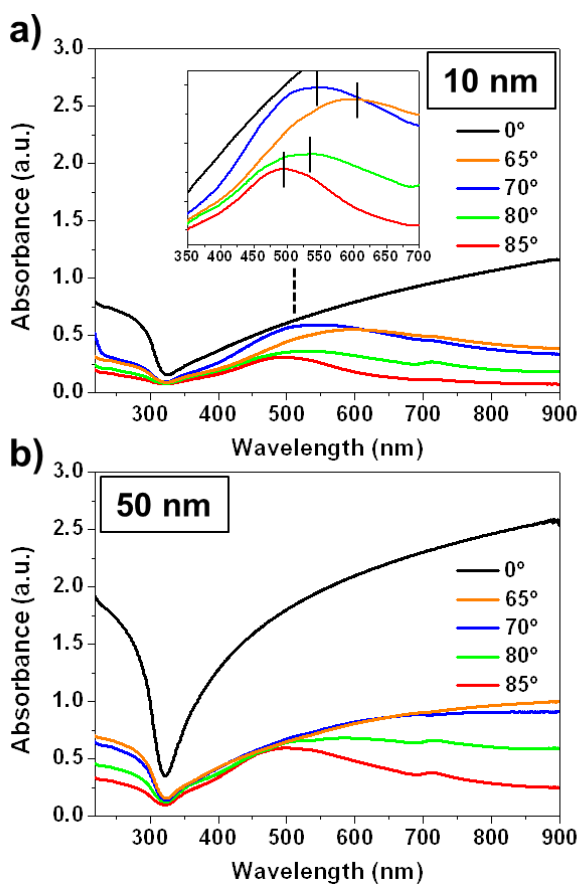

Figure 2. Absorbance spectra recorded for silver layers with a) 10 and b) 50 nm nominal thickness deposited on a glass slide at zenithal angles of 0º, 65º, 70º, 80º and 85º. The inset in panel a) shows the changes of the absorption maxima with the deposition angle.

A similar tendency was found for silver layers of intermediate nominal thicknesses of 20, 30 and 40 nm (Fig. 3). The broad absorption between 200 and 320 nm presented in all the curves can be related with both, light scattering in the interface with the substrates [Ehrenreich H., Phys. Rev. B 1962] and the combination of the SPR with a minimum at ~310 nm which is characteristic of the silver systems. At such wavelength the real and imaginary parts of the dielectric function of silver almost vanish in relation with interband transitions [Linnert T., J. Amer. Chem. Soc. 1990]. Different authors have also reported two absorption bands at 305 and 350 nm associated with the presence of Ag+ and elemental Ag atoms correspondently [Mitchell C. E. J., Surf. Sci. 2001][Chiaretta D., Non-Crystal. Sol. 2006]. In this case, besides the strong SPR absorption hamper the resolution of bands due to metal ions [Ehrenreich H., Phys. Rev. B 1962], the possibility of silver oxide presence has been discarded by following the absorption after an oxidation/reduction cycle, noticing a displacement and narrowing of the surface plasmon resonance related to a rearrangement of the silver clusters (data non shown) as the main modification of the spectra.
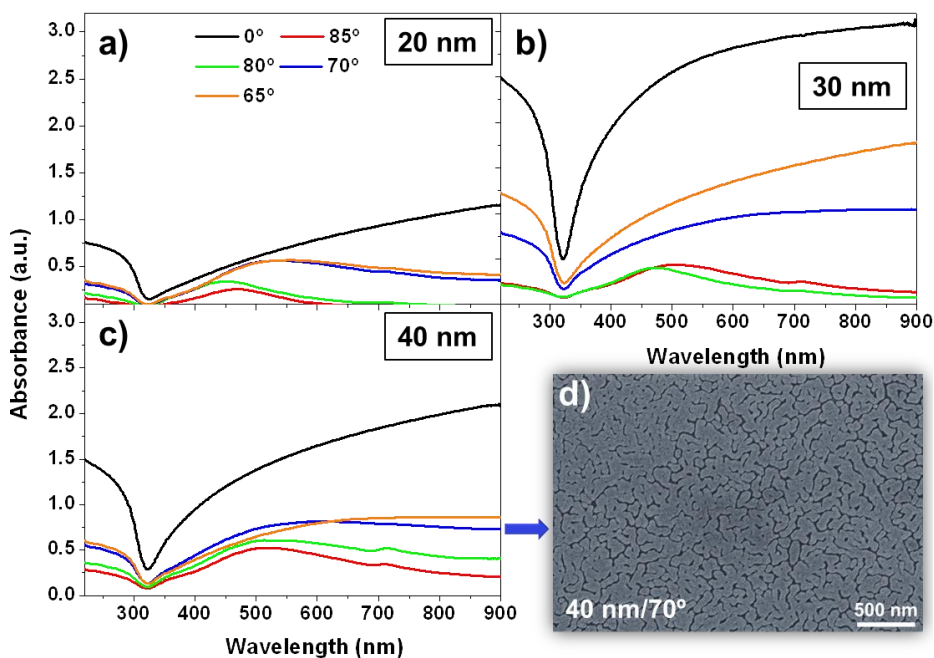

Figure 3. Absorbance spectra recorded for silver layers with 20, 30 and 40 nm nominal thickness deposited on glass at the zenithal angles of 0°, 65°, 70, 80 and 85°.

The formation of isolated silver particles at the highest zenithal angles could be confirmed by SEM observation. This analysis showed that silver deposited under

these conditions aggregates in the form of small NPs with a morphology that depended on the angle of evaporation and the amount of evaporated silver. **Figure 4** gathers a series of normal and cross section SEM micrographs showing the characteristics of the silver grains formed in samples 50nm/85º and 10nm/85º. This figure clearly demonstrates that silver evaporated at zenital angles forms small particles without completely covering the substrate. The histogram included in the figure shows that the average particle size increases with the amount of evaporated silver, as expected for a progressive percolation and agglomeration of the initial silver nuclei into bigger particles. This assessment of the evolution of particle sizes also proved for other deposition angles and equivalent thicknesses, comply with an ample series of results in literature reporting that evaporation of small amounts of silver at normal deposition angles leads to the formation of discrete particles [Lee M. H., Thin. Sol. Films 1992][Yang K. Y., Appl. Phys. Lett. 2009][Siozios A., Nanolett. 2012]. For higher amounts of evaporated silver, i.e., the conditions where a mirror like behavior was found (cf. Figure 2), a homogenous and completely percolated metal film could be observed by SEM (Fig. 3 d)).
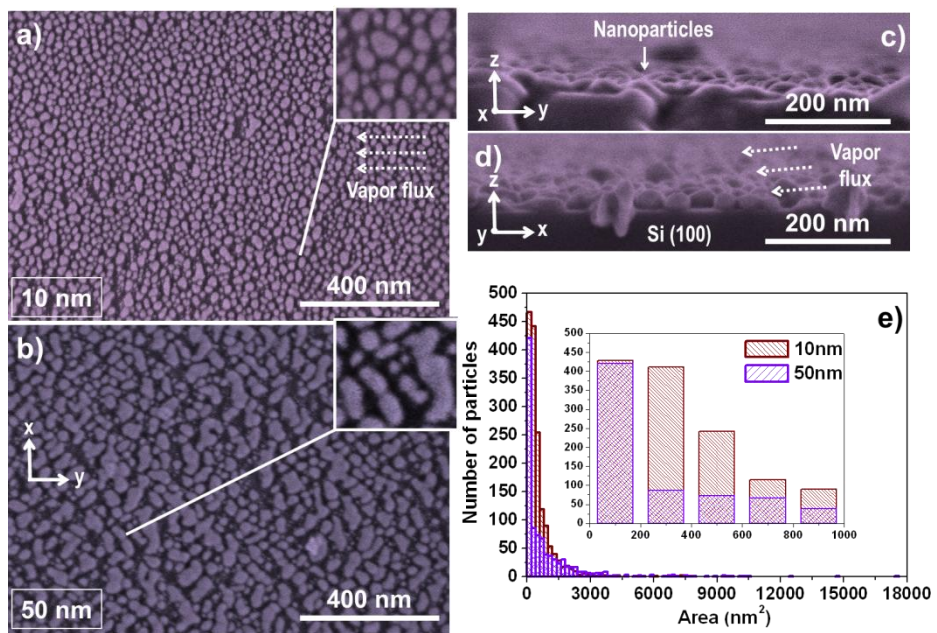

Figure 4. Normal (a, b) and cross section (c, d) SEM micrographs of samples 10nm/85º (a) and 50nm/85º (b, c, d). Arrows inserted in the micrographs indicate the direction of arrival of silver flux during the preparation of the samples. Coordinate axis defined with respect to this direction are also included for clarity. The insets in a) y b)

show an enlargement of the micrograph for a better view. Cross section micrographs (c, d) have been taken by turning the 50 nm sample during analysis as indicated by the coordinate axis in the figure. The histograms in e) show the particle size distributions obtained from images a) and b) for each studied sample.

A close look to the cross section images in Figure 4 c) and d) and to the shape of the NPs in the normal images (a, b) reveals that, even if irregular, they present a certain elongation perpendicular to the direction of evaporation. This asymmetry had a critical influence on the optical properties of these deposited particles. From now on the following notation will be used when indicating absorption for linear polarized light: linear polarized light perpendicular/*parallel* to the flux direction (x)/(*y*), i.e. in the long/*short* axis growth of the nanoparticles (Fig. 3 a and b), will be denoted as 0º/*90º* and the corresponding SPR as longitudinal/*transversal*. **Figure 5** shows the absorption spectra of samples 10nm/80º and 50nm/85º under linear polarized light. In the two cases, the most significant feature was the difference in the wavelength position and width of the plasmon absorption band when turning the polarizer 90º. This optical dichroism must result from the excitation of distinct plasmon resonances along the nanoparticles (longitudinal plasmon L-SPR) and perpendicularly to them (transverse plasmon T-SPR). The different plasmon wavelengths of the two bands indicate that the electromagnetic coupling along the nanoparticle longest dimension is stronger than along the perpendicular direction. For the two samples, the L-SPR depicts a red shift by, respectively, 56 and 84 nm accompanied by a broadening in the shape. Similar wavelength modifications and broadenings, although to a different extent depending on the sample, were also found for the samples that depicted a clear plasmon absorption band as seen in Table 1.
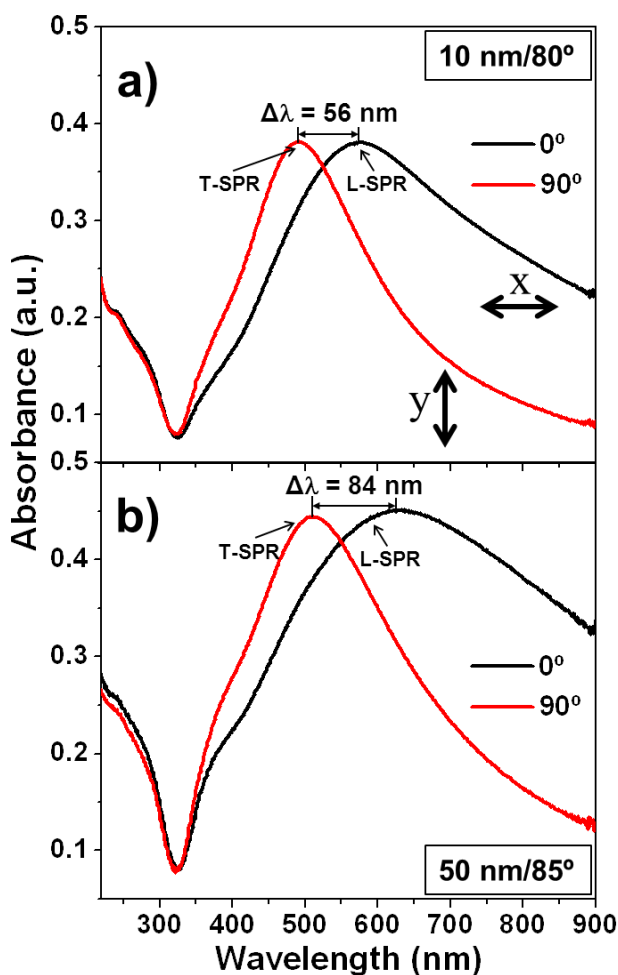
Figure 5. Absorption spectra recorded with linearly polarized lights at 0º and 90º for samples 10nm/80º (a) and 50nm/85º (b).

Table 1. Wavelength difference (dichroism) between L-SPR and T-SRP maxima of the synthesized samples by recording the spectra with linearly polarized light at 0º and 90º. The cells in blank correspond to samples depicting a mirror like behavior where no well-defined SRP could be observed.

Angle / Thickness	65º	70º	80º	85º
10 nm	46 nm	62 nm	56 nm	25 nm

20 nm	84 nm	40 nm	13 nm	16 nm
30 nm	-	-	14 nm	44 nm
40 nm	-	-	109 nm	51 nm
50 nm	-	-	-	84 nm

At this point it is worthy of note that samples prepared by GLAD while rotating the substrate or by normal evaporation and a small nominal thickness were characterized by small and rather symmetrical silver NPs and did not present any significant difference in their absorption spectra when examined with polarized light at 0º and 90º (Fig. 6). This result further supports that the optical anisotropy depicted in Figure 4 has to be associated with the elongated shape of the silver NPs prepared in a GLAD configuration.
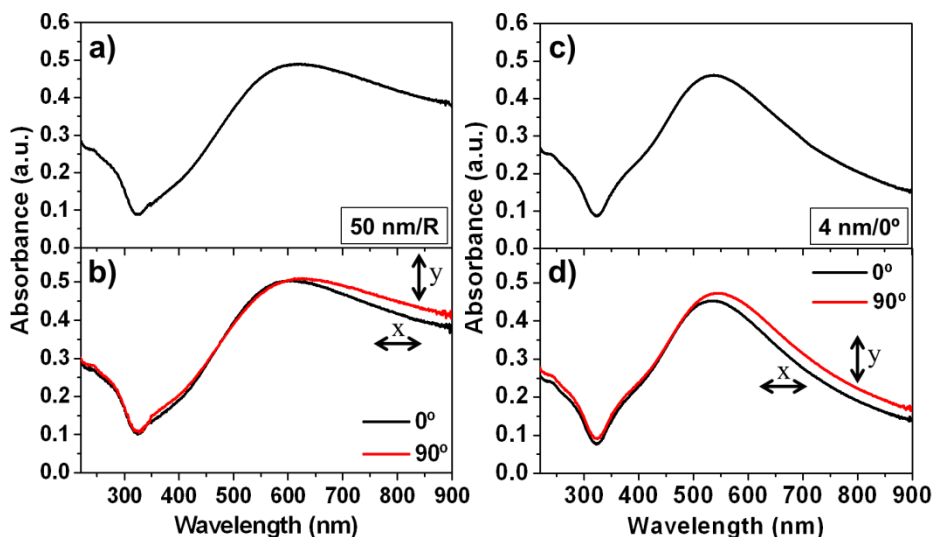
Figure 6. UV-vis absorption spectra recorded with linearly polarized light at 0º and 90º for samples prepared at a GLAD geometry by rotating the substrate (left) and by deposition of the silver at normal geometry (right).

5.3.2. Laser post-treatment of silver NPs prepared by GLAD

A well-known phenomenon observed when deposited silver NPs are laser irradiated is their coarsening and agglomeration into particles of bigger size [Ebothé J., Mat. Chem. Phys. 2009][Cattaruzza E., Appl. Surf. Sci. 2011][Tawfick S., Adv. Mater. 2012]. For

the anisotropic particles prepared here by GLAD, this should normally lead to the overlapping of the L-SPR and T-SPR and therefore to the decrease of the dichroism. **Figure 7** shows a series of normal SEM micrographs taken for sample 50 nm/85º exposed to laser illuminations with increasing laser irradiances in the range between 141 and 424 kWcm^{-2}. This set of micrographs reveals a progressive modification of the particles from an elongated to a spherical shape and, to a first glance, the formation of bigger particles when the irradiance is progressively increased. A closer look to the particle morphologies in the sample irradiated with the maximum power of the laser (see the high magnification SEM image in Fig. 7 f)) shows that together with the big spherical NPs (diameters between 40 to 100 nm) there are also very small spherical NPs (diameters below 10 nm), thus defining a kind of bimodal (an even trimodal) distribution of particle sizes. For intermediate or the lowest irradiance conditions (i.e. 141 and 212 kW/cm^2), although a small number of spherical NPs can be devised in the image, most of them continue having an irregular and elongated shape.
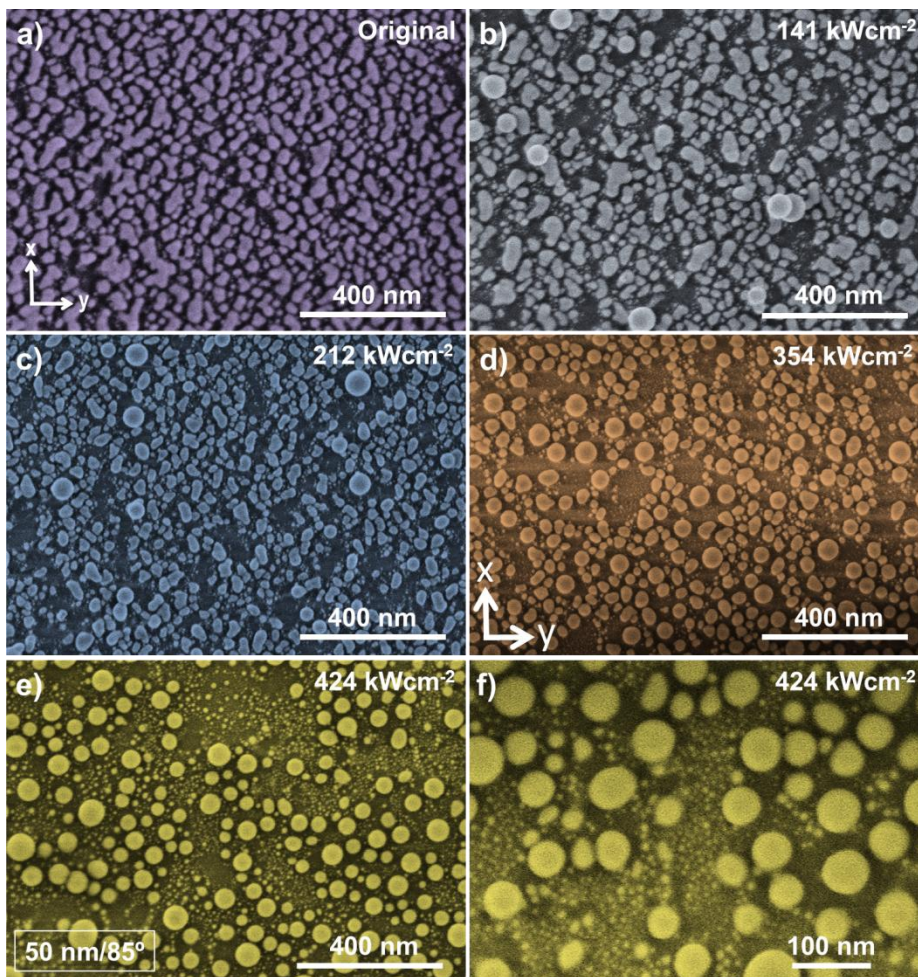
Figure 7. Normal view SEM micrographs of sample 50 nm/85° subjected to increasingly higher laser irradiances as indicated in the images from a) to f). Panel f) shows a higher magnification micrograph to better devise the heterogeneous distribution of particle sizes present in the sample after treatment at the highest irradiance conditions.

Unfortunately, the characterization of these samples by high resolution SEM in cross section mode is hampered by charging problems associated to the use of fused silica as substrate for the laser treatments. Nevertheless, a deeper look to the characteristics of the particles after the different irradiation experiments is achievable by AFM. The topographic images and fast Fourier transforms (FFTs) for sample 50nm/85° presented in **Figure 8** confirm the previous assessment on the evolution of particle size and shape derived from the SEM analysis. Thus, the evolution of the

topography of the samples (see the intensity scale in panels a) to c) and the histograms in panel e)) agrees with an increase in the particle height associated with the formation of cylindrical and/or rounded particles of bigger size. Meanwhile, the histograms included in the same figure clearly indicate that both the average particle size and the width of the particle size distribution increase with the irradiance, in agreement with the SEM observation of these samples in Figure 7. The RMS roughness values collected in Figure 8 d) confirm these tendencies. Similarly, the FFTs included in the figure provide additional evidences of the coarsening of the silver NPs when subjected to laser irradiation. For the original sample the FFT diagram, is characterized by a relatively large and rectangular area which agrees with the presence of small particles with elongated shape. Increasingly higher laser irradiances produce a decrease in the size of the FFT diagram and its transformation into a symmetric pattern, both features agreeing with the formation of spherical silver particles. Thus, the height histograms demonstrate the increment in the height out of plane of the NPs with the laser treatment, meanwhile the FFT devoted to the in-plane features show the transformation into rounder nanoparticles.
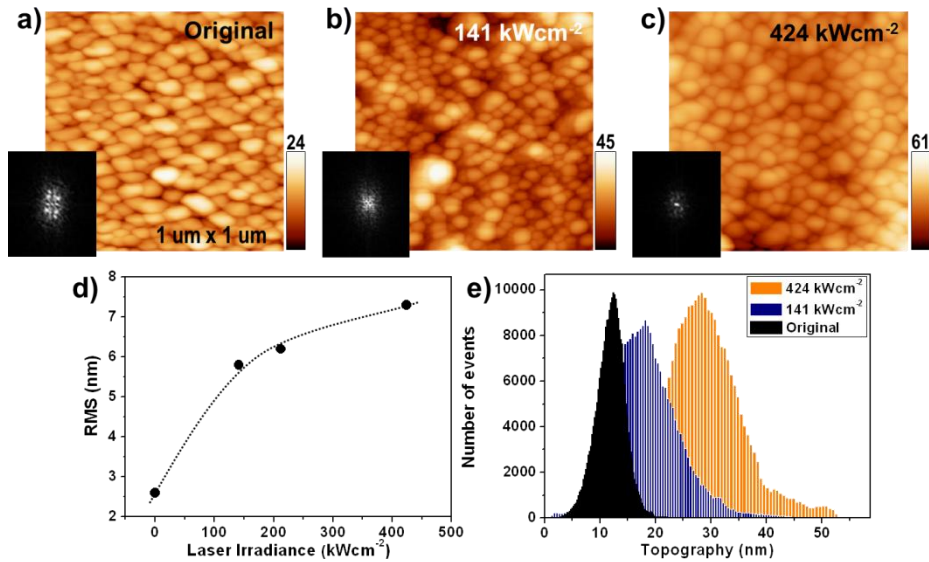
Figure 8. a)-c) AFM topographic images and Fourier transforms (FFTs) as insets of sample 50nm/85º as prepared by GLAD and after being subjected to increasingly higher laser irradiances as indicated; d) RMS roughness as a function of the laser irradiance; e) height histograms of the representative images in a)-c).

The changes experienced by the morphology and size of the silver particles upon laser irradiation had a direct correlation onto the optical behavior of samples. A first

effect is observed in the wavelength position of the L-SPR maximum that could be tuned along the visible range as a function of the irradiance parameter. A direct consequence of such a tuning for a given sample was the modification of its dichroism. A clear example of this effect is reported in **Figure 9** showing the transmittance spectra recorded with linearly polarized light at 0º (L-SPR) and 90º (T-SPR) for sample 50 nm/85º subjected to increasingly higher laser irradiances. The as-grown sample present a L-SPR at ∼ 570 nm that splits into two peaks, one well defined at higher wavelengths (720 nm) and a another one at ∼ 550 nm. The former is also observed with very little intensity in the T-SPR spectrum that, otherwise, remained almost unmodified. A similar effect was described and modeled in a previous work regarding the ns-laser treatment of silver nanostripes deposited on SiO_2 nanocolumns [Nouneh K., Alloys and Comp. 2011]. At medium irradiances from 177 to 248 kWcm^{-2}, the 720 nm band in the L-SPR spectrum shifted to the red and merged with the component at around 550 nm. Except for the removal of the shoulder at 720 nm, little changes can be observed in the T-SPR spectra for this range of irradiances. Treatment under higher irradiances from 318 to 424 kWcm^{-2} progressively transformed the plasmon contributions recorded with the two polarizations of light into a unique complex band appearing at around 400 nm for the maximum power of the laser. In this final band, up to three different features can be distinguished in the spectra recorded either at 0º or 90º polarizations.

Resulting from these changes in the absorption spectra, the color appearance of the sample illuminated with polarized white light changed as a function of both the laser irradiance and the polarization of light as reported in Fig. 9 c). Turning the polarizer, the full color scale (0º) obtained when exciting the L-SPR turns almost monochromatic at 90º. The wide variety of colors and its dependence on the polarization of light opens the possibility to create a full pallet of polarized dependent colors based on the Plasmon absorption of silver NPs. Due to the focusing properties of the laser, the previous colors could be produced according to given patterns and be used for optical encoding [Van Kranenburg H., Mater. Sci. and Eng. R 1994][Han R., Appl. Phys. Lett. 2011].
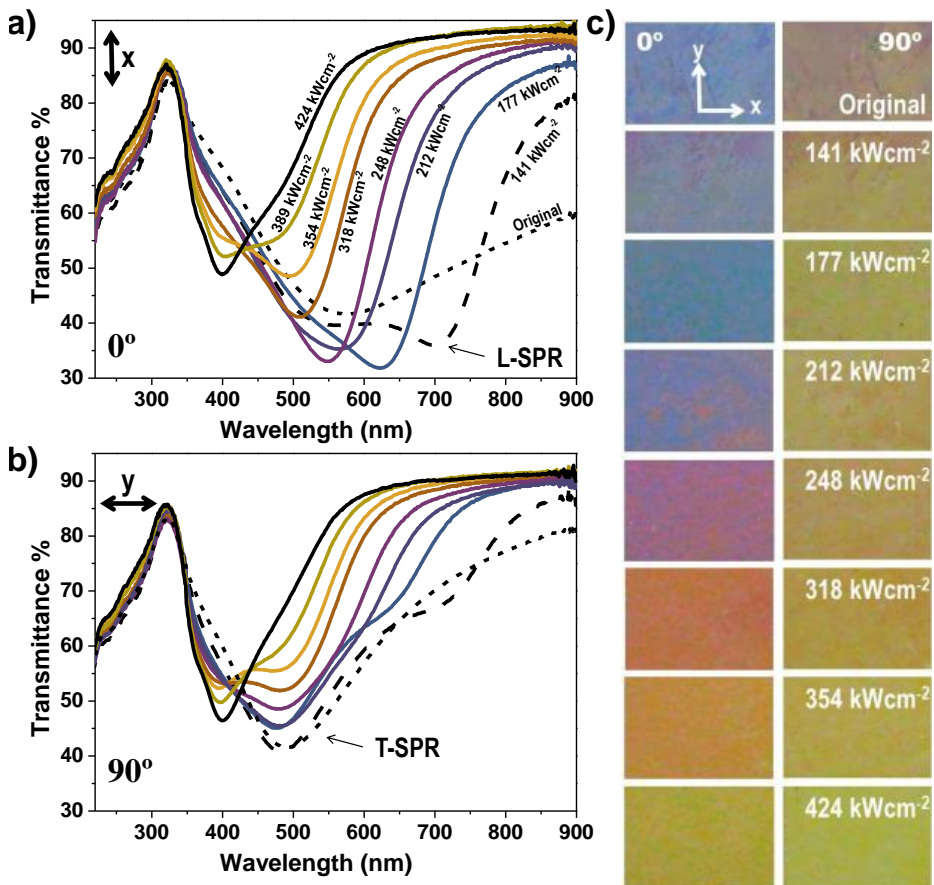
Figure 9. Transmission spectra recorded with linearly polarized light at 0º a) and 90º b) for sample 50 nm/85º subjected to laser treatments with increasing irradiances between 141 and 424 kW/cm². Color code is the same in both graphs; c) color photographs taken for the same samples illuminated with polarized (0º and 90º) white light showing the production of a color scale when exciting the longitudinal plasmon.

The behavior of sample 50nm/85º described in Figure 8 was similarly reproduced by all the samples where an optical anisotropy was already apparent in the "as prepared" films (Table 1). In all cases, irradiation at the minimum laser irradiance produced a shift to longer wavelengths in the position of the plasmon band recorded with the 0º polarized light. As a consequence, the difference in the SPR position recorded with 0º and 90º polarized lights increased, leading to a maximum difference in the SPRs and, hence, in the color appearance of the samples when examined with white light (cf. Figure 8 (right)). Laser irradiation at intermediate powers produced in all cases a progressive diminution of the plasmon shift that decreased smoothly to zero at the maximum irradiances.   A maximum shift of 200 nm was obtained for sample

50nm/85º. To summarize the effect of laser on the different samples, **Figure 10** shows a plot of the magnitude of the plasmon shifts between the SPR maxima obtained with 0º and 90º linearly polarized lights when the different samples were subjected to laser irradiation at increasingly higher irradiances. It must be noted that practically no anisotropy enhancement was obtained for samples prepared at normal evaporation or by rotating the substrate during evaporation in a GLAD configuration that, as previously indicated, did not present a noticeable anisotropy in the "as prepared" state.
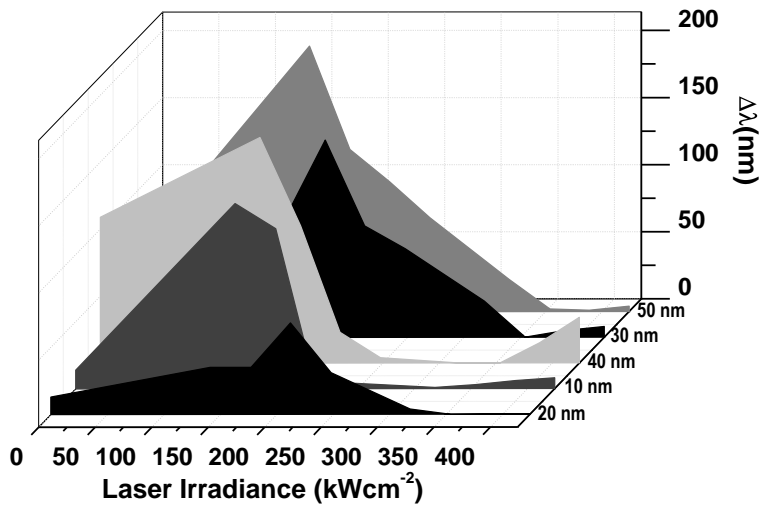
Figure 10. Evolution of the SPR shift between the UV-Vis spectra recorded with 0º and 90º polarized lights for the different studied samples treated with increasingly higher laser irradiances.

5.3.3. GLAD formation of silver NPs

Growth of silver nanocolumns by glancing deposition is known to yield a very interesting optical phenomenology, widely studied since the eighties of the last century [Bloemer M. J., Phys. Rev. B 1998][Liu Y., Appl. Phys. Lett. 2006][Zhao Y. P., J. Appl. Phys. 2006][Horcas I., Rev. Sci. Instrum. 2007]. By contrast, the initially formed particles deposited at glancing angles and their modification by laser irradiation has not deserved much attention. Our results have shown that silver NPs prepared by evaporation in a GLAD configuration present optical anisotropy likely linked with their elongated shape with the longest dimension perpendicular to the direction of evaporation. Asymmetric growth of GLAD microstructures is a common phenomenon in thin films that sometimes becomes apparent by the agglomeration of the individual nanocolumns in the form of "bundles" [Yang K. Y., Appl. Phys. Lett. 2009][Rycenga

M., Chem. Rev. 2011]. The asymmetric NP shape obtained here must be a first indication of this tendency to form anisotropic structures, already at the initial nucleation steps. Our results have also shown that a plasmonic structure appears for certain angles of evaporation and relatively low amounts of evaporated metal. For other preparation conditions with a higher amount of silver, the silver layer presents a mirror like behavior where no SPR can be devised. We attribute this result to the percolation of the silver into a continuous structure where no isolated particles can be differentiated. We have found that the elongated particles prepared at GLAD present a dichroic behavior when examined with linearly polarized light that is not found when evaporated at normal geometry [Lee M. H., Thin. Sol. Films 1992][Yang K. Y., Appl. Phys. Lett. 2009][Siozios A., Nanolett. 2012]. This dichroism and its evolution upon laser irradiation must be a result of the change of the morphological characteristics of the NPs.

5.3.4. Laser irradiation of elongated silver NPs

In general, deposited silver NPs subjected to laser irradiation tend to agglomerate into bigger particles with spherical shape [Ebothé J., Mat. Chem. Phys. 2009][Cattaruzza E., Appl. Surf. Sci. 2011][Tawfick S., Adv. Mater. 2012], producing a red shift in the position of the plasmon. The observed optical behavior found when our samples were subjected to low laser irradiances was more complex and resulted in an enhancement in the optical anisotropy when using polarized light. In the "as deposited" state the NPs prepared at glancing angles appear to be rather flat (c.f., Figure 4c) and elongated in the direction to the arrival of the incoming flux of silver during evaporation. This morphology must be the cause of the different shape of the L-SPR and T-SPR spectra and the observed shift in their maxima. According to the literature [Link S., Phys. Chem. B 1999][Zeng J., Chem. -Eur J.], among the factors contributing to the red shift in the position of the plasmons, the elongated aspect ratio, the interaction with the substrate and the irregular shapes with relatively sharp corners in these NPs can be quoted.

Laser irradiation produces a progressive change in both the T-SPR and L-SPR modes that must be accounted for by some modifications in the morphology of the NPs. The pictorial model presented in **Figure 11** tries to illustrate the morphological changes of the silver NPs evidenced by the SEM and AFM analysis of the original and laser irradiated samples (c.f., Figures 7 and 8). According to it, evaporation at glancing angles leads to the growth of elongated particles of different sizes and shapes but with a preferential orientation of their longest dimension perpendicular to the evaporation

direction (Figure 11a). The actual averaged anisotropy of the evaporated particles depend on both the amount of evaporated material and the zenithal angle of deposition as supported by the Plasmon shifts reported in Table 1. According to the optical characterization results summarized in this table, when the deposited amount of silver increases, percolation of the NPs takes place (Figure 11b) and the SPR absorption becomes substituted by a continuous and intense reflection behavior. Our results have also shown that the rather scattered distribution of particle sizes characteristic of the GLAD samples (c.f. Fig. 4 b) can be modified by laser irradiation. At the lowest irradiance values, the initial broad L-SPR band splits into two, one of them shifted to longer wavelengths (c.f., Figure 9a). According to Figure 11c, these changes may be attributed to the preferential merging of the smallest particles along the largest axis of the biggest ones and to a change in the edge sharpness and likely the planarity of the resulting particles. The sum of all these effects would produce an additional increase in the optical anisotropy of the system and lead to an enhancement of the dichroism.

At medium irradiance values the T-SPR and L-SPR maxima shifts continuously to shorter wavelengths while the optical anisotropy is progressively lost with the value of this parameter (c.f., Figures 9a and 9b). In the final situation, the irradiated samples have lost their optical anisotropy and their spectra are characterized by a complex band at around 400 nm where up to three different components can be differentiated. This progressive change can be attributed to a progressive detachment of the particles from the surface and the adoption of a spherical shape (Figure 11d). A partial melting of the silver aggregates, in line with previous studies on ns-laser interaction with metallic silver [Yang K. Y., Appl. Phys. Lett. 2009][Link S., Phys. Chem. B 1999] can be claimed to justify these results. In agreement with Figures 7e and 7f, this final situation would be characterized by a wide distribution of quasi spherical particles sizes, thus accounting for the three features observed in the transmission spectra of the highly irradiated samples. It is worth stressing that even if on average no large variations in particle sizes exist between the "as prepared" and the highly irradiated samples, large changes in the SPR maxima and the development of dichroism appear in the GLAD grown and mildly laser treated NPs. The aforementioned factors of NP high aspect ratio, interaction with the substrate and/or the development of sharp corners [Rycenga M., Chem. Rev. 2011][Zeng J., Chem. -Eur J.] would be the factors contributing to both the initial enhancement of dichroism at low laser irradiances and its removal and red shift in the position of the Plasmon maxima after irradiating with high laser powers.
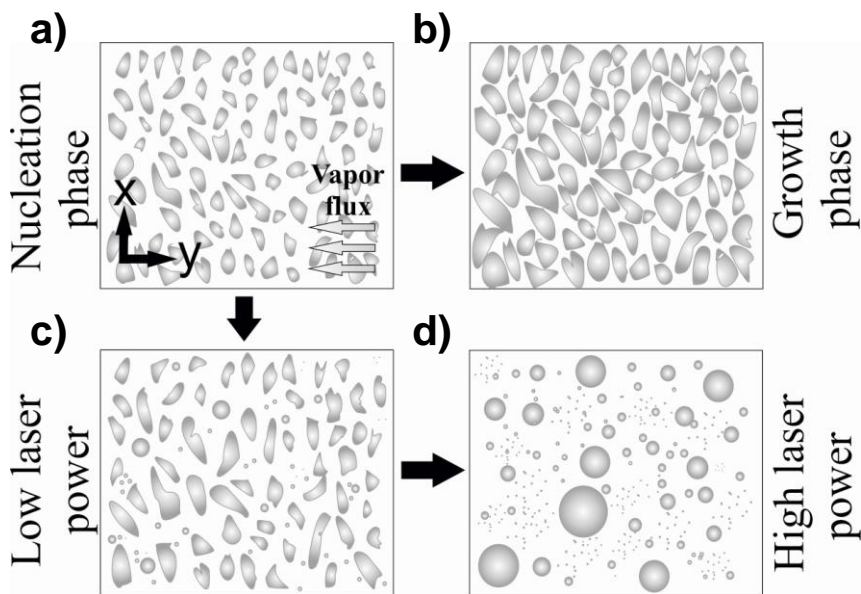
Figure 11. Scheme showing the evolution of particle size and shapes upon laser irradiation of the silver NPs prepared under GLAD configuration. a) Elongated silver NPs grown by GLAD. b) Percolation of the NPs to form a continuous granular film. c) Effect of low laser irradiances on the NP size and shapes. d) Effect of high laser irradiances on the NP size and shapes.

5.4. Conclusion

In the previous results and discussion it has been shown that silver NPs prepared by evaporation at glancing angles depict a strong dichroism that can be enhanced by a mild laser irradiation. These optical effects were attributed to the formation of flat and elongated NPs when the evaporation is carried out along this geometry and to the modification of these morphological characteristics when the prepared samples are treated with laser. By controlling the amount of deposited material, the evaporation angle and the laser irradiance, it has been possible to successfully prepare a large set of dichroic color patterns. The simplicity of the method, not requiring of any template or 1D periodic roughness effect of the substrate or the use of complex lithographic techniques and its compatibility with any kind of substrate material are some of the most advantageous features of the procedure. Its use for optical encoding by moving the laser beam along certain predefined patterns is likely one of the applications of the developed technology with more potentiality.

5.5. References

Álvarez R. et al., Theoretical and experimental characterization of TiO_2 thin films deposited at oblique angles. Journal of Applied Physics D: Applied Physics 44(38), 385302 (2011).

Bloemer M. J. et al., Optical properties of submicrometer-size silver needles. Physical Review B 37(14), 8015-8021 (1988).

Camelio S. et al., Anisotropic optical properties of silver nanoparticle arrays on rippled dielectric surfaces produced by low-energy ion erosion. Physical Review B 80(15), 155434 (2009).

Cattaruzza E. et al., Modifications in silver-doped silicate glasses induced by ns laser beams. Applied Surface Science 257(12), 5434-5438 (2011).

Cavallini M., Albonetti C., Biscarini F., Nanopatterning soluble multifunctional materials by unconventional wet lithography. Advanced Materials 21(10-11), 1043-1053 (2009).

Chaney S. B., Zhang Z. Y., Zhao Y. P., Anomalous polarized absorbance spectra of aligned Ag nanorod arrays. Applied Physics Letters 89, 053117 (2006).

Chiaretta D. et al., Structural and optical characterization of Rf-sputtered metal cluster doped silica thin films. Journal of Non-Crystalline Solids 352(23-25), 2548-2552 (2006).

Ebothé J. et al., Laser treatment of seed-mediated nanostructured silver film morphology. Materials Chemistry and Physics 113(1), 187-191 (2009).

Ehrenreich H., Philipp H. R., Optical Properties of Ag and Cu. Physical Review 128(4), 1622-1629 (1962).

Ferraris M. et al., Silver nanocluster–silica composite coatings with antibacterial properties. Materials Chemistry and Physics 120(1), 123-126 (2010).

Fort E., Ricolleau C., Sau-Pueyo J., Dichroic thin films of silver nanoparticle chain arrays on facetted alumina templates. Nano Letters 3(1), 65-67 (2003).

Giannini V. et al., Plasmonic Nanoantennas: Fundamentals and Their Use in Controlling the Radiative Properties of Nanoemitters. Chemical Reviews 111(6), 3888-3912 (2011).

Gonzalez-Garcia L. et al., TiO_2–SiO_2 one-dimensional photonic crystals of controlled porosity by glancing angle physical vapour deposition. Journal of Materials Chemistry 20(31), 6408-6412 (2010).

Han R. et al., Size-dependent photochromism-based holographic storage of Ag/TiO_2 nanocomposite film. Applied Physics Letters 9(22), 221905 (2011).

Hawkeye M. M., Brett M., Glancing angle deposition: Fabrication, properties, and applications of micro- and nanostructured thin films. Journal of Vacuum Science and Technology A 25, 1317-1335 (2007).

Hodkinson I., Wu Q. H., Inorganic Chiral Optical Materials. Advanced Materials 13(12-13), 889-897 (2001).

Horcas I. et al., WSXM: A software for scanning probe microscopy and a tool for nanotechnology. Review of Scientific Instruments 78, 013705 (2007).

Hutter E., Fendler J. H., Exploitation of Localized Surface Plasmon Resonance. Advanced Materials 16(19), 1685-1706 (2004).

Kaempfe M. et al., Formation of metal particle nanowires induced by ultrashort laser pulses. Applied Physics Letters 79(12), 1876-1878 (2001).

Lee M. H., Dobson P. J., Cantor B., Optical properties of evaporated small silver particles. Thin Solid Films 219(1-2), 199-205 (1992).

Liang H. et al., Highly Surface-roughened "Flower-like" Silver Nanoparticles for Extremely Sensitive Substrates of Surface-enhanced Raman Scattering. Advanced Materials 21(45), 4614-4618 (2009).

Linnert T. et al., Long-lived nonmetallic silver clusters in aqueous solution: preparation and photolysis. Journal of The American Chemical Society 112(12), 4657-4664 (1990).

Link S., El-Sayed M., Spectral properties and relaxation dynamics of surface plasmon electronic oscillations in gold and silver nanodots and nanorods. Journal of Physical Chemistry B 103(40), 8410-8426 (1999).

Liu Y. et al., Angle dependent surface enhanced Raman scattering obtained from a Ag nanorod array substrate. Applied Physics Letters 89, 173134 (2006).

Mertens H., Polman A., Plasmon-enhanced erbium luminescence. Applied Physics Letters 89, 211107 (2006).

Messier R., Venugopal V. C., Sunal P. D., Origin and evolution of sculptured thin films. Journal of Vacuum Science and Technology A 18, 1538-1545 (2000).

Mitchell C. E. J. et al., Direct observation of behaviour of Au nanoclusters on TiO_2(1 1 0) at elevated temperatures. Surface Science 490(1-2), 196-210 (2001).

Nouneh K. et al., Kinetics of picosecond laser treatment of silver nanoparticles on ITO substrate. Journal of Alloys and Compounds 509(40), 9663-9668 (2011).

Rycenga M. et al., Controlling the synthesis and assembly of silver nanostructures for plasmonic applications. Chemical Reviews 111(6), 3669-3712 (2011).

Sanchez-Valencia J. R. et al., Incorporation and Thermal Evolution of Rhodamine 6G Dye Molecules Adsorbed in Porous Columnar Optical SiO_2 Thin Films. Langmuir 25(19), 9140-9148 (2009).

Sanchez-Valencia J. R. et al, Tunable In-Plane Optical Anisotropy of Ag Nanoparticles Deposited by DC Sputtering onto SiO_2 Nanocolumnar Films. Plasmonics 5(3), 241-250 (2010).

Sanchez-Valencia J. R. et al., Selective dichroic patterning by nanosecond laser treatment of Ag nanostripes. Advanced Materials 23(7), 848-853 (2011).

Siozios A. et al., Optical Encoding by Plasmon-Based Patterning: Hard and Inorganic Materials Become Photosensitive. Nano Letters 12(1), 259-263 (2012).

Suzuki M. et al., Direct formation of arrays of prolate Ag nanoparticles by dynamic oblique deposition. Japanese Journal of Applied Physics 44 (II, 1-7), L193 (2005).

Tawfick S, De Volder M, Copic D, Park S J, Oliver C R, Polsen E S, Roberts M J and Hart A J 2012 *Adv. Mater.* **24** 1628.

Van Kranenburg H., Lodder C., Tailoring growth and local composition by oblique-incidence deposition: a review and new experimental data. Materials Science and Engineering R: Reports 11(7), 295-354 (1994).

Wenzel T. et al., Shaping nanoparticles and their optical spectra with photons. Applied Physics B 69(5), 513-517 (1999).

Yang K. Y., Choi K. C., Won C., Surface plasmon-enhanced spontaneous emission rate in an organic light-emitting device structure: Cathode structure for plasmonic application. Applied Physics Letters 94(17), 173301 (2009).

Zeng J., Roberts S., Xia Y., Nanocrystal-Based Time–Temperature Indicators. Chemistry – A European Journal 16(42), 12559-12563 (2010).

Zijlstra P., Chon J. W. M., Gu M., Five-dimensional optical recording mediated by surface plasmons in gold nanorods. Nature 459, 410-413 (2009).

6. 1D Photonic Sensors
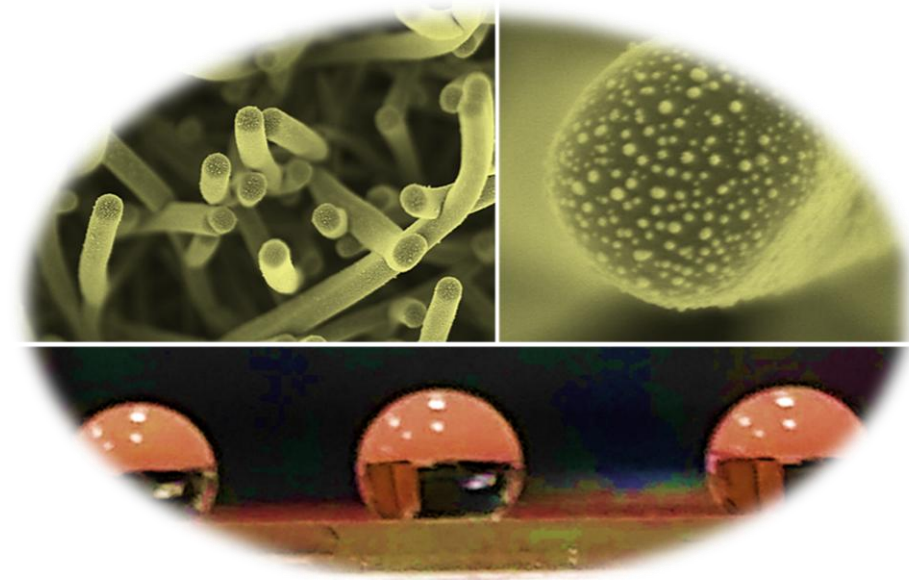
Abstract

The fabrication of large area substrates for SERS of Rh6G is addressed by two distinct vacuum approaches. In one case, Ag NPs deposited by GLAD on fused silica are treated with a Nd:YAG laser and their SERS effect compared. In the second approach, Ag NPs of three nominal thicknesses are deposited on nano-TiO_2 NTs of two different wall thickness, achieving highly hydrophobic and adequate SERS surfaces. The Raman enhancement factor is calculated in all the cases and correlated to the samples characteristics.

An oxygen photonic sensor based on the excitonic luminescence of ZnO NTs is devised and tested.

6.1. Introduction

6.1.1. 1D TiO$_2$ NTs decorated with Ag NPS for SERS

The **ideal** analytical technique should have at least the following characteristics [Skoog D. A., Saunders College Publishing 1998]:

- High sensitivity and wide dynamic range: Extremely low detection limits, i.e. single molecule detection, should be feasible. The technique should allow the determination and analysis of the whole concentration range of the analyte, from one molecule to 100% concentration. In order to avoid saturation of the detector employed, dilution is frequently done, but it slows down the process.
- High accuracy and precision: no systematic bias and high reproducibility.
- Suitable for both quantitative and qualitative analysis.
- Noninvasiveness and Nondestructiveness: It is desirable to recover the sample intact, without being subjected to any chemical or physical changes.
- Great flexibility: any substrate should be appropriate and sample preparation should not be necessary.
- Lack of interferences: absolute selectivity; capacity to distinguish between two almost identical analytes.
- Fast, highly automatized and low cost: high throughput, little or no personnel required, inexpensive overall operation, no tedious calculations, etc.
- Compactness and Portability (optional): ideal for field analysis and not limited to fixed locations.

Obviously, there is not still an analytical tool that satisfies all these requirements. However, last decades advancements in many instruments components and the introduction of new and more powerful methods for analysis have pushed the boundaries of many analytical techniques, which now comply many of the above mentioned characteristics. This is especially true for Raman spectroscopy, a non-destructive technique, with negligible or no sample preparation, unprecedented high specifity, high flexibility, rapid, adequate for quantitative and qualitative analysis, and even with portable equipment available (there are plenty of portable Raman spectrometers manufacturers) [Schmitt M., J. Raman Spectrosc. 2006].

Given its versatility and non-destructive nature, Raman spectroscopy is currently applied in broad range of fields [Das R. S., Vib. Spectrosc. 2011]:

- Forensic science: applied to the analysis of explosives, drugs, fibers, body fluids, lipsticks, paints, etc.
- Biology and diagnosis: useful living cells/tissue biochemical information without the need of markers, strains or fixatives. Evaluation of the quality of natural food. Mapping of the components presents in cells. Analysis of biomedical materials and disease diagnosis.
- Environmental monitoring: Hazardous agents in trace amount in environmental samples can be safely monitored on-line.
- Crystalline studies: Raman is sensitive to the degree of crystallinity and orientation in a sample. However, a quantitative measure of crystallinity requires comparison and calibration with other techniques.
- Materials science: highly adequate for the characterization of superconductors, semiconductors, carbonaceous materials, polymers, archaeological materials, nanomaterials, etc.
- Pharmaceuticals: characterization of drugs formulations, detection of counterfeit medicines, investigation of kinetic processes and even the ability to discern enantiomers of chiral substances and to determine the absolute configuration of small molecules (Raman optical activity spectroscopy) [Parchaňský V., RSC Adv. 2014][Kiefer J., Analyst 2015].

Basic principles of Raman spectroscopy

Upon irradiation of a molecule with monochromatic radiation, three distinct phenomena can occur: absorption, reflection or scattering of incident light. There are two types of scattering, elastic and inelasric illustrated in Figure 1. In the former, the incident photon does not suffer any change in its frequency or energy (*Rayleigh scattering*), whereas in the latter the photon can gain vibrational energy from the molecule increasing its frequency (*anti-stokes Raman scattering*), or it can lose energy by interaction with the molecule resulting in a lower frequency photon (*stokes Raman scattering)*.* These shifts in frequency of the inelastically scattered light are characteristic of the nature of each bond (vibrations) present in the molecule, providing with structural and chemical information. Moreover, not all vibration modes associated

*Stokes Raman scattering is by far the strongest of the two inelastic scattering processes

with a bond are observable; according to a gross selection rule a mode will be Raman active if it involves a change in the polarizability of the molecule [Das R. S., Vib. Spectrosc. 2011][Atkins P., Oxford 2010].
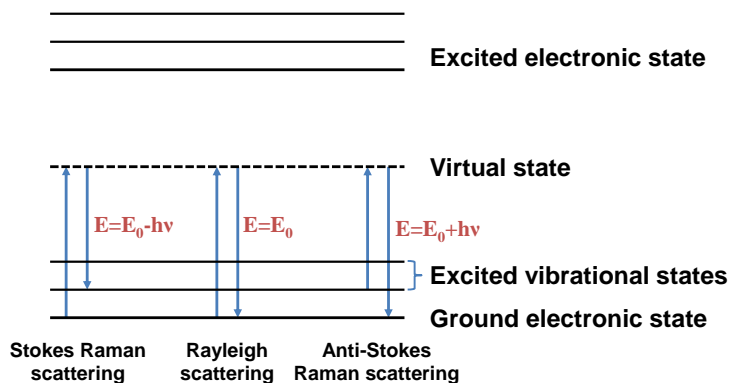

Figure 1. Mechanism of Raman scattering.

One the key aspect of Raman spectroscopy is the high selectivity of the technique. Almost identical compounds usually present well differentiated features in the Raman spectrum that can be used as a "fingerprint" of every molecule. As a representative example, Figure 2 shows a series of Raman spectra of saturated fatty acids (only differing in the number of carbon atoms in the chain) and unsaturated fatty acids (with differences in the position and number of the double carbon bonds), that present features which allow to differentiate them [Wu H., PNAS 2011]. This aspect of the Raman spectroscopy is very attractive since it has potential applications as for instance in medicine, since it allows to detect "a priori" unknown substances in the blood or cells.
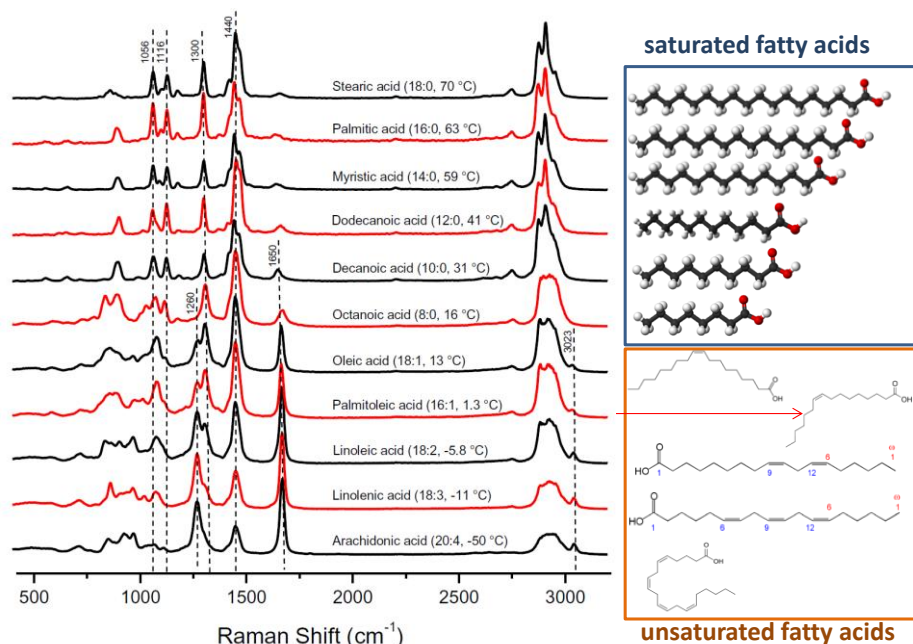
Figure 2. Raman spectra of representative saturated and unsaturated fatty acids. The saturated fatty acids differ in the number of carbons and the unsaturated fatty acids in the position and number of the carbon double bonds [Wu H., PNAS 2011].

Raman spectroscopy usually requires high intensity lasers. The photons from the laser are absorbed from the molecules (even if the molecules do not possess any electronic transition at the laser energy), exciting the electrons to a virtual energy state. This transition is highly unlikely and only around 10^{-6} of the incident photons are scattered, hindering the detection of molecules present at low concentrations. This lack of sensitivity (conversion efficiency of the Raman effect) is one of the major drawbacks associated to Raman spectroscopy. The conversion efficiency of the Raman effect can be enhanced for what is known as "resonance conditions", that occur when the incident laser energy is close to a real electronic transition of the molecule.

The relatively low intensity of Raman signals can be enormously enhanced by several orders of magnitude by taking advantage of a strengthening effect present in the proximity of metallic nanostructrures, known as Surface Enhanced Raman Scattering (SERS). The interaction between light and the surface electrons of the conduction band of a metal nanoparticle (MNP) causes their collective oscillation with a resonant frequency dependent on their identity and composition, size, geometry, dielectric environment and particle-to-particle distance of the MNPs. This phenomenon is

generally known as surface plasmon resonance (SPR) and is manifested in transition metal nanoparticles as an absorption peak in the visible range.

As already mentioned, only a small fraction of incident photons are inelastically scattered, making the technique unsuitable for trace analysis. The intensity of Raman scattering, and thus the intensity of Raman signals, is proportional to the scattering cross-section, the intensity of the radiation source and the amount of analyte. The light source intensity can be augmented, but it might probably entail degradation of organic samples. The amount of analyte is something one would like to minimize, so the most convenient signal enhancing mechanism must involve the cross-section (σ). In SERS, the Raman signal of molecules adsorbed to or between MNPs is increased due to two distinct enhancement mechanisms: electromagnetic (EM) and chemical. The EM factor arises from the coupling of the EM field of the conduction band of a MNP and coulombic fields of a near or adsorbed molecule, distorting its electronic structure and thus its polarizability (α). Due to the fact that σ is proportional to the square of α, the intensity suffers a dramatic increase. The chemical mechanism also affects α by means of more subtle chemical interactions between the NPs and the adsorbate. The EM mechanism is considered to have a much higher enhancing factor over the chemical one, of around two orders of magnitude, and it can influence molecules up to circa 10 nm away from the NP [Petryayeva E., Anal. Chim. Acta 2011].

When the distance between adjacent MNPs is much smaller than the wavelength of light, their transient dipoles couple and their EM fields interfere coherently, giving rise to the so-called hot spot regions (Fig. 3). This is the reason behind even higher Raman signal enhancement factors compared to single or isolated MNPs.
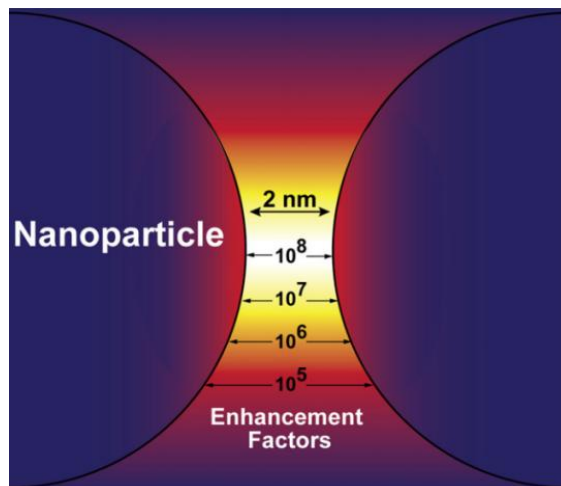
Figure 3. Evolution of SERS enhancement factor as a function of the relative position in hot spot [Petryayeva E., Anal. Chim. Acta 2011].

One of the main drawbacks for the fabrication large area SERS sensors is the homogeneus dispersion of those "hotspots" on the samples, since they are usually synthesized by electron-lithography, which requires expensive equipment and time. One alternative is to create nanoparticles with different shapes such as nanorods, cubes prisms or stars [Yang Y., Nanotechnology 2006][Rycenga M., J. Phys. Chem. Lett. 2010][Mulvihill M. J., J. Am. Chem. Soc. 2010], which provoke an enhancement of the electromagnetic field in the vicinity of the edges. For example, the dispersion of colloidal solutions of silver particles with different shapes on a glass slide has shown a very high SERS activity for detecting organic molecules [Yang Y., Nanotechnology 2006][Rycenga M., J. Phys. Chem. Lett. 2010][Mulvihill M. J., J. Am. Chem. Soc. 2010]. The effect of the "hotspot" regions produced by elongated silver particles fabricated in the previous chapter by GLAD has been tested in terms of the SERS efficiency to detect very diluted solutions.

To fabricate highly efficient SERS-based sensors, an additional property needs to be taken under consideration: the water contact angle, in particular hydrophobicity. TiO_2 is very well known to be hydrophobic, with water contact angles that depend strongly on the microstructure, porosity and crystallinity. The hydrophobic surfaces allows to concentrate molecules a certain micro-area, which can be even reduced to nano-areas for superhydrophobic surfaces (with WCA>175º). The idea behind is simple: for the sensing of a very diluted solution of a certain analyte, a very small volume drop needs to be placed at the proximity of the metal nanoparticles. This is easily

achievable by spreading the metallic nanoparticles on a surface, and drying the required drop on it. Although the principle is easy, the drops are spread on the surface, covering areas that can range from cm to nm sizes (depending on the volume of the initial drop). The radius (r) of the liquid- solid interface (remember it contains the required analyte molecules) follow the equation of the Figure 4, where R is the radius of the spherical drop prior to the deposition on the surface and θ is the water contact angle [De Angelis F., Nat. Photonics 2011]. In the examples of the figure, superhydrophilic (θ=0.4º) and superhydrophobic (θ=179.8º), for a small volume drop of 5 μL (Radius, R=1.06 mm), the liquid-solid area would change from 295 to 4.3×10^{-5} mm^2, respectively.

$$r/_R = \left(\frac{4}{\beta}\right)^{1/3} \sin \theta, \quad \beta = (2 + \cos \theta)(1 - \cos \theta)^2$$
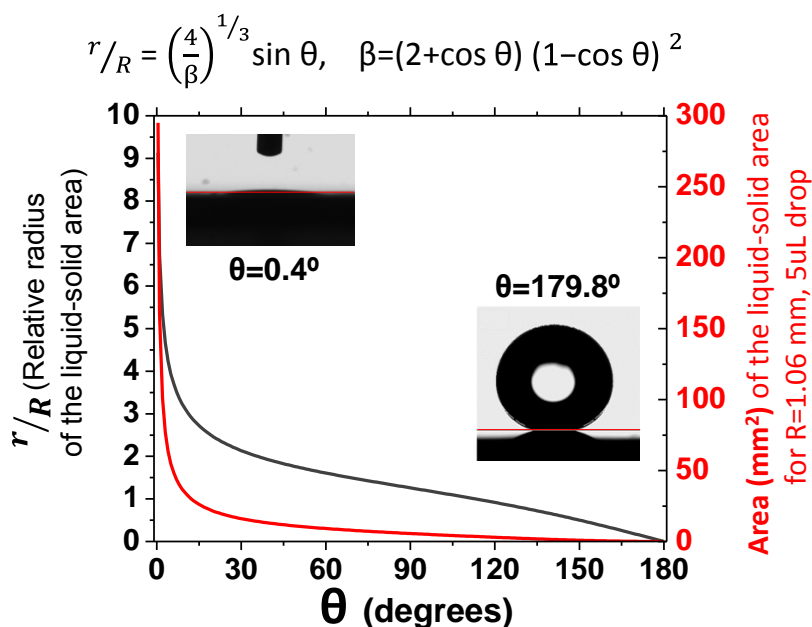

Figure 4. Liquid-solid relative radius with respect to the spherical water drop prior to deposition on the surface (black line) and area covered by a 5μL water drop (red line).

This effect for superhydrophobic surfaces (that differs eight orders of magnitude which respect to superhydrophilic) brings the area covered by the liquid to the sub-squared microns range, and therefore enhances significantly the surface concentration of the analyte. This concentration effect has been recently used to enhance the detection limit of SERS based sensors to the femto- and atto- molar range, extremely close to single molecule detection [De Angelis F., Nat. Photonics 2011]. Although these authors reached the ultimate detection limit (single-molecule), the methodology to fabricate these sensors is based in electronic lithographic techniques, which are very

expensive and do not allow the fabrication of big areas. Some of the superhydrophobic-SERS-based sensors are presented in Figure 5, where it can be observed the complexity of the nanopilars, whith metallic nanoantennas with conical shapes and concentric resonators [De Angelis F., Nat. Photonics 2011]. The state of the art in SERS still lacks the production of cheap and big areas sensors, to detect ultralow concentrations of unknown compounds.
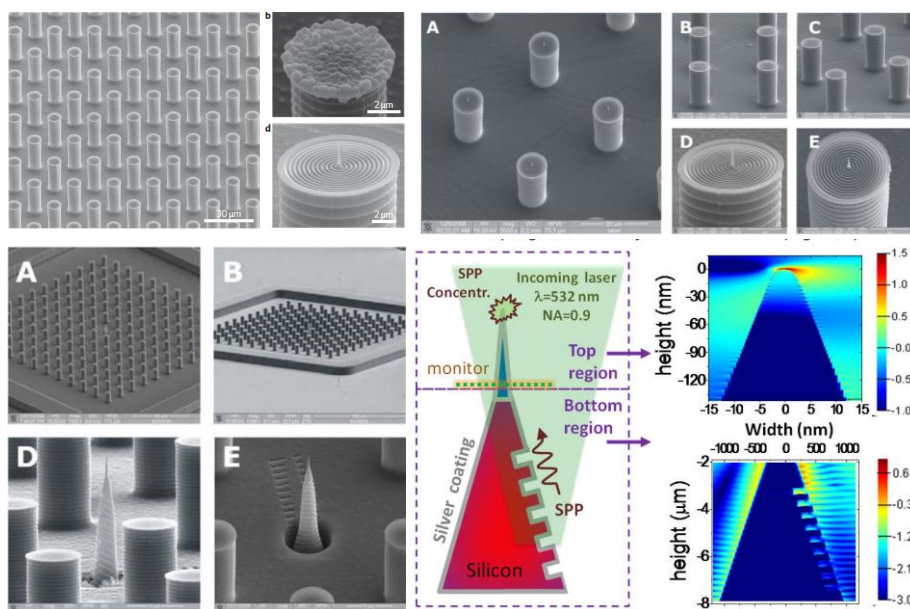

Figure 5. Examples of nanopillars and silver nanoantenas fabricated by electron beam lithography for hydrophobic SERS applications [De Angelis F., Nat. Photonics 2011].

In this chapter we have followed two strategies for the fabrication of SERS-based sensors. Both sensors, although based in the SERS amplification provoked by silver nanoparticles, intended to take advantage of different film properties:

1. In an attempt to increase the amount of "hotspot" regions in the sample, elongated silver nanoparticles were deposited by the Glancing Angle Deposition (GLAD) technique. The idea was to enhance the Raman signal at the proximity of the elongated particles to detect low concentration of molecules.

2. The second strategy was based on the hydrophobicity of silver nanoparticles deposited on top of TiO_2 NTs. The hydrophobicity of the samples linked to the SERS effect inherent to metallic nanoparticles made possible their use as ultra-sensitive sensors for detection of low concentrated solutions.

Due to the limitation of the two laser sources available in the laboratory, the molecule Rhodamine 6G was chosen as reference analyte, since it possesses an absorption band at 530 nm, very close to the 532 laser wavelength accessible in the laboratory. This allowed us to work under resonance Raman conditions, and therefore augmenting the SERS effect of the sensors. All of these effects (SERS, hydrophobicity and resonance) were joined together to increase the sensitivity of the sensors to the maximum.

The ultimate detection limit achievable by SERS is one molecule and outstanding achievement that has already been realized in 1997 [Lee E. C., Annu. Rev. Phys. Chem. 2012]. However, it must be emphasized that the devices used to achieved such detection limits tend to be quite complex and expensive to fabricate, thus making them completely inadequate for the development of a SERS array. Here, the intention was not to attain extremely low detection limits, but rather to fabricate larger area SERS devices suitable for the production of arrays.

6.1.2. ZnO Nanotubes-Based Photonic Sensor

ZnO thin films and nanostructures have been widely applied as gas and volatile organic compounds sensors through both conductometric and optical approaches [Zhang Y., J. Phys. Chem. C 2009][Cho S., Sens. Actuat. B 2012][Sanchez-Valencia J. R., J. Phys. Chem. C 2014]. In a recent article of the *Nanotechnology on Surfaces* research group [Sanchez-Valencia J. R., J. Phys. Chem. C 2014], the fabrication of a photonic oxygen sensor based on the excitonic luminescence of ZnO polycrystalline films prepared by PECVD was presented. The material exhibited a high sensibility to oxygen present in the environment or dissolved in water. Herein, the same concepts have been applied to the realization of a reversible oxygen photonic sensor based on the UV emission quenching of the ZnO NTs.

6.2. Objectives

❖ Fabricate high-density hydrophobic 1D TiO_2 nanotubes decorated with Ag NPs evaporated in two different manners: thermal evaporation and e-beam evaporation at glancing angles, both in vacuum.

❖ Characterize these nanostructures by electron microscopy techniques: SEM, HAADF-STEM y HRTEM.

❖ Test the SERS capabilities of these samples for different thicknesses of NT walls and amount of deposited Ag. In the case of GLAD Ag, study the effect of laser treatment for two irradiances on SERS effect.

❖ Produce samples large enough for the analysis of an analyte array.

6.3. Methodology

6.3.1. 1D TiO$_2$ NTs decorated with Ag NPS for SERS

a) Substrates preparation

Samples were fabricated on n-type Si(100) from Topsil semiconductor materials. The substrates were cutted in different sizes, ranging from 2.5x2.5 cm to 5x2.5 cm, rinsed in acetone and dried with a flux of dry nitrogen. Fused silica from Sico Technology GmbH was cleaned in the same manner and employed as reference.

b) Samples fabrication

An initial layer of approximately 200 nm of mesoporous TiO$_2$ was deposited by PECVD to provide the substrates with certain roughness. The deposition conditions were: plasma source operating at 650 W, substrates at room temperature, total pressure in the chamber was around 8.6x10^{-3} mbar, and oxygen was employed as reactive gas.

Pc was purchased from Fluka and used as received. Pc NWs were grown by OPVD under the following conditions: Ar pressure of 0.02 mbar, substrate temperature of 180 ºC and growth rate of 0.4 Å/s (measured by QCM). The final thickness was set to 1.2 kÅ in QCM, which corresponds roughly to 2-3 μm long NWs.

Nano-TiO$_2$ was deposited with two different thicknesses, 200 nm and 400 nm. The deposition conditions were as follow: plasma source operating at 650 W, Ar and O$_2$ were used in a relation of 9:1, while keeping the total pressure close to 6x10-3 mbar. Again, the deposition was carried out at room temperature. The samples were later heated in air at a temperature of 350 ºC to fully with a ramp of 2ºC/min to evacuate the Pc resulting in highly dispersive hollow nanostructures. A higher annealing to 400ºC was also performed.

Silver NPs were deposited by two different techniques:

I) PVD under vacuum at a base pressure of 10^{-5} mbar. Three different nominal thickness were tested, 1, 2 and 3 nm.

II) GLAD, see Chapter 5 (Methodology section). The silver nominal thickness was 1 nm and the evaporation angles used were: 65º and 85º.

c) Analyte rhodamine 6G solutions

Rhodamine 6G was purchased from Sigma-Aldrich and used as received. The solutions were prepared with ultrapure Milli-Q water immediately before use. In order to prepare all solutions, only successive dissolutions of 1:10 or 1:100 were made.

d) Characterization

Structural characterization. SEM micrographs were acquired in a Hitachi S4800 working at 2 kV. The samples were dispersed onto Holey carbon films on Cu or Ni grids from Agar scientific for TEM characterization. HAADF STEM was carried out with a FEI Tecnai Orisis TEM/STEM 80-200 and a FEI Tecnai F30 S-Twin STEM microscopes operating at 200 kV .

Micro-Raman spectroscopy. All measurements were carried out in LabRAM Horiba Jobin Yvon spectrometer equipped with a confocal microscope with a 100X objective and a green laser of 532 nm wavelength. The measurement conditions are mentioned in the results section for each case.

6.3.2. 1D ZnO sensor

a) Samples fabrication

A thin layer of columnar SiO_2 (300 nm) was deposited by glancing angle deposition (GLAD) as described elsewhere [Sanchez-Valencia J. R., Langmuir 2009], which has no fluorescence under the UV light excitation employed. ONWs of MePTCDI were then grown by PVD, which were ultimately covered by a 200 nm ZnO shell as described in chapter 2 and emptied after heating in vacuum at 350 ºC for 3 hours. Reference thin film sensors were also fabricated.

b) Characterization

SEM micrographs were acquired in a Hitachi S4800 working at 2 kV. UV-Vis analysis of the samples was done in a Cary 100 spectrometer from Varian. Fluorescence spectra were recorded in a Jobin Yvon Fluorolog-3 spectrofluorometer using an excitation wavelength of 280 nm and scanning the emission spectra between 350 and 750 nm with a 2 nm monocromator step.

6.4. Results and discussion

6.4.1. GLAD of silver for the fabrication of SERS sensors

The elongated silver nanoparticles illuminated with laser at different powers fabricated by GLAD in the previous chapter were tested here in terms of the Raman enhancement to detect the organic molecule Rh6G in water solutions.

The original silver deposited at 65º and 85º with a nominal thickness of 10 nm present slightly different water contact angles of 105 and 97º as it is shown in Figure 6. The laser illumination at low powers of the 65º deposited GLAD sample increases the WCA, reaching a maximum of 115º at 188 kWcm^{-2}. By contrast, the illumination at 550 kWcm^{-2} drastically decreases the WCA to 94º. The GLAD at 85º presents an initially lower WCA, which decreases slowly with the laser power, reaching a minimum of 88º for the illumination at 942 kWcm^{-2}. As it was detailed in the Figure 4 of the Introduction, the WCA determines the area of the liquid-solid area and therefore it can alter significantly the surface concentration of the analyte sensed. By contrast, the relatively low changes in the WCA would not change dramatically this liquid-solid area, which is indicated in the Figure 6 for some representative laser powers.
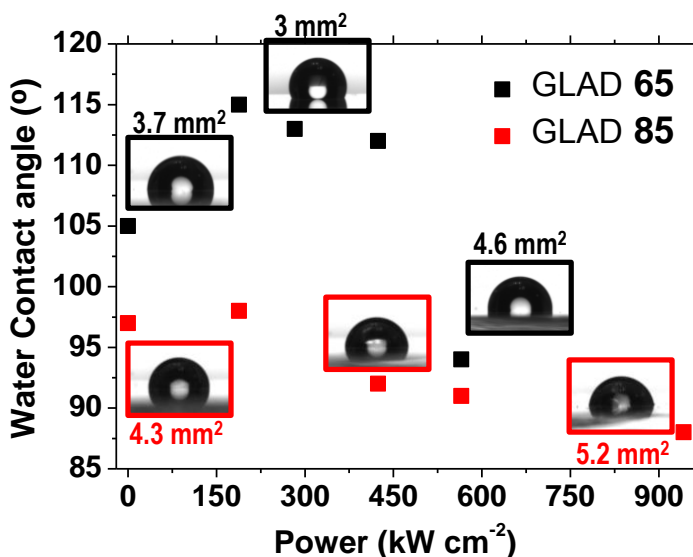

Figure 6. Evolution of the Water Contact Angle as a function of the Laser Illumination Power. A picture of a water drop of 1uL deposited on top of some representative samples are included together with their corresponding liquid-solid area.

For the evaluation of the SERS effect, drops of 5 μL of water solutions of Rhodamine 6G (Rh6G) at 10^{-6}, 10^{-8} and 10^{-10} M were utilized. The evaporation of the drops was performed under ambient conditions and was completed in around 30-35 minutes. The GLAD samples deposited at 65º of evaporation angle present a relatively high intensity of the SERS signal, which allows the detection of concentrations as low as 10^{-8} M. It needs to be remarked that the bands in the spectrum correspond to the Rh6G Raman bands, easily recognizable by the intense narrow bands at 612, 1306, 1362 and 1506 cm^{-1}. The intensity of the Rh6G signal decreases for laser illuminated samples, making impossible to detect concentrations of 10^{-8} M samples for powers higher than 565 $kWcm^{-2}$. This behavior is reasonable at high powers, since the model proposed in the previous chapter assumes that the elongated nanoparticles get more rounded. By contrast, for low laser powers the dichroism reported in the previous chapter was enhanced, indicating that the aspect ratio of the nanoparticles increases. But this effect occurs at the expense of reducing the number of them by fusion of close particles. The results of Figure 7 indicate that the SERS signal of these samples cannot be enhanced by laser illumination, obtaining a monotonous decrease of the sensitivity of the sensor.

By contrary, the GLAD samples at 85º, which initially present a very poor sensitivity, present an intensification of the SERS signal for low laser power illumination (see Figure 7 bottom). It can be easily observed in the Figure 7 that the illumination at 188 and 424 $kWcm^{-2}$ enhances significantly the signal, although not enough to allow the detection of 10^{-8} M. In addition, the illumination at higher power (942 $kWcm^{-2}$), decreases the SERS signal, in concordance with the model proposed in the previous chapter.
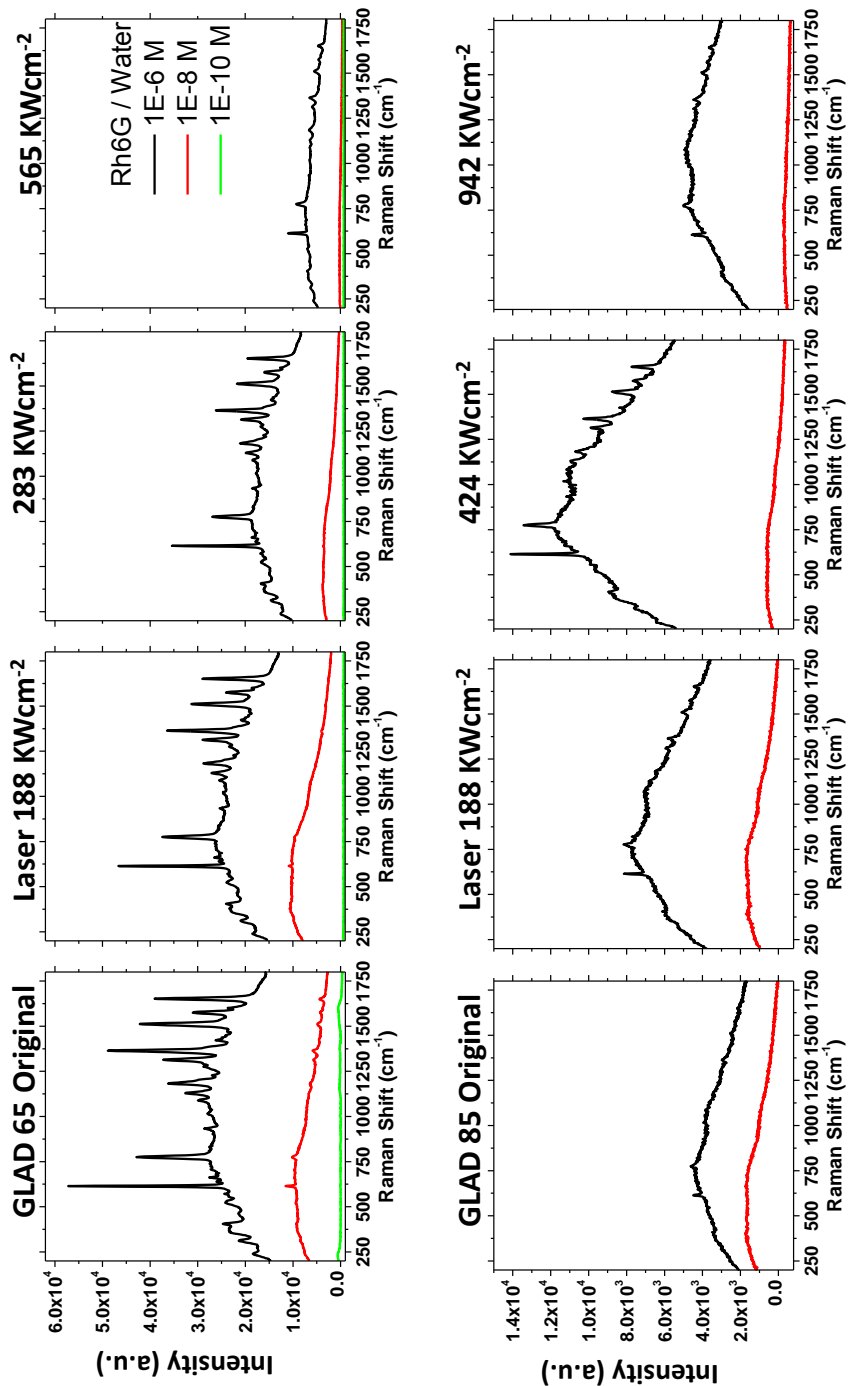
Figure 7. Raman spectra of 5uL drop of a solution Rh6G/water at the indicated concentrations dried at the surface of silver deposited by GLAD at 65º (top) and 85º (bottom) treated with different laser powers.

The results support that the increase/decrease in the aspect ratio of the nanoparticles can be used to tune the sensitivity of the SERS based sensor. To quantify this behavior the Enhancement Factor (EF) is often used, that is defined as:

$$EF = \frac{\frac{I_{SERS}}{N_{SERS}}}{\frac{I_R}{N_R}} \quad \text{(Equation 1)}$$

Where I_{SERS} and I_R are the Raman intensities measured on the SERS and non-SERS samples (fused silica slide), respectively, divided by the number of molecules probed by the Raman microscope in every case (N_{SERS} and N_R). The Enhancement Factors are calculated assuming that the molecules are homogeneously distributed over the liquid-solid area (discussed in the introduction), which depend on the WCA shown in Figure 6. Figure 8 shows the enhancement factors calculated from the Raman signal for the silver elongated particles deposited by GLAD as well as the laser treated samples at different laser powers. The initial Enhancement Factor for GLAD at 65º depicts a relatively high value of 5350. This EF decreases drastically for laser illuminated samples, reaching a minimum of EF=800 for the sample treated with 565 kWcm^{-2}. By contrast, the EF for GLAD silver at 85º presents a very low value of 90, which increases for low laser powers, reaching a maximum of 780 for 424 kWcm^{-2}. For higher illumination powers, the EF decreases to a minimum of 165 for 942 kWcm^{-2}. The low values of EF observed for the original GLAD 85 in comparison with the GLAD 65 can be understood taking into consideration the different silver amount for both samples. The evaporation rate in GLAD is proportional to the cosine of the deposition angle, meaning that for a 10 nm of nominal thickness (measured at 0º), the silver deposited at 65 and 85 degrees is 4.2 and 0.9 nm, respectively. To take into consideration this effect, the Figure 8 also shows the Enhancement Factors for 1 and 2 nm silver thin films deposited at a normal configuration. These two samples present a different EF of 1120 and 270 for 2 and 1 nm silver thickness, respectively.
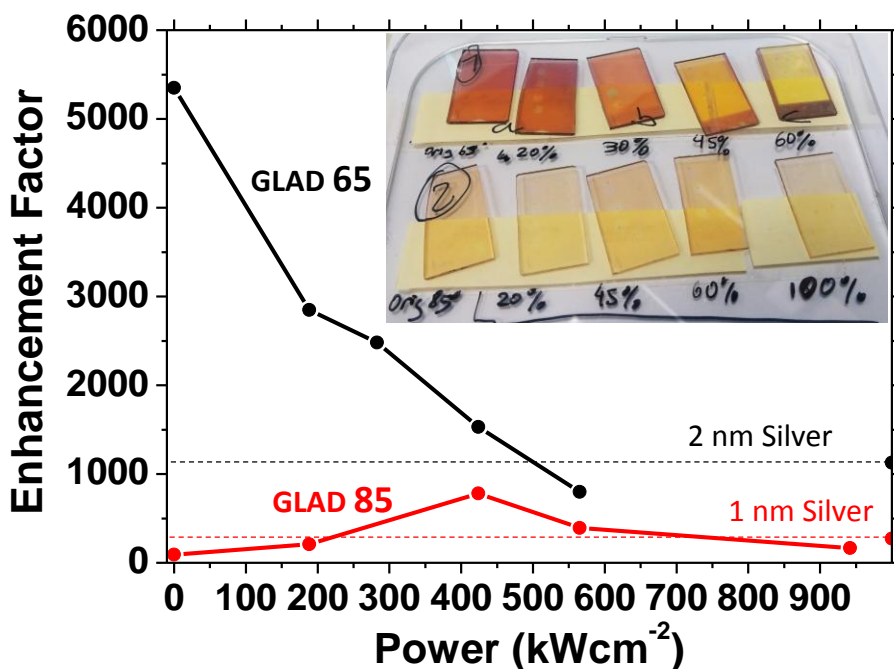
Figure 8. SERS Enhancement factors calculated for the silver deposited by GLAD at 65º (black) and 85º (red) treated with different laser powers. For comparison, a 2 nm and 1 nm silver film deposited under a perpendicular angle (0º).

Although the enhancement factors obtained by means of Eq.1 are not very high compared to NPs deposited at normal geometry (dashed lines in Figure 8), the results indicate that the geometrical modification of silver elongated particles by laser irradiation can be used to tune the Surface Enhanced Raman signal.

6.4.2. TiO$_2$ NTs / Ag NPs for the fabrication of SERS sensors

The second type of SERS-based sensor devices fabricated are based in TiO$_2$ Nanotubes. The fabrication procedure is depicted in Figure 9 and comprises several steps which can be divided in 4 stages:

I)   Formation of a thin layer of mesoporous TiO$_2$ by PECVD which provides the necessary roughness for the growth of PC NWs by OPVD.

II)   Growth of the nano-TiO$_2$ shell by PECVD and empty of the nanostructures by heating in air (not shown).

III)   Deposition of Ag NPs by PVD in high vacuum.

IV)   Deposition of the analyte solution drops, dry in air and sensing with Raman spectroscopy.
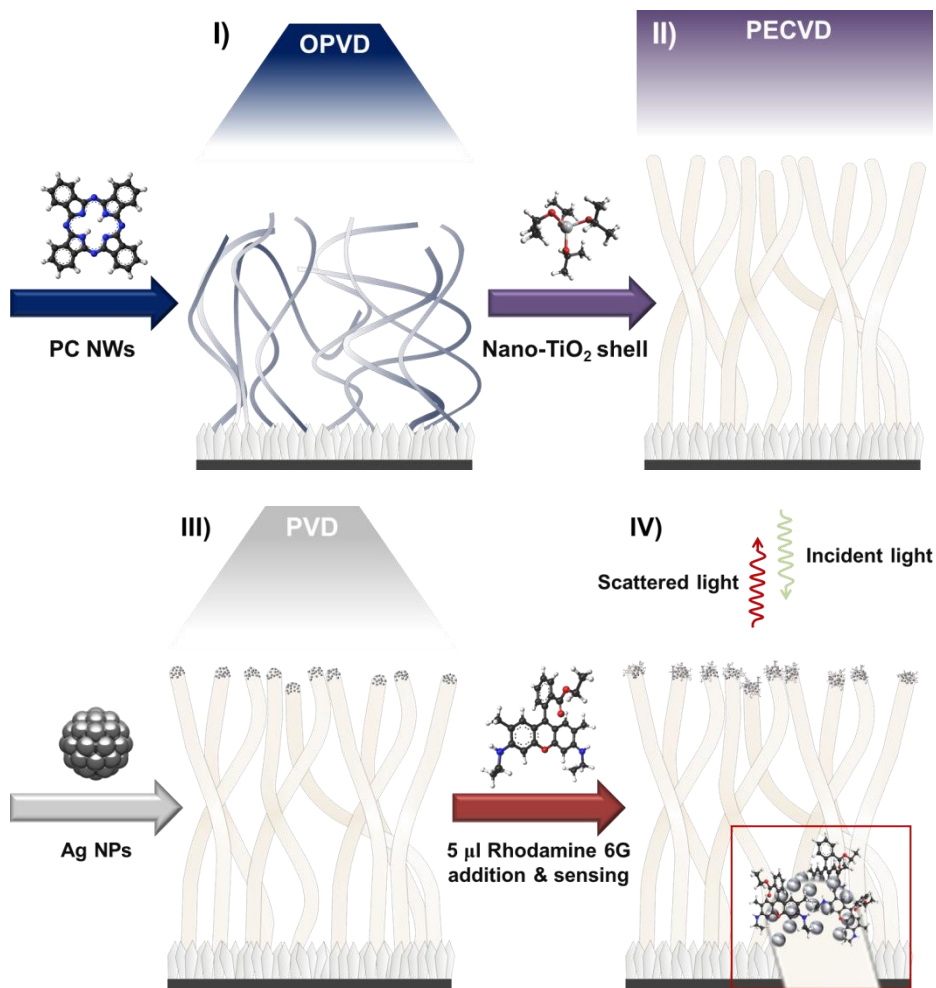
Figure 9. Fabrication of a SERS-based sensor device: I) formation of the NWs, II) growth of the TiO₂ shell, III) deposition of Ag NPs, and IV) analyte deposition and measurement.

The PECVD of nano-TiO$_2$ shells was accomplished by employing a deposition atmosphere highly rich in Ar and with a minority of O$_2$ [Borrás A., J. Electrochem. Soc. 2007]. The surface of the prepared shells is relatively smooth with no mesopores, presenting good characteristics to act as a 1D substrate for Ag NPs. In addition, the amorphous TiO$_2$ (as well as silver nanoparticles) has no Raman activity and therefore it will not produce any interference with the analyte signal.

245

Furthermore, as seen in Figure 6 a)-b), with only 200 nm of TiO_2 most of the tips are pointing upwards, although the rest of the NW might be oriented randomly. With 400 nm, Figure 10 c)-d), the orientation of the tips and the NWs body is much more evident. Moreover, the high density of NTs that has been achieved with this process is demonstrated in Figure 10 e), where a relatively large area was scanned. The tips of the 400 nm NTs present tiny pores as a consequence of postheating (Fig. 10 d); the internal NW pressure generated as a consequence of Pc sublimation is released through that pores.
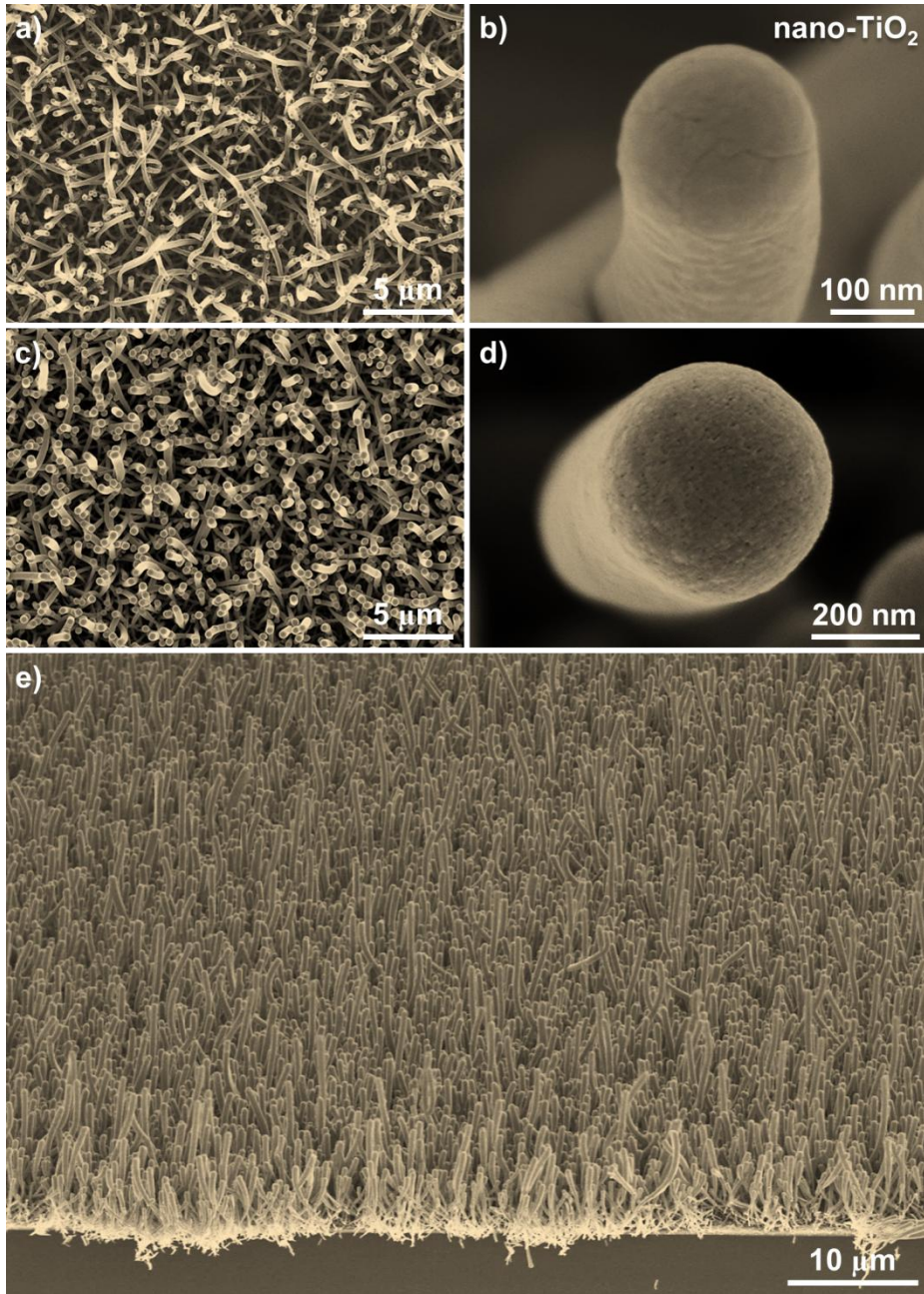
Figure 10. SEM images of nano-TiO$_2$ shell of 200 nm (a) and 400 nm (c). Magnified view of 200 nm (b) and 400 nm (d) nano-TiO$_2$ NWs. Panel (e) is a SEM cross section with a tilt angle of 15º of the sample with a 400 nm shell.

Figure 11 shows the homogeneous microstructure and smooth surface formed under the TiO$_2$-nanoporous conditions (Fig. 11 a). In this case, the shell presents a continuous cross section (Fig. 11 c) with non-appreciable pores (it has not been annealed, so the organic material is still inside). In previous articles it has been demonstrated that these experimental conditions lead to the formation of microporous thin films with a relative high volume of pores. Nano-TiO$_2$ shells are amorphous since the fabrication process has been carried out at room temperature.
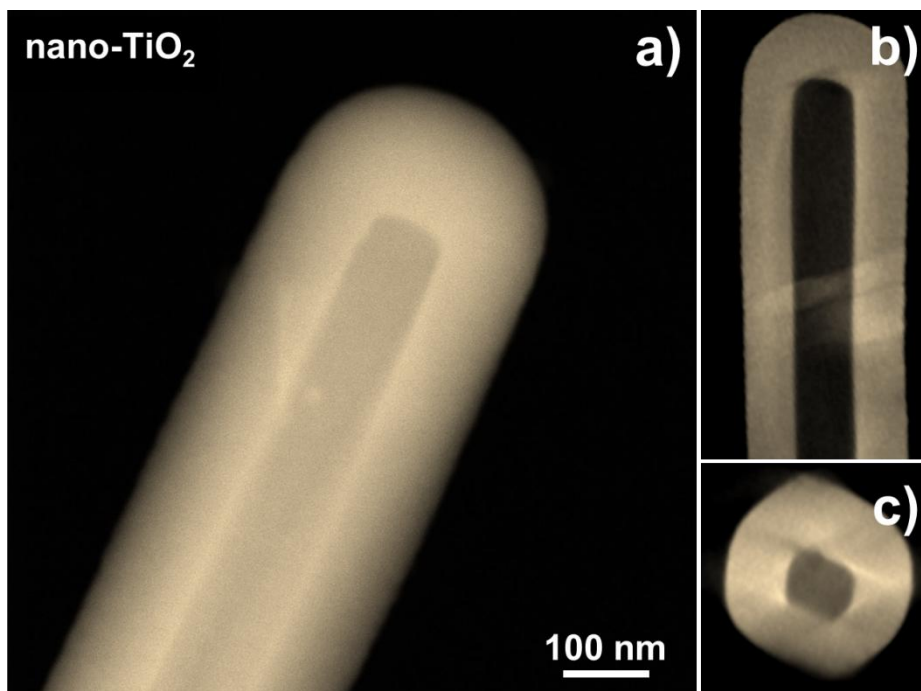

Figure 11. Nano-TiO$_2$ Nanotubes. HAADF-STEM (a-c) characterization of nanotubes formed by continuous nanoporous TiO$_2$ walls. Panel a) presents the smooth surface characteristic of this TiO$_2$ deposited by PECVD at RT under argon/oxygen plasma. The wall is a continuous layer showing no visible pores by HAADF-STEM. Snapshots of the HAADF-STEM 3D reconstruction show the homogeneous thickness of the TiO$_2$ wall (b) and the squared cross section of the core of the nanotube (c).

By controlling the deposition rate and time, Ag NPs of different size distribution were obtained by PVD in high vacuum. The SEM picture of Figure 12 shows the Ag NPs obtained by deposition of 2 nm of Ag (nominal) on Si (100). The nanoparticles are rounded with an average NP area of 78.4 nm^2 calculated with ImageJ, resulting in a surface plasmon resonance absorption situated at 430 nm.
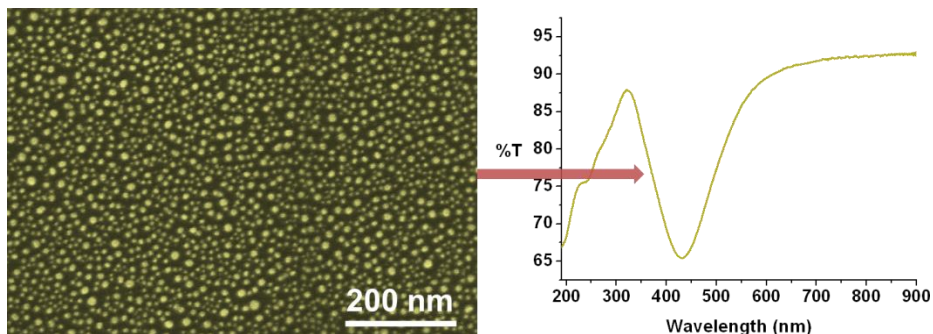
Figure 12. SEM image of 2 nm (nominal) Ag NPS on Si (left) and its corresponding UV-Vis spectrum on fused silica (right).

Nano-TiO$_2$ NWs were then decorated with Ag following the same methodology, obtaining the hierarchical nanostructures observed in Figure 13 for a 400 nm NW and 1, 2 and 3 nm Ag NPs. The sample with 1 nm nominal thickness presents a very few amount of silver nanoparticles at the tip of the NTs while the sample with 3 nm Ag possesses very big nanoparticles. By contrast, it can be noticed a quite uniform distribution of Ag NPs all over the TiO$_2$ NWs for the sample with 2 nm of nominal Ag thickness For a very efficient SERS-based sensor, a compromise must be reached between the surface density of NPs and their size. There is an optimal diameter value for Ag NPs situated around 30-50 nm where the enhancement factor is maximum and tens of nanometers in size difference lead to orders of magnitude of difference in Raman intensities [Stamplecoskie K. G., J. Phys. Chem. C 2011]. Comparing the SEM pictures with the literature, the sample with 2 nm of silver thickness has a very high potential for SERS.
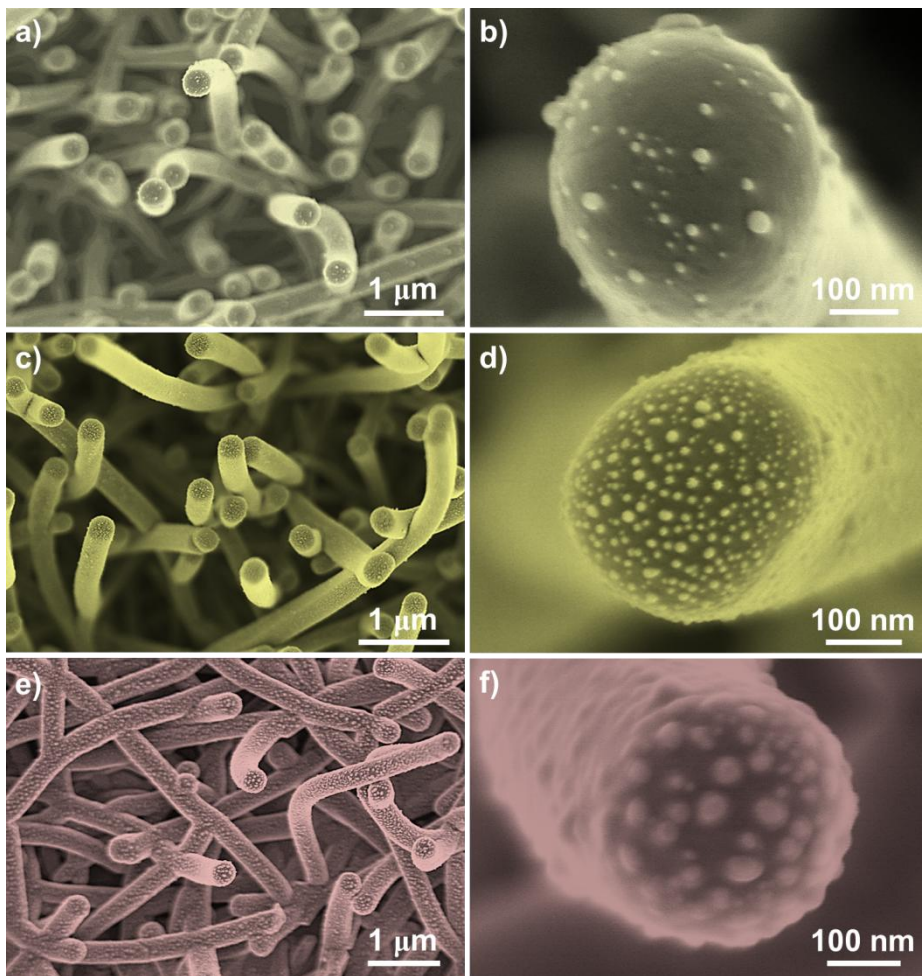
Figure 13. SEM images of 1 (a,b), 2 (c, d) and 3 nm (e,f) nominal Ag NPS on 400 nm nano-TiO$_2$ NTs at two different magnifications.

The crystallinity of the Ag NPs may be appreciated in the HRTEM micrograph of Fig. 10 a) and even with atomic-resolution detail when zooming in one NP just as in Fig. 10 b). The Ag NP digital diffractogram pattern (DDP) corresponds to the [011] zone axis of the cubic phase of Ag.
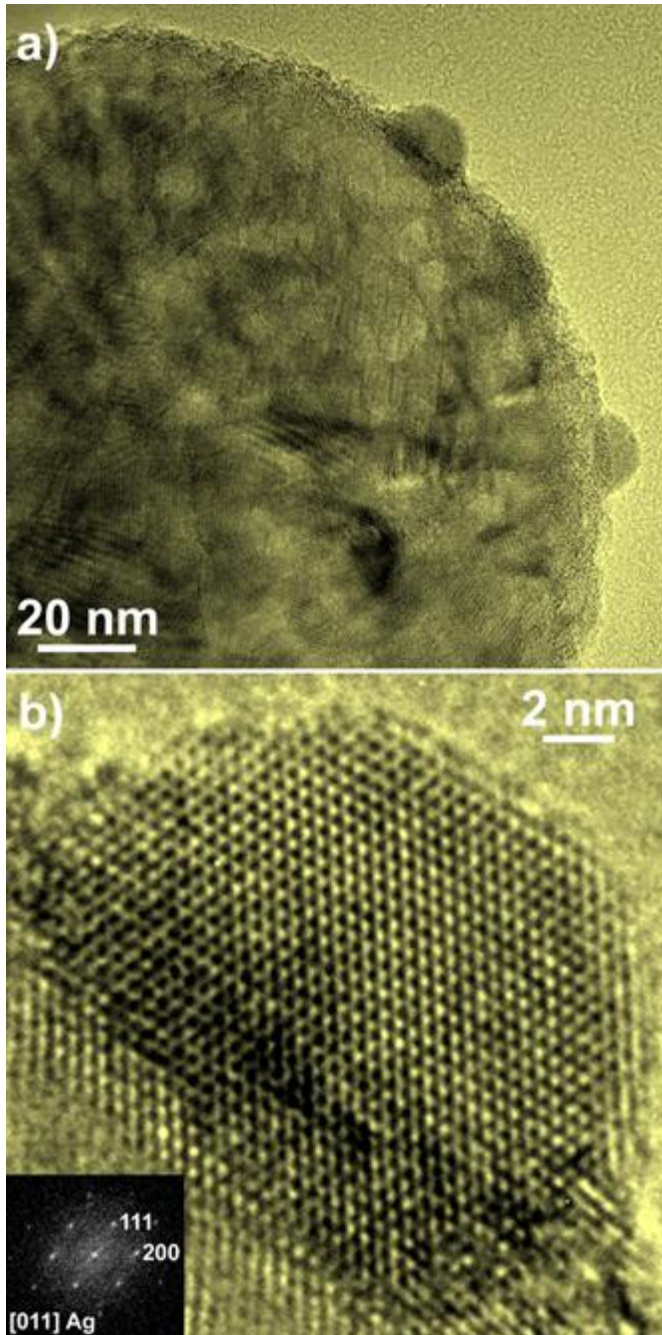
Figure 14. High-Resolution TEM micrograph of 130 nm (nominal) Ag NPS on 400 nm nano-TiO$_2$ NWs (a) and a magnified view of one Ag NP (b). The DDP of the selected NP is presented in the inset.

As it has been mentioned in the introduction, the water contact angle is crucial for an improved sensitivity of the sensor since the hydrophobic samples present a reduced liquid-solid contact area that concentrates the analyte molecules as the water drop is drying. The water contact angle of the studied samples depends on the thickness of silver deposited. Figure 15 presents a series of pictures showing the evaporation of a 5uL drop of water on top of TiO_2 NTs with different silver thickness of 1 (left), 2 (middle) and 3 nm (right). Figure 16 shows the fitted WCA at different times of the evaporation process for the different samples investigated, where it can be appreciated that the WCA of 1nm Ag thickness is lower than the 2 and 3 nm. The Initial WCA also affects to the evaporation time since the higher the initial WCA, the lower evaporation time for the three samples investigated. One important characteristic of the evaporation process is that the liquid-solid area is not significantly altered during the evaporation process. To visualize this effect, higher magnification pictures have been taken at different evaporation times for TiO_2 NT with 1 nm Ag sample (see Fig. 15 right). The initial contact diameter (top) is approximately the same than the one taken at 35 min (bottom). This measured diameter is around 1.87 mm, meaning a solid-liquid contact area of 2.75 mm^2, very close to the theoretical one calculated in the Figure 4, 2.6 mm^2 for an initial WCA of 125º (see Figure 16). This is a very important aspect of the evaporation process, since the assumed area where the analyte is distributed is the theoretically calculated from the initial WCA and therefore the subsequent calculations of the Enhancement Factors will be valid.

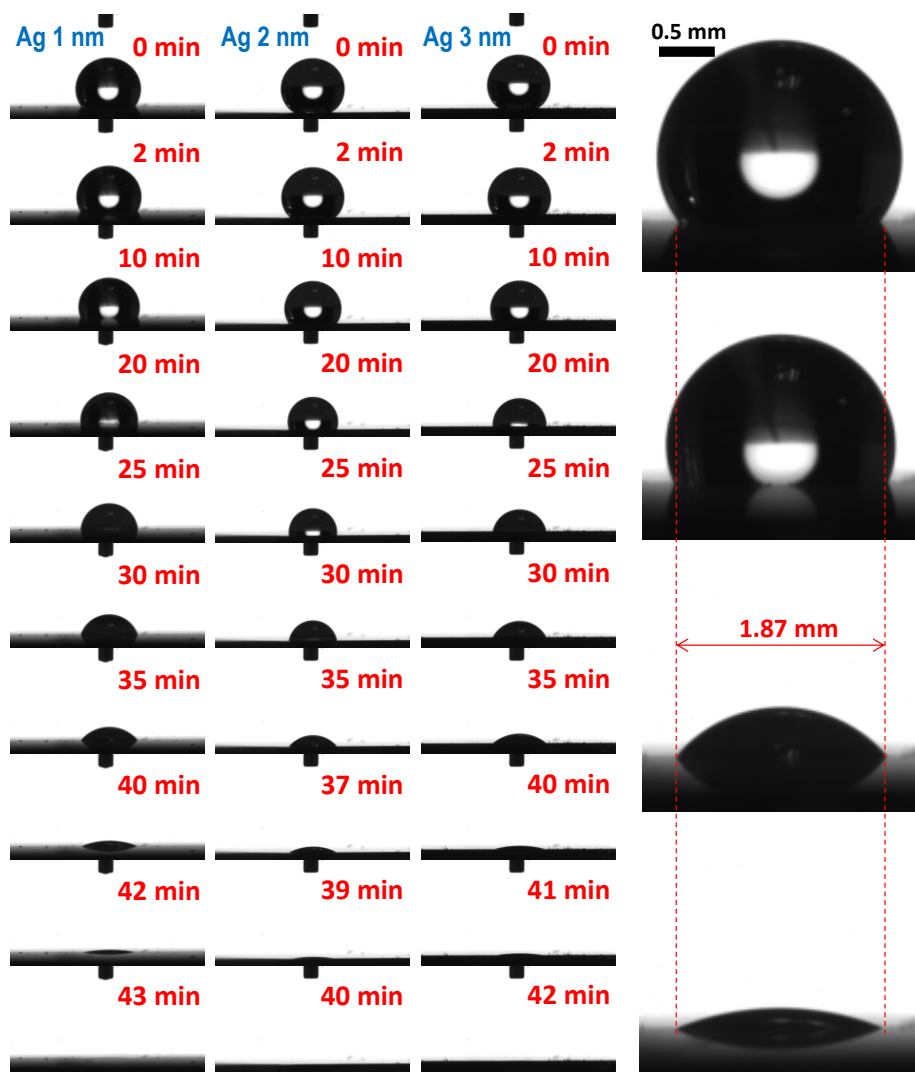**Figure 15.** Left) Pictures of the evaporation process of a 5uL water drop deposited on top of TiO₂ NTs samples with different thickness of silver at different times. Right) a higher magnification image showing the liquid-solid diameter contact.
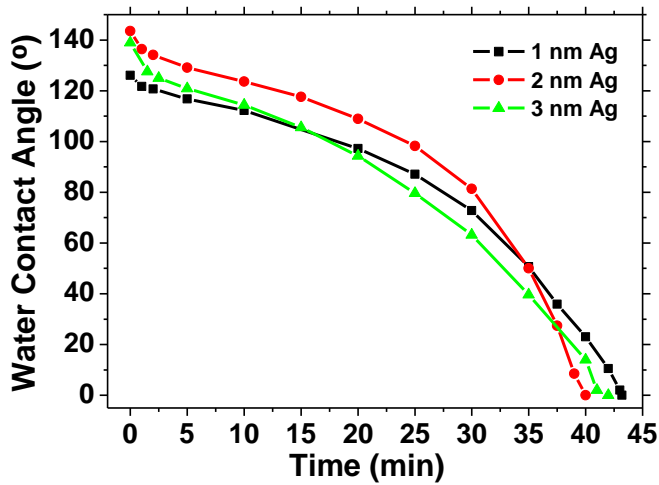
Figure 16. Water Contact Angle evolution of the evaporation process for a 5uL water drop deposited on TiO$_2$ NTs samples with 1, 2 and 3 nm thickness of silver.

One of the most important aspects of the sensors proposed in this chapter is that they can be fabricated over big areas with a very high homogeneity. Figure 17 shows some pictures of samples deposited on 2x3 cm silicon substrates, although samples bigger than 10x10 cm can be fabricated in the laboratory. The a-c) pictures of the figure show how an array of drops can be deposited on the samples and after their evaporation (d,e) can be easily located with the Raman microscope. The Figure 17 e) shows an enhanced contrast area indicated by a red square in d), where it can be observed the three drops evaporated area. The fact that the dried drops can be observed to the naked eye makes the subsequent Raman measurement much easier.
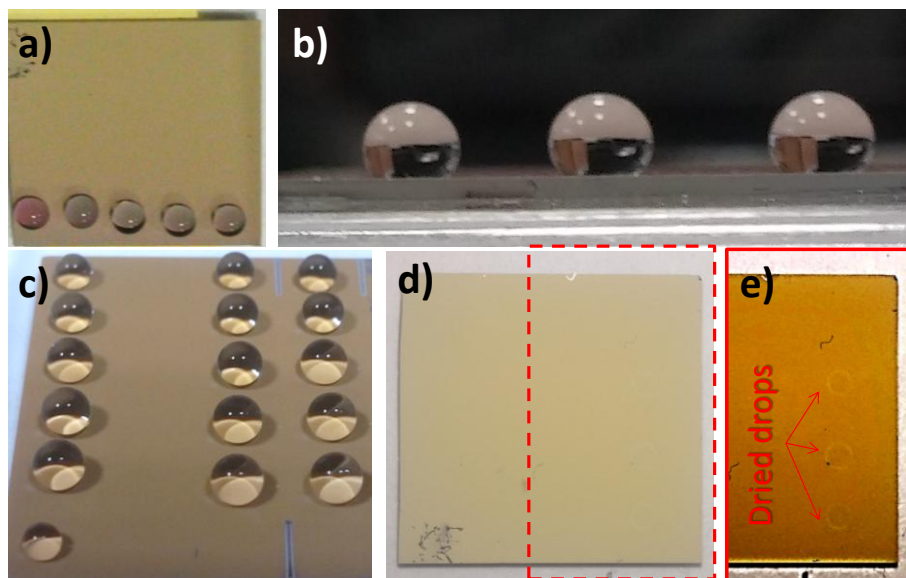
Figure 17. a-c) Pictures of the SERS samples with 5uL drops of Rh6G/water at different concentrations. d) Picture of a TiO_2 NT with 2nm Ag after the drop evaporation. e) Same picture than d) with enhanced contrast to make visible the evaporated drops.

In order to optimize the Raman signal, a preliminary study was performed to optimize several aspects of the sensor. First the annealing temperature used for the evacuation of the phthalocyanine: the sublimation temperature of the Pc molecules is very close to the crystallization temperature of the TiO_2. The crystallization to anatase (it needs to be reminded that is performed prior to the silver deposition), that in principle is not unfavorable for SERS, showed a very poor Raman signal at low Rh6G concentrations. This effect can be observed Figure 18 (green curve for the sample annealed to 400ºC), where the measurement of a 5 μL droplet of Rh6G/water at 10^{-10} M does not show any band apart from the three anatase peaks at 399, 520 and 643 cm^{-1}.The second aspect studied for the SERS sensor optimization was the TiO_2 shell, where two different thickness of 200 and 400 nm were fabricated. It can be easily recognized that the thicker shell of 400 nm presented an improved sensitivity.
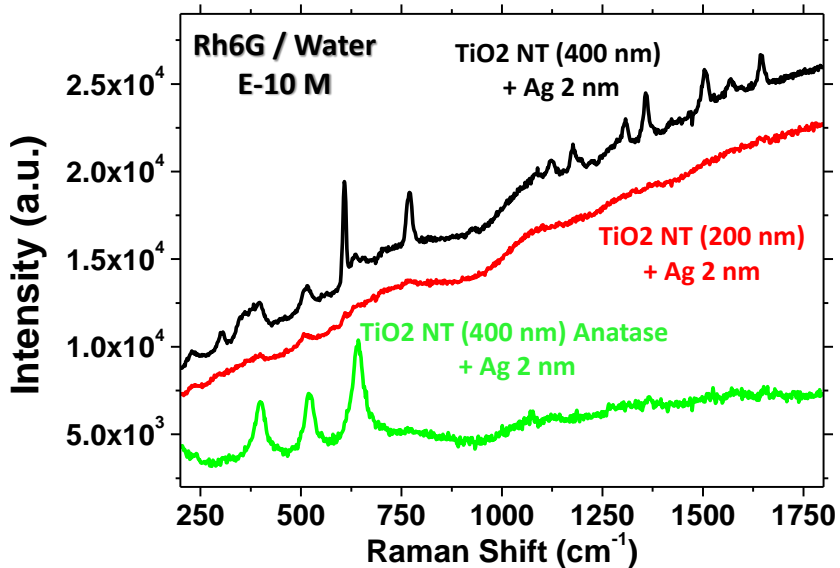
Figure 18. Raman spectra of a 5 μL drop of a solution Rh6G/water at 10^{-10} M dried at the surface of TiO_2 NT with 2 nm of silver nominal thickness. The difference between the samples are the TiO_2 shell thickness (black and green curve 400 nm, red curve 200 nm) and the temperature used in annealing step to remove the Pc (black and red curve 350ºC, green curve 400ºC).

Once that the effect of the TiO_2 Nanotubes has been studied, the next step is the optimization of the silver thickness. For the evaluation of the SERS effect, drops of 5uL of water solutions of Rhodamine 6G (Rh6G) at 10^{-6}, 10^{-8}, 10^{-10} and 10^{-12} M were utilized. As it is shown in Figure 19, the amount of silver deposited on the TiO_2 NTs completely modifies the SERS spectra. The sample with 1 nm of nominal thickness presents a very poor Raman signal where the minimum concentration detected was 10^{-8} M. The same behavior can be observed for the sample with 3 nm of silver thickness although with a higher intensity than the case of 1 nm. The Raman spectrum measured for the case of a dried drop of 10^{-6} M has been also added for comparison. By contrast, the sample with 2 nm of thickness presented a very high SERS signal, where it was possible to detect down to 10^{-12} M. Taking into account the volume of the drop (5 μL), only 3 millions of molecules have been deposited over an area of ca. 1.3 mm^2 (liquid-solid area of Figure 4 for a WCA of 143º).
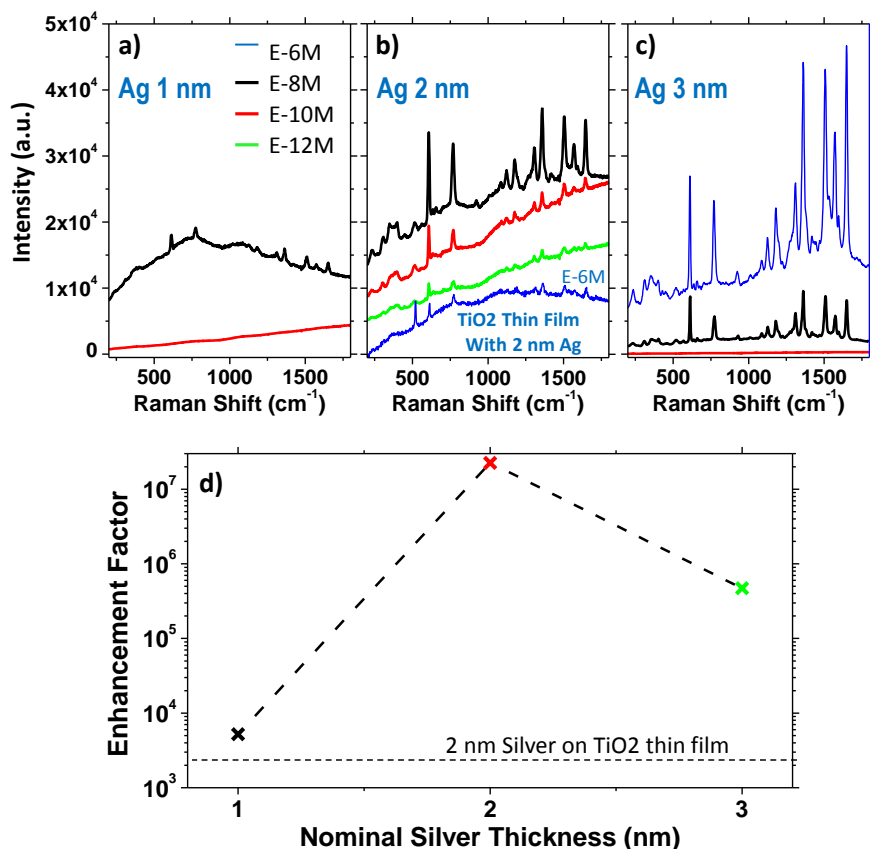
Figure 19. a-c) Raman spectra of 5 μL drops of Rh6G/water solutions at the indicated concentrations dried at the surface of TiO$_2$ NT with 1 (a), 2 (b) and 3 nm(c) of silver thickness. In b) also the Raman spectrum of 2 nm silver deposited on an equivalent TiO$_2$ thin film was added for comparison. d) SERS Enhancement factors calculated for the three silver thicknesses investigated and the TiO1 thin film reference with 2 nm Ag.

The calculation of the Enhancement Factor was performed in the same way than for silver deposited by GLAD. Figure 19 d) shows the enhancement factors calculated for the 1, 2 and 3 nm silver thicknesses. It can be observed that the 1nm Ag present a low Enhancement Factor (EF=5000), in the same order of magnitude than the 2 nm of silver deposited on an equivalent TiO$_2$ thin film (EF=2800). The deposition of 2 nm of silver thickness over the TiO$_2$ NT increases drastically the Enhancement Factor, reaching a very high value of 2x10^7. This EF is consistent with the sensitivity limit of 10^{-12} M shown in Figure 19 b). By contrast, the deposition of higher silver amount (3

nm), decreases the EF to 4x10^{5}. The very high sensitivity obtained together with the compatibility for big area deposition, open a new and very promising way for the utilization of TiO_2 NTs decorated with silver NP for future SERS based nanosensoric applications.

6.4.3. 1D ZnO Nanotubes-Based Photonic Sensor

Figure 20 shows the photoluminescence spectra of a reference nanocolumnar polycrystalline ZnO film and ZnO NTs sample. These two samples were deposited simultaneously on fused silica substrates, for the sake of comparison. The polycrystalline ZnO emission spectrum is dominated by a sharp and intense exciton ultraviolet (UV) emission at ~380 nm and a broad and low intense visible emission in the region 450-700 nm. The ZnO visible emission is attributed to defects as zinc vacancies (blue emission) and oxygen vacancies (green emission) [Sanchez-Valencia J. R., J. Phys. Chem. C 2014]. In the present case, the level of such defects is low, as addressed by the low intensity of the visible emission what has been attributed to a suppression of band-gap electronic defects by hydrogen species from the plasma during the synthesis.

The photoluminescence spectra of the ZnO NTs samples show a defect related visible emission that is even of lower intensity than the reference film. This proves that the deposition on the 1D nanostructured substrates do not increase the number of defects in the resulting conformal oxide network. However, the PL spectra of both samples are not equivalent. Thus, while the PL band of the reference peak is sharper and centered at 378 nm, being originated by recombination of free excitons, the emission of ZnO nanotubes is broader and red-shifted, which indicates the domain of lower energy phonon replicas components [Romero-Gómez P., J. Phys. Chem. C 2010]. These results are congruent with the higher stress, smaller crystallite size and lower texture development of the ZnO NTs sample with respect to the reference sample as discussed in Chapter 1. These factors likely explain the observed shift and overall shape of the UV PL of the ZnO NTs. Moreover, a certain additional contribution to the observed red-shift of the UV PL band due to the anisotropic character of the oriented ZnO NTs emission cannot be discarded [Gao M., J. Phys. Chem. C 2010]. The excitonic emission of the ZnO NTs is a function of the oxygen concentration in the environment.
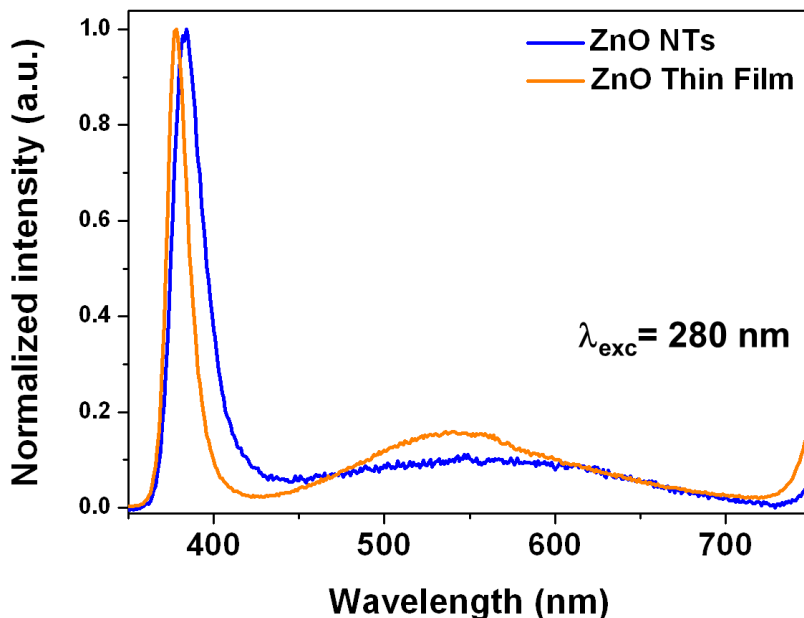
Figure 20. Room temperature luminescence emission spectrum of the ZnO NTs deposited on fused silica compared with the poly-crystalline thin film reference deposited in the same experimental conditions. The excitation wavelength was 280 nm.

Figure 21 plots the luminescent emission intensity for thin film and NTs at 384 nm during several cycles of vacuum and oxygen up to atmospheric pressure. The luminescence intensity decreases and increase reversibly in both cases with the partial oxygen pressure. This behavior has been recently reported in thin films and was found to be associated to a high surface to bulk ratio. Furthermore, the nanostructuration of this material in the form of NTs enhances its sensing properties, as it has been just demonstrated with the fabrication of a photonic sensor, allowing its implementation in multifunctional devices.
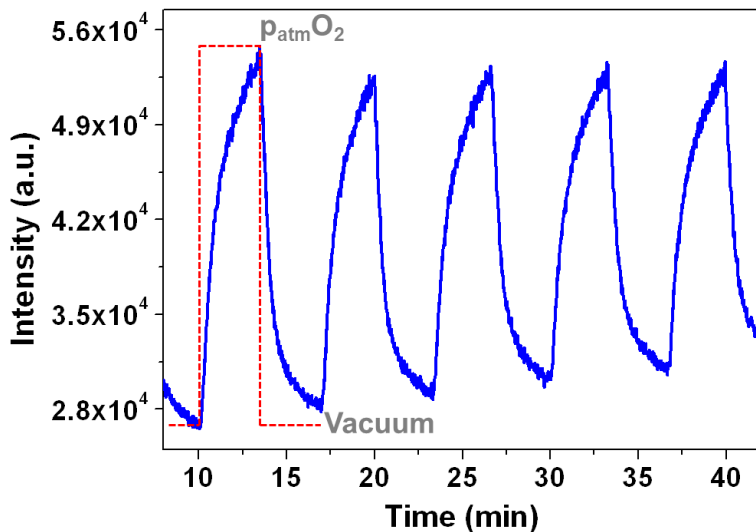
Figure 21. Evolution of the ZnO NTs exciton photoluminescence intensity when successively exposed to cycles of vacuum and oxygen at atmospheric pressure. The experiment in each cycle was stopped when a 70% of the intensity change was measured before reaching the steady state. The excitation wavelength was 280 nm.

6.5. Conclusions

Two approaches have been followed for the fabrication of SERS based sensors.

The approach based on the GLAD of silver showed relatively small enhancement factors and consequently low sensitivity when comparing to silver nanoparticles deposited at normal geometry. By contrast, the illumination with a commercial nanosecond pulsed laser allowed to tune the SERS signal. In this way, the most elongated nanoparticles (deposited at the glancing angle of 85º) presented an increase of the EF for low illumination powers. This behavior is consistent with the model proposed in the previous chapter, where the aspect ratio of the NPs is increased and therefore enhancing the "hotspot" effect. By contrast, the irradiation with high powers decreases the EF, also consistent with the model where the elongated particles get more rounded.

On the other hand, the second approach based in a multistep process to obtain TiO_2 NTs decorated with silver NPs showed very high enhancement factors. The TiO_2 NTS with 2 nm nominal thickness of silver presented a very high EF of $2x10^7$. The very high sensitivity obtained together with the compatibility for big area deposition, open a new and very promising way for future SERS based nanosensoric applications.

Even though no quantitative studies have been undertaken, the oxygen sensor based on ZnO NTs has proven equal or improved capabilities as its thin film counterpart.

6.6. References

Atkins P., Julio de P., Physical Chemistry 9th ed. ISBN: 978-0-19-954337-3. Oxford University Press. Oxford, United Kingdom (2010).

Borrás A. I. et al., Type of Plasmas and Microstructures of TiO_2 Thin Films Prepared by PECVD. Journal of the Electrochemical Society 154(12), 152-157 (2007).

Cho S. et al., Ethanol sensors based on ZnO nanotubes with controllable wall thickness via atomic layer deposition, an O_2 plasma process and an annealing process.

Das R. S., Agrawal Y. K., Raman spectroscopy: Recent advancements, techniques and applications. Vibrational Spectroscopy 57(2), 163-176 (2011).

De Angelis F. et al., Breaking the diffusion limit with super-hydrophobic delivery of molecules to plasmonic nanofocusing SERS structures. Nature Photonics 5, 682-687 (2011).

Gao M. et al., Directly Probing the Anisotropic Optical Emission of Individual ZnO Nanorods. Journal of Physical Chemistry C 114(25), 11081-11086 (2010).

Kiefer J., Noack K., Universal enantioselective discrimination by Raman spectroscopy. Analyst 140, 1787-1790 (2015).

Lee E. C., Etchegoin P. G., Single-Molecule Surface-Enhanced Raman Spectroscopy. Annual Review of Physical Chemistry 63, 65-87 (2012).

Mulvihill M. J. et al., Anisotropic Etching of Silver Nanoparticles for Plasmonic Structures Capable of Single-Particle SERS. Journal of The American Chemical Society 132(1), 268-274 (2010).

Parchaňský V. et al., Inspecting chiral molecules by Raman optical activity spectroscopy. RSC Advances 4(100), 57125-57136 (2014).

Petryayeva E., Krull U., Localized surface plasmon resonance: Nanostructures, bioassays and biosensing—A review. Analytica Chimica Acta 706(1), 8-24 (2011).

Romero-Gómez P. et al., Tunable Nanostructure and Photoluminescence of Columnar ZnO Films Grown by Plasma Deposition. Journal of Physical Chemistry C 114(49), 20932-20940.

Rycenga M. et al., Understanding the SERS Effects of Single Silver Nanoparticles and Their Dimers, One at a Time. Journal of Physical Chemistry Letters 1(4), 696-703 (2010).

Sanchez J. R. et al., Incorporation and Thermal Evolution of Rhodamine 6G Dye Molecules Adsorbed in Porous Columnar Optical SiO_2 Thin Films. Langmuir 25(16), 9140-9148 (2009).

Sanchez J. R. et al., Oxygen Optical Sensing in Gas and Liquids with Nanostructured ZnO Thin Films Based on Exciton Emission Detection. Journal of Physical Chemistry C 118(18), 9852-9859 (2014).

Schmitt M., Popp J., Raman spectroscopy at the beginning of the twenty-first century. Journal of Raman Spectroscopy 37(1-3), 20-28 (2006).

Skoog D. A., Holler F. J. and Nieman T. A., Principles of Instrumental Analysis , 5th Edition. ISBN: 0-03-002078-6. Saunders College Publishing. Philadelphia, USA (1998).

Stamplecoskie K. G., Scaiano J. C., Optimal Size of Silver Nanoparticles for Surface-Enhanced Raman Spectroscopy. Journal of Physical Chemistry C 115(5), 1403–1409 (2011).

Wu H. et al., In vivo lipidomics using single-cell Raman spectroscopy. PNAS 108 (9), 3809–3814 (2011).

Yang Y. et al., Aligned silver nanorod arrays for surface-enhanced Raman scattering. Nanotechnology 17(10), 2670-2674 (2006).

Zhang Y. et al., Brush-Like Hierarchical ZnO Nanostructures: Synthesis, photoluminescence and gas sensor properties. Journal of Physical Chemistry C 113(9), 3430-3435 (2009)

7. Enhanced performance of phthalocyanine nanowires conductometric sensors by heat and light activation
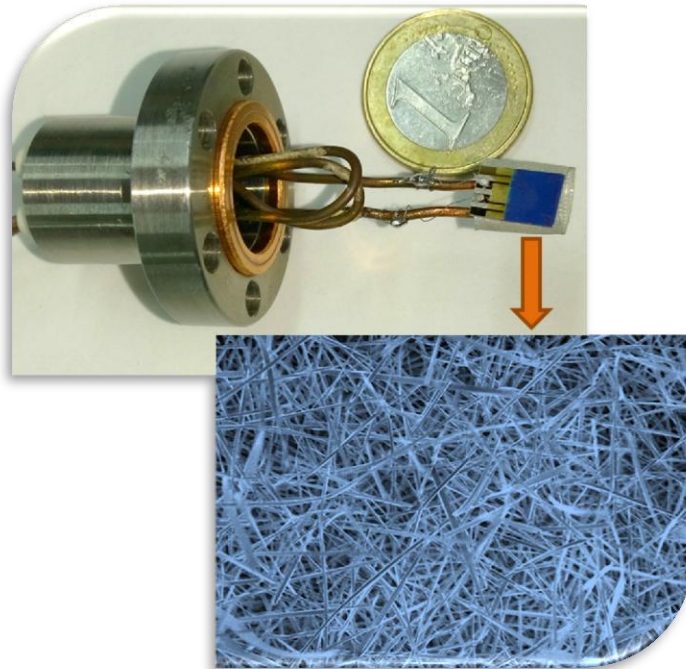
Abstract

Nanotrees of metal-free phthalocyanine (H$_2$Pc) are generated directly on commercial electrodes with the aim of fabricating conductometric oxygen gas sensors. The effect of temperature and light on the device performance is evaluated. The behavior of these 1D nanosensors is compared with the classical thin film one so as to study the role of surface are.

7.1. Introduction

The necessity for low-cost, low-power, flexible and reliable sensors which could potentially be integrated into modern electronic gadgets and wearables has drawn considerable attention to the field of organic semiconductors. Moreover, due to the strong dependence of their properties on ambient conditions, they are appropriate for the fabrication of a wide range of sensors such as temperature, radiation, pressure, radiation, chemical, etc. [Belghachi A., J. Phys. D: Appl. Phys. 1988][Moiz S. A., Jpn. J. Appl. Phys. 2005][Manunza I., Appl. Phys. Lett. 2006][Roberts M. E., PNAS 2008][Agostinelli T., J. Appl. Physiscs 2009][Roberts M. E., Org. Electron. 2009].They can be used either to monitor vital internal body parameters related to healthcare [Lochner C. M., Nat. Commun. 2014][Zang Y., Nat. Commun. 2015] or external ones such as environmental agents (both hazardous and vital ones) [Liao F., SENSOR. ACTUAT. B CHEM. 2005][Das A.,SENSOR. ACTUAT. B CHEM. 2009][Knopfmacher O., Nat. Commun. 2014], opening the possibility for a truly full sensing ecosystem. Among the different types of possible sensors, organic gas sensors pose as an attractive near future and more realistic possibility towards their implementation in commercial devices.

Some gas sensor requirements are [Sberveglieri G., Springer 1992]:

(1) Reversible adsorption of gas species.
(2) High sensitivity while maintaining weak interactions with the gas species (ease of reversibility, 1).
(3) High selectivity, ideally specificity* for a given gaseous agent.
(4) Short response and recovery time.
(5) Stability of the sensing material.
(6) Inexpensive. If aimed to portable devices, then it should have a low power consumption and a relatively small size.

Some of the major drawbacks associated with the use of organic semiconductor molecules are their chemical degradation (stability) against some gaseous agents and long-term reliability issues [Potje-Kamloth K., Crit. Rev. Anal. Chem. 2002][][]. In contrast to their inorganic counterparts, organic molecules offer an enormous degree of structural flexibility and diversity through molecular engineering, which along with

*Selectivity: it refers to the extent to which a method can determine (a) particular analyte(s) in a complex mixture without the interference from other components in the mixture.
Specificity: it is defined as the ultimate selectivity, i.e. 100% selectivity (no interferences). [Vessman J., Pure Appl. Chem. 2001]

improved device fabrication, offers the chance to overcome these problems. Moreover, they can exhibit considerably higher sensitivity and selectivity*, lower operation temperature (even room temperature operation), shorter response and recovery time than commonly used metal oxides [Miasik J. J., J. Chem. Soc., Faraday Trans. (1) 1986][Nalwa H. S., Academic Press 2001][Tanese M. C., Nuovo Cimento Soc. Ital. Fis., C 2008][Marinelli F., SENSOR. ACTUAT. B CHEM. 2009].

Due to their good chemical and thermal stability, unpolimerized phthalocyanines have been one of the most studied families of organic semiconductors in the field of gas sensing. They can be readily vacuum deposited on almost any substrate by thermal evaporation to produce high-quality amorphous or crystalline films [Sadaoka Y., J. Mater. Sci. 1990], which facilitates even further the fabrication of sensing devices. The conductance of films made up of phthalocyanines (the great majority are p-type semiconductors) at room temperature and exposed to air is quite low, but when temperatures are raised above 100 ºC, the conductivity tends to increase significantly [Miasik J. J., J. Chem. Soc., Faraday Trans. (1) 1986][Bohrer F. I, J. Am. Chem. Soc. 2007].

Upon exposure of metallophthalocyanines (MPcs) to electrophicilic gases such as NO_x, Cl_2, F_2, BF_3, O_2, etc. an increase in the conductivity is produced due to the formation of charge-transfer complexes, which leads to the injection of holes into the film and a consequent increase in conductivity. On the other hand, reducing gases, such as NH_3, tend to decrease the conductivity owing to an speculated electron donation from the reducing gas to trap charge carriers [Miasik J. J., J. Chem. Soc., Faraday Trans. (1) 1986]. The chemisorption of oxygen by a metallophthalocyanine follows the formation of a charge-transfer complex as schematized in Figure 1, where a superoxide adduct of MPc is also depicted [Zwart J., J. Mol. Catal. 1979][Yahiro H., Micropor. Mesopor. Mat. 2005].
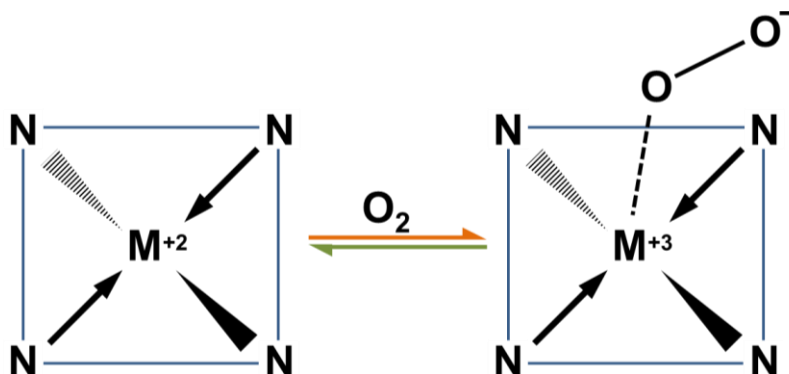
Figure 1. Scheme of the adsorption of oxygen to the metal of a generic metallophthalocyanine. Adapted from [Bohrer F. I, J. Am. Chem. Soc. 2007].

In the case of metal-free phthalocyanine (H_2Pc), it seems that electrophilic species, including oxygen, are adsorbed to the compound by weak interactions with the four meso-nitrogens of H_2Pc or by hydrogen bonds to the two inner hydrogens, leading to a slight conductivity increase, although not as pronounced as in MPc [Wright J. D., Prog. Surf. Sci. 1989][Gould R. D., Coord. Chem. Rev. 1996][Kudo K., Jpn. J. Appl. Phys. 1997][Guillaud G., Coord. Chem. Rev. 1998].

The adsorption of analytes to phthalocyanines is considered to occur exclusively at the very surface of the films due to steric hindrance related to the tightness of phthalocyanines crystal structure [Bohrer F. I, J. Am. Chem. Soc. 2007][Contour J. P., J. Catal. 1973]. In this sense, phthalocyanine nanowires (NWs) should pose a unique opportunity to enhance the sensing properties of these compounds owing to the larger surface area exposed to the analyte compared to the usual thin film approach. Interestingly, almost all studies devoted to phthalocyanines as gas sensors are restricted to thin films [Liu C. J., SENSOR. ACTUAT. B CHEM. 1998][Bohrer F. I, J. Am. Chem. Soc. 2007][Yang R. D., J. Chem. Phys. C 2009][Paoletti A. M., sensors 2009]. As a previous step to the fabrication of a gas sensor based on phthalocyanine ONWs, it is worth quoting the work from reference [Wang F., J. Mater. Chem. C 2013]. In that work, zinc octaethylporphyrin (ZnOEP)* NWs were grown, transferred to prepatterned electrodes and their photoresponse evaluated.

*Even though a porphyrin has been used for that study, they are structurally related to phthalocyanines.

In this work, the direct growth of H_2Pc NWs on commercial electrodes at relatively low temperature has been addressed, avoiding any transference process. In order to increase the organic semiconductor specific area even further, nanotrees were generated as previously discussed in Chapter 4. The devices oxygen-sensing capabilities were examined at room temperature, 50 ºC, 100 ºC and under the presence of UV irradiation, red and green light, by conductometric measurements. Finally, the impact of combined irradiation and heating on the sensors response was evaluated.

7.2. Objectives

The main goals associated to this chapter are:

❖ Fabrication of an oxygen sensor based on phthalocyanine (H_2Pc) nanotrees without the need of subsequent transference processes.

❖ Study of the electrical properties and response behavior of the sensors to oxygen.

    ➢ Evaluate the influence of temperature and light irradiation on the sensor performance at a maximum temperature of 100 ºC.

    ➢ Evaluate the response at 100 ºC to more discrete light sources such as LEDs.

❖ Comparison of the sensor response with its thin film counterpart.

7.3. Methodology

Sensors fabrication. Commercial electrodes purchased from Micrux® with 15 pairs of interdigitated microelectrodes separated by 10 μm were used as received. Prior to the sublimation of H_2Pc, gold seeds were deposited so as to provide the necessary roughness for the growth of NWs. The deposition of metallic seeds was done by magnetron sputtering at 0.1 mbar employing and Emitech K550 sputter coater equipped with a gold target; to avoid the slightest possibility of conduction through the NPs, the deposition was performed at 12.5 mA 10 s (below the usual 15 s normally used, see Chapter 2), observing no conduction. The growth of nanotrees was carried out just as described in the methodology section of Chapter 3 or Appendix A, but with only one step of ramification of 1.5 kÅ (QCM).

Sensors characterization. The electrical characterization of the sensors and their response evaluation were performed with a 2635A system sourcemeter working in sweep voltage mode for the I-V curves and in sweep current mode at a fixed potential of 5V for the sensor response. The devices were mounted in a chamber with argon

(características) and oxygen (características) inlets, and a small melted-silica window for light irradiation experiments. The samples were fixed to a heateable sample holder with an attached K-type thermocouple.

7.4. Results and discussion

7.4.1. Fabrication of the 1D organic semiconductor-based sensors

With the methodology developed for the growth of nanotrees, it has been possible to attain an ultra-high density "nanoforest" of H_2Pc NWs directly grown on commercial electrodes at relatively low temperatures (< 200 ºC), as demonstrated in Figure a-b). It is worth mentioning that this procedure avoids additional transference steps between substrates while providing an extreme density unlike a previous work [Wang F., J. Mater. Chem. 2013]
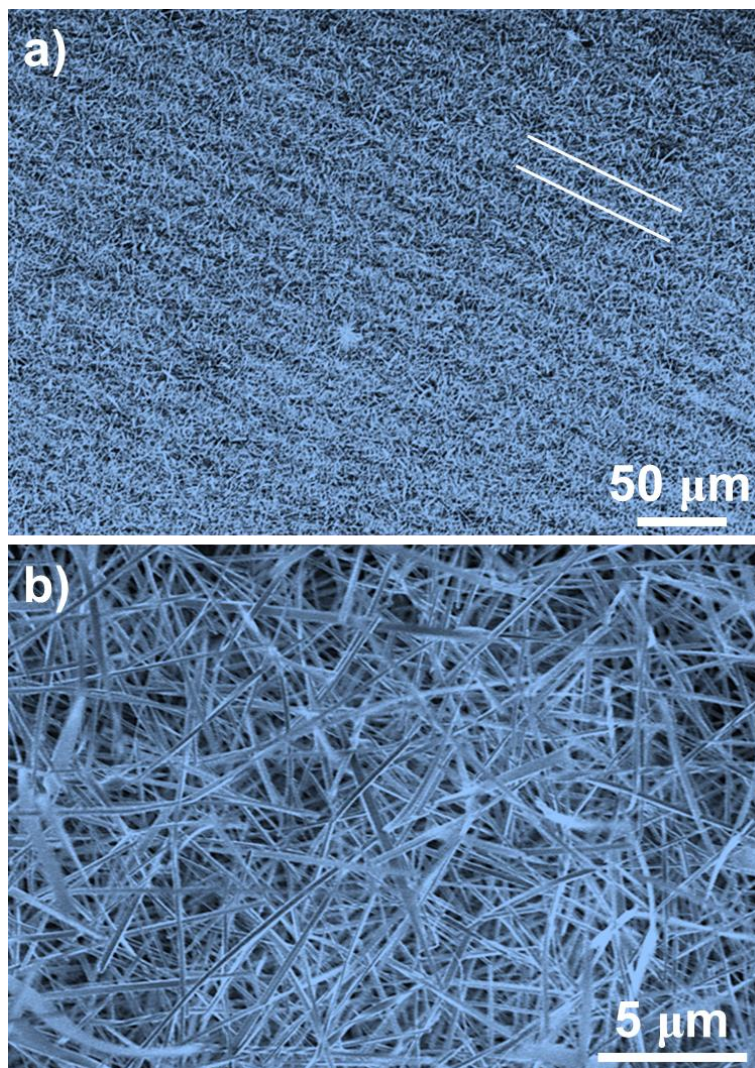
Figure 2. (a) SEM image of a nanoforest of H$_2$PC nanotrees on Micrux® electrodes. (b) Amplified zone of a) showing the highy interconnected network.

7.4.2. Electrical characterization of the sensors

I-V curves between -5 V and 5 V were registered for the sensors under different temperatures and constantly flowing argon. It was observed that the resistance of the sensors was diminished by a factor of 5 when the temperature of the device was set to 50 ºC. After increasing to 100 ºC, the resistance dropped by nearly 100 times with respect to the room temperature situation. This respectable change in conductivity of the sample with temperature is expected from such an organic semiconductor. Despite

the values of resistance might seem high, it must be kept in mind that the conduction in these devices is achieved throw a hopping mechanism between NWs.
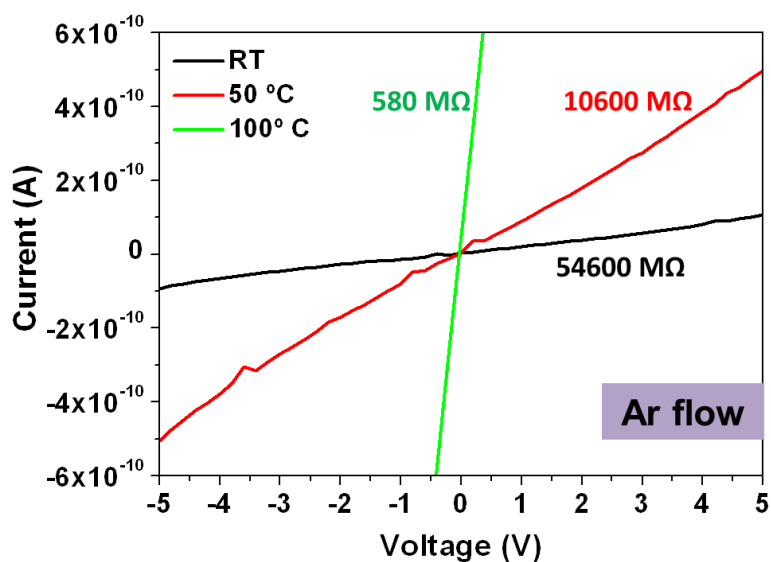

Figure 3. I-V curves for nanotrees on Micrux® at different temperatures and under constant argon flux.

By resgistering the I-V curves at 100 ºC and switching the gas flux into the chamber from Ar to O_2, after 30 minutes of stabilization time before recording the curves, an appreciable change in conductivity was observed (Fig. 4). In spite of the fact that this behavior has been reported already [Kudo K., Jpn. J. Appl. Phys. 1997], it should be barely noticeable, whereas in this study the current has increased by nearly an order of magnitude. This may attributed to the much higher surface area exposed by the nanotrees, which could be maximizing the doping effect of oxygen.
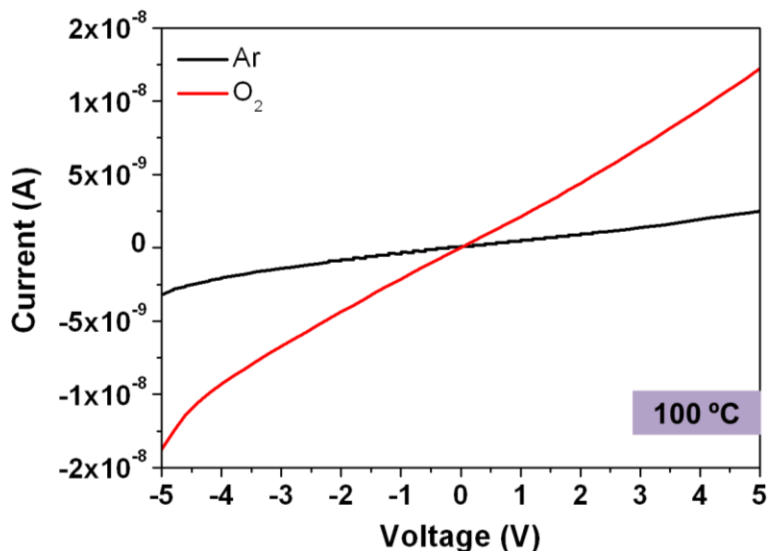
Figure 4. I-V curves for nanotrees on Micrux® at 100 ºC under argon (black) or oxygen (red) atmosphere.

7.4.3. Oxygen sensing

The response of the sensors to oxygen was evaluated at different working temperatures and under combined irradiation, imposing in all cases a bias of 5 V to the sensors. As it can be noticed in Figure 5 for the room temperature case, by alternating between oxygen an argon a saw-like current response was obtained, but with no obvius effects on conductivity, something which could be masked by the noticeable drift in the curve (marked with an arrow in Fig. 5). Upon visible* light irradiation, the current increases by three orders of magnitude, denoting and enhanced sensor response due to light activation. Above the H_2Pc band gap of 1.88 eV [Kumar G. A., J. Mater. Sci. 2000], which corresponds roughly to 659.5 nm, (659.5 nm), it is expected that the conductivity rises due to the semiconductor nature of these molecules. On the other hand, UV+visible* (denoted by UV in Fig. 5) light does not produce any further conductivity changed compared to visible light only.

*Near infrared radiation (NIR) was not eliminated from the light source, however it should not affect the measurements due to the higher band gap of H_2Pc. NIR did not produced any significant change in temperature during measurements as evidenced by the thermocouple.
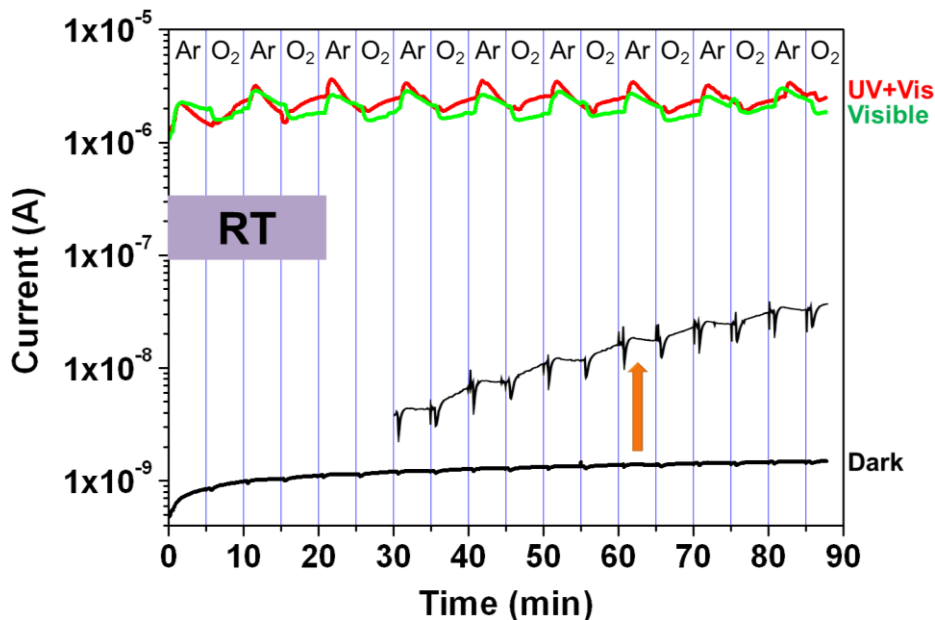
Figure 5. Sensor response at room temperature to oxygen and argon at room temperature under no irradiation (black), visible light (green) and UV+visible light (red).

Rising the temperature to 50 ºC augments the current of non illuminated sensors by one order of magnitude, but it did not increase even more the response when subjected to illumination (Fig. 6). A zoom of the non irradiated curve reveals that the saw-like features of the curves were much more defined at 50 ºC (marked with an arrow in Fig. 6) compared to the room temperature situation, making clear again the role of temperature in sensor performance.
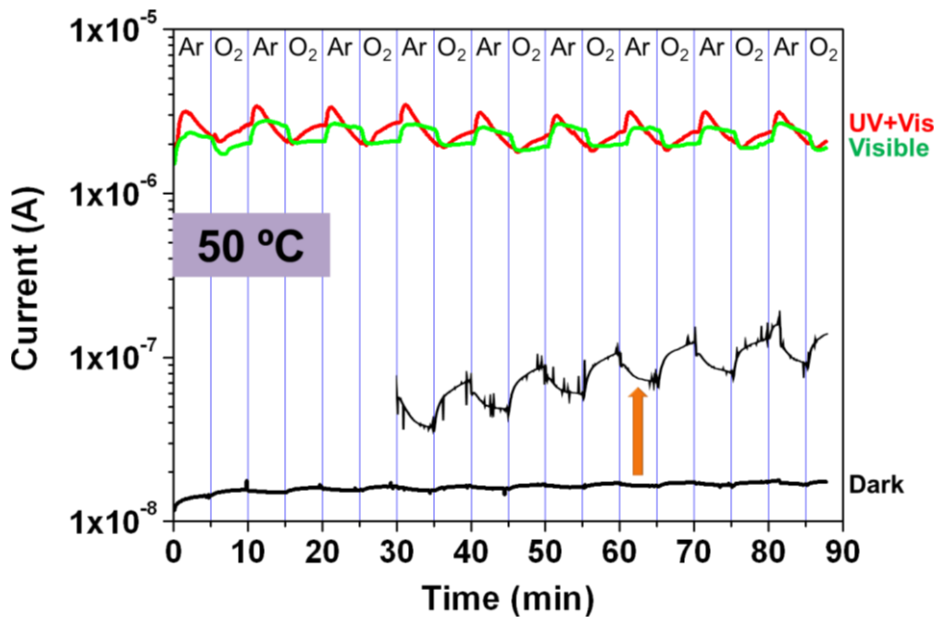
Figure 6. Sensor response at 50 ºC to oxygen and argon at room temperature under no irradiation (black), visible light (green) and UV+visible light (red).

Finally, the response to oxygen was evaluated at 100 ºC, observing one more time no significant changes in the conductivity of the irradiated samples with regard to room temperature and 50 ºC cases. However, the current of the non irradiated scenario has augmented one order of magnitude again and the drift seems to have vanished completely.

The electrical measurements at a slightly higher temperature and under UV+visible light were also carried out, observing that at 115 ºC the photoresponse has improved compared to 100 ºC. However, no further studies were performed ath higher temperatures beacuse one of the objectives in this chapter was to stay below 100 ºC.
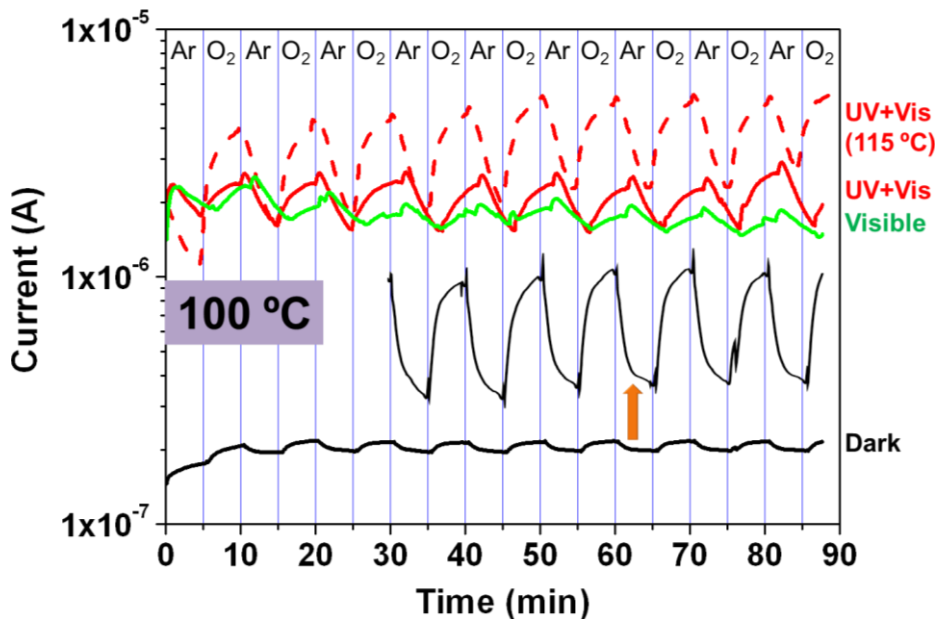
Figure 6. Sensor response at 100 ºC to oxygen and argon at room temperature under no irradiation (black), visible light (green) and UV+visible light (red).

The reason why irradiaton with UV+visible light did not present significant changes compared to visible light may be due to the tiny difference in power density of the visible and UV+visible radiation, which was roughly 73 mW/cm^2 (Table 1).

Table 1. Power densities for the Xenon lamp with no filters (UV+Vis) and with a methacrylate filter (Visible). Values are expressed in mW/cm^2

Light source	UVA+UVB (280-400)	Vis+NIR (400-2500)	UV+Vis+NIR (280-2500)
Xenon lamp (UV+Vis)	42.8	1730	1772.8
Xenon lamp (Visible)	0	1700	1700

Irradiation experiments at 100 ºC were also carried out using a series of three LEDs: red, green and blue (Fig. 7). This time the flux of oxygen was kept inenterrupted during the whole experiment, switching instead the light source. It may be appreciated that once the LEDs were turned on, the current jumped instantly, and when turned off the current dropped immediately. Note that the current changes were not marked in this

case, but it was only due to the low power of the LEDs employed as observed in Table 2.

Table 2. Power density of the different light sources employed expressed in mW/cm^2. The measurements were done at the same working distance than the sensors irradiation experiments, 5 cm for the LEDs and 15 cm for the Xenon lamp.

Light source	UVA+UVB (280-400)	Vis+NIR (400-2500)	UV+Vis+NIR (280-2500)
Xenon lamp	42.8	1730	1772.8
RED LED	0	5.38	5.38
GREEN LED	0	2.93	2.93
BLUE LED	0	2.89	2.89
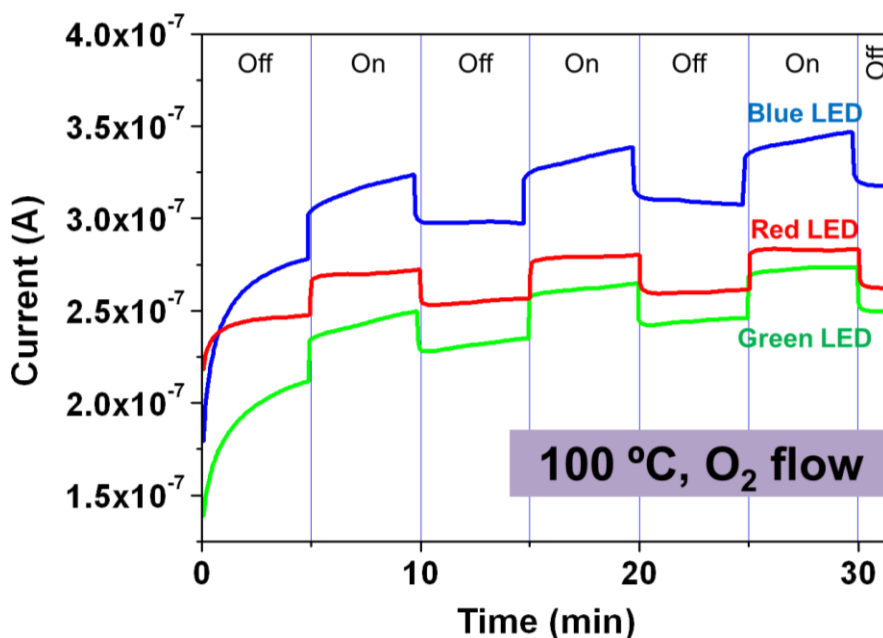
Figure 7. Sensor response at 100 ºC to oxygen under intermitent irradiation with red, green or blue LEDs

The aim of working with LEDs instead of conventional broad-irradiation spectrum light sources was to discard any thermal effect associated to the irradiation source and to study the influence on the sensor behavior when irradiated with a discrete light source. It was expected to observe noticeable changes in the reponse to oxygen owing to

preferential absorption of different LED lights by the molecule, i.e. if the LED light falls into an absorption band of H_2Pc, and the LED power density (Table 2). According to the UV-Vis spectrum of H_2Pc in Figure 8 and Table 2, the red LED should have given the highest response to oxygen and the green LED the lowest one, but this has not been the case (Fig. 7). The low power density of the LEDs originated a small increase in the current, so the trends could be perfectly masked by the drift of the sensor.
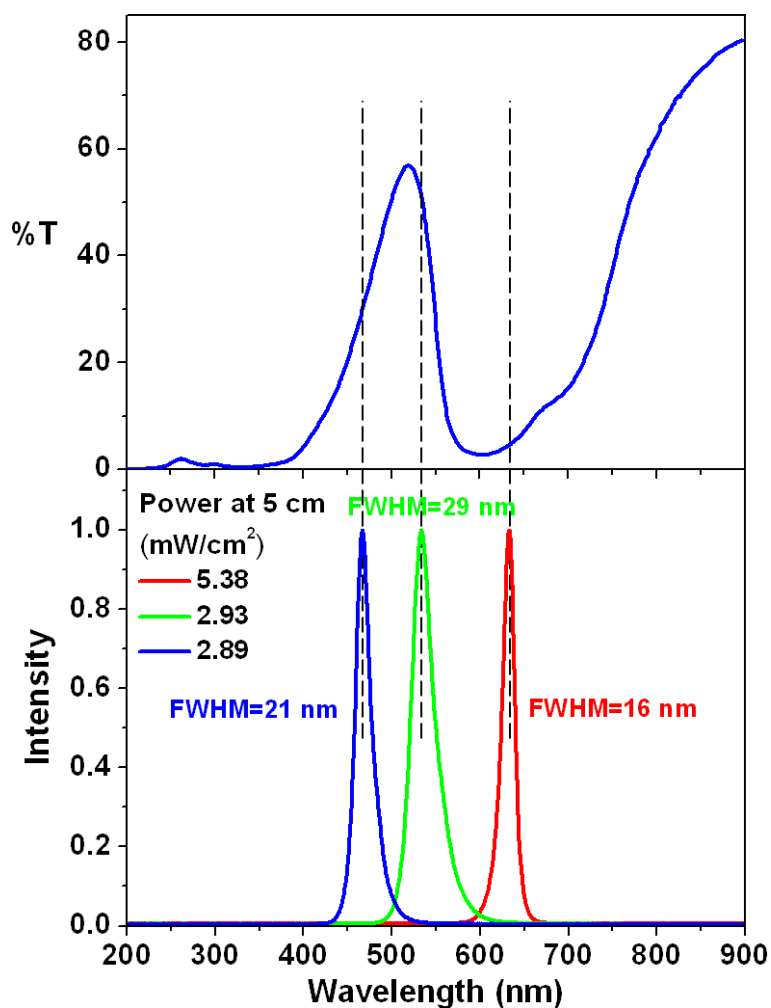

Figure 8. (Up) UV-Vis spectrum of H_2Pc and (Down) emission spectrum of red, green and blue LEDs.

7.5. Conclusions

The fabrication of H_2Pc Nanotrees-based sensors has been successfully addressed, producing an ultra-high density nanoforest with two simple vacuum deposition methods, magnetron sputtering for the seeds and OPVD for the nanotrees, on commercial substrates and at mild temperatures (< 200 ºC). Against expectations (due to a low sensitive molecule), the response to oxygen was evident even at temperatures below 100 ºC., which could probably be attributed to the high specific area of these 1D nanostructures. Moreover, the enhancement in the oxygen response by irradiation turned out to be quite spectacular. Finally, the experiments with LEDs were somewhat inconclusive, suggesting that more powerful LEDS should be used before arriving at any conclusion.

7.6. References

Agostinelli T. et al., A planar organic near infrared light detector based on bulk heterojunction of a heteroquaterphenoquinone and poly[2-methoxy-5-(2'-ethyl-hexyloxy)-1,4-phenylene vinylene]. Journal of Applied Physics 104(11), 114508 (2009).

Belghachi A., Collins R. A., Humidity response of phthalocyanine gas sensors. Journal of Physics D: Applied Physics 21(11), 1647 (1988).

Bohrer F. I. et al., Gas Sensing Mechanism in Chemiresistive Cobalt and Metal-Free Phthalocyanine Thin Films. Journal of The American Chemical Society 129(17), 5640-5646 (2007).

Contour J. P., Lenfant P., Vijh A. K., Gas-phase chemisorption and electroreduction of oxygen on phthalocyanines. Journal of Catalysis 29(1), 8-14 (1973).

Das A. et al., Low cost, portable, fast multiparameter data acquisition system for organic transistor odour sensors. Sensors and actuators B: Chemical 137(2), 586-591 (2009).

Gould R. D., Structure and electrical conduction properties of phthalocyanine thin films. Coordination Chemistry Reviews 156, 237-274 (1996).

Guillaud G., Simon J., Germain J. P., Metallophthalocyanines: Gas sensors, resistors and field effect transistors. Coordination Chemistry Reviews 178-180 (2), 1433-1484 (1998).

Knopfmacher O. et al., Highly stable organic polymer field-effect transistor sensor for selective detection in the marine environment. Nature Communications 5(2954), 1-9 (2014).

Kudo K. et al., Evaluation of Electrical Properties of Evaporated Thin Films of Metal-Free, Copper and Lead Phthalocyanines by In-Situ Field Effect Measurements. Japanese Journal of Applied Physics 36(11), 6994 (1997).

Kumar G. A. et al., Physical and optical properties of phthalocyanine doped inorganic glasses. Journal of Materials Science 35(10), 2539-2542 (2000).

Liao F., Chen C., Subramanian V., Organic TFTs as gas sensors for electronic nose applications. Sensors and Actuators B: Chemical 107(2), 849-855 (2005).

Liu C. J. et al., Titanyl phthalocyanine gas sensor for NO_2 detection. Sensors and Actuators B: Chemical 52(3), 264-269 (1998).

Lochner C. M. et al., All-organic optoelectronic sensor for pulse oximetry. Nature Communications 5(5745), (2014).

Manunza I., Sulis A., Bonfiglio A., Pressure sensing by flexible, organic, field effect transistors. Applied Physics Letters 89, 143502 (2006).

Marinelli F. et al., An organic field effect transistor as a selective NO_x sensor operated at room temperature. Sensors and Actuators B: Chemical 140(2), 445-450 (2009).

Miasik J. J., Hooper A., Tofield B. C., Conducting polymer gas sensors. Journal of the Chemical Society, Faraday Transactions 1: Physical Chemistry in Condensed Phases 82(4), 1117-1126 (1986).

Moiz S. A., Ahmed M. M., Karimov K. S., Effects of temperature and humidity on electrical properties of organic semiconductor orange dye films deposited from solution. Japanese Journal of Applied Physics 44(3), 1199-1203 (2005).

Nalwa H. S., Handbook of Surfaces and Interfaces of Materials – Surface and Interface Phenomena. ISBN: 0-12-513910-1. Academic Press. San Diego, USA (2001).

Paoletti A. M. et al., Titanium and Ruthenium Phthalocyanines for NO_2 Sensors: A Mini-Review. Sensors 9(7), 5277-5297 (2009).

Potje-Kamloth K., Chemical Gas Sensors Based on Organic Semiconductor Polypyrrole. Critical Reviews in Analytical Chemistry 32(2), 121-140 (2002).

Roberts M. E. et al., Water-stable organic transistors and their application in chemical and biological sensors. PNAS 105(34), 12134-12139 (2008).

Roberts M. E. et al., Flexible, plastic transistor-based chemical sensors. Organic Electronics 10(3), 377-383 (2009).

Sadaoka Y. et al., Effects of morphology on NO_2 detection in air at room temperature with phthalocyanine thin films. Journal of Materials Science 25(12), 5257-5268 (1990).

Sberveglieri G., Gas Sensors: Principles, operation and developments. ISBN: 978-94-010-5214-6. Springer Science+Business Media Dordrecht (1992).

Tanese M. C. et al., Overview of recent developments in organic thin-film transistor sensor technology. Il Nuovo Cimento C 31(4), 457-473.

Vessman J. et al., SELECTIVITY IN ANALYTICAL CHEMISTRY (IUPAC Recommendations 2001). Pure and Applied Chemistry 73(8), 1381-1386 (2001).

Wang F. et al., One-step fabrication of an ultralong zinc octaethylporphyrin nanowire network with high-performance photoresponse. Journal of Materials Chemistry C 1(3), 422-425 (2013).

Wright J. D., Gas adsorption on phthalocyanines and its effects on electrical properties. Progress in Surface Science 31(1-2), 1-60 (1989).

Yahiro H. et al., An EPR study on oxygen molecule adduct of Co(II)-phthalocyanines encapsulated into zeolites. Microporous and Mesoporous Materials 79(1-3), 291-297 (2005).

Yang R. D. et al., Analyte chemisorption and sensing on n- and p-channel copper phthalocyanine thin-film transistors. Journal of Chemical Physics 130(16), 164703 (2009).

Zang Y. et al., Flexible suspended gate organic thin-film transistors for ultra-sensitive pressure detection. Nature communications 6(6269), 1-9 (2015).

Zhang C., Chen P., Hu W., Organic field-effect transistor-based gas sensors. Chemical Society Reviews 44(8), 2087-2107 (2015).

Zwart J., Van Wolput J. H. M. C., Characterization by E.S.R. of a Polymer Attached Cobalt(II)-Phthalocyanine Catalyst. Journal of Molecular Catalysis 5(3), 235-239 (1979).

8. General conclusions

The fabrication of new 1D hybrid and heterostructured nanomaterials has been studied and optimized for different applications. These novel nanostructures have been succesfully implemented in different devices: solar cells based on inorganic nanotubes of ZnO, TiO$_2$ and multishell ZnO@TiO$_2$; transparent conductive electrodes based on platinum nanostructures; piezoelectric nanogenerators based on 1D core@shell heterostructures consisting in ZnO and gold and platinum metallic contacts; tunable dichroic optical filters based on glancing angle deposited silver nanoparticles; Surface enhanced Raman based sensors comprising silver deposited by GLAD and silver nanoparticles decorating TiO$_2$ NTs; oxygen photonic sensor based on the excitonic luminescence of ZnO NTs; oxygen conductometric sensors activated by heat and light based on phthalocyanine nanotrees.

Chapter 2

1) A reliable full vacuum methodology for the fabrication of semiconducting nanotubes made of ZnO and TiO$_2$ with single and multishell configurations has been presented. The versatility of the plasma techniques such as PECVD and dc-sputtering for the growth of metal nanoparticles and metal oxide layers has been exploited here for the formation of nanostructured nanotubes with tailored shells in terms of microstructure, porosity, structure and thickness on an ample variety of substrates ranging from FTO supports to metal nanoparticles.

2) The procedure provides hollow's cross sections in the form of square or rectangle keeping memory of the flat surface of the organic single crystal used as templates. The performance of the ZnO and anatase nanotubes as photoanodes in DSSC has been analyzed as a function of the shell thickness, finding an increase of efficiency with this parameter. In the case of multi-shell nanotubes, mixed results were obtained for amorphous and crystalline TiO$_2$, however, it has been found that the addition of a thin TiO$_2$ shell turned out to be detrimental for the performance of the cells.

Chapter 3

1) A new plasma assisted methodology for the fabrication of transparent metallic electrodes has been developed. One- and two-dimensional metallic structures has been fabricated. *Remote Oxygen Plasma Etching decomposes the PtOEP molecule providing the formation of metallic Pt structures. *Thermal

mobilization of the PtOEP molecules improves homogeneity and density of the Pt structures, reducing the SPE treatment duration.

2) Transmittance of the Pt layers and nanocolumns depends strongly on the thickness and post-treatment. UV-VIS and UV-VIS-NIR characterization reveals highly homogeneous transmittance in these wavelengths with an ample variety in the transmission range (from 10 % to 70 %).

3) Samples prepared under RPAVD conditions are amorphous meanwhile the post-treatment yields crystallization of the Pt. *Deposition conditions of the sacrificial PtOEP layers drastically affect to the final Pt nanoelectrode porosity and microstructure UV-Vis transmission and XPS results indicated the total decomposition of the organic counterpart and formation of metallic Pt.

4) The Current vs Voltage current shows the high conductivity of the films able to drive stable currents of around 0.1 A.

5) Transparency and conductivity in 2D nanoelectrodes has been related with the thickness and microstructure of the sacrificial PtOEP.

Chapter 4

1) The ZnO grown at room temperature by PECVD has proven to exhibit adequate electric and piezoelectric characteristics.

2) The development of 1D core@shell nanostructures with application in the field of piezoelectricity has been addressed. It has been possible to generate and thoroughly characterize complete nanogenerators with the structure Pt NWs@ZnO@Au following a full vacuum fabrication approach. In spite of the fact that the fabricated device was short circuited, it does not mean that the system is not appropriate for its implementation in piezoelectric generators, but just that more care must be taken to avoid that issues (PMMA infiltration for example). Moreover, these nanostructures have proven to be excellent samples for the development and refinement of more powerful EDX mapping and analysis techniques, as exemplified in Appendix B.

3) Thin film and 1D piezoelectrics have been successfully fabricated on flexible substrates. Despite not having performed quantitative studies, it has been demonstrated that the fabricated devices truly work as piezoelectrics, paving the way for more detailed studies.

Chapter 5

1) In the previous results and discussion it has been shown that silver NPs prepared by evaporation at glancing angles depict a strong dichroism that can be enhanced by a mild laser irradiation. These optical effects were attributed to the formation of flat and elongated NPs when the evaporation is carried out along this geometry and to the modification of these morphological characteristics when the prepared samples are treated with laser.

2) By controlling the amount of deposited material, the evaporation angle and the laser irradiance, it has been possible to successfully prepare a large set of dichroic color patterns. The simplicity of the method, not requiring of any template or 1D periodic roughness effect of the substrate or the use of complex lithographic techniques and its compatibility with any kind of substrate material are some of the most advantageous features of the procedure. Its use for optical encoding by moving the laser beam along certain predefined patterns is likely one of the applications of the developed technology with more potentiality.

Chapter 6

1) The approach based on the GLAD of silver showed relatively small enhancement factors and consequently low sensitivity when comparing to silver nanoparticles deposited at normal geometry. By contrast, the illumination with a commercial nanosecond pulsed laser allowed to tune the SERS signal. In this way, the most elongated nanoparticles (deposited at the glancing angle of 85º) presented an increase of the EF for low illumination powers. This behavior is consistent with the model proposed in the previous chapter, where the aspect ratio of the NPs is increased and therefore enhancing the "hotspot" effect. By contrast, the irradiation with high powers decreases the EF, also consistent with the model where the elongated particles get more rounded.

2) On the other hand, the second approach based in a multistep process to obtain TiO_2 NTs decorated with silver NPs showed very high enhancement factors. The TiO_2 NTS with 2 nm nominal thickness of silver presented a very high EF of $2x10^7$. The very high sensitivity obtained together with the compatibility for big area deposition, open a new and very promising way for future SERS based nanosensoric applications.

3) Even though no quantitative studies have been undertaken, the oxygen sensor based on ZnO NTs has proven equal or improved capabilities as its thin film counterpart.

Chapter 7

1) The fabrication of H_2Pc Nanotrees-based sensors has been successfully addressed, producing an ultra-high density nanoforest with two simple vacuum deposition methods, magnetron sputtering for the seeds and OPVD for the nanotrees, on commercial substrates and at mild temperatures (< 200 ºC).

2) The response to oxygen was evident even at temperatures below 100 ºC., which could probably be attributed to the high specific area of these 1D nanostructures. Moreover, the enhancement in the oxygen response by irradiation turned out to be quite spectacular. Finally, the experiments with LEDs were somewhat inconclusive, suggesting that more powerful LEDS should be used before arriving at any conclusion.

Appendix A. Growth of organic nanowires

The intention of this appendix is to summarize the optimal conditions found for the growth of several (metal) organic nanowires (NWs) on different substrates. Not all of the organic and metalorganic molecules included here were employed in previous chapters, but they have been used during the Ph.D. thesis period for other applications.

The sample holder employed for the depositions is depicted in Fig. 1a. It is comprised of two drilled stainless steel sheets (1) sandwiching the heating element, sample fixing clip (2), electrical connections for the heater (3), type K thermocouple for accurate temperature measurement (4) and drilled holes to fix the sample holder inside the chamber (5). The heating element consists of nichrome wire coiled around a macor ceramic and sandwiched between two more macor ceramics.
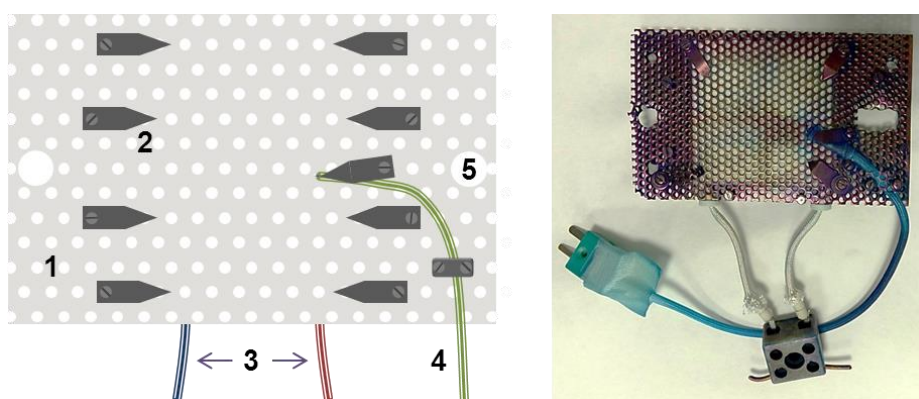

Figure 1. Representation of the sample holder used to grow nanowires and its individual components (left) and a photograph of a real sampleholder (right).

Numerous different molecules have been successfully grown into NWs, including perylenes, porphyrins and phthalocyanines. Columnar thin films of metal oxides produced by PECVD were found to be the most adequate substrates for obtaining NWs in high density. Otherwise stated, all metal oxides were fabricated by PECVD on Si or fused silica (Q). GLAD refers to columnar thin films fabricated by glancing angle deposition and Au NPs refers to gold nanoparticles produced by magnetron sputtering (Emitech K550 sputter coater), using generally 12.5 mA 15 s for Si or Q and 10 mA 15 s for micrux electrodes (to avoid shortcircuits). Gold may be replaced by silver nanoparticles (Ag NPs) deposited on Si or Q with a housemade chamber; the deposition condition for attaining Ag NPs was: 15 minutes, 1 mbar of Argon pressure and 400 V of applied potential [Sánchez-Valencia J. R., Advanced Materials].

The evaporator-to-sample distance has always been fixed to 6.5 cm and the gas chosen for the experiments was Argon otherwise stated.

It is worth mentioning that not only rigid and conventional substrates for NWs were employed, but also flexible ones such as polydimethylsiloxane (PDMS), polytetrafluoroethylene (PTFE) and Indium tin oxide coated PET (ITO/PET).

2,9-DIMETHYL-ANTHRA(2,1,9-DEF,6,5,10-'E'F')DIISOQUINOLINE-1,3,8,10-TETRAONE (MePTCDI)

Substrates: ZnO, TiO$_2$, SiO$_2$

Substrate temperature: 110 ºC – 120ºC

Growth rate (QCM): 0.3 Å/s
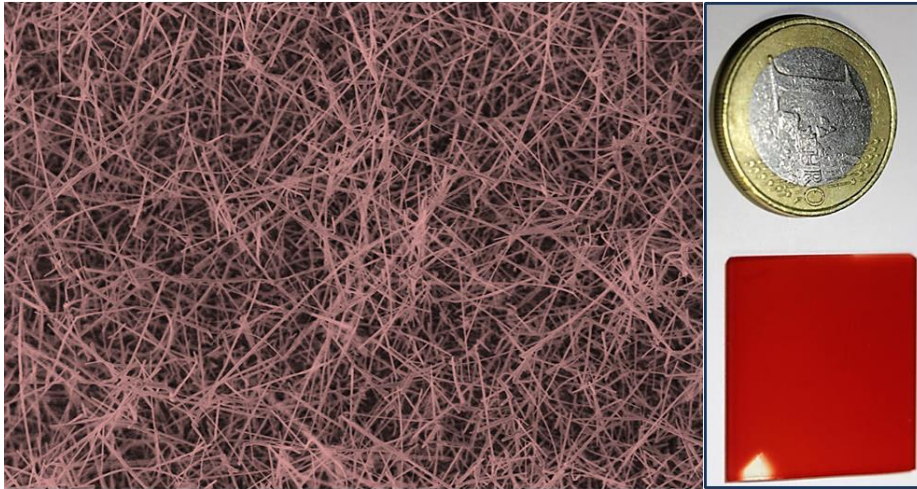
Pressure: 0.02 mbar

Figure 2. SEM image of MePTCDI on ZnO (PECVD)/Si (up) and its corresponding UV-Vis spectrum on TiO₂ (PECVD)

Octaethylporphyrin (OEP)

Substrates: ZnO, TiO₂, SiO₂

Substrate temperature: 80-85 ºC

Growth rate (QCM): 0.40-0.45 Å/s
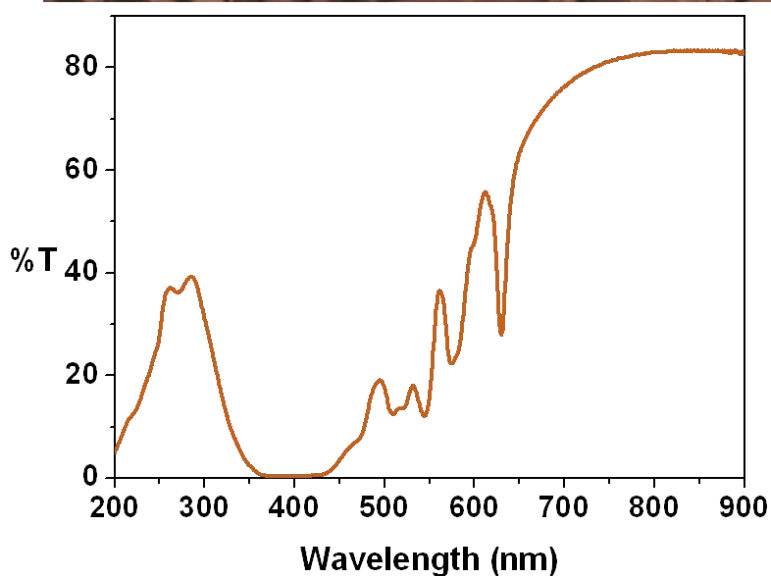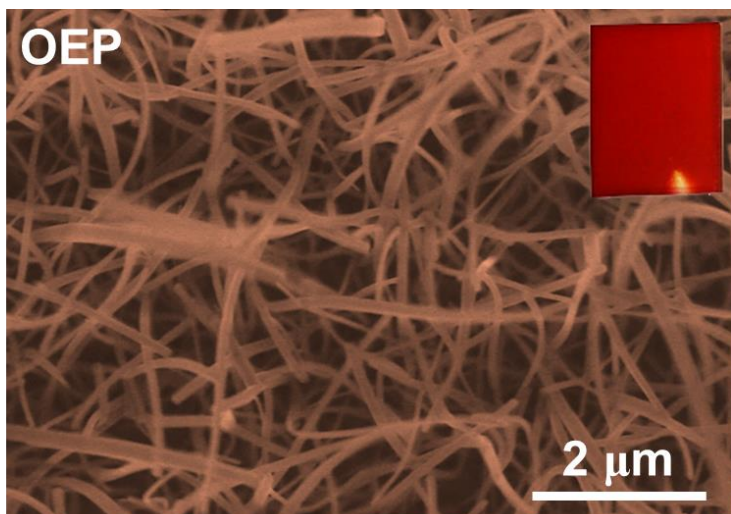
Pressure: 0.02 mbar

Figure 3. SEM image of OEP on SiO$_2$ (PECVD)/Si (up) and its corresponding UV-Vis spectrum on Q.

Platinum Octaethylporphyrin (OEP)

Substrates: ZnO, TiO$_2$, SiO$_2$, Ag NPs on PDMS

Substrate temperature: 90-100 ºC

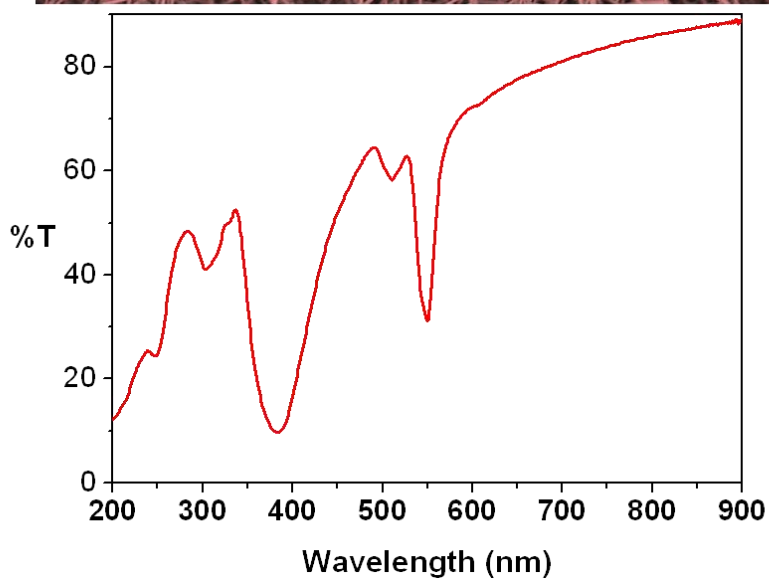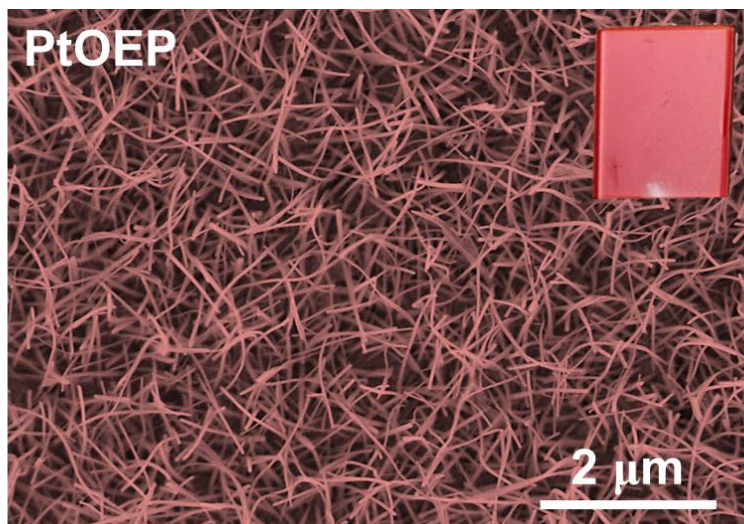**Growth rate (QCM):** 0.40-0.45 Å/s

Pressure: 0.02 mbar

Figure 4. SEM image of PtOEP NWs on TiO$_2$ (PECVD)/Si (up) and its corresponding UV-Vis spectrum on Q.

Phthalocyanine (H$_2$Pc)

Substrates: ZnO, TiO$_2$, SiO$_2$ (both GLAD and PECVD), Au NPs on Si, Q, micrux, PTFE and ITO/PET

Substrate temperature: 170-200 ºC

Growth rate (QCM): 0.45-0.50 Å/s

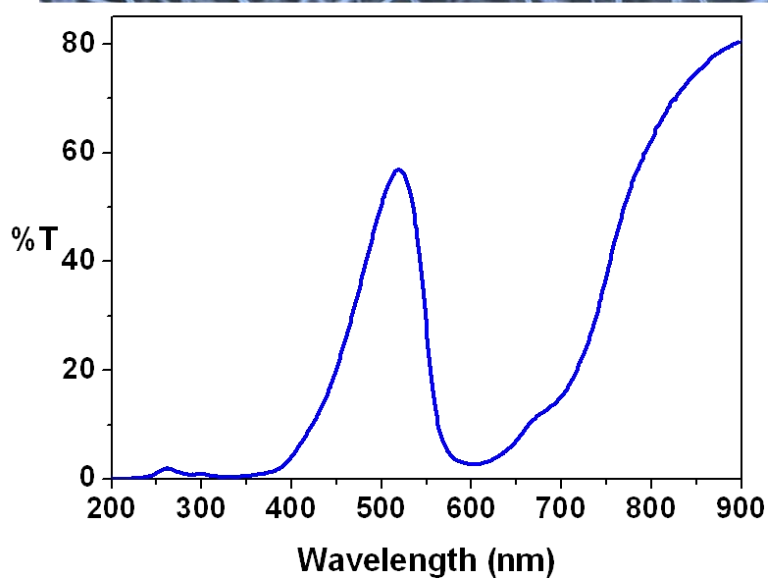**Pressure: 0.02 mbar**
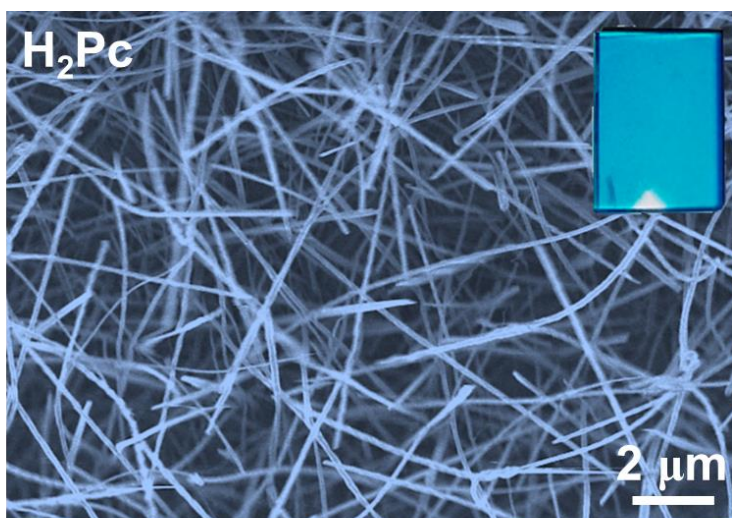
Figure 5. SEM image of H₂Pc NWs on Au NPs/(ITO/PET) (up) and its corresponding UV-Vis spectrum on SiO₂ (PECVD)/Q.

Cobalt, nickel, zinc and copper phthalocyanines (CoPc, NiPc, ZnPc and CuPc)

Substrates: ZnO, TiO₂, SiO₂ (both GLAD and PECVD), Ag NPs on Si and Q

Substrate temperature: 180-220 ºC

Growth rate (QCM): 0.3-0.45 Å/s

Pressure: 0.02 mbar
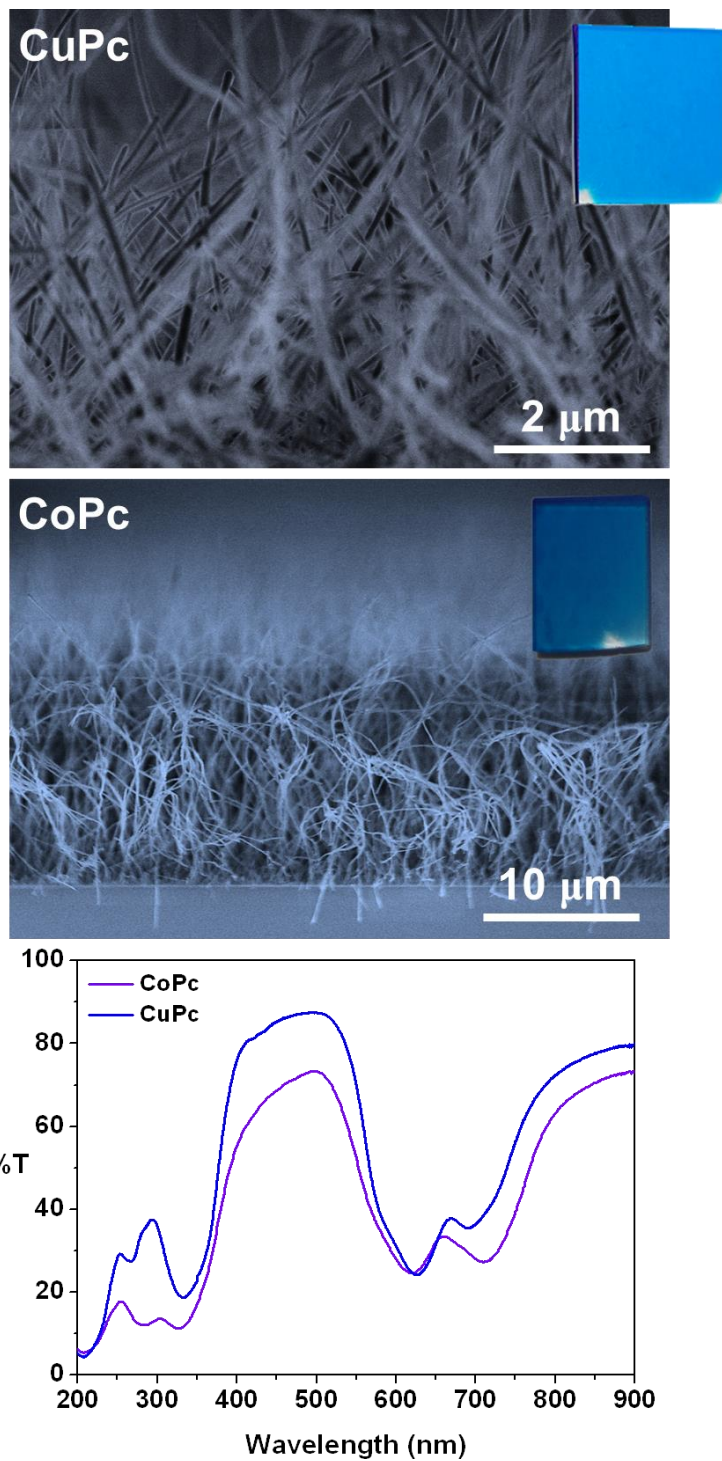
Figure 6. SEM micrographs of CuPc Nws on Au NPs/ITO (up), long CoPc NWs on TiO$_2$ (middle) and their corresponding UV-Vis spectrum on Q.

Fluorinated copper phthalocyanine (F$_{16}$CuPc)

Substrates: TiO$_2$, micrux, Ag NPs on Si and Q

Substrate temperature: 165-180 ºC

Growth rate (QCM): 0.45 Å/s
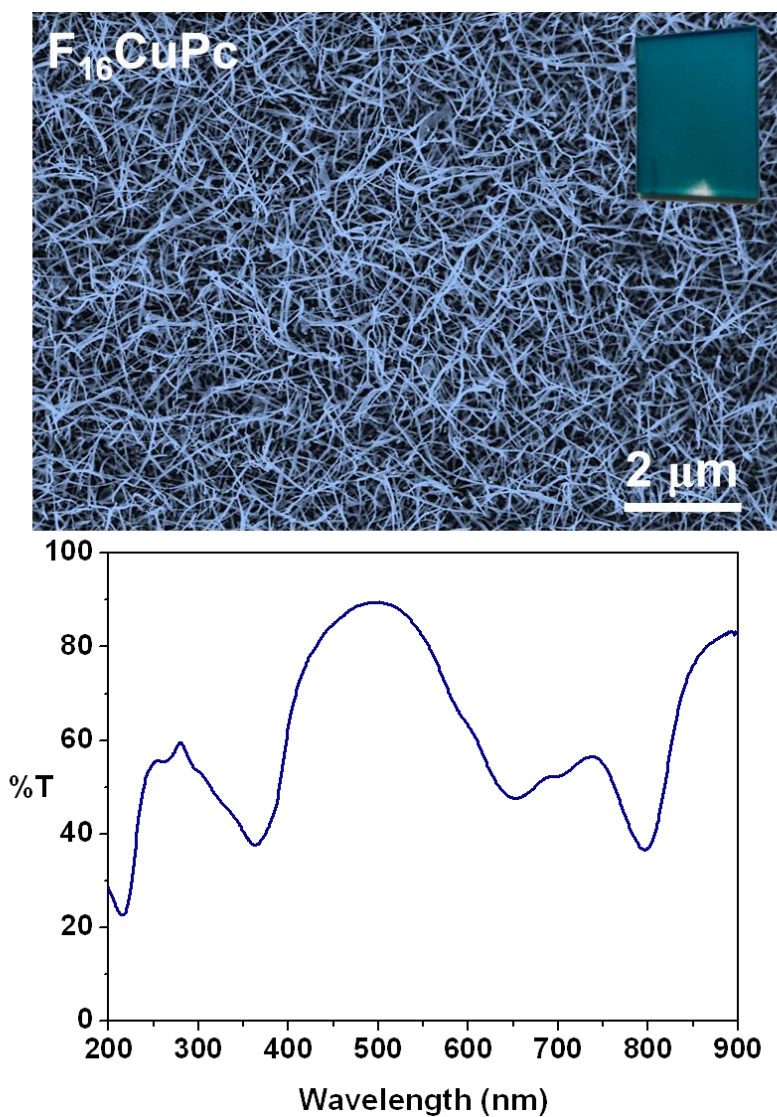
Pressure: 0.02 mbar

Figure 7. Figure 8. SEM image of F$_{16}$CuPc NWs on Ag NPs/Si (up) and its corresponding UV-Vis spectrum on Q.

Iron phthalocyanine (FePc)

Substrates: Al*/Si, Al foil, Cu (GLAD) on Si, thick Cu foils, TiO$_2$

Substrate temperature: 220 ºC

Growth rate (QCM): 0.4 Å/s

Pressure: 0.02 mbar
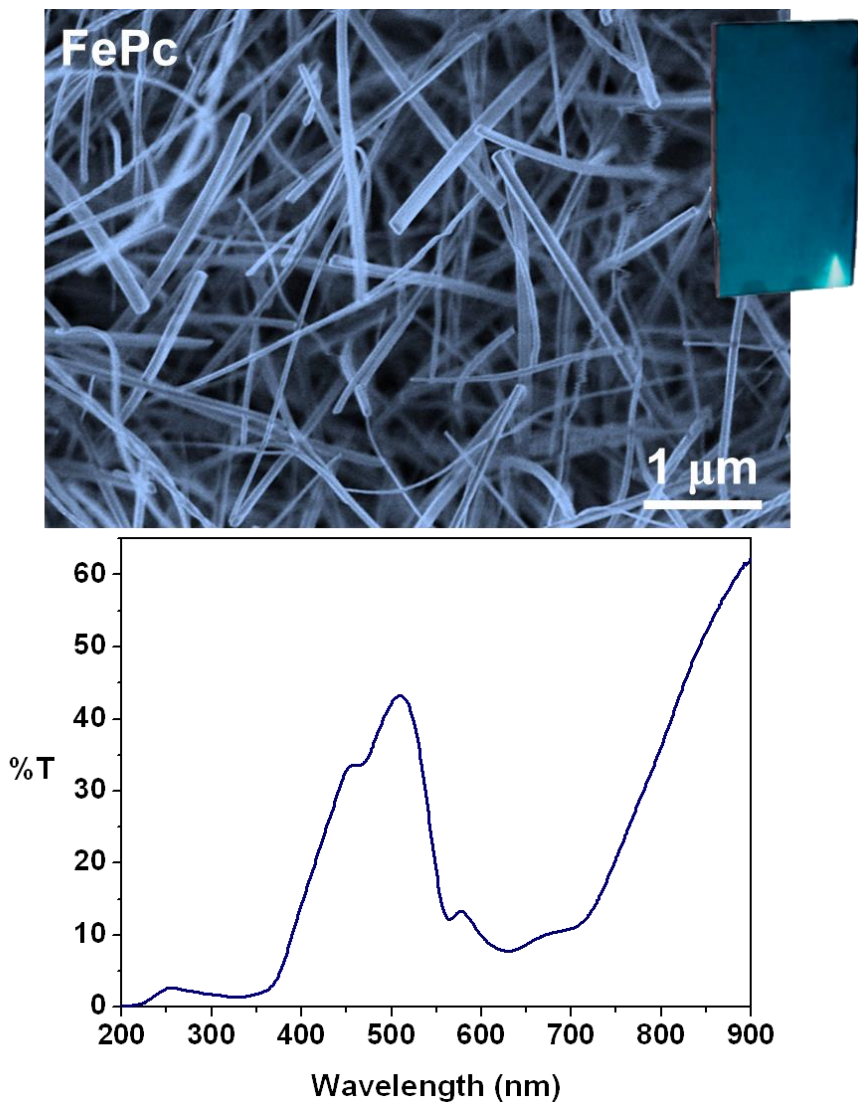
Figure 8. SEM image of FePc NWs on Al/Si (up) and its corresponding UV-Vis spectrum on TiO$_2$/Q.

* Evaporated under high-vacuum conditions.

Chlorinated iron phthalocyanine (ClFePc)

Substrates: Al*/Si, Cu (GLAD) on Si, thick Cu foils

Substrate temperature: 210 ºC

Growth rate (QCM): 0.4-0.45 Å/s

Pressure: 0.02 mbar
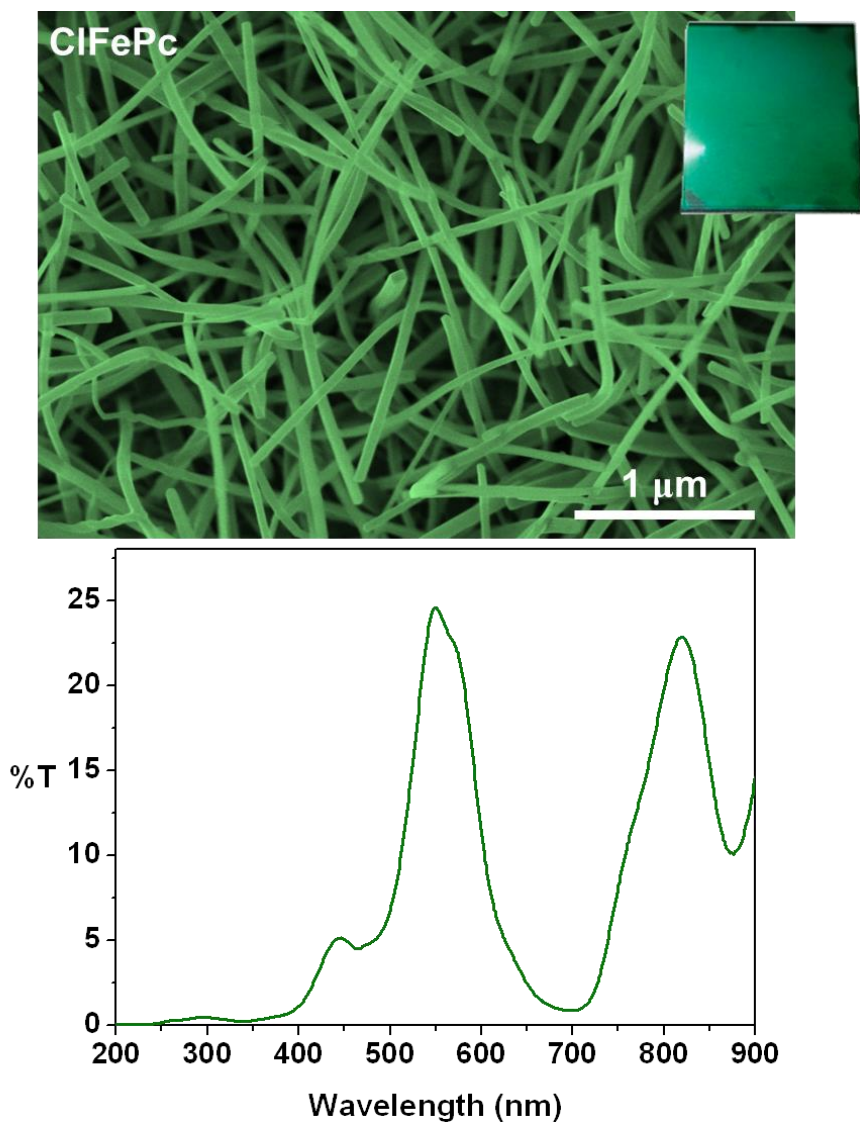
Figure 9. SEM image of ClFePc NWs on Al/Si (up) and its corresponding UV-Vis spectrum on TiO$_2$/Q.

* Evaporated under high-vacuum conditions.

Chlorinated silicon phthalocyanine (Cl$_2$SiPc)

Substrates: Al, Si, SiO$_2$ on Si and Q

Substrate temperature: 200 ºC

Growth rate (QCM): 0.1-0.15 Å/s
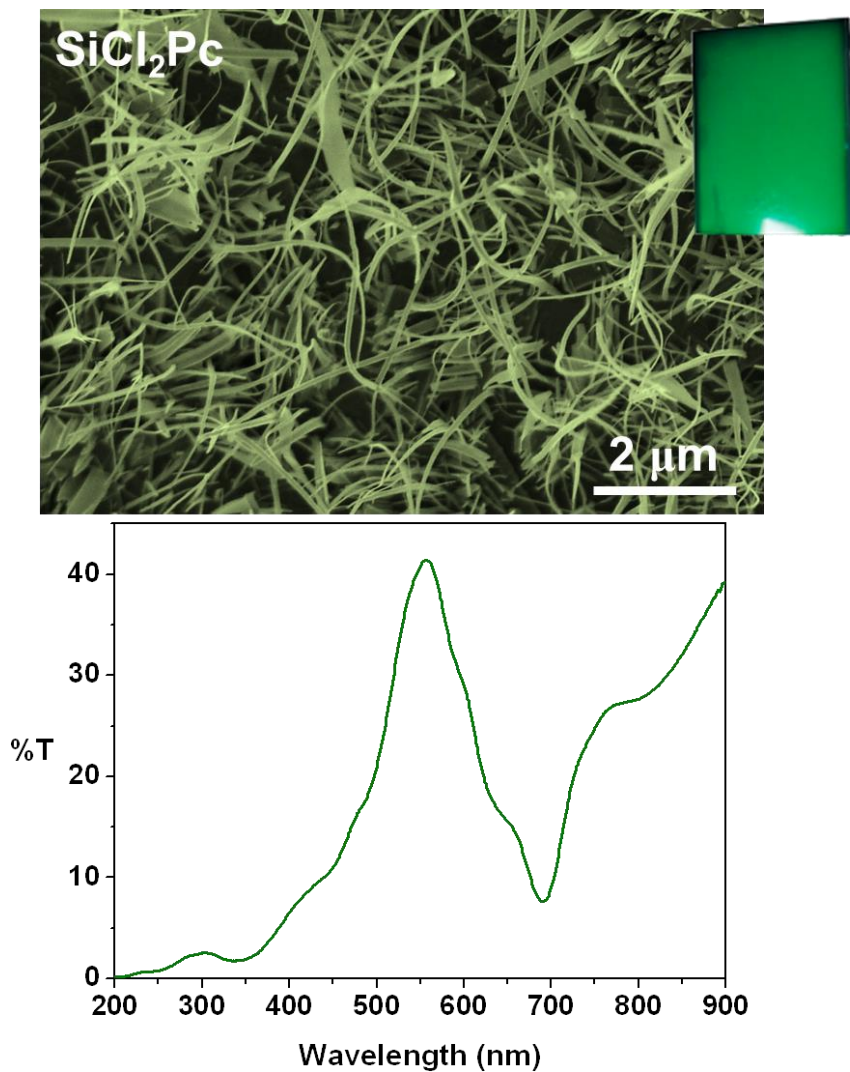
Pressure: 0.3 mbar

Figure 10. SEM image of Cl$_2$SiPc NWs on SiO$_2$ (GLAD)/Si (up) and its corresponding UV-Vis spectrum on SiO$_2$ (GLAD)/Q.

Nanotrees

The methodology developed by Borrás and Alcaire et al. to produce highly connected NWs [Borrás A. I., Adv. Materials][Alcaire M., Nanoscale 2011] has been extended to other non-metallic molecules to generate hyperbranched NWs, giving rise to highly dense nanoforests. The technique consists in a three step process: deposition of the primary NWs, plasma etching and deposition of the secondary NWs. The last 2 steps, namely the ramification process, can be repeated as many times as wanted in order to attain a higher number of ramifications and thus density. Fig. 11 is an example of Pc nanotrees were the ramifications are clearly visible (note that no UV-Vis spectrum is shown due to nearly 100% light absorption in that region) .
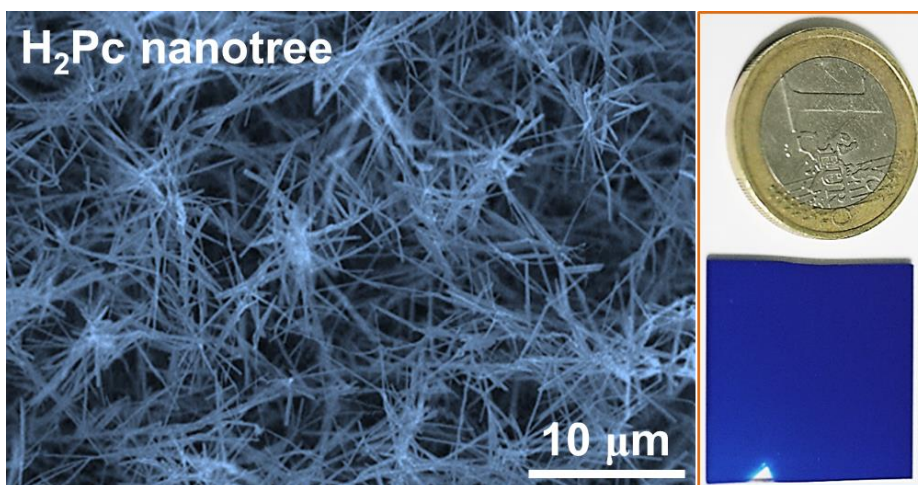
Figure 11. SEM images of a H_2Pc nanoforest.

The experimental conditions for the fabrication of the nanotrees were as follows:

Substrates: TiO$_2$, SiO$_2$, ZnO, Ag or Au NPs on Si, Q, micrux, ITO/PET.

NWs growth

Substrate temperature: 160-180 ºC

Growth rate (QCM): 0.45 Å/s

Pressure: 0.02 mbar

Plasma etching

Substrate temperature: RT

Plasma-to-substrate distance: 10 cm

Plasma power: 300 W

Gas composition: 20% Ar, 80% O_2

Pressure: 0.02 mbar

Plasma duration: 20 minutes for NWs up to 1 kÅ and 40 minutes for NWs of around 3 kÅ.

References

Alcaire M. et al., Soft plasma processing of organic nanowires: a route for the fabrication of 1D organic heterostructures and the template synthesis of inorganic 1D nanostructures. Nanoscale 3(11), 4554-4559 (2011).

Borrás A. I. et al., Connecting organic nanowires. Advanced Materials 21, 4816-4819 (2009).

Sánchez-Valencia J. R. et al., Selective Dichroic Patterning by Nanosecond Laser Treatment of Ag Nanostripes. Advanced Materiales 23, 1-5 (2010).

Appendix B. A novel 3D absorption correction method for quantitative EDX-STEM tomography

Abstract

This appendix presents a novel 3D method to correct for absorption in energy dispersive X-ray (EDX) microanalysis of heterogeneous samples of unknown structure and composition. By using STEM-based tomography coupled with EDX, an initial 3D reconstruction is used to extract the location of generated X-rays as well as the X-ray path through the sample to the surface. The absorption correction needed to retrieve the generated X-ray intensity is then calculated voxel-by-voxel estimating the different compositions encountered by the X-ray. The method is applied to a core/shell nanowire containing carbon and oxygen, two elements generating highly absorbed low energy X-rays. Absorption is shown to cause major artefacts of in reconstruction, in the form of an incomplete recovery of the oxide and an erroneous presence of carbon in the shell. By applying the correction method, these artefacts are greatly reduced. The accuracy of the method is assessed using reference X-ray lines with low absorption.

1. Introduction

EDX microanalysis in the transmission electron microscope (TEM) is a valuable technique for materials characterisation [1-4]. Until recently, the technique has been limited by poor collection efficiency, and hence

relatively long acquisition times [4,5]. With the advent of larger, silicon drift [6] and multiple detectors [7], modern systems offer higher acquisition rate for a lower dose. EDX chemical mapping has benefited greatly from this technological breakthrough, especially in helping the extension to (quantitative) 3D mapping, as observed recently with a wider range of applications [8-15] compared to the early work of the pioneers [16-18].

In a scanning electron microscope (STEM), 2D imaging can be extended to three-dimensional (3D) imaging by using tomography. Electron tomography (ET) is nowadays a well-established technique in the physical sciences, especially using high angle annular dark field (HAADF) imaging [19-21]. To be suitable for tomographic reconstruction, the electron-specimen interaction should satisfy the "projection requirement": the signal should vary at least monotonically with thickness and composition [22]. When detecting secondary signals, such as an X-rays for EDX, the interaction with the specimen needs to be considered as well. To illustrate the interactions of primary electrons and secondary X-rays with the specimen, two electron paths through a core/shell nanowire are considered (see the arrows in Fig. 1). The generated X-ray intensities along these symmetric paths are identical. However, as the path towards the EDX detector for the right-

hand position is longer (and goes through the core), X-rays are more likely to be absorbed in the specimen, yielding a lower X-ray intensity. Variations due to absorption or changes in specimen composition may be indistinguishable when absorption is significant, as typically observed for low energy X-rays or/and thick samples. This paper aims to correct for the absorption effect in order to retrieve the monotonicity of the EDX signal and improve the reliability of the 3D EDX-STEM reconstructions. It is worth noting that other phenomena, beyond the scope of the current work, might also break the monotonic behaviour of the EDX signal, such as channelling effect [23] and detector shadowing by the sample holder and the sample grid [13].

X-ray absorption is one of the most important limitations for quantitative EDX analysis, even with thin specimens. Goldstein et al. [24] proposed to correct for the absorption in the Cliff-Lorimer approach (CL) [25] by multiplying the intensity by a correction factor (A). This factor is derived from Beer's law and requires a measurement of the mass-thickness. To overcome the complications arising from external measurement of thickness and density, several approaches have been proposed: for instance by using the difference in absorption between two emitted X-ray lines [26], or measuring spectra at different tilt angles [27] or sample thicknesses [28]. A more recent approach, the

ζ-factor method [29], solved this problem in a more general way by measuring the current. All these approaches were established for thin films and aim to measure an accurate absorption correction factor A, supposing a homogeneous specimen where X-rays are generated and absorbed. To apply this approach to a sample with a heterogeneous structure, such as the core/shell nanowire of Fig. 1, the structure has to be known to predict the X-ray generation as a function of depth as well as the X-ray path to the surface through different materials. This problem can be addressed with 3D EDX-STEM tomography since information about X-rays generated from each voxel and their path through all the encountered voxels to reach the surface becomes available.

The present work introduces a novel "3D absorption correction" approach: An example of artefact-free EDX-STEM tomography is presented, using a core/shell nanowire as test sample. The accuracy of the absorption correction method is assessed using X-ray lines with significant absorption and high energy X-ray lines with relatively low absorption as a reference.

2. Materials and Methods

2.1. Core@multi-shell nanowire

The sample used for the present investigation is an organic/inorganic core/multi-shell 1-D nanostructure, with potential applications in photonics and as nanogenerators. A HAADF-STEM image of the nanowire tip is shown in Fig. 2(a) and a description of the different elements present in the sample is schematized in Fig. 2(b). The PtOEP core is grown from silver nanoparticle seeds by physical vapour deposition and is composed of platinum, nitrogen and carbon. The first shell of the 1-D nanodevice is generated by soft plasma etching of the PtOEP to yield platinum. An unexpected AgPt phase is present in the core and forms a thin layer around it. The second shell is formed of ZnO grown by plasma enhanced chemical vapour deposition [30]. The external shell is fabricated by conformal deposition of a thin layer of gold by means of DC sputtering at room temperature.

2.2. EDX-STEM tomography

The ET experiment was performed on an FEI Osiris TEM (FEI company) operating at 200kV and equipped with a high brightness X-FEG gun and a Super-X EDX system comprising 4 detectors. Each detector has an active area of 30 mm^2, achieving 0.9 sr solid angle in total. As shown in Fig. 3, the 4 detectors are arranged around the electron beam axis. The elevation angle (for the centre of each detector) is 22° and the azimuth angles are 45°, 135°, 225° and 315° for detector

1, 4, 3 and 2 respectively. The signal from different detectors is summed before amplification and cannot be separated through post-processing. The NWs were dispersed on a commercial TEM grid possessing a 5 nm-thick carbon film on a thicker 30 nm holey carbon film (Pacific Grid Tech), which was mounted on a Fischione 2020 single-single tomography holder (Fischione Instruments, USA). A NW oriented parallel to the rotation axis was selected, and the tilt series was acquired manually, from -60˚ to +70˚ with a 10˚ tilt increment. At each tilt angle, a HAADF-STEM image with frame size of 1024 x 1024 and a pixel size of 1.09 nm was acquired, followed by an EDX map of a selected region, with a map size of 80 x 92 and a pixel size of 4.5 nm. The beam current was 600 pA. To reduce beam damage, a dwell time of 40 ms was used, corresponding to an acquisition time of 5 min per map. Depending on the acquisition geometry, some of the X-rays rays emitted from a region of interest are obstructed by surrounding objects such as the sample holder and supporting grid. As the elevation angle is low, the shadow cast onto the detectors varies rapidly with tilt angle around 0°. To minimize the effect of shadowing, only the two detectors facing the sample were used during the tilt series; i.e. detector 1 and 2 for positive tilt (including 0° tilt) and detector 3 and 4 for negative tilt.

The sum of all spectra of the tilt series is plotted in Fig. 4 with a solid curve. The energy range between 3.5 and 7 keV is not displayed, as it contains no X-ray lines of importance. X-ray lines for the six elements that composed the core/shell nanowire (C, O, Zn, Pt, Au, Ag) are observed. Carbon and oxygen have only one resolved line, the O Kα and C Kα, respectively, which have the lowest energy of the analysed X-ray lines. Cu Kα and Ni Kα peaks are spurious X-rays generated from the supporting nickel grid and the sample holder. The Si and Cl signals are likely due to contamination from volatile organosilicon compounds used in the desiccator where the silver seeds were storage.

Also in Fig. 4, the mass absorption coefficients μ/ρ of X-rays absorbed in PtC_{25} and ZnO, two compositions chosen to approximate the nanowire core and shell respectively, are plotted as a function of energy with red and blue curves. The jumps in the curves are the X-ray absorption edges, corresponding to the ionization energy of inner shell electrons. These edges are situated at slightly higher energy than the corresponding X-ray lines; for instance the centre of Zn Lα peak is slightly left of the corresponding jump on the blue curve. Zn Kα and Pt Lα have a μ / ρ about two orders of magnitude lower than the three most highly absorbed X-rays (C Kα, O Kα, Zn Lα), making the Zn Kα

intensity a suitable internal reference, with low absorption compared to the Zn Lα intensity.

The EDX maps were acquired using the software TIA (FEI company) and exported for post-processing. Apart from alignment, all data processing were done with python packages. Hyperspy, a python-based software for hyperspectral data processing [31], was used as a central data processing platform and to implement the absorption correction procedure. The data were de-noised using singular value decomposition (SVD) for principal component analysis (PCA) [32]. X-ray intensities were extracted from EDX spectra by fitting (peaks and background) of experimental spectra using an EDX-specific model [33]. TomoJ was then used for alignment by automatic feature tracking [34]. The reconstructions were performed using the simultaneous algebraic reconstruction technique (SART) algorithm [35], and the obtained volumes rendered using Mayavi [36]. Elemental compositions were quantified using the quantification method by CL [25] and the k-factors provided by the EDX manufacturer Bruker. A total variation minimisation (TV) algorithm from Chambolle [37] was used to improve the signal-to-noise ratio in the obtained reconstructions. One iteration of the absorption correction, including the reconstruction of all X-ray intensities, takes about 24 minutes on a standard computer (one

processor of 3.4 GHz). The slower parts of the process were parallelised and the time per iteration was reduced to 6 minutes with 8 processors.

3. Calculation

In the classical CL approach, the composition C is related to the X-ray intensities I measured from a thin film [25]. With two elements A and B, the CL approach can correct for the absorption using [24]:

$$\frac{C_A}{C_B} = k_{AB} \frac{I_A I_A}{I_B I_B},$$

where k is the CL factor, also known as the k-factor, and A is the absorption correction factor. The more recent ζ-factor method incorporates the total dose during acquisition D_e, obtaining in this way a measurement of the composition and the mass-thickness ρt as:

$$C_A = \frac{\zeta_A I_A I_A}{\zeta_A I_A I_A + \zeta_B I_B I_B},$$

$$\rho t = \frac{\zeta_A I_A I_A + \zeta_B I_B I_B}{D_e},$$

where ζ is the ζ-factor [38]. Both k-factors and ζ-factors can be determined theoretically and experimentally.

The X-ray absorption in a material is predicted by Beer's law: the X-ray intensity I emerging from a thin film of thickness *t* is: $I = I_0 \exp\left(-\frac{\mu}{\rho}\rho t\right)$, where I_o is the primary X-ray intensity, μ/ρ is the mass absorption coefficient and ρ is the density. With $\varphi(\rho z)$ the depth distribution of the generated X-rays in the sample, and assuming a homogeneous X-ray absorption along the path z to the surface, the absorption correction factor *A* is obtained by integrating Beer's law as follow:

$$A = \frac{I_0}{I} = \frac{\int_0^{\rho t} \varphi(\rho z) d(\rho z)}{\int_0^{\rho t} \varphi(\rho z) \exp\left(-\frac{\mu}{\rho}\rho z \csc\alpha\right) d(\rho z)},$$

where α is the take-off angle and z csc α is equal to the distance from the generation point to the surface. A uniform generation of X-rays along the depth can be reasonably assumed within the thin film: $\varphi(\rho z)$ is equal to unity and Eq. 3 is simplified to (Philibert [39]) :

$$A = \frac{\frac{\mu}{\rho}\rho z \csc\alpha}{1 - \exp\left(-\frac{\mu}{\rho}\rho z \csc\alpha\right)},$$

This expression for *A* is used in both the CL and ζ-factor methods [24, 38].

Correcting the absorption in 3D allows us to refine the approximation of a constant generation and of a homogeneous X-ray path by

considering the X-ray generation in each voxel and the different voxels encountered in the X-ray path to the surface. The X-ray generation is thus assumed to be constant in each voxel and the X-ray path is assumed to be homogeneous within each voxel encountered.

In Fig. 5(a), a section through the x-z plane of the 3D matrix of elemental composition $\mathbf{C}$ is represented with a grid. A precipitate is represented with a darker grey than a surrounding matrix. The X-ray path, represented by the arrow, has a different length in each encountered voxel. In a standard reference frame, the z axis is parallel to the electron beam as shown in Fig. 5(a). In Fig. 5(b), a new reference frame x^*, y^* and z^* is defined with x^* axis parallel to the detector direction. The composition matrix in this reference frame ($\mathbf{C}^*$) is obtained by rotating $\mathbf{C}$ by the elevation angle, the sample tilt and the azimuth angle of the detector. In each encountered voxel of the matrix $\mathbf{C}^*$, the X-ray path has the same length (the voxel size Δx), thus simplifying the calculation of the absorption correction factor A^*_j of voxel $x^* = j$.

An X-ray intensity I_0 is generated in voxel j from a particular element and an X-ray intensity I_j is emitted from voxel j before entering voxel $j+1$, as defined in Fig. 5(b). The ratio I_j over I_0 can be obtained by integrating over the voxel, as in Eq. 3. Since Δx is small, the integral is

approximated by the function itself, $\int_0^{\Delta x} f(x)dx = f(\frac{\Delta x}{2})\Delta x$, and Eq.3

becomes:

$$\frac{I_j}{I_0} \approx \exp\left\{-\left(\frac{\mu}{\rho}\right)_j \rho_j \frac{\Delta x}{2}\right\}.$$

The final intensity I, emitted from voxel $x^* = n_{max}$ at the surface of the

sample, is calculated by applying to I_j the absorption correction factor

obtained with Eq. 5, of each subsequent voxel $x^* = j + n$ encountered

along the X-ray path:

$$\frac{I}{I_j} = \exp\left\{-\sum_{n=j+1}^{n_{max}} \left(\frac{\mu}{\rho}\right)_n \rho_n \Delta x\right\}.$$

The absorption correction factor A^*_j is obtained by combining Eq. 5 and

6:

$$\frac{I}{I_0} = \frac{1}{A^*_j} = \exp\left\{-\left(\frac{\mu}{\rho}\right)_j \rho_j \frac{\Delta x}{2} - \sum_{n=j+1}^{n_{max}} \left(\frac{\mu}{\rho}\right)_n \rho_n \Delta x\right\}.$$

$$(7)$$

The final absorption correction matrix A is obtained by calculating the

factors A^* for all elements and all voxels x^*, y^* and z^*, and rotating

them into the standard x, y, z reference frame.

In the acquired data, two detectors were used and the individual

detector signals cannot be separated. The directions to the two detectors

are approximated by a single mean direction; for example the detectors 1 and 2 with 45° and 315° (-45°) azimuth respectively (see Fig. 3) are approximated with 0° azimuth.

In Eq. 7, a value of density is needed for each voxel. With the ζ-factor method, the density can be obtained from the measured mass-thickness (Eq. 2(b)). With the CL method, the density can be estimated from the matrix of elemental fraction C with a weighted mean ($\rho = \sum C_{el}\, \rho_{el}$) or a harmonic mean ($1/\rho = \sum C_{el}\, /\rho_{el}$) or can be estimated from an external signal such as the HAADF-STEM tomogram.

As the absorption correction factors depend on the composition and vice versa, an iterative approach is required for both classical and 3D absorption correction. The general approach is the same: the iteration is initialised by calculating a composition C_0 with no absorption correction from the X-ray intensity I. In each iteration step, the absorption correction factors A_i are calculated from the composition C_i and applied to the X-ray intensity (I^*A_i) to obtain a new composition C_{i+1}.

For 3D absorption correction, the iterative process needs to include reconstruction and projection steps as shown in Fig. 6. The 3D matrix of elemental composition, $\mathbf{C}_0$, is first approximated without absorption

correction: the tilt series of intensities, $\mathbf{I}_{til,0}$, are reconstructed (rec) and the reconstructed intensities, $\mathbf{I}_{vol,0}$, are quantified (quant). This first approximation $\mathbf{C}_0$ is used to calculate the absorption correction matrix, $\mathbf{A}_1$.

The absorption correction matrix $\mathbf{A}_1$ could be applied directly to the reconstructed intensity $\mathbf{I}_{vol,0}$. However, the reconstruction might introduce artefacts as absorption effects are likely to break the tomographic requirement. The absorption correction matrix ($\mathbf{A}_1$) is thus applied to the tilt series of recorded intensities $\mathbf{I}_{til,0}$ and thus required to be projected about the tilt axis. A direct projection, rotation of the matrix and sum along the beam direction, of $\mathbf{A}_1$ is not possible as the absorption correction is not a linear operation. A corrected $\mathbf{I}_{til,1}$ is projected instead and compared to the projected $\mathbf{I}_{vol,0}$ to obtain an absorption correction factor $\mathbf{A}_{til,1}$ for the tilt series:

$$A_{til,i} = \frac{[I_{vol,i}]_{til}}{[I_{vol,0}]_{til}} = \frac{[I_{vol,0}A_i]_{til}}{[I_{vol,0}]_{til}},$$

where i is the number of iterations and the square bracket indicates a direct projection. The matrix of intensities $\mathbf{I}_{vol,1}$, 1 is reconstructed from $\mathbf{I}_{til,1}$, and equal to $\mathbf{I}_{til,0}\,\mathbf{A}_{til,1}$, and quantified to obtain a new $\mathbf{C}_1$ for the next step of the iteration. The loop is stopped when the result of an

iteration is close to the previous iteration, typically less than 0.001 wt% difference.

4. Results

To prevent beam damage, the electron dose seen by the sample is limited by reducing the time spent per spectrum. The raw spectra are therefore noisy with a mean number of counts per channel less than one. An effective de-noising technique is needed, as illustrated in Fig. 7. The set of data contains millions of spectra characterising only a limited set of chemical phases. This is a favourable case for a multivariate statistical approach such as principal component analysis. Using PCA, the set of spectra is decomposed and then a model of the data is reconstructed leaving out the components characteristic of the noise [40]. Prior to the decomposition, the data were scaled to take into account Poisson statistics [41]. Masking regions with lower counts, the vacuum and the carbon film, improves the separation between the noise and the signal components. To prevent any mixing between X-ray maps of low and high energy due to covariance, PCA is applied separately on the low and high energy part of the data set, as indicated by the split spectrum of Fig. 7. By inspection of the scree plot and the noise content in the individual components, the first eight and four components were

chosen to reconstruct the model for the low and high energy datasets, respectively. As seen in Fig. 7, the PCA-adjusted spectrum is relatively noise-free and the continuous background is well defined. The noise is significantly reduced in the raw intensity map for O Kα.

After noise filtering, the intensities are extracted and background corrected. Alignment of Ag Lα intensity maps is performed by automatic feature tracking and subsequently applied to the remaining elemental tilt series.

A general decrease of X-ray intensity due to shadowing is observed for maps close to 0° tilt, even when only the two EDX detectors facing the sample are employed. To correct for this effect, each intensity map is divided by the total intensity in the map. The normalised maps are then multiplied by the required factor to conserve the total intensities in the tilt series [15].

The first 3D matrix of absorption correction factors $\mathbf{A}_1$ is obtained as described in the first line of Fig. 6. The reconstructed intensities are smoothed using a TV algorithm and the obtained intensities quantified using the CL quantification method. With this approach, the composition is normalised to 100% and voxels of vacuum and voids in the nanowire are filled with noise. Trial-and-error showed that all

voxels in the composition matrix emitting a total X-ray intensity below 7 counts are masked (30 counts are emitted in average from the voxel of the shell). $\mathbf{A}_1$ is obtained with Eq. 7 and the correction for O Kα is shown in Fig. 8. The detector direction lies in the xz plane with an angle of 22° with x axis and goes in the direction of positive x and negative z, as indicated by the trail in the vacuum in the xy section of Fig. 8. The correction is stronger in the direction opposite to that of the detector. A linear structure is observed along this direction. Voids are observed inside the core with lower absorption correction.

After the calculation of the first absorption correction matrix $\mathbf{A}_1$, the tilt series are corrected as described in Eq. 8 and a new $\mathbf{A}_2$ is calculated. The effect of absorption correction after one and two iterations are considered in Fig. 9. In this figure, the grey scale gives the O Kα intensity of x-tilt sections, also known as sonogram, through the tilt series ($\mathbf{I}_{til}$) for map a, map b and map c, and through the corresponding projected reconstruction ($[\mathbf{I}_{vol}]_{til}$ as defined in Eq. 8) for map d, map e and map f. The x-tilt section is positioned where the shell surrounds the core, as modelled by two circles in map g. Map h shows a projection of this model, which is only an approximation as the real shell shows a faceted aspect.

A jump in O Kα intensity is observed at zero tilt in Fig. 9(a) for the raw tilt series. This jump can be linked to an absorption effect: X-rays generated in the side of the shell opposite to the detectors travel further in the nanowire and are thus more likely to be absorbed. The jump reveals the change of detectors at 0° tilt (from detectors 3 and 4 to detectors 1 and 2, see Fig. 3). With the 3D absorption correction calculated after one iteration (map b), the intensity of the more absorbed side of the shell is increased: the jump in intensity is greatly reduced, but can be still observed with an inverted contrast. With the absorption correction calculated after two iterations (map c), the jump is hardly noticeable.

As observed for all the projections (maps d, e, f and h), a corrected tilt series (one that conforms to the projection requirement) shows smoothly evolving contrast along the tilt direction. The jump observed in map a is thus an indication of that the violation of the projection requirement. With reconstruction algorithms such as SART, the difference between the raw data $\mathbf{I}_{til}$ and the projected reconstruction $[\mathbf{I}_{vol}]_{til}$ is minimised during the reconstruction process, thanks to the so-called data fidelity constraint. In other words, maps d, e and f are the closest approximation of maps a, b and d, respectively. The incoherent jump in map a is approximated by a smoothly evolving contrast in map

b, resulting in an important difference between map a and map b. After absorption correction, $\mathbf{I}_{til}$ and $[\mathbf{I}_{vol}]_{til}$ are more similar, indicating that a higher data fidelity is reached.

The iterative convergence of the absorption correction (see Fig. 6) is considered in more detail in Fig. 10. The convergence criterion, the root-mean-square (RMS) of the difference of the reconstruction corrected after i iterations and $i+1$ iterations, is plotted as a function of the number of iterations. In this logarithmic plot, the same linear behaviour is observed after the first iteration for the different X-rays, indicating a fast convergence. A higher convergence criterion is observed for X-ray lines with the higher absorption correction (O Kα, C Kα and Zn Lα).

The reconstructed intensities of elements present in the shell of the nanowire are shown in Fig. 11: the shell is composed of zinc and oxygen. For both elements, the reconstructions obtained without or with absorption correction are compared. The corrected intensities of Zn Kα are not displayed as the absorption correction is small, with 95% of the voxels having an absorption correction below 0.5% (compared to 27% for the Zn Lα intensity). The uncorrected intensities of the Zn Kα (map f) are thus used as an absorption-free reference. The effect of absorption can be observed comparing O Kα intensity (map a) with Zn

Kα intensity (map f). In map a, the shell appears almost absent for low values of z in the zy section but appears more even in the xy section. A similar but less marked drop in intensity can be observed in map d for the Zn Lα intensity. The absorption effect is thus observed primarily along the z axis, which is inconsistent with the position of the detectors, situated close to the xy plane and not along the beam direction (z axis). This inconsistency is an artefact of the reconstruction algorithm due to the uncorrected X-ray maps not being true projections.

This reconstruction artefact is greatly reduced by applying the absorption correction as the Zn Lα intensity in map e of Fig. 11 appears to match closely the Zn Kα intensity in map c. The O Kα intensity in map b now looks similar to the Zn Kα intensity, but an over-correction is observed with high intensity at low value of z. For a more accurate comparison, a profile along the z axis going through the shell at the position indicated by the coloured lines in Fig. 11(a-f) is considered in Fig. 11(g). The intensities plotted are smoothed by TV filter and normalised with the maximum of the profile in the right part of the shell that shows less absorption effect. An absorption effect is clearly observed on the left part of the shell for O Kα and Zn Lα intensities. After absorption correction, a close match is observed between Zn Lα and Zn Kα intensities. The O Kα intensity is closer to Zn Kα intensities,

although slightly over-corrected. This can be attributed to the weighted mean approach used to estimate the density from the composition.

Assuming the intensity of HAADF-STEM images is proportional to the mass thickness, the density can be estimated by scaling the HAADF-STEM images to a region with a known density. Using the weighted mean approach, both core and shell have similar density but when using the HAADF-STEM approach, the density of the core is significantly lower that the density of the shell. With a shell expected to be composed of ZnO and the weighted mean density in the shell close to the density of the ZnO, this density is used to scale the HAADF-STEM images. The obtained density is used to calculate the absorption correction. By calculating the absorption correction with the HAADF-STEM density, a more accurate result is obtained as observed in the profile of Fig. 11(g) with the corrected O Kα intensity now closer to the Zn Kα intensities. It is worth noting that the density obtained with HAADF-STEM images introduces a different source of inaccuracies; for example a contrast variation in the shell due to diffraction. The weighted mean density is kept as a method of choice for a direct evaluation of the 3D absorption correction, as it does not required any a-priori knowledge of the sample.

The reconstructed intensities of the elements present in the core are shown in Fig. 12: the core is formed of a porous mixture of carbon and platinum and contains small particles composed of silver. Platinum and silver form a layer around the core and a layer of gold is observed on the tip of the nanowire in map f. A schematic picture of the sample is shown in Fig. 2(a). A larger void is observed at the tip of the core.

Reconstructions obtained without and with absorption correction are compared. The corrected intensities of Pt Lα and Ag Lα are not displayed as the absorption is small. The C Kα intensity has the highest value of absorption correction. In map a, the C Kα intensity is present in the shell with strong variation in contrast. As the supporting film is composed of carbon, a value of C Kα intensity emitted from the film is estimated for each tilt from regions that are known to be film only and removed from the tilt series before the reconstruction. In map b, the resulting C Kα intensity reconstruction is generally lower in the shell and the shape of the core observed in the xz section is better defined. In some regions with high z value, the intensity of the shell is however similar to the one in the core. After absorption correction, the C Kα intensity (map c) in the core is clearly above the intensity in the shell.

A profile along z through the core is plotted in Fig. 12(e). As for the shell in Fig. 11, intensities are smoothed by a TV filter and normalised

with the maximum of the profile. An important shoulder is observed for high values of z on the C Kα profile. The shoulder is significantly reduced, first by correcting for the supporting film, then by correcting for absorption. These processing steps contribute towards a more uniform C Kα intensity inside the core.

The absorption correction for the two strongest absorbing X-ray lines provides an important improvement that can be appreciated in 3D in Fig. 13. The green and red isosurfaces indicate a high O Kα and C Kα intensity respectively. The threshold values used are indicated by a horizontal dashed blue line in the z profiles of Fig. 11(g) and Fig. 12(e). The shell formed by the uncorrected O Kα intensity is not complete: a hole is observed for low value of z in Fig. 13(a). With a higher value of threshold, a complete shell can be obtained. The core formed by the uncorrected C Kα intensity shows an appendage towards high values of z. With higher values of threshold, the appendage is suppressed, but the void at the tip of the core is then not visible. Correcting for absorption in Fig. 13(b), the shell is complete for any value of threshold and the void at the tip of the core can be observed without any appendage for an appreciable range of thresholds. The artefacts and their correction can be appreciated with more details in the supplementary animated figure (appendix A) varying the view and the thresholds of the

isosurfaces. The second video shows a reconstruction of X-ray lines from the different elements.

5. Discussion

Absorption introduces a contrast mechanism that breaks the "projection requirement" if not taken into account. The reconstruction algorithm finds the closest estimation that respects the requirement by introducing an artefact observed as a gradient of intensity in the unexpected direction of the electron beam. By applying the proposed 3D absorption correction, this artefact is almost totally removed in the case of the moderately absorbed Zn Lα intensity, as observed in Fig. 11(g) with a close match with Zn Kα intensity in term of shape. The Zn Kα intensity has shown little absorption in the nanowire. Moreover, the risk of mixing Zn Lα and Zn Kα signals in the PCA de-noising process is prevented by applying PCA separately on low and high energy datasets, as proposed in [42]. The Zn Kα intensity is thus considered as an absorption-free reference for the Zn Lα intensity. The reference is relative as the cross-section of Zn Kα and Zn Lα is different, but as the part of the shell facing the detector emits X-rays with low absorption, an absolute reference can be deduced. As the shell is expected to be composed by a single phase of Zn and O and no experimental evidence

shows the opposite, the Zn Kα intensity is also considered as an absorption-free reference for O Kα intensity.

Being more absorbed than the Zn Lα, the O Kα intensity requires a higher absorption correction and is thus more sensitive to inaccuracies. In Fig. 11, the absorption artefact is greatly reduced with a corrected O Kα intensity close to the Zn Kα intensity. The absorption correction shows however to be sensitive to the method used to obtain the density. Deducing the density from the composition, porosities have to be differentiated from the material by using a mask, as compositions are normalised to 100%. This approach relies on the accuracy of masking porosities, which is limited for instance by sub-pixel voids. If we take the HAADF signals as proportional to the mass-thickness, the density of the porous core is directly estimated without masking. A lower density of the core is obtained with this approach, resulting in an improved absorption correction for O Kα intensity as observed in Fig. 11. However, the accuracy of this approach is limited by the need of a reference and by possible diffraction artefact leading to variation in intensity. Moreover, an a-priori knowledge of the sample is needed to scale the density.

The C Kα line is the most absorbed lines of the analysed X-rays and an important increase of C Kα intensity in the core is observed in Fig. 12

with the absorption correction. As the carbon is situated mainly in the core, all C Kα X-rays have an approximately similar path through the shell to reach the surface. The structure of the core formed by C Kα intensity is thus less affected by absorption than the shell formed by O Kα intensity. The accuracy of the absorption correction for this line is difficult to evaluate, having no reference for the carbon composition. The C Kα intensity emitted from the supporting film is observed to lower the quality of the core reconstruction in Fig. 12(a). A simple correction by intensity subtraction is shown to improve the core reconstruction. The accuracy of this approach is however limited by the high noise level of the C Kα intensity still present after PCA de-noising. The best way to prevent the problem of spurious X-rays from the film is to use a film free of elements present in the sample.

An important limitation of the EDX analysis is the low number of collected X-ray counts despite the high efficiency EDX system. In our case, the electron dose is limited to prevent significant beam damage and thus individual spectra have a low number of X-ray counts. The dataset is however formed of a high number of spectra measured on similar phases: a favourable case for statistical methods such as PCA. Using PCA to de-noise, each spectrum is significantly improved as

shown in the Fig. 7. As the background is significantly smoothed, the accuracy of the background correction by fitting is greatly improved.

Two detectors are used for each tilt and the collected signal cannot be unmixed. In the proposed approach for 3D absorption correction, the absorption that takes place along the two paths is approximated by one single mean path. This approximation is reasonable for the core/shell nanowire, as the structure is coarsely symmetric along the "single" path. The "one-path" approximation is however likely to be less appropriate when samples with more complex structures or to be inappropriate when all four detectors are used. It is our hope that, with future microscopes, the signal of the four detectors will be recorded and processed separately. The 3D absorption correction can then be applied to the X-ray intensities of each detector, providing a 3D absorption correction applicable for all nanostructures.

For the absorption correction to be accurate, all X-ray intensities need to be accurately reconstructed. Reconstruction techniques, such as the SART algorithm used here, are known to suffer from artefacts when the tilt series have a low number of projections and/or a limited tilt range forming the so-called "missing wedge" [43]. Due to the low number of projections, the reconstructed intensity is correlated to the size of the object. This is observed with the reconstructed shell from the model in

Fig. 9(g) and from the measured X-ray intensity in Fig. 11(g): the smaller part of the shell has a lower intensity. Due to the missing wedge, other variations in contrast depending on the angular position are observed in the reconstructed model of the shell. These two artefacts are not expected to have a major influence on the accuracy of the absorption correction: the composition variation is limited as the composition is normalised to 100% and as the X-ray lines are expected to suffer proportionally with these artefacts. The composition of Zn in the large and small part of the shell are indeed observed to be much closer to that expected from the Zn $K\alpha$ intensity. Another artefact linked to the low number of projections is the loss of contrast between internal voids and the material: some remaining Zn $K\alpha$ and O $K\alpha$ intensity is observed in the core in Fig. 11(g), when the core is expected to be free of these elements. Albeit in small quantity, these mis-placed intensities increase the calculated absorption of the core, contributing to the over-correction of O $K\alpha$ intensity. A more recent reconstruction algorithm based on compressed sensing (CS) has shown to be more robust to low number of projections and the missing wedge [43]. The mentioned artefacts are expected to be reduced with such a method, resulting in an improved absorption correction. Although not present in the case of a nanowire, another artefact could have an important impact

on the absorption correction: if the sample is slab-like, the reconstruction of the slab using emitted the X-ray intensities is likely to suffer of truncation artefacts. The best way to prevent this is to use a needle sample extracted with a focused ion beam (FIB).

Finally, a major source of uncertainty for any EDX quantification procedure is the k-factors. The used k-factors, provided by the manufacturer, are derived from first principle, an approach likely to suffer significant systematic error [44]. To reduce this error, k-factors should be experimentally determined, requiring standards with multiple elements of known composition and thickness. With the more recent ζ-factor quantification method, these constraints are reduced as single element standards or a universal thin film standard can be used. Such approach has shown to reduce significantly the systematic error [38]. Moreover, this method provides, alongside the measurement of the composition, a measurement of the mass-thickness, from which a density can be derived and used in the proposed 3D absorption correction. Such a density is expected to be more sensitive to porosity as it is obtained directly from the X-ray intensity with no normalisation, see Eq. 2(b). This promising technique cannot however be used for the present dataset because of two unmet requirements: an accurate measurement of the current and a constant detector efficiency over the

full tilt range are needed. A finer control of the detector shadowing is also required, for example by improving the acquisition using different grid geometries and sample holder, or by using a FIB-needle sample. Overcoming these experimental limitations is crucial for making EDX-STEM technique fully quantitative and applicable to a wide range of nanomaterials.

6. Conclusions

A novel 3D absorption correction method is proposed for 3D EDX-STEM tomography. The assumptions of the classical absorption correction methods, constant X-ray generation and homogeneous absorption along the path to the surface, are refined by considering X-ray generation and absorption voxel by voxel. The approach is applied on the three highly absorbed X-ray lines, Zn Lα, O Kα and C Kα, measured on a core/shell nanowire. The accuracy of the approach is assessed comparing X-ray lines with high absorption (Zn Lα, O Kα) and low absorption (Zn Kα). The absorption is the cause of an important artefact in the reconstruction, observed as X-ray intensity variation in the unexpected direction of the beam and resulting in a discrepancy of the shell and an appendage of the core. Applying the 3D absorption correction, this artefact is greatly reduced: the shell

morphology formed by the O Kα intensity projection is near complete and the appendage of the core formed by the C Kα intensity projection is removed. Thanks to the 3D absorption correction, 3D EDX/TEM tomography can be extended to highly

References

[1] J. I. Goldstein, Principles of Thin Film X-Ray Microanalysis, in: J. J. Hren, J. I. Goldstein, D. C. Joy (Eds.), Introduction to Analytical Electron Microscopy, Springer US, 83–120, 1979.

[2] S. J. B. Reed, Electron microprobe analysis, 2nd edition, Cambridge University Press, 1997.

[3] D. B. Williams, C. B. Carter, The Transmission Electron Microscope, Springer US, 1996.

[4] M.Watanabe, X-Ray Energy-Dispersive Spectrometry, in: S. J. Pennycook, P. D. Nellist (Eds.), Scanning Transmission Electron Microscopy, Springer New York, 291–351, 2011.

[5] P. Schlossmacher, D. O. Klenov, B. Freitag, S. von Harrach, A. Steinbach, Nanoscale chemical compositional analysis with an innovative S/TEM-EDX system, Microsc. and Anal. 142 (2010) S5.

[6] L. Strueder, P. Lechner, P. Leutenegger, Silicon drift detector - The key to new experiments, Naturwissenschaften 85 (11) (1998) 539–543.

[7] H. Von Harrach, P. Dona, B. Freitag, H. Soltau, A. Niculae, M. Rohde, An integrated multiple silicon drift detector system for transmission electron microscopes, J. Phys.: Conf. Ser. 241, 2010.

[8] K. Lepinay, F. Lorut, R. Pantel, T. Epicier, Chemical 3D tomography of 28nm high K metal gate transistor: STEM XEDS experimental method and results, Micron 47 (2013) 43–49.

[9] P. Burdet, J. Vannod, A. Hessler-Wyser, M. Rappaz, M. Cantoni, Three-dimensional chemical analysis of laser welded NiTi-stainless steel wires using a dual-beam FIB, Acta Mater. 61 (8) (2013) 3090–3098.

[10] A. Genc, L. Kovarik, M. Gu, H. Cheng, P. Plachinda, L. Pullan, B. Freitag, C. Wang, XEDS STEM tomography for 3D chemical characterization of nanoscale particles, Ultramicroscopy 131 (2013) 24–32.

[11] P. Burdet, C. Hébert, M. Cantoni, Enhanced quantification for 3D energy dispersive spectrometry: Going beyond the limitation of large

volume of X-ray emission, Microsc. and Microanal. 20 (5) (2014) 1544–25.

[12] B. Goris, L. Polavarapu, S. Bals, G. Van Tendeloo, L. Liz-Marzan, Monitoring galvanic replacement through three-dimensional morphological and chemical mapping, Nano Lett. 14 (6) (2014), 3220-3226.

[13] C. S. M. Yeoh, D. Rossouw, Z. Saghi, P. Burdet, R. K. Leary, P. A. Midgley, The Dark Side of EDX Tomography - Modelling detector shadowing to aid 3D chemical signal analysis, Microsc. and Microanal. In press.

[14] G. Haberfehlner, A. Orthacker, M. Albu, J. Li, G. Kothleitner, Nanoscale voxel spectroscopy by simultaneous EELS and EDS tomography, Nanoscale 6 (23) (2014) 14563-14569.

[15] T. J. A. Slater, A. Macedo, S. L. M. Schroeder, M. G. Burke, P. O'Brien, P. H. C. Camargo, S. J. Haigh, Correlating Catalytic Activity of Ag-Au Nanoparticles with 3D Compositional Variations, Nano Lett. 14 (4) (2014) 1921-1926.

[16] G. Möbus, R. Doole, B. Inkson, Spectroscopic electron tomography, Ultramicroscopy. 96 (3-4) (2003) 433–451.

[17] Z. Saghi, X. Xu, Y. Peng, B. Inkson, G. Möbus, Three-dimensional chemical analysis of tungsten probes by energy dispersive x-ray nanotomography, Appl. Phys. Lett. 91 (25) 2007.

[18] M. Schaffer, J. Wagner, B. Schaffer, M. Schmied, H. Mulders, Automated three-dimensional X-ray analysis using a dual-beam FIB, Ultramicroscopy 107 (8) (2007) 587–597.

[19] P. Midgley, M. Weyland, 3D electron microscopy in the physical sciences: The development of Z-contrast and EFTEM tomography, Ultramicroscopy 96 (3-4) (2003) 413–431.

[20] P. Midgley, R. Dunin-Borkowski, Electron tomography and holography in materials science, Nat. Mater. 8 (4) (2009) 271–280.

[21] R. Leary, Z. Saghi, M. Armbrüster, G. Wowsnick, R. Schlögl, J. Thomas, P. Midgley, Quantitative high angle annular dark-field scanning transmission electron microscope (HAADF-STEM) tomography and high resolution electron microscopy of unsupported intermetallic $GaPd_2$ catalysts, J. of Phys. Chem. C 116 (24) (2012) 13343–13352.

[22] P. Hawkes, The electron microscope as a structure projector, in: Electron Tomography: Methods for Three- Dimensional Visualization of Structures in the Cell, Springer US, 83–111, 2006.

[23] J. Bullock, C. Humphreys, A. Mace, H. Bishop, J. Titchmarsh, Crystalline effects in the analysis of semiconductor materials using Auger electrons or X-rays, Inst. Phys. Conf. Ser. No.76, Section 9 (1985) 405-410.

[24] J. I. Goldstein, J. Costley, G. Lorimer, R. J. B. Reed, Quantitative X-ray analysis in the electron microscope, in: O. Johart (Ed.), Scanning Electron Microscopy, vol. 1, IITRI, Chicago IL, 315–324, 1977.

[25] G. Cliff, G. Lorimer, The quantitative analysis of thin specimens, J. Microsc. 103 (2) (1975) 203–207.

[26] Z. Horita, K. Ichitani, T. Sano, M. Nemoto, Applicability of the differential X-ray absorption method to the determinations of foil thickness and local composition in the analytical electron micrscope, Phil. Mag. A, 59 (5) (1989) 939–952,

[27] P. J. Statham, M. D. Ball, An indirect method for determining mass thickness for absorption corrections in the microanalysis of thin

foils, in: D. B. Wittry (Ed.), Microbeam Analysis, San Francisco Press, San Francisco, CA, 165–168, 1980.

[28] O. Eibl, New method for absorption correction in high-accuracy, quantitative EDX microanalysis in the TEM including low-energy X-ray lines, Ultramicroscopy 50 (2) (1993) 179–188.

[29] M. Watanabe, Z. Horita, M. Nemoto, Absorption correction and thickness determination using the ζ factor in quantitative X-ray microanalysis, Ultramicroscopy 65 (3-4) (1996) 187–198.

[30] M. Macias-Montero, A. N. Filippin, Z. Saghi, F. J. Aparicio, A. Barranco, J. P. Espinos, F. Frutos, A. R. Gonzalez-Elipe, A. Borras, Vertically Aligned Hybrid Core/Shell Semiconductor Nanowires for Photonics Applications, Adv. Funct. Mater. 23 (48) (2013) 5981–5989.

[31] Hyperspy: Hyperspectral data analysis toolbox, http://hyperspy.org.

[32] E. R. Malinowski, Factor Analysis in Chemistry, 3rd Edition, John Wiley & Sons Inc, 3 ed, 2002.

[33] D. Rossouw, P. Burdet, F. de la Peña, C. Ducati, B. R. Knappett, A. E. H. Wheatley, P. A. Midgley, Multicomponent Signal Unmixing

from Nanoheterostructures: Overcoming the Traditional Challenges of Nanoscale X‑ray Analysis via Machine Learning, Nano Let. In press.

[34] C. O. Sorzano, C. Messaoudi, M. Eibauer, J. R. Bilbao-Castro, R. Hegerl, S. Nickell, S. Marco, J. M. Carazo, Marker-free image registration of electron tomography tilt-series, BMC Bioinformatics 10 (1) (2009) 124.

[35] A. H. Andersen, A. C. Kak, Simultaneous Algebraic Reconstruction Technique (SART): A superior implementation of the ART algorithm, Ultrasonic Imaging 6 (1) (1984) 81–94.

[36] P. Ramachandran, G. Varoquaux, Mayavi: 3D Visualization of Scientific Data, Comput. Sci. Eng. 13 (2) (2011) 40–51.

 [37] A. Chambolle, An Algorithm for Total Variation Minimization and Applications, J. Math. Imaging Vis. 20 (1-2) (2004) 89–97.

[38] M. Watanabe, D. B. Williams, The quantitative analysis of thin specimens: a review 27 of progress from the Cliff-Lorimer to the new ζ-factor methods, J. Microsc. 221 (2) (2006) 89–109.

[39] J. Philibert, A method for calculating the absorption correction in electron-probe microanalysis, in: H. H. Pattee, V. E. Cosslett, A.

Engström (Eds.), Proceedings of the 3rd International Congress on X-Ray Optics and Microanalysis, Academic Press, New York NY, 1963.

[40] G. Lucas, P. Burdet, M. Cantoni, C. Hébert, Multivariate statistical analysis as a tool for the segmentation of 3D spectral data, Micron 52-53 (2013) 49–56.

[41] M. Keenan, P. Kotula, Accounting for Poisson noise in the multivariate analysis of ToF-SIMS spectrum images, Surf. Interface Anal. 36 (3) (2004) 203–212.

[42] P. Burdet, S. Croxall, P. Midgley, Enhanced quantification for 3D SEM-EDS: Using the full set of available X-ray lines, Ultramicroscopy 148 (2015) 158–167.

[43] Z. Saghi, D. Holland, R. Leary, A. Falqui, G. Bertoni, A. Sederman, L. Gladden, P. Midgley, Three-dimensional morphology of iron oxide nanoparticles with reactive concave surfaces. A compressed sensing-electron tomography (CS-ET) approach, Nano Let. 11 (11) (2011) 4666–4673.

[44] D. Newbury, D. B.Williams, J. I. Goldstein, C. Fiori, Observation on the calculation of kAB factors for analytical electron microscopy, in:

D. B.Williams, D. C. Joy (Eds.), Analytical Electron Microscopy, San Francisco Press, San Francisco CA, 276–278, 1984.

Figure
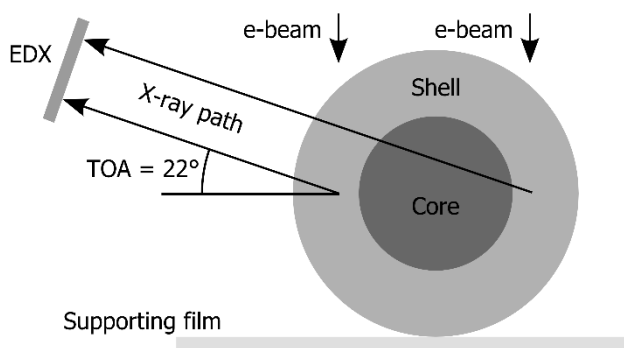
Figure 1: X-ray absorption in a core/shell nanowire. The X-rays are generated in a nanowire supported by a film. The arrows show two X-ray paths through the sample towards an EDX detector. A typical take-off angle (TOA) is given.
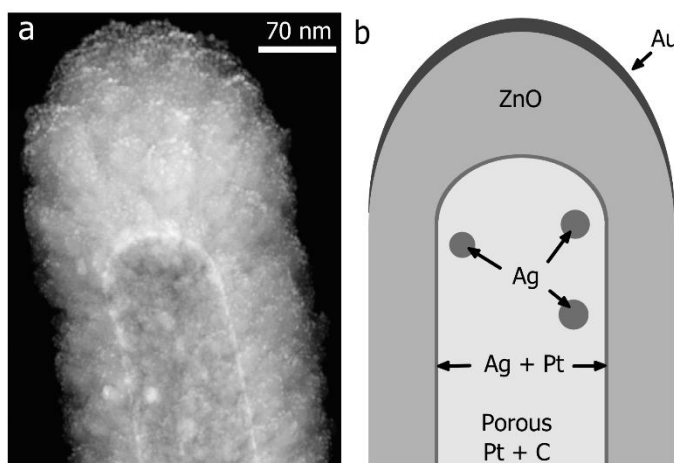
Figure 2: Tip of a core/shell nanowire. (a) High angular dark field (HADF) micrograph. (b) Schematic pictures of the sample. The elements composing the different phases are indicated.
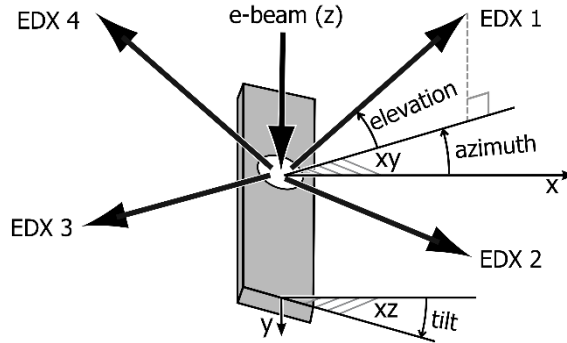
Figure 3: Geometry for 3D TEM-EDX acquisition. The grey box represents the sample holder. The electron beam direction is vertical and defines the z axis. The elevation angle is the take-off angle for a surface tilted 0°. The azimuth is the angle between x axis and the projection of the detector direction on a surface tilted 0°. The y axis is the rotation axis of the tilt.
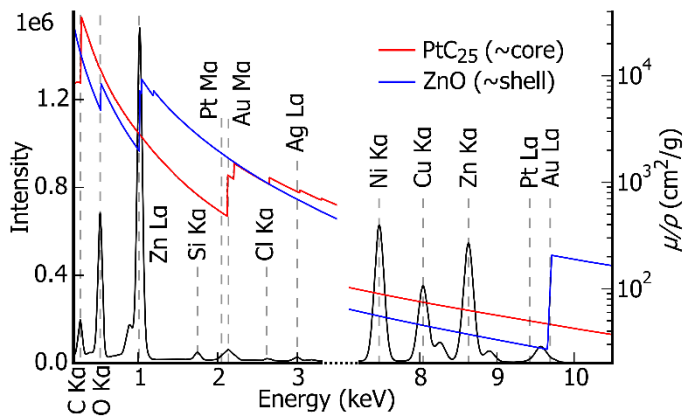
Figure 4: X-ray lines emitted from a core/shell nanowire and corresponding absorption coefficient. The EDX spectrum, a sum over all spectra of the tilt series, is plotted with a plain curve (left scale). The mass absorption coefficients μ/ρ of X-rays absorbed in PtC_{25} and ZnO, composition approximating the core and the shell respectively, are plotted as a function of energy with dashed curves (right scale). The centre of the main X-ray peaks are indicated by vertical dashed lines. Minor lines are not labelled.
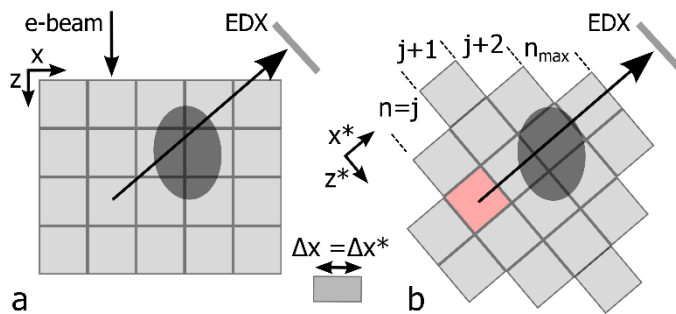
Figure 5: Calculation of the absorption correction matrix, A from the the matrix of elemental fraction $\mathbf{C}_{vol}$. The arrows indicate the path of the X-ray towards the detector. The array of square represent the voxel. The grey scale represents the elemental fraction of one element in the voxel. The same elemental map is represented in the two different referentials. In (a), z axis is parallel to the electron beam. In (b), x axis is parallel to the detector direction.
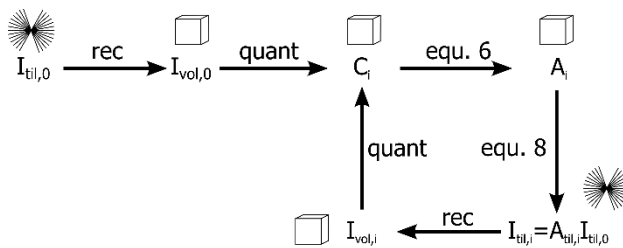
Figure 6: Details of the iterative process for 3D absorption correction. Composition **C** are quantified (quant) from X-ray intensities **I** that are corrected by absorption correction factors **A**. The 3D intensities matrix **I**$_{vol}$ are reconstructed (rec) from tilt series of intensities **I**$_{til}$ at each *i* step of the iteration.
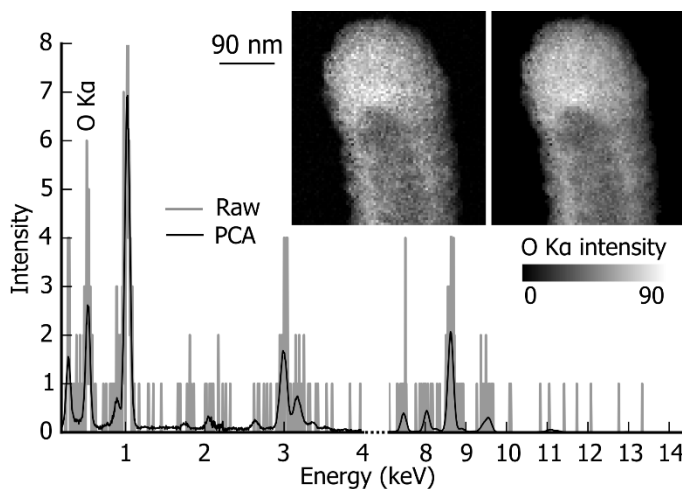

Figure 7: Noise reduction using PCA. A spectrum is plotted before (grey) and after PCA decomposition/reconstruction (black). The spectrum is extracted from the data set at the position of an Ag particle. The raw intensity map for O Kα (acquired at tilt 0°) is plotted before

(left hand side) and after PCA decomposition/reconstruction (right hand side).
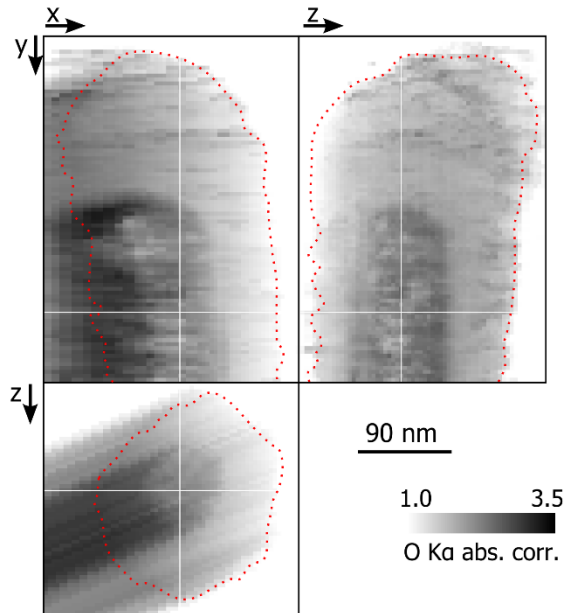
Figure 8: Details of the 3D absorption correction factors. The maps give the absorption correction matrix $\mathbf{A}_1$, first iteration, for the O Kα intensity as orthogonal sections of the 3D volume. The white lines show the position of the orthogonal sections. The red dashed line shows the limit outside which the total X-rays intensity is below 7 counts.
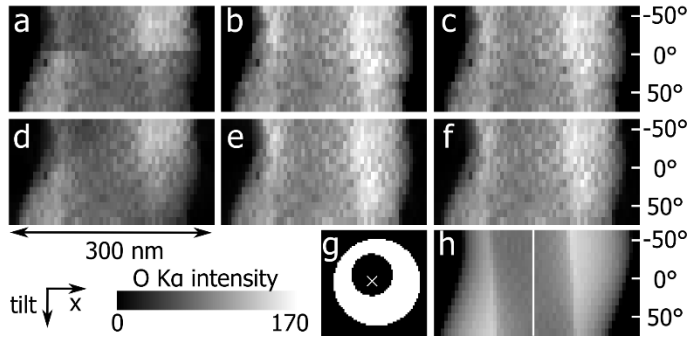
Figure 9: 3D Absorption correction effect on tilt series after one and two iterations. The maps give the O Kα intensity as x-tilt sections: the tilt series ($\mathbf{I}_{til}$ for map a, map b and map c) and the direct projection of $\mathbf{I}_{vol}$ ([$\mathbf{I}_{vol}$]$_{til}$ for map d, map e and map f). Map a and d are not corrected for absorption. Map b and e are corrected after one iteration. Map c and f are corrected after two iterations. Map h is the direct projection of a model of the shell shown in map g.
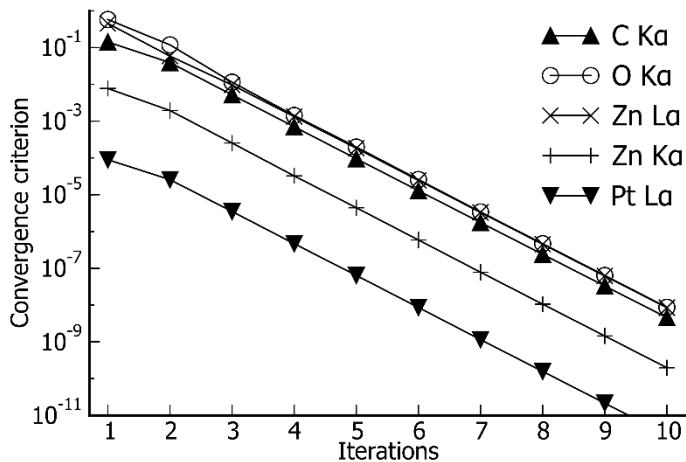
Figure 10: Convergence of the iterative process for the 3D absorption correction calculation. The convergence criterion is the RMS over the difference of the reconstruction corrected after i iterations and $i+1$ iterations ($\mathbf{I}_i$- $\mathbf{I}_{i+1}$). The X-ray lines are sorted by increasing energy.
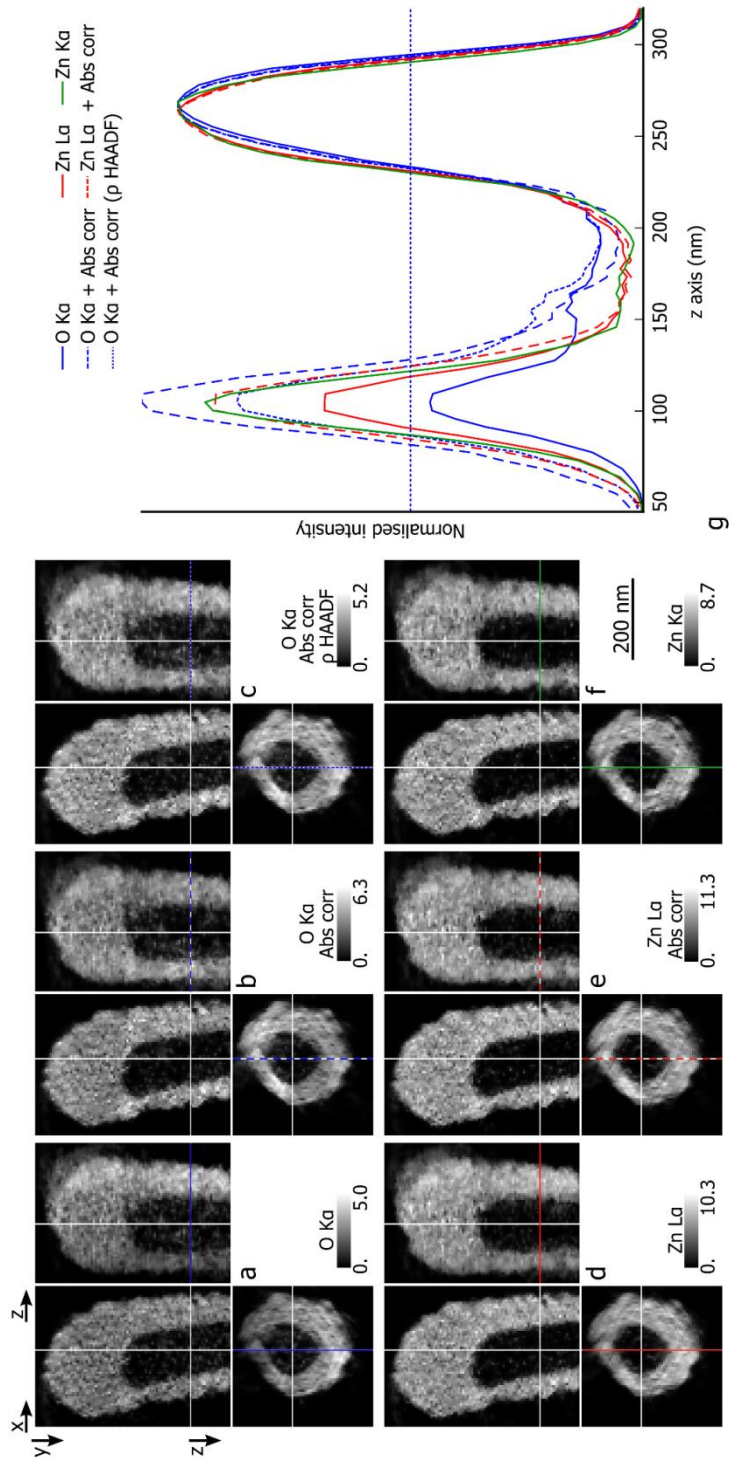
Figure 11: Details of the reconstruction of the shell. Comparison of intensities without (maps a, d, f), with 3D absorption correction after 10 iterations. The density is estimated from weighted mean (Abs corr) in maps b and e and from HAADF images (Abs corr ρ HAADF) in map c. The grey scale maps give the orthogonal sections of the reconstructed volume of the intensity of O Kα (maps a, b, c), Zn Lα (maps d, e) and Zn Kα (map f). The white lines show the position of the orthogonal sections. In (g), profiles along z are plotted for O Kα, Zn Lα and Zn Kα intensities. The position of profiles is indicated with coloured lines in the orthogonal sections. Intensities are normalised with the maximum of the profile in the right part of the shell that shows less absorption effect. The horizontal dashed blue lines show the values used for the isosurfaces in Fig. 13. All intensities are smoothed by TV filter.
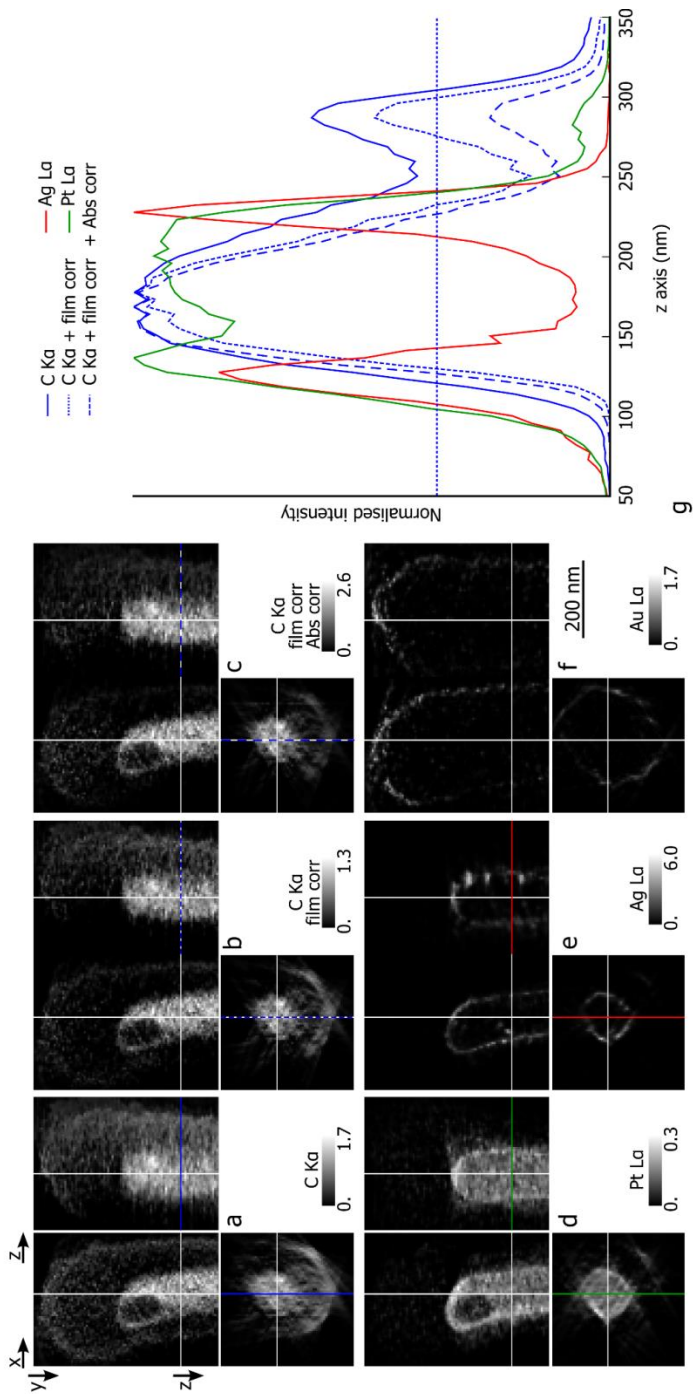
Figure 12: Details of the reconstruction of the core. Comparison of intensities without (maps a, b, d, e) or with 3D absorption correction

after 10 iterations ("Abs corr" in map c). The grey scale maps give the orthogonal sections of the reconstructed volume of the intensity of C Kα (maps a, b, c), Pt Lα (map d), Ag Lα (map e) and Au Lα (map f). Map b and c are corrected for the carbon supporting film (film corr). The white lines show the position of the orthogonal sections. In (f), profiles along z are plotted for C Kα, Pt Lα and Ag Lα intensities. The position of profiles is indicated with coloured lines in the orthogonal sections. Intensities are normalised with the maximum of the profile. The horizontal dashed blue lines show the values used for the isosurfaces in Fig. 13. All intensities are smoothed by TV filter.
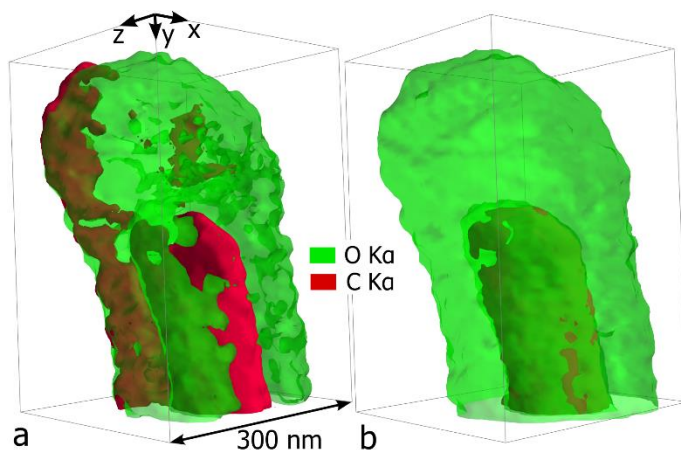

Figure 13: Details of measured core and shell. The isosurfaces are reconstructed from the volume of O Kα and C Kα intensity without and with 3D absorption correction calculated after 10 iterations for figure (a) and (b), respectively. The thresholds used to generate the

isosurfaces are indicated in Fig. 11(g) and in Fig. 12(e) by a dashed blue line.